

**INVESTIGATION ON THE FLOW SEPARATION  
CONTROL OF AIRFOIL WITH BIO-INSPIRED NOSE**

**A thesis submitted to the  
*University of Petroleum & Energy Studies***

**For the award of  
*DOCTOR OF PHILOSOPHY*  
in  
*Aerospace Engineering***

**BY**

**Mohamed Arif. R**

**March 2021**

**SUPERVISOR**

**Dr. Rajesh Yadav**



**Department of Aerospace Engineering  
School of Engineering  
University of Petroleum and Energy Studies  
DEHRADUN-248007: Uttarakhand**

**INVESTIGATION ON THE FLOW SEPARATION  
CONTROL OF AIRFOIL WITH BIO-INSPIRED NOSE**

**A thesis submitted to the  
*University of Petroleum & Energy Studies***

**For the award of  
*DOCTOR OF PHILOSOPHY*  
in  
*Aerospace Engineering***

**BY**

**Mohamed Arif. R  
(SAP ID- 500057670)**

**March 2021**

**Supervisor**

**Dr. Rajesh Yadav**  
*Assistant Professor (SG)*  
Department of Aerospace Engineering  
University of Petroleum and Energy Studies



**Department of Aerospace Engineering  
School of Engineering  
University of Petroleum and Energy Studies  
DEHRADUN-248007: Uttarakhand**

**March 2021**

**DECLARATION**

I declare that the thesis entitled “**INVESTIGATION ON THE FLOW SEPARATION CONTROL OF AIRFOIL WITH BIO-INSPIRED NOSE**” has been prepared by me under the guidance of **Dr. Rajesh Yadav**, Assistant professor in Department of Aerospace Engineering, University of Petroleum & Energy Studies. No part of this thesis has formed the basis for the award of any degree or fellowship previously.

A handwritten signature in black ink, appearing to read 'Arif. R.', is written over a horizontal line. The signature is stylized and cursive.

**Mohamed Arif. R**

School of Engineering  
University of Petroleum & Energy Studies  
Dehradun-248007: Uttarakhand

DATE: 25.03.2021

## CERTIFICATE

I certify that **Mohamed Arif. R** has prepared his thesis entitled “**Investigation on the flow separation control of airfoil with bio-inspired nose**”, for the award of PhD degree of the University of Petroleum & Energy Studies, under our guidance. He has carried out the work at the Department of Aerospace Engineering, University of Petroleum & Energy Studies.



**Supervisor**

**Dr. Rajesh Yadav**

*Assistant Professor (SG)*

Department of Aerospace Engineering

University of Petroleum and Energy Studies

Date: 25. 03. 2021

## ACKNOWLEDGEMENT

First and foremost, I am extremely grateful to my guide, **Dr. Rajesh Yadav**, Assistant Professor - Selection Grade at University of Petroleum and Energy Studies, for his invaluable advice, continuous support, and patience during my PhD study. His immense knowledge and plentiful experience have encouraged me in all the time of my academic research.

I would like to thank **Dr Ugur Guven**, Former senior Professor, The SRC panel members and The Head of the Aerospace engineering department, at University of Petroleum and Energy Studies for their insightful comments and encouragement.

I would also like to thank **Dr. L.R. Ganapathy Subramanian**, Professor & HOD and **Dr. R. Vasudevan**, Professor at SRM University for all their support to complete my PhD without any difficulties. I would like to thank all my colleagues. it is their kind help and support that have made my PhD successful.

Finally, I would like to express my gratitude to all my family members. Without their tremendous understanding and encouragement in the past few years, it would be impossible for me to complete my study.

## **ABSTRACT**

In general, the flow separation phenomenon influences the aerodynamic performance of an aircraft highly. Flow separation is inevitable as the flow is viscous, but it can be delayed, i.e. the separation point can be moved downstream further by energising the boundary layer. Hence, the wake region and the drag can be reduced. The development of various flow control methods helps the aircraft to enhance its operation economically. The flow control methods mainly categorised as passive and active method.

This paper mainly aims to achieve an optimum flow separation control over the airfoil using a passive flow control method by introducing a bio-inspired nose (Cetacean species - aquatic marine mammals) near the leading edge of the NACA airfoil. In addition, to find the optimized leading-edge nose design for NACA 4 and 6 series airfoils for flow separation control.

To achieve the flow control, two distinguished methods have been implemented on the leading edge of the NACA 2412 airfoil: i) Forward Facing step - which induces multiple acceleration at low angle of attack ii) Cavity/Backward facing step - which creates recirculating region (axial vortices) at high angle of attack. The computational analysis has been done for NACA 2412 airfoil with different bio-inspired nose designs at low subsonic speed. 54 different bio-inspired nose designs which are inspired by the cetacean family marine mammals have been considered for the analysis.

It has been found that at low angle of attack, longer bio-inspired nose enhances the aerodynamic efficiency because of multiple accelerations on the nose by forming a forward-facing step. However, it is not effective at a high angle of

attack due to early flow separation starting at the leading edge of the longer nose. At a high angle of attack, deeper depth nose design is more effective than the shallow depth nose design due to the vortex formation by forming a cavity shape on the nose, which delays the flow separation. However, deeper depth nose design is not effective at low angle of attack due to the movement of the stagnation point above the nose, which affects the pressure distribution and reduces the aerodynamic force. The shorter nose with a medium depth cavity shows optimum enhancement within the operative range of angles of attack. The length and depth of the bio-inspired nose play an important role to change the aerodynamic performance of the airfoil than the diameter of the nose circle.

The optimum bio-inspired nose airfoil (The porpoise airfoil: shorter length and medium depth i.e., depth - 2.25 % of chord, nose length - 0.75 % chord, and nose diameter – 2 % chord) delay the flow separation and improves the aerodynamic efficiency by increasing the lift and decreasing the parasitic drag within the operative range of angle of attack. As the angle increase the effect of flow separation control also increases.

Different bio-inspired noses that are inspired by the cetacean species have been analyzed for different NACA 4 & 6 Series airfoils at low and high subsonic speeds. Bio-inspired nose with different nose length, nose depth, and nose circle diameter have been analyzed on airfoils with different thicknesses, different camber, and different camber locations to understand the aerodynamic flow properties such as vortex formation, flow separation, aerodynamic efficiency and moment. The porpoise nose design (shorter length and medium depth i.e. depth - 2.25 % of chord, nose length - 0.75 % chord, and nose diameter – 2 % chord) delays the flow separation and improves the aerodynamic efficiency by increasing the lift and decreasing the parasitic drag (without affecting the pitching moment) for all the NACA 4 & 6 series airfoils irrespective of airfoil geometry such as different thicknesses, different camber and different camber location.

The addition of bio inspired nose (porpoise nose) on the thin airfoil increases the stalling characteristics of low thickness airfoil, and its stalling performance

matches with the thick airfoil. Hence, it is found that the low thickness airfoils with porpoise nose can be used instead of thick airfoils, which produces lesser drag at low angles of attack than thick airfoils and gives more or less same performance as the thick airfoils at high angles of attack. And it is also found that the airfoil aerodynamic performance has been altered and matched with other NACA airfoils by adding the porpoise nose. Hence it is found that this porpoise nose can be used to alter the aerodynamic performance of the airfoil instead of morphing of wing upto certain extend.

The maximum improvement in aerodynamic efficiency is achieved using the porpoise nose after the stall angle. The porpoise nose on NACA 2412 airfoil shows maximum increment in aerodynamic efficiency by 66.5% at 18° angle of attack for Re. No. of  $3 \times 10^6$ . The porpoise nose on NACA 66215 shows maximum increment in aerodynamic efficiency by 77.7%, at 12° angle of attack for Re. No. of  $9 \times 10^6$ .

The porpoise nose design effectively controls the flow separation until the shock formation occur on the airfoil. It is effective upto the critical Mach number. Hence it can be incorporated in UAV's, propeller aircrafts, turbo-prop aircrafts, and short-range jet transport aircrafts.

This universal optimum nose design (porpoise nose) improves aerodynamic performance and increases the structural strength of the aircraft wing compared to other conventional movable high lift devices and flow control devices. This universal leading-edge flow control device can be adapted to aircraft wings incorporated with any NACA 4 & 6 series airfoil.

The 3D simulation is done to find the optimum span wise length and the position of nose on finite wing. Nose with spanwise length of 100%, 50%, and 25% of a finite wingspan ( $1b$ ,  $0.5b$ , and  $0.25b$ ) and positions such as root, mid portion, and tip of the finite wing were considered for the analysis. The porpoise nose design delays the flow separation and improves the aerodynamic efficiency at high angles of attack ( $> 6^\circ$ ) without adversely affecting the performance significantly at low angles of attack ( $< 6^\circ$ ). The effectiveness of porpoise nose on flow separation control increases with increasing angles of attack and speed.



The finite wing with porpoise nose of full spanwise length showed better aerodynamic efficiency than other spanwise length nose models.

The porpoise nose on the finite wing with NACA 2412 shows maximum increment in aerodynamic efficiency by 42% at 18° angle of attack for Re. No. of  $3 \times 10^6$ . The effectiveness of porpoise nose on flow control decreases as the spanwise length of porpoise nose decreases. Even the porpoise nose with 25% of wing span length shows the increment in aerodynamic efficiency by 15% at 18° angle of attack for Re. No. of  $3 \times 10^6$  without adversely affecting the aerodynamic performance at low angles. The smaller length porpoise nose located at wing root can be effectively used for the flow control of UAV's and smaller aircrafts.

The effectiveness of porpoise nose 50% of wing span length was decreasing when its location moved from wing root to wing tip. because the flow is merely two dimensional near the root section of wing and it becomes three dimensional near wing tip. However, after stalling angle, the porpoise nose positioned at different location along the wing span shows almost similar improvement on increase in aerodynamic efficiency, as the flow separates form the surface.

Finally, the effectiveness of porpoise nose on flow separation control has been compared with other conventional flow control methods and high lift methods. It is found that most of the methods augment the aerodynamic efficiency only during the take-off / landing and adversely affect the cruise performance of the aircraft. Hence it is observed that the fixed leading edge porpoise nose design shows the increment in aerodynamic efficiency within the working range of angle of attack and it is feasible to mount in the existing aircraft wing without many practical complications.

# CONTENTS

Declaration	i
Certificate	ii
Acknowledgement	iii
Abstract	iv
Table of Contents	viii
List of Figures	xi
List of Tables	xxiv
Nomenclature	xxv
Abbreviations	xxviii
1 INTRODUCTION	1
1.1 Boundary Layer separation	1
1.2 Flow separation control methods	6
1.2.1 Active Flow Control	7
1.2.2 Passive Flow Control	8
1.3 Structure of thesis	16
2 LITERATURE REVIEW	18
2.1 Active flow control	18
2.2 Passive flow control	27
2.2.1 Vortex generators	27
2.3 Trailing edge devices	39

2.4 Leading edge devices	47
2.5 Summary	65
2.6 Motivation and Objective	65
3. RESEARCH METHODOLOGY	68
3.1 Introduction to computational method	68
3.1.1 Introduction to CFD	68
3.1.2 Governing equations of CFD	81
3.1.3 Governing equations of Turbulence models	85
3.1.4 Force Coefficients	89
3.2 Geometric modelling	92
3.2.1 Design of bio-inspired nose on NACA 2412 airfoil	94
3.2.2 Design of bio-inspired nose on NACA 4 series airfoils	98
3.2.3 Design of bio-inspired nose on NACA 6 series airfoils	100
3.2.4 Bio – Inspired nose on finite wing	100
3.3 Boundary conditions and Solver settings	102
3.4 Mesh Independence Study for 2D analysis	105
3.4.1 Solver Validation for 2D analysis	111
3.5 Mesh Independence Study for 3D analysis	114
3.5.1 Grid convergence index (GCI)	116
3.6 Experimental Validation for 2D analysis	120
4 RESULTS AND DISCUSSIONS	127
4.1 Low speed analysis on NACA airfoils	127
4.1.1 Optimum Bio-Inspired nose for NACA 2412 airfoil	127
4.1.2 Effect of Bio-Inspired nose on NACA 4 Series airfoils	137
4.1.3 Effect of Bio-Inspired nose on NACA 6 Series	

airfoils	150
4.2 High subsonic speed analysis on NACA airfoils	153
4.2.1 Optimum Bio-Inspired nose for NACA 2412 airfoil	153
4.2.2 Optimum Bio-Inspired nose for NACA 66215	157
4.3 Optimum Bio-Inspired nose for a finite wing	170
4.4 Comparison of porpoise with conventional flow control devices	182
5 CONCLUSION	196
6 REFERENCES	202
Appendix – A : Research Publications	216

## LIST OF FIGURES

Figure 1.1	: Structure of boundary layer on an airfoil	1
Figure 1.2	: Structure of boundary layer on a flat plate (Shahmohamadi and Rashidi, 2017)	2
Figure 1.3	: Velocity profiles around the separation point	3
Figure 1.4	: Mean features of boundary layer on a low Reynolds number airfoil	4
Figure 1.5	: $C_p$ distribution of airfoil with separation bubble (Choudhry et al. 2015)).	5
Figure 1.6	: Movement of separation point on airfoil surface at different angles of attack (Brendel and Mueller, 1988).	5
Figure 1.7	: Blowing and suction slots on airfoil [Zhang et al. 2018]	8
Figure 1.8	: A synthetic jet actuator (Donovan et al. 1998)	8
Figure 1.9	: Different vane type vortex generators (Lin, 2002)	9
Figure 1.10	: Riblets (Viswanath, 2002)	10
Figure 1.11	: Leading edge serrations (Soderman, 1972)	10
Figure 1.12	: Leading and trailing edge flaps (Salmi, 1950)	12
Figure 1.13	: Krueger flap (Bahrff et al. 2016)	12
Figure 1.14	: Airfoil with drooped leading edge and trailing edge gurney flap (Chandrasekhara, 2010).	14
Figure 1.15	: Leading edge tubercles (Wang and Zhuang, 2017)	16
Figure 2.1	: Airfoil with L.E. suction slot (Mccullough and Gault, 1948).	18
Figure 2.2	: The swept wing with area suction ejector flap	

	(Anderson et al. 1957).	19
Figure 2.3	: The synthetic jet actuators on Cessna182 model (Ciuryla et al. 2007).	20
Figure 2.4	: The Piezo-stack vortex generator on MAV delta wing (Mystkowski and Jastrzębski, 2013).	20
Figure 2.5	: The synthetic jet actuator arrays on wing (Tang et al. 2014).	21
Figure 2.6	: The synthetic and continuous jet actuators on cascade blade (De Giorgi et al. 2015).	21
Figure 2.7	: The synthetic jet actuators with backward-facing step (Xu et al. 2015).	22
Figure 2.8	: The active flow control on heavy ground vehicles (Seifert et al. 2015).	22
Figure 2.9	: The synthetic jet actuators on NACA 2412 (Arif et al. 2017).	23
Figure 2.10	: The NACA 0012 airfoil with L.E. vibrating diaphragm (Di et al. 2017)).	23
Figure 2.11	: The NACA 4412 airfoil with L.E. narrow drill channels (Beyhaghi, and Amano, 2017).	24
Figure 2.12	: The HAWT with split blade (Moshfeghi et al. 2017).	24
Figure 2.13	: The NACA0012 airfoil with suction control (Zhang et al. 2017).	24
Figure 2.14	: NACA 0012 wing with the lateral synthetic jet actuator (Dghim et al. 2018).	26
Figure 2.15	: The NACA 0012 with injection and suction control (Zhang et al. 2018).	26
Figure 2.16	: The NASA hump with injection and suction control (Xu et al. 2020).	27
Figure 2.17	: Different vortex generators arrangements (Griffin, 1996).	28
Figure 2.18	: The vortex generator proposed for a marine use	

	(Brandner and Walker, 2001).	28
Figure 2.19	: Different types of low-profile Vortex generators (VGs) (Lin, 2002).	29
Figure 2.20	: Mitsubishi Lancer Evolution with VGs (Koike et al. 2004).	29
Figure 2.21	: Different vortex generator shapes (Heyes and smith, 2005).	30
Figure 2.22	: Vortex generator on NACA0012 airfoil(Shan et al. 2008).	31
Figure 2.23	: NACA 4424 airfoil with fouling (Khor and Xiao, 2011).	32
Figure 2.24	: NACA 0018 foil with endplate (Gim and Lee, 2013).	32
Figure 2.25	: Vortex Generator on NACA 4412 (Agarwal and kumar, 2014).	33
Figure 2.26	: Serrate-Semi-Circular bio-inspired riblets (Saravi et al. 2014).	34
Figure. 2.27	: The counter rotated triangular VG on wind turbine blade (Manolesos et al. 2015).	34
Figure 2.28	: Vortex generator on a heavy-class helicopter fuselage (Gibertini et al. 2015).	35
Figure 2.29	: The double VG on S809 Airfoil (Haipeng et al. 2017).	36
Figure 2.30	: Vortex generator on winglet control surface (Brüderlin et al. 2017).	36
Figure 2.31	: Dimples on Darrieus VAWT (Sobhani et al. 2017).	37
Figure 2.32	: Vortex generator with free and forced flow conditions (Baldacchino et al. 2018).	37
Figure 2.33	: Wind turbine blade with vortex generators and M-plate (Zhang et al. 2019).	38
Figure 2.34	: Riso_B1_18 airfoil with a cavity (Fatehi et al. 2019).	38
Figure 2.35	: Flexible flaps on NACA0020 (Reiswich et al. 2020).	39
Figure 2.36	: The L.E. flaps and split flaps on a rectangular wing (Lange and May, 1948).	40
Figure 2.37	: Different type of L.E. flaps on wing-fuselage combination	

	(Hopkins, 1949).	40
Figure 2.38	: Different type of L.E. and T.E. flaps on sweptback wing (Salmi, 1950).	41
Figure 2.39	: Different type of L.E. and T.E. flaps on NACA 64A010 (Kelly and Hayter, 1953).	41
Figure 2.40	: The wing-turboprop engine assembly with L.E. and T.E. flaps (Gentry et al. 1994).	42
Figure 2.41	: The Helicopter rotor blade with L.E. and T.E. flaps (Noonan et al. 2001).	43
Figure 2.42	: The single slotted airfoil with gurney flaps (Wang et al. 2008).	44
Figure 2.43	: The slotted, Natural Laminar flow S103 airfoil (Somers, 2012).	44
Figure 2.44	: The semi-circular dimple and Gurney flap on NACA-0015 (Ismail and Vijayaraghavan, (2015).	44
Figure 2.45	: The suction slots on Wells turbine blade (Shehata et al. 2017).	45
Figure 2.46	: The wing with flexible and variable camber T.E. flap (Lu et al. 2017).	46
Figure 2.47	: Different T.E. configuration on HAWT blade (Chen and Qin 2017).	46
Figure 2.48	: The micro tabs on HAWT blade (Ebrahimi and Movahhedi, 2018).	46
Figure 2.49	: Handley Page slots on a wing model (Weick and Wenzinger, 1932).	47
Figure 2.50	: Airfoil with leading edge flap and split flap (Fullmer, 1947).	48
Figure 2.51	: Airfoil with leading edge serrations (Soderman, 1972).	48
Figure 2.52	: The leading-edge device on supercritical wing (Mann et al. 1983).	49
Figure 2.53	: The leading-edge extension on thick delta wing	



	(Ghaffari and Lamar, 1985).	50
Figure 2.54	: Airfoil with drooped leading edge and gurney flap (Chandrasekhara et al. 2004).	50
Figure 2.55	: The wind turbine airfoil with leading edge bump (Asli et al. 2015).	51
Figure 2.56	: The cranked arrow wing with inboard L.E. flaps (Toyoda et al. 2015).	51
Figure 2.57	: The wavy leading edge on NACA 00012 (Serson et al. 2015).	52
Figure 2.58	: The L.E. tubercle on a S814 tidal turbine (Shi et al. 2016).	52
Figure 2.59	: Airfoil with conventional slat and Krueger flap (Bahrff et al. 2016).	53
Figure 2.60	: Airfoil with Krueger flaps (Akaydin et al. 2016).	53
Figure 2.61	: A small plate near the L.E. of NACA 4405 Airfoil (Zhou et al. 2017).	54
Figure 2.62	: The micro cylinder on NACA 0012 airfoil leading edge (Luo et al. 2017).	54
Figure 2.63	: Airfoil with sinusoidal and spherical tubercle leading edge (Aftab et al. 2017).	55
Figure 2.64	: Airfoil with boundary layer trip (Sreejith and Sathyabhama, 2018).	56
Figure 2.65	: The leading-edge curved serrations on airfoil (Juknevicius et al. 2018).	56
Figure 2.66	: Leading edge vortex generators on pitching plate (Leknys et al. 2018).	57
Figure 2.67	: Airfoil with leading edge pitching plate (Leknys et al. 2018).	58
Figure 2.68	: S809 airfoil with the oscillating micro cylinder (Shi et al. 2019).	58
Figure 2.69	: The leading-edge comb extensions on airfoil (Geyer et al. 2020).	59

Figure 2.70	: The different leading-edge modifications on NACA 6-Series airfoil (Kelly J. A ., 1950).	60
Figure 2.71	: The leading-edge profile modifications on NACA 6-Series airfoil (Maki and Hunton, 1956).	60
Figure 2.72	: The modified forward contour of NACA 641-212 airfoil (Hicks et al. 1975).	61
Figure 2.73	: The upper-surface modifications on NACA 6-Series airfoil (Szelazek and Hicks, 1979).	61
Figure 2.74	: The profile modifications at L.E. and T.E. of EA-6B airfoil (Allison et al. 1995).	62
Figure 2.75	: The drooped leading edge airfoil (Sankar et al. 2000).	63
Figure 2.76	: Divergent trailing edge DLBA 186 supercritical airfoil (Yoo, 2001).	63
Figure 2.77	: Wing with and without L.E serrations (Wang and Zhuang, 2017).	63
Figure 2.78	: $C_l/C_d$ curve for different wavy airfoils (Tang et al. 2020).	64
Figure 3.1	: Main elements of CFD framework	68
Figure 3.2	: Various flow physics in CFD	69
Figure 3.3	: a) A pressure based segregated algorithm, b) a pressure based coupled algorithm, c) a density based algorithm	78
Figure 3.4	: Forces acting on an airfoil	89
Figure 3.5	: Different nose shapes of Cetacean species	92
Figure 3.6	: Methodology flow chart	93
Figure 3.7	: NACA 2412 airfoil	95
Figure 3.8	: Square grid created with respect to camber line	95
Figure 3.9	: NACA 2412 airfoil with bio-inspired nose design	96
Figure 3.10	: NACA 2412 airfoil with different bio-inspired nose designs	96
Figure 3.11	: NACA 4 series airfoils of different thickness, camber,	

	and camber location	97
Figure 3.12	: Airfoils with bio-inspired nose designs of different diameters	99
Figure 3.13	: Grid drawn with reference to chord and camber line of airfoil	99
Figure 3.14	: C-Domain with semi finite wing	101
Figure 3.15	: Semi finite wing (with NACA 2412 airfoil) with different leading-edge configurations	101
Figure 3.16	: Computational domain and mesh	107
Figure 3.17	: Coefficient of drag of NACA 2412 airfoil for different no of sections on airfoil at Reynolds Number of $3 \times 10^6$	108
Figure 3.18	: Coefficient of lift of NACA 2412 airfoil for different turbulence model at Reynolds Number of $3 \times 10^6$	109
Figure 3.19	: Coefficient of lift and drag of NACA 2412 airfoil for different turbulence model at Reynolds Number of $3 \times 10^6$	110
Figure 3.20	: Coefficient of lift of NACA 2412 airfoil at Re. No $3 \times 10^6$	113
Figure 3.21	: Drag polar curve of NACA 2412 airfoil at Re. No. $3 \times 10^6$	113
Figure 3.22	: 3D C- Domain with structured mesh	114
Figure 3.23	: The structured mesh of interior of the 3D C- Domain and different semi finite wing configurations.	115
Figure 3.24	: The computational domain with coarse, medium and fine meshes.	118
Figure 3.25	: The plot of $C_l / C_d$ with varying grid spacings.	120
Figure 3.26	: a) SRM IST – KTR low subsonic wind tunnel with pressure scanner setup. b) infinite wing model inside the test section	121
Figure 3.27	: Top view(a), and side view (b) of infinite wing model with porpoise nose airfoil. and	

	(c) Pressure scanner.	122
Figure 3.28a	: Coefficient of normal and axial of Porpoise airfoil at Re. $1.9 \times 10^5$	124
Figure 3.28b	: Coefficient of lift and drag of Porpoise airfoil at Re. $1.9 \times 10^5$	124
Figure 3.29a	: $C_p$ distribution on Porpoise airfoil at 6 deg angle	125
Figure 3.29b	: $C_p$ distribution on Porpoise airfoil at 12 deg angle	125
Figure 3.30	: Coefficient of lift and drag of NACA 2412 and Porpoise airfoil	126
Figure 4.1	: $C_d$ graph for NACA 2412 airfoils with different nose length	128
Figure 4.2	: $C_d$ graph for NACA 2412 airfoil with different nose cavity depth	128
Figure 4.3	: Pressure contour of NACA 2412 and modified airfoil at $4^\circ$ and $16^\circ$ angle of attack.	129
Figure 4.4	: NACA 2412 airfoil with grid.	131
Figure 4.5	: $C_l / C_d$ graph for NACA 2412 and bio-inspired nose airfoils with shallow cavity	131
Figure 4.6	: $C_l / C_d$ graph for NACA 2412 airfoils with deeper cavity	132
Figure 4.7	: $C_l / C_d$ graph for airfoils with shorter nose and medium depth cavity	132
Figure 4.8	: $C_l / C_d$ graph for NACA 2412 and bio-inspired nose airfoils	133
Figure 4.9	: The Dall's porpoise and modified NACA 2412 – J2 airfoil	133
Figure 4.10	: Nose profiles of NACA 2412 – J2 and Porpoise airfoil	134
Figure 4.11	: $C_p$ distribution of NACA 2412 – J2 and Porpoise airfoil	135
Figure 4.12	: $C_l$ graph for NACA 2412 – J2 and Porpoise airfoil	135
Figure 4.13	: $C_d$ graph for NACA 2412 – J2 and Porpoise airfoil	136
Figure 4.14	: Comparison of $C_l / C_d$ graph for NACA 2412 and	

	porpoise airfoil with bio – inspired nose airfoils	137
Figure 4.15	: $C_l / C_d$ graph for NACA 2418 and bio-inspired nose airfoils	139
Figure 4.16	: $C_l / C_d$ graph for NACA 2212 and bio – inspired nose airfoils	139
Figure 4.17	: $C_l / C_d$ graph for NACA 4412 and bio – inspired nose airfoils	140
Figure 4.18	: a) Different nose profiles and b) $C_p$ distribution of NACA 2418 airfoil with bio-inspired nose of different nose circle diameters	141
Figure 4.19a	: $C_l / C_d$ graph for NACA 2418 and its bio – inspired nose airfoils	142
Figure 4.19b	: $C_l / C_d$ graph for NACA 2212 and its bio – inspired nose airfoils	142
Figure 4.19c	: $C_l / C_d$ graph for NACA 4412 and its bio – inspired nose airfoils	143
Figure 4.20	: Drag polar of NACA 4 series symmetric airfoils of different thickness (6%, 8%, 12%, 15%, 21% & 24% of chord) and its modified airfoils	145
Figure 4.21	: $C_l$ and $C_d$ of NACA 4 series symmetric airfoils of different thickness (8%, 12%, 15%, 18%, 21% & 24% of chord) and its modified airfoils	146
Figure 4.22	: Drag polar of NACA 4 series unsymmetrical airfoils of different thickness (6%, 8%, 15%, 18%, 21% & 24% of chord) and its modified airfoils	147
Figure 4.23	: Drag polar of NACA 4 series unsymmetrical airfoils of different camber location (30%, 50%, 60%, & 70% of chord) and its modified airfoils	149
Figure 4.24	: Drag polar of NACA 4 series airfoils of different camber and its modified airfoils	150
Figure 4.25	: Drag polar of NACA 6 series airfoils of different	

	thickness	151
Figure 4.26	: Drag polar of NACA 6 series airfoils of different design lift coefficient	151
Figure 4.27	: Drag polar of NACA 6 series airfoils of different min pressure location	152
Figure 4.28	: Force coefficients of NACA 2412 and Porpoise airfoil at $Re. 3 \times 10^6$	154
Figure 4.29	: $C_l/C_d$ of NACA 2412 and Porpoise airfoil at $Re. No. of 3 \times 10^6$	154
Figure 4.30	: a) Pressure and b) Velocity contours of airfoils at $16^\circ$	155
Figure 4.31	: a) Shear stress distribution b) turbulent intensity of NACA 2412 and Porpoise airfoils at $16^\circ$ , c) Velocity distribution(Q-Criterion) of NACA and Porpoise at $18^\circ$ .	156
Figure 4.32	: Lift & drag coefficient of NACA and porpoise airfoils at $Re. 9 \times 10^6$	157
Figure 4.33	: Streamline pattern with velocity distribution of airfoils at $3^\circ$	158
Figure 4.34	: Streamline pattern with velocity distribution of airfoils at $6^\circ$	159
Figure 4.35	: a) Turbulent kinetic energy and b) Shear stress distribution of NACA2412 and Porpoise airfoils at $6^\circ$ .	160
Figure 4.36	: a) Turbulent kinetic energy and b) Shear stress distribution of NACA 2412 and Porpoise airfoils at $12^\circ$ .	161
Figure 4.37	: Streamline pattern with velocity distribution of airfoils at $12^\circ$	162
Figure 4.38	: Streamline pattern with velocity distribution of airfoils at $18^\circ$	163
Figure 4.39	: Lift and drag coefficient of airfoils at $Re. 12 \times 10^6$	164
Figure 4.40	: Lift and drag coefficient of airfoils at $6^\circ, 12^\circ$ & $15^\circ$ and	

	Re. $17 \times 10^6$ .	164
Figure 4.41	: a) Shear stress distribution and b) Velocity contour of airfoils at $12^\circ$ and Re. $12 \times 10^6$	165
Figure 4.42	: a) Shear stress distribution and b) Velocity contour of airfoils at $12^\circ$ and Re. $17 \times 10^6$	166
Figure 4.43	: $C_l$ and $C_d$ values of porpoise airfoil at a) $6^\circ$ and b) $12^\circ$ for different Reynolds number	168
Figure 4.44	: Classification of aircrafts based on cruising Mach number	169
Figure 4.45	: Lift and drag coefficient of wings at Re. $3 \times 10^6$	171
Figure 4.46	: a) Increment in $C_l/C_d$ of porpoise nose on airfoil and wing b) Velocity distribution (Q-Criterion) of NACA & porpoise nose wings at $18^\circ$	172
Figure 4.47	: Increment in $C_l/C_d$ for wing with different porpoise nose geometries	173
Figure 4.48	: Velocity distribution (Q-Criterion) of Porpoise nose wing with different spanwise length and location at $12^\circ$	174
Figure 4.49a	: Streamline pattern of wing with NACA 2412 at $18^\circ$ angle	176
Figure 4.49b	: Streamline pattern of porpoise nose with $0.25b$ at root ( $18^\circ$ angle)	176
Figure 4.49c	: Streamline pattern of Porpoise nose with $0.5b$ at mid ( $18^\circ$ angle)	177
Figure 4.49d	: Streamline pattern of Porpoise nose with $0.5b$ at tip ( $18^\circ$ angle)	177
Figure 4.49e	: Streamline pattern of Porpoise nose with span $1b$ Full at $18^\circ$ angle. (side view and top view)	178
Figure 4.50	: Streamline pattern with velocity distribution of NACA wing and porpoise nose wing with full spanwise length ( $1b$ ) at $12^\circ$ angle	179
Figure 4.51	: Lift and drag coefficient of Porpoise nose wing with different length and location at $6^\circ$	180

Figure 4.52	: Velocity distribution (Q-Criterion) of Porpoise nose wing with different spanwise length and location at 6°	181
Figure 4.53	: Comparison of aerodynamic efficiency of Base and Porpoise airfoil at $Re\ 3.1 \times 10^6$ .	184
Figure 4.54	: Comparison of (a) aerodynamic efficiency of Base airfoil and Wavy LE airfoil. (b) increment in aerodynamic efficiency of Wavy LE airfoil and Porpoise airfoil	185
Figure 4.55	: Comparison of (a) aerodynamic efficiency of Base airfoil and Drooped LE and TE modified airfoil. (b) increment in aerodynamic efficiency of Drooped LE and TE modified and Porpoise airfoil	186
Figure 4.56	: Comparison of (a) aerodynamic efficiency of Base model and airfoil with Slat. (b) increment in aerodynamic efficiency of airfoil with slat and Porpoise airfoil.	187
Figure 4.57	: Comparison of (a) aerodynamic efficiency of Base airfoil and LE Thickness and TE modified airfoil. (b) increment in aerodynamic efficiency of LE Thickness and TE modified airfoil and Porpoise airfoil	188
Figure 4.58	: Comparison of (a) aerodynamic efficiency of Base airfoil and airfoil with LE Micro Cylinder. (b) increment in aerodynamic efficiency of airfoil with LE Micro Cylinder and Porpoise airfoil	189
Figure 4.59	: Comparison of (a) aerodynamic efficiency of Base airfoil and airfoil with TE modification. (b) increment in aerodynamic efficiency of airfoil with TE modification and Porpoise airfoil	190
Figure 4.60	: Comparison of (a) aerodynamic efficiency of Base airfoil and Slotted flap airfoil. (b) increment in aerodynamic efficiency of Slotted flap airfoil and Porpoise	191
Figure 4.61	: Comparison of (a) aerodynamic efficiency of Base airfoil and airfoil with backward step at 0.75C. (b) increment	



	in aerodynamic efficiency of airfoil with backward step at 0.75C and Porpoise airfoil	192
Figure 4.62	: Comparison of (a) aerodynamic efficiency of Base airfoil and airfoil with VG at 0.2C. (b) increment in aerodynamic efficiency of airfoil with VG at 0.2C and Porpoise airfoil	193
Figure 4.63	: Comparison of (a) aerodynamic efficiency of Base airfoil and airfoil with Slot. (b) increment in aerodynamic efficiency of airfoil with slot and Porpoise airfoil	194

## LIST OF TABLES

Table 3.1	: Coefficient of lift and drag of NACA 2412 at 8-degree angle of attack and Reynolds Number of $3 \times 10^6$ for different $Y^+$ values	108
Table 3.2	: Coefficient of lift and drag of NACA 2412 at 10-degree angle of attack and Reynolds Number of $3 \times 10^6$ for different turbulence models	111
Table 3.3	: The coefficient of lift and drag values for wing of different mesh cell counts	116
Table 3.4	: The GCI and Asymptotic range of convergence for $C_l$ , and $C_l/C_d$ with varying grid spacings with a constant refinement ratio of 1.3	119
Table 4.1	: Range of optimum nose circle diameter	141

## NOMENCLATURE

$P$	- Static pressure
$\tau$	- Shear stress
$R$	- Resultant aerodynamic force
$m$	- Aerodynamic moment
$Re$	- Reynolds number
$L'$	- Lift per unit span
$D'$	- Drag per unit span
$N'$	- Normal force per unit span
$A'$	- Axial force per unit span
$c$	- Chord
$S$	- Reference area
$P_\infty$	- Freestream static pressure
$q_\infty$	- Freestream dynamic pressure
$\alpha$	- Angle of attack
$\frac{dy}{dx}$	- Slope of airfoil
$L/D$	- Lift to drag ratio – Aerodynamic efficiency

- $C_p$  - Coefficient of pressure
- $C_{P_l}$  - Coefficient of pressure at lower surface
- $C_{P_u}$  - Coefficient of pressure at upper surface
- $C_{f_u}$  - Coefficient of friction at upper surface
- $C_{f_l}$  - Coefficient of friction at lower surface
- $C_l$  - Coefficient of lift
- $C_d$  - Coefficient of drag
- $C_n$  - Coefficient of normal force
- $C_a$  - Coefficient of axial force
- $C_{m_{LE}}$  - Coefficient of moment at Leading edge
- $C_{L_{max}}$  - Maximum lift coefficient
- $\rho$  - Density
- $V$  - Velocity
- $L$  - Characteristic length
- $\mu$  - Dynamic viscosity
- $\kappa$  - Turbulence kinetic energy
- $\varepsilon$  - Turbulence dissipation rate
- $\omega$  - Specific dissipation rate
- $C_q$  - Suction coefficient
- $P_{oc}$  - The order of convergence
- $r$  - The grid refinement ratio
- $f$  - The discrete solutions
- $h_1, h_2$  - Grid spacing.
- $N$  - Total grid points

$D$	- Flow domain dimension
$Er$	- Estimated fractional error
$\epsilon$	- Relative error measure of property
$F_s$	- Factor of safety
$\Omega$	- Volume of CV
$\vec{R}$	- The spatial discretization
$\bar{M}$	- The mass matrix
$\frac{\partial \vec{R}}{\partial \vec{w}}$	- The flux Jacobian
$\vec{\tau}$	- The stress tensor
$\vec{F}_C$	- The convective flux tensor
$\vec{k}_D$	- The diffusive flux tensor
$\vec{Q}_v$	- The volume sources
$\vec{Q}_s$	- The surface sources
$Pr$	- Prandtl number

## ABBREVIATIONS

LBL	- Laminar boundary layer
TBL	- Turbulent boundary layer
SSB	- Short separation bubble
LoSB	- Long separation bubble
LE	- Leading edge
TE	- Trailing edge
LSB	- Laminar separation bubble
BL	- Boundary layer
VG	- Vortex generators
TLE	- Tubercle leading edge
DNS	- Direct Numerical Solution
RANS	- Reynolds-averaged Navier-Stokes equations
LES	- Large eddy simulation equations
URANS	- Unsteady Reynolds-averaged Navier-Stokes
RSM	- Reynolds stress models
NW	- Near-wall

VKL scale	- Von Karman length-scale
MAV	- Micro aerial vehicle
SJA	- Synthetic-jet-actuator
CJA	- Continuous -jet-actuator
CFJ	- Co-Flow Jet
HAWT	- Horizontal axis wind turbine
VAWT	- Vertical axis wind turbine
LEE	- Leading-Edge Extension
SCF	- Slat - Cove filler
SGF	- Slat gap filler
DTE	- Divergent T.E
TSR	- Tip speed ratio
GCI	- Grid convergence index

# CHAPTER 1

## INTRODUCTION

### 1.1 Boundary layer separation

Flow around the airfoil has two regions such as viscous region near the wall (boundary layer) and inviscid region away from the wall (free stream). Boundary layer starts with laminar boundary layer (LBL) which is thin and has low velocity gradient, then transit to turbulent boundary layer (TBL) which is thick and has higher velocity gradient near the wall as mentioned in Fig 1.1. Outside boundary layer velocity gradient are so small and shear stress is negligible. Within the boundary layer, normal component of the velocity is usually much smaller than streamwise component of velocity. In laminar boundary layer, transverse transport of momentum takes place on a microscopic scale. But in turbulent boundary layer it happened in macroscopic scale. In turbulent boundary layer slow moving lower layer particles moves upward and fast-moving higher layer particles moves towards the surface. The shear stress at the wall for TBL is higher than LBL.

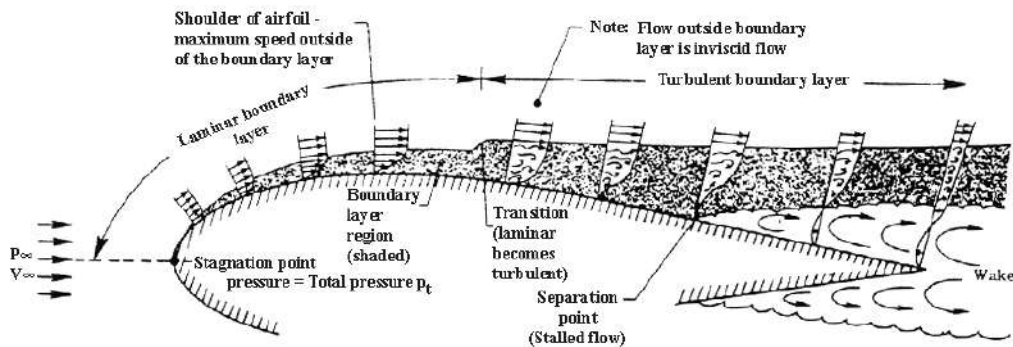
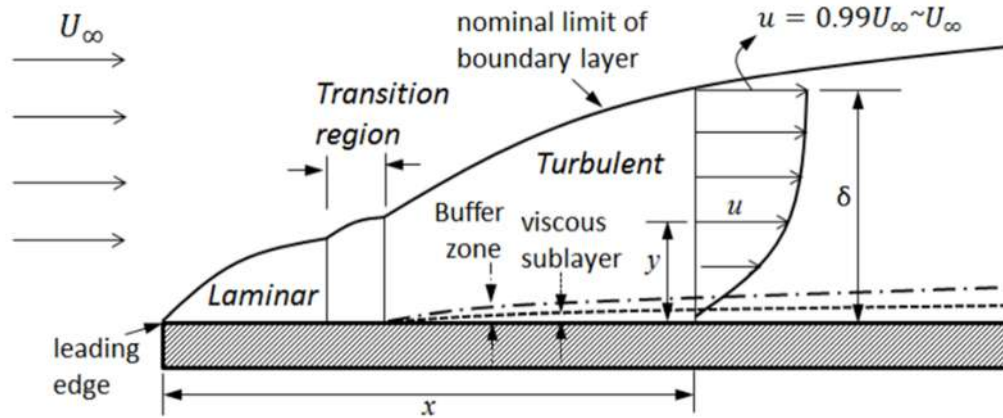


Figure 1.1: Structure of boundary layer on an airfoil



Turbulent flow consists of irregular three-dimensional fluctuations (mixing/ eddying motion), and velocity at point is a function of time. These fluctuations increase the viscosity, shear forces, skin friction drag etc. Turbulent boundary layer penetrates the increasing pressure region and extend for longer distance, i.e. delays the separation and reduces the pressure drag.



**Figure 1.2:** Structure of boundary layer on a flat plate (Shahmohamadi and Rashidi, 2017)

The velocity profile of laminar and turbulent boundary layer is different (Fig 1.2 and 1.3). In LBL, the energy of freestream is conveyed to the flow near the wall. So appreciable proportion of boundary layer flow velocity is reduced. In TBL, the large mass interchanges are present in the transverse direction to the surface so freestream easily penetrates to the layer closer to the surface. Thin region adjacent to the surface is purely viscous layer, this is called viscous sublayer (where velocity falls sharply). So viscous shear stress relation should be applied only in this viscous sublayer not throughout TBL. Under favourable pressure gradient conditions, the streamwise pressure force suppress the shear stress, so flow is attached. But in unfavourable pressure gradient, the pressure force enhances the shearing action. So, flow decelerates, then separates and reverses for strong positive pressure gradient. From the separation point, boundary layer separates from the surface. The mass flow in front and behind the separation point is same above the separation region (Fig 1.3).

LBL has greater extend of lower energy flow near wall, so causes separation. But TBL stick better to surface. Because of separation wake thickness increases,

it reduces the pressure near trailing edge and increases the pressure drag. At larger angles, separation points move forward and results in larger wake. This affects the larger low-pressure region on the airfoil suction side and lift which leads to stall. For low Reynolds number, disturbances will be damped by viscous effect and boundary layer will remain laminar. At high Reynolds number disturbance may grow, so boundary layer become unstable and transits to TBL. Boundary layer transition is due to pressure gradient, surface roughness, compressibility effect, surface temperature, suction/ blowing at surface, turbulence in freestream, etc.

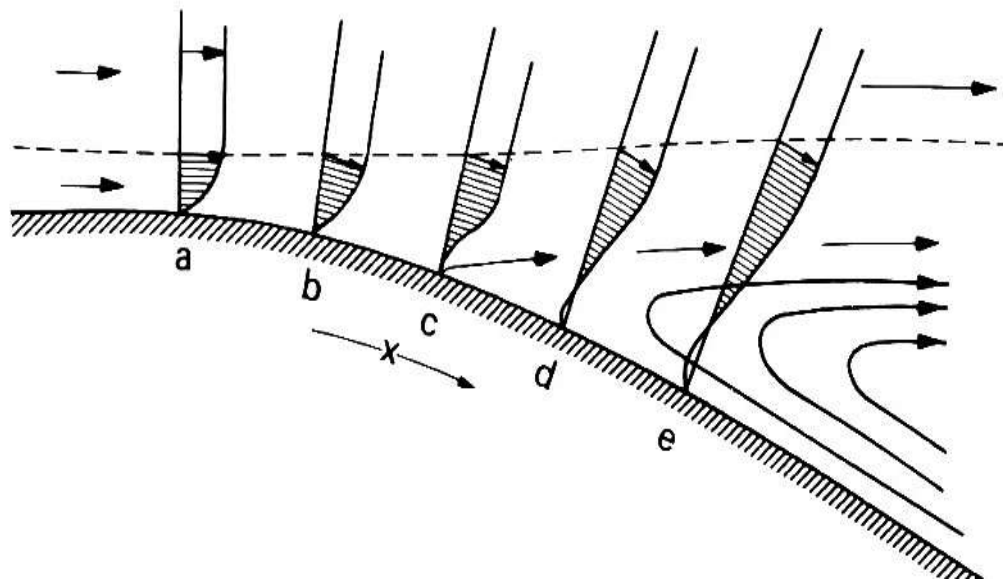


**Figure 1.3:** Velocity profiles around the separation point

The laminar flow separates from the nose and reattaches again on the surface of the airfoil after certain distance and forms the recirculation region between the separation and reattachment point. This region is called laminar separation bubble (Fig.1.4). Within the bubble region, the separated flow undergoes laminar to turbulent transition, hence energizes the flow and makes it reattaches again on the wall of airfoil. As the Reynolds number increases, bubble length decreases. The bubble length increases for increase in the incident angle of airfoil before airfoil stalls. Thinner airfoil produces longer bubbles than thicker airfoils (Owen and Klanfer, 1955). The separation bubble is adversely affecting the aerodynamic and stall performance of airfoils.

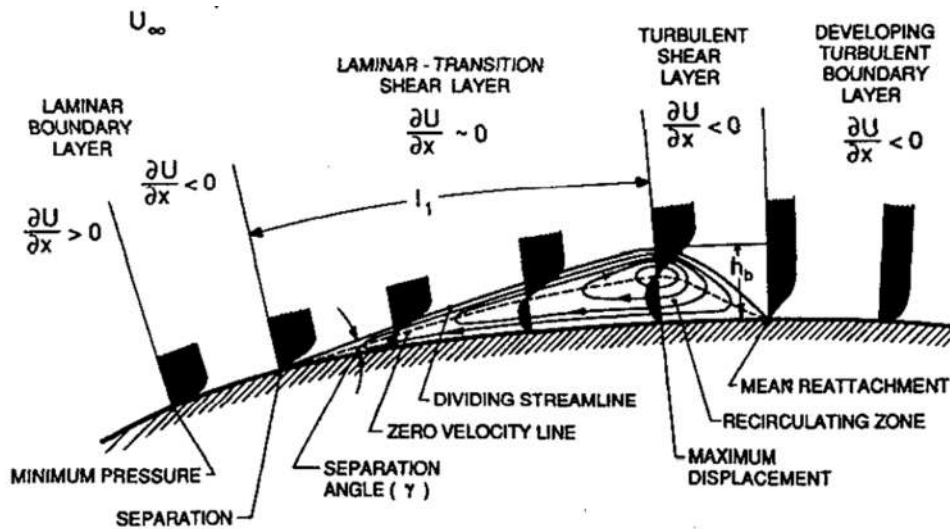


**Figure 1.4** Mean features of boundary layer on a low Reynolds number airfoil. At moderate angles, separation bubble will appear on airfoil upper surface. Small disturbances grow at low Re. No. in separated boundary layer. Separated boundary layer undertakes transition and reattaches again as TBL on surface. Below this the fluid is trapped and forms bubble shape streamline. It has constant pressure at the front and increasing pressure with circulatory motion at the back.

A short separation bubble (SSB) covers a chordwise extent of less than one percent. Therefore, it does not influence the peak suction pressure and pressure distribution around the airfoil to a large extent. If angle increases bubble moves slowly forward and final stall happens. On the other hand, a long separation bubble (LoSB) can cover several percent of the airfoil chord or extend even in wake region with large effect on the peak suction value. therefore, severely affects the pressure distribution and forces generated by the airfoil (Fig 1.5). Bubble length increases with increase in incidence angle. This causes continuous reduction of leading edge (L.E.) suction peak and lift (common in thin airfoil). If Reynolds number is  $<400$ , then long bubble would appear. If Reynolds number is  $>550$ , then short bubble will form. According to Owen Klanfer criterion, both the above conditions may occur for intermediate Reynolds number. SSBs are commonly observed on thin airfoil sections near the leading edge where large pressure gradients exist and have been studied extensively (Crabtree, 1959; Von Doenhoff, 1938; Tani, 1939; Owen and

Klanfer, 1953). It has been shown that an increase in the angle of attack or a reduction in the Reynolds number can lead to the ‘bursting’ of the bubble resulting in the formation of a LoSB or an unattached free shear layer.

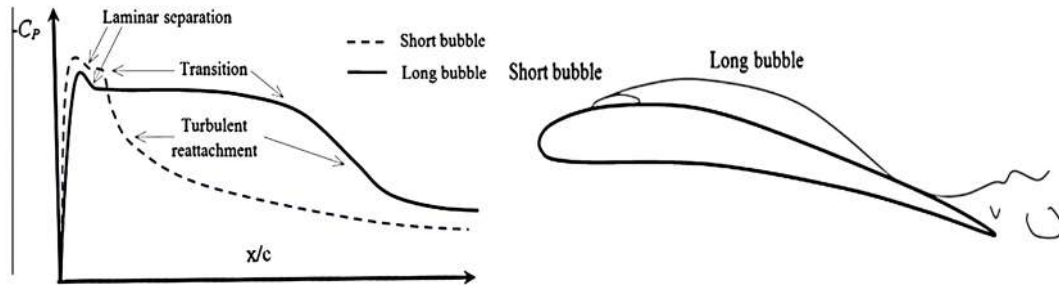


**Figure 1.5:**  $C_p$  distribution of airfoil with separation bubble (Choudhry et al. 2015)).

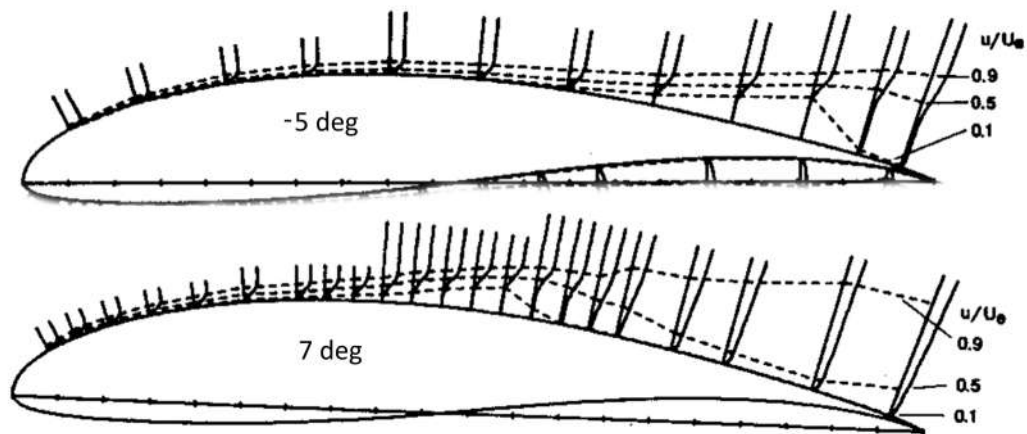


**Figure 1.6** Movement of separation point on airfoil surface at different angles of attack (Brendel and Mueller, 1988).

As the angle of attack increases the separation point moves forward towards the leading edge (Fig 1.6). Hence at high angles, flow separates from the leading edge of the airfoil, so airfoil stalls. At high angles of attack, high lift devices are the main lift augmented method, which increases wing area, angle of incidence, camber and circulation. The high lift devices increase lift and drag. So, it is used only at take-off and landing phases. Maximum lift is limited by boundary layer separation and onset of supersonic flow.

Laminar airfoils are associated with laminar separation bubble (LSB) and transition. LSB is easily formed in laminar flow and increases drag due to

bubble and turbulent flow after the bubble. Unfortunately keeping the surface smooth is not possible as there will be a surface roughness, dust deposits, ice and moisture formation, rivets, etc. So, these affects the laminar flow, and cause B.L. transition and increase the drag. Because of these drawbacks, variety of flow control methods and devices are used to extend the laminar flow and to avoid separation or promote the transition and eliminates the bubble and reduces the drag.

## **1.2 Flow separation control methods**

In general, the flow separation phenomenon influences the aerodynamic performance of an aircraft highly. In an aircraft wing, flow separation occurs when the kinetic energy of the boundary layer decreases due to surface friction. This causes a wake region, which produces a pressure difference in the direction of the flow and creates an undesirable force called drag. Flow separation is inevitable as the flow is viscous but it can be delayed, i.e. the separation point can be moved downstream further by energising the boundary layer (B.L). So that the wake region and the drag can be reduced. The development of various flow control methods helps the aircraft to enhance its operation economically. Flow separation is delayed by two methods. The active flow control technique consumes external energy to alter the flow condition such as tangential blowing, synthetic jets, pulsed jets, suction, and plasma actuators. Passive flow control method includes, (i) fixed mechanical devices installed at leading edge and trailing edge (turbulators, riblets, vortilons, vortex generators (VG) etc.) and (ii) profile modifications (surface roughness, dimples, bumps etc.) to alter the flow condition without using external energy. Both active and passive methods are employed in aerodynamic research. Mostly the passive control method is used for the flow control on an aircraft wing/airfoil as well as in commercial applications. Most of the passive control methods concentrate on modifying the flow structure near the leading edge (L.E) and trailing edge (T.E) of the airfoil. Particularly the leading-edge portion is focused because the flow separation point will be in and around that region at high angles of attack, which causes highly separated flow and drag. Similarly, most of the methods are applied on

the suction side of the airfoil where high quality attached airflow must be maintained for better aerodynamic efficiency.

Numerous boundary layer control methods delay the flow separation and greatly reduce the parasite drag thereby increases the aerodynamic performance of aircraft wing/airfoil1 at low speeds. Mostly flow separation control methods are employed on the aircraft wing at high angle of attacks such as Take-off and Landing phase of the aircraft where the separation is prominent. The subsequent section describes the previous studies done on the different flow control methods as follows.

- a. Active Flow Control
  - i. Blowing or Suction Jet
  - ii. Vibrating Mechanism
- b. Passive Flow Control
  - i. Vortex Generators
  - ii. Profile Modifications
  - iii. L.E. and T.E. Devices

### **1.2.1 Active Flow Control**

The tangential injection of air from the upper surface of the airfoil near to the leading edge (before the separation point) adds the momentum to the slow-moving B.L, moves the separation point rearwards, hence reduce the drag. The suction slots positioned near the rear portion of the airfoil (after the separation point) removes the slow-moving flow and separated flow. This adds momentum to the B.L, sucks the separated flow so that flow is attached to further distance, and reduce the wake and drag. In some cases, both tangential injection near the L.E. and suction near the T.E. (Fig. 1.7) reduce the drag effectively [Zhang et al. 2018]. The position of suction slots near the L.E. (to enhance the flow control at high angle of attack) and the position of blowing of air near the T.E. (to maintain the attached flow over the airfoils) show increase in aerodynamic efficiency.

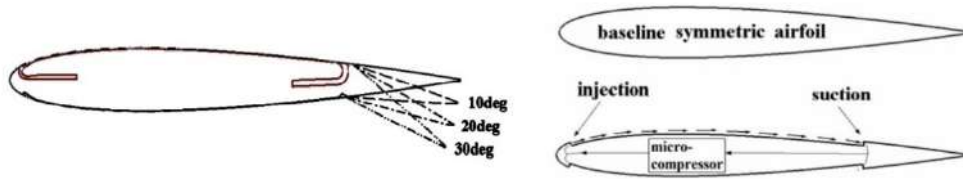


**Figure 1.7:** blowing and suction slots on airfoil [Zhang et al. 2018]

A synthetic jet [Donovan et al. 1998 and Tang et al. 2014] is formed by drawing and pushing air through the same opening at high frequencies (Fig. 1.8). This jet increases momentum to airflow without adding mass (zero mass jet). Oscillatory injection of jet was further efficient than steady blowing of jet. Instead of using pump / compressor to inject / suck the air through the slots, synthetic jet actuators are used to create the synthetic jet. Actuator may consist of vibrating diaphragm, moving piston, or rotating blade placed inside the cylinder (Arif et al. 2017) which reciprocates the air through the slot due to their up and down movement.

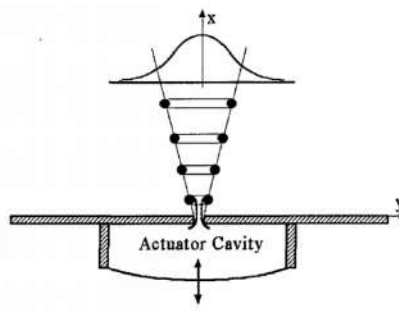


**Figure 1.8:** A synthetic jet actuator (Donovan et al. 1998)

### 1.2.2 Passive Flow Control

Usually, to energize the slow-moving B.L. on the upper surface, a small vane is attached near L.E., which is called a vortex generator (Fig. 1.9). The vane produces the axial vortex due to the pressure difference across vanes. Therefore, it increases the kinetic energy of B.L. near the wing surface, and delays the flow separation and aerodynamic stalling. However, the fixed vane type VGs are high drag devices when the airfoil/wing is at low angle of attack as it disturbs the smooth flow. So, it is desirable only during a small part of the total operating time. It was preferred that the height of the VG is equal to the

B.L height. However, it will cause excess drag at low angles. It is found that the low-profile VGs with the device heights of 10% to 50% of boundary-layer height produces the same or even larger amount of normalized circulation downstream of the vane with much lower device drag [Gámiz et al. 2014]. Particularly vortex generator with 20% of the boundary-layer thickness is preferable. The most effective range is about  $5 - 30h$  ( $h$  – height of vortex generator) upstream of baseline separation. The inclined pair of vortex generator arranged near L.E. and T.E. demonstrates improved control of separation and L/D of the airfoil [Haipeng et al. 2017]. The vortex generator placed closer to the separation point is more effective. The spacing between the VG affect the performance of the VGs [Zhen et al. 2011].

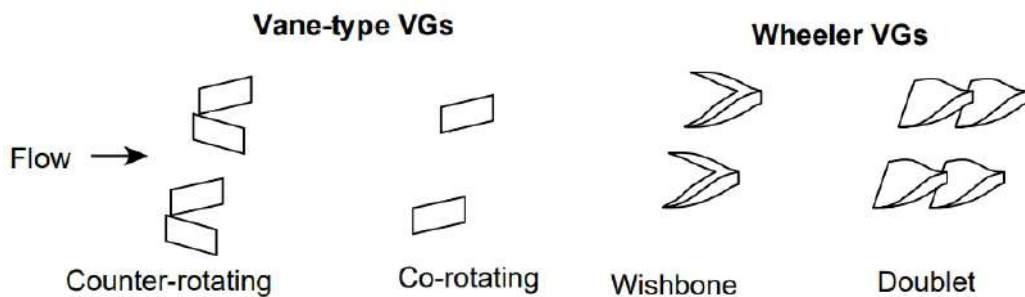


**Figure 1.9:** Different vane type vortex generators (Lin, 2002)

The separation point on the airfoil will vary as the angle varies. As the angle increases, the point of separation shifts frontward to the L.E. and finally separates from airfoil. For the effective operation of VGs, its position should be varied as the angle changes. However, it is practically not possible/difficult to incorporate a movable vortex generator in the aircraft wing. In commercial aircraft wing, the fixed position of VGs near the L.E. portion is chosen to reduce the drag at high angle where the drag is very high. Moreover, the smaller number of low-profile VGs are used to get the enough flow control at high angle and to avoid additional drag by the vortex generates at low angle of attack such as cruising. Another passive control method is the bio-inspired riblet surfaces (Fig. 1.10) used for reduction of the skin friction drag. It will be efficient if it is in same orientation ( $<10^\circ$ ) [Viswanath 2020].



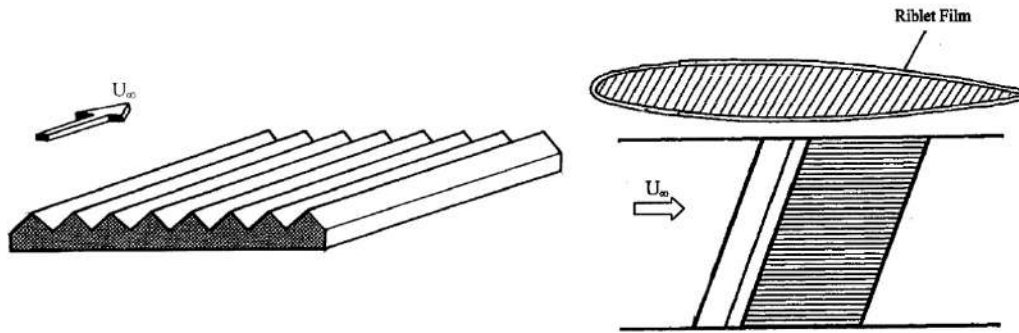


**Figure 1.10:** Riblets (Viswanath, 2002)

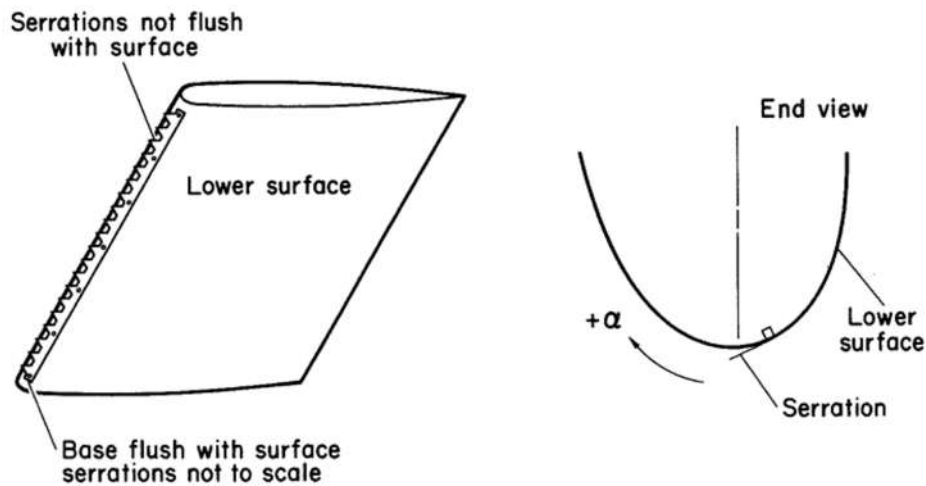


**Figure 1.11:** leading edge serrations (Soderman, 1972)

The laminar to turbulent flow transition on the airfoil helps the flow separation control. The highly sticking turbulent flow reattaches again on the surface and delays the separation. To induce the transition, tripwire, micro cylinders are placed in front of the leading edge of the airfoil/wing. It increases the  $L/D$  after the stalling angle (Luo et al. (2017)). The turbulent transition on the airfoil is induced by many methods such as the dimples (small size cavities) on the upper surface of the airfoil [Sobhani et al. 2017]. Trip wire placed in front of the L.E. and on the upper surface [Leknys et al. 2018], Stationary and oscillating cylinder [Shi et al. 2019] in front of the airfoil, vibrating diaphragm strips on the upper surface of the airfoil, the leading edge serrations (Fig. 1.11) at the L.E. of the airfoil [Soderman 1972], and Turbulators such as roughness strip, zig-zag strip placed on the L.E. of the airfoil. The larger serration causes to stall sooner because it obstructed the flow over the upper surface. So, the

smaller serration is used to eliminate the L.E. separation and to delay the T.E. separation at higher angles. Small cavities on the upper surface of the airfoil used to trap the vortex in it. The low-pressure region inside the cavity sucks the separated flow and enhance the aerodynamic efficiency at high angles of attack [Fatehi et al. 2019]. The oscillating cylinder delays the separation and increases the L/D more than the stationary cylinder. A similar effect of improvement can be achieved by increasing the static cylinder about 4 times the initial diameter (Shi et al. (2019)). The tripping device promotes the early transition of flow and shows a reduction in the bubble, upgrades the L/D, and stall angle (Choudhry et al. (2015)). Under dynamic stall, the flow is in a high flow separation condition, which makes the airfoil behaves as a bluff body. The thin tripwire placed near a leading edge reduces the maximum lift and flow fluctuations. The change in diameter of thin wire does not have any impact on the flow separation. It is quantified that the tripwire is not a possible mode of flow control under dynamic stall (Leknys et al. (2018)). A small plate placed near the L.E, produces an interference flow, and the plate effectively reduces the detachment of the flow and provides a relatively high  $C_l$  at a large angle. A small plate suppresses the separation bubble formed at high angles of attack. However, after a stalling angle, the bubble appears again and reduces the effect of the plate (Zhou et al. (2017)). The B.L trip reduces/removes the laminar separation bubble (LSB). It increases the L/D with a noticeable increase in drag at large angles (Sreejith & Sathyabhama (2018)). The pitching flat plate attached to L.E. and T.E. of wing become inactive at high incident angles (Leknys et al. (2018)). The maximum size leading-edge serrations barricade the flow on the suction side, and minimum size serration eliminates or delays the separation depending on the location on the airfoil at maximum angles (Soderman (1972)). The L.E serration with the highest amplitude and wavelength shows significant improvement in both performance and noise reduction (Juknevicius et al. (2018)). The leading-edge imperfection (a slight displacement of half aerofoil profile with respect to the other) increases the drag higher than the lift, therefore, aerodynamic efficiency decreases as the displacement grows (Ayuso and Meseguer (2014)).

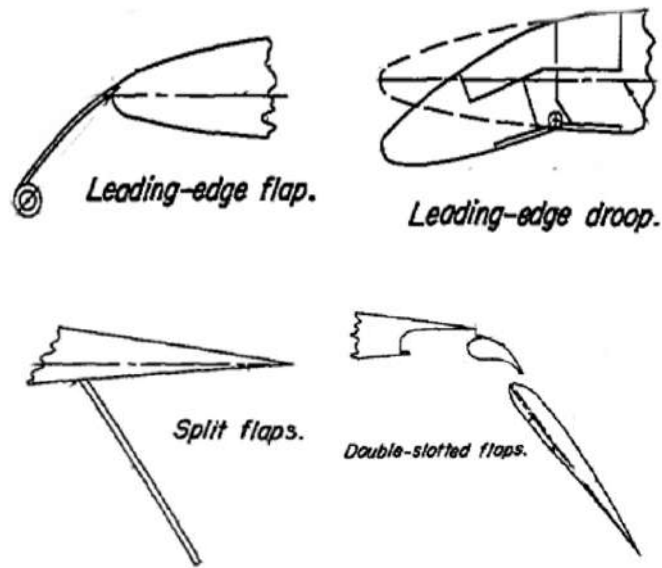


**Figure 1.12:** leading and trailing edge flaps (Salmi, 1950)

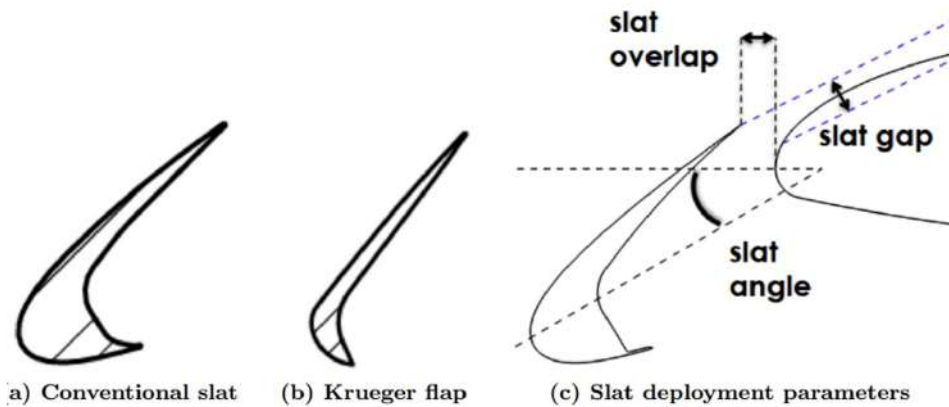


**Figure 1.13:** Krueger flap (Bahrff et al. 2016)

The flaps (Salmi 1950) fixed to the L.E. and T.E. of the airfoil /wing (Fig. 1.12) increases the lift by increasing the camber. These high lift devices increase the flow separation and drag. So, the slots (gap between the flap and the airfoil) are introduced on the aircraft wing to allow the air to pass through the slot and to add the energy to the B.L. Moreover, this flaps and slots are effective only at high angles. The Krueger flap (Fig. 1.13) exhibited a more prominent flow acceleration in the gap region and deceleration around the cavity region than a conventional slat [Bahrff et al. 2016].

Increasing the leading-edge radii and camber enhances the maximum lift without affecting stall behaviour. Increasing the leading-edge radii without changing the camber revealed no enhancement on the lift and stalling properties. The camber modifications and a slight L.E. droop along with an increased L.E. radius is effective enough in delaying the L.E. separation and substantial increases in the maximum  $C_l$ . The thickness increased near L.E. on upper surface improves the maximum  $C_l$  and stall than thickening on lower surface or L.E. radius [Kelly J. A 1950, Szelazek and Hicks 1979, Hicks 1975 and Sankar et al. 2000]. In the drooped leading-edge airfoil (Fig. 1.14), maximum of 25% of chord of the airfoil near the L.E. is deflected downwards so that the nose of the airfoil is aligned with flow streamlines. This ensures the attached flow over the airfoil upto certain distance over the upper surface of the airfoil even at high angles. It has lower suction peak, milder adverse pressure gradient, smaller separated flow and better stalling characteristics. In addition, lower drag even at high angles. Lower suction peak decreases the maximum lift slightly. Moreover, using the T.E. Gurney flap of  $0.01c$  height, recovers the loss of lift due to drooped L.E., without increasing the drag penalty [Chandrasekhara 2010]. At low angles, the lift coefficient increases by increasing the thickness but not affected by the leading-edge profile modifications. Adverse pitching moment increases with additional thickness and with leading-edge profile exponent (Merz and Hague (1975)). At low speed, the leading-edge modification increases the maximum lift coefficient and stalling angle with no increment in pitching moment. However, at high-speed, it decreases the maximum lift coefficient because of compressibility effects (Maki and Hunton (1956)). The drooped leading-edge delays the L.E separation (Fortin (2019)). The Drooping leading edge with increased leading-edge nose circle radius increases the maximum  $C_l$  and decreases the drag at high angles of attack. But at low and moderate angles, it shows an increased drag penalty and pitching moment (Hicks et al. (1975)). The drooped airfoil shows a lesser adverse pressure gradient and no stall at modest angles of attack. But it stalls dynamically with lesser drag and pitching moments at higher angles of attack (Sankar et al. (2000)). The drooped leading edge reduces the dynamic stall and drags with lesser pitching-moment and positive damping (Chandrasekhara et al.

(2004)). It reduces the lift due to a drooped edge. The loss in lift can be recovered with the help of a small Gurney flap attached at the trailing edge without increasing the drag (Chandrasekhara (2010)). The drooped-nose with extensible L.E. flap and round leading edge increases the  $C_{lmax}$ . It helps to reduce the drag increment due to the T.E. split flap (Lange and May (1948)). The drooped leading edge and trailing edge increase the stall angle and L/D after stall (Aziz et al. (2019)). Compared to the trailing-edge modification, the leading-edge modification shows a higher increment in the maximum lift coefficient (Allison et al. (1995)). The triangular protrusion at the leading edge can significantly enhance the lift produced by an airfoil (Bodavula, et al., 2019). At low Reynolds number the pre-stall aerodynamic characteristics of airfoil is greatly improved and the stall is mitigated with smaller protrusion near the leading edge (Bodavula, et al., 2019).

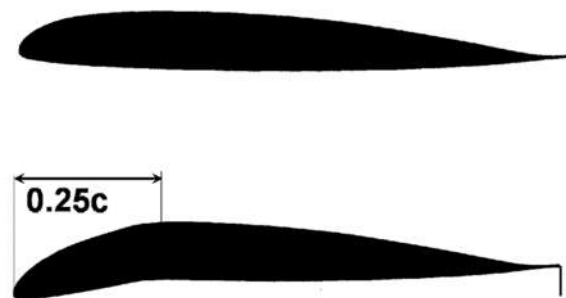


**Figure 1.14:** Airfoil with drooped leading edge and trailing edge gurney flap (Chandrasekhara, 2010).

The bio-inspired flow-separation control method is an emerging field. This includes the design inspired by marine mammals, birds, etc. The wavy leading edge (Fig. 1.15) on the airfoil profile is inspired by the flipper of a Humpback whale. The wavelength and amplitude are the important geometrical parameters to design the L.E. tubercles. The wavy leading edge shows enhancement in the lift to drag ratio with suppressed fluctuations. This is due to the generation of vortex pair from the peak (Tong et al. (2018), Rostamzadeh et al. (2013)). The wavy design increases the aerodynamic efficiency (lift increases and drag decreases) at high angles (Kobæk and Hansen (2016),

Colpitts et al. (2020)). The L.E. flow remains attached after stall. However, the strong spanwise pressure gradients reduce a lift coefficient for the angles less than the stall angle. The addition of wave shape increases the surface area of the wing and increases the friction drag at low angles. The greater number of waves on the wing lowers the aerodynamic efficiency. Hence, for higher aerodynamic performance, the less count of waves is preferable [Lin et al. 2012]. In post-stall, the sinusoidal leading edge with the largest wavelength and smallest amplitude improves the lift coefficients (Chong et al. (2015), Fernando et al (2018)). The wavelength and the leading-edge radius show a minor effect than the amplitude of protuberances on the forces and moments (Johari et al. (2007)). The protuberances on the nose decrease the aerodynamic force (lift) for a lesser incident angle because of flow disturbance by protuberances ((Chaitanya et al. (2017)). But shows a smooth stall trend at larger angles. The bumps acted as a vortex generator which creates a high momentum vortex that prevents deep stall (Asli et al. (2015)). As the airfoil thickness and flow Reynolds number increases, the effectiveness of wavy leading-edge decreases (De Paula and Meneghini (2016), De Paula et al. (2017)). The wavy leading edge adversely works on L/D but eliminates the lift coefficient fluctuations as the wavelength increases. The flow tries to attach behind the waviness crest, detach behind the troughs (Serson et al. (2015)). The tubercle design reduces the maximum lift value but increases the lift coefficients after stall situations. The full span tubercles amplify the lift and slightly increases the drag but overall, increases the aerodynamic efficiency. However, the effect reduces with a reduction in the length of the tubercle along with the span of the wing. It also reduces the induced drag (Shi et al. (2016)). The sinusoidal serrations on the L.E. improve the power output for the turbine at a low Tip-Speed Ratio (TSRs). The flow separation is considerably decreased with a positive torque generation (Wang and Zhuang (2017)). The tubercle leading edge (TLE) with sinusoidal and spherical shape reduces the aerodynamic efficiency. This reduction by spherical TLE is less than sinusoidal TLE. The spherical TLE controls the leading-edge separation bubble at high angles and improves the  $C_{lmax}$  (Aftab et al. (2017)). The improvement in stall delay and the maximum lift coefficient by the sinusoidal leading-edge wing after stall is boosted by a smart flap (Mehraban et

al. (2020)). A corrugated dragonfly airfoil gives significantly improved aerodynamic performance than the conventional airfoil / flat plate at low Re. numbers. The protrusion of the corners on the corrugated airfoil act as “turbulators” and generates the unsteady vortices. This promotes switching of laminar to turbulent and avoids laminar separation. The unsteady vortices confined in the valleys of the corrugated airfoil pushes the high momentum flow to near wall and increase the energy for the B.L flow and reduce the adverse pressure gradient, and separations [Tang et al. 2020].

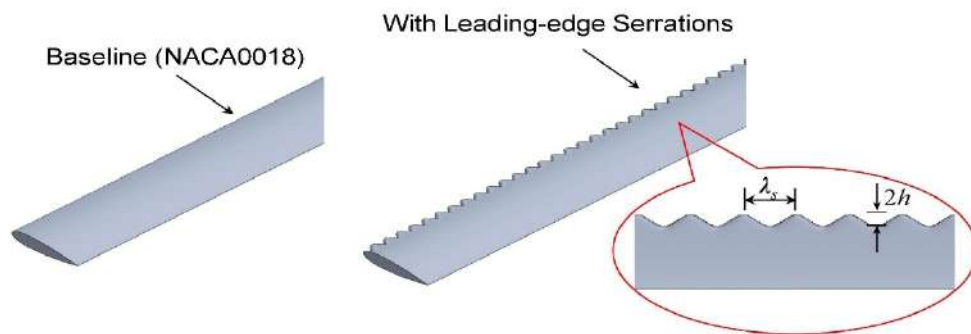


**Figure 1.15:** leading edge tubercles (Wang and Zhuang, 2017)

For the flow separation control of airfoil /wing, the passive flow control methods are preferable compared to the active flow control methods due to this simplicity and ease of mounting in existing aircraft wings. In passive flow control methods, controlling the flow near the leading edge is most preferable as most of the flow changes occur on this region than the trailing edge of the airfoil/wing. Hence, this research focus on the flow separation control method near the leading edge of airfoil/wing using the passive flow control.

### 1.3 Structure of thesis

This current chapter discuss the boundary layer formation, flow separation phenomenon, and drag of an airfoil/wing. It also discuss the different flow separation control methods to delay the flow separation and decrease the drag. At the end of the chapter, the structure of the thesis is included.

Chapter 2 discuss previous researches done on the flow separation control of airfoil and wings at subsonic speed. It is mainly focus on the passive flow

separation control methods, particularly the modifications done near the leading edge of the airfoil or wing, as it is the interest of this current research.

Chapter 3 discuss the design and computational methodology used for the analysis. It explains the governing equation of numerical methods, turbulence models, boundary conditions. It also discuss the geometry creation of various bio-inspired designs, computational domain creation, mesh generation for 2D and 3D models, mesh independence study, and solver validation.

Chapter 4 discuss the numerical results for the effect of different bio-inspired design on flow separation control on NACA 4 and 6 series at low and high subsonic speeds. It discusses the geometrical parameters of optimum bio-inspired design (porpoise nose), and the effect of porpoise nose on flow separation control on 2D airfoil and 3D wing at low and high subsonic speeds. It also presents the optimum bio-inspired nose aerodynamic performance enhancements compared to the conventional airfoils.

Finally, Chapter 5 discuss the important findings of the current research on the flow separation control by the bio inspired nose. It also suggest the ways to extend this current research in future works.



## CHAPTER 2

### LITERATURE SURVEY

Several flow control methods are used to delay the flow separation and to achieve better aerodynamic efficiency on airfoil/aircraft wing. The following section explains the previous researches done on the different flow control methods to improve the aerodynamic performance of an aircraft.

#### 2.1 Active Flow Control:

A L.E. suction slot on an NACA 631-012 (Fig. 2.1) was studied by **McCullough G. B., and Gault D. E. (1948)**. The separation originating from the L.E. was moved downstream so boosts the lift until separation originate from the T.E. and control the stall. It was noticed that the best control of stall and separation will be obtained if the suction slot is located after the separation point. Ravindran S. S. (1999) examined the oscillating type suction and blowing tangential jet at L.E., and discovered the improvement in separation delay and lift enhancement. James et al. (2018) explored the secondary blowing jet at 0.6c position for angles 2 - 18° for NACA0012 and 2 - 20° for LA203A with blowing jet speed equals to max of 0.4V (free stream velocity). The results indicated that the Steady flow jet on suction portion of aerofoil achieved good boundary separation, stall delay with increases in lift for both cases.

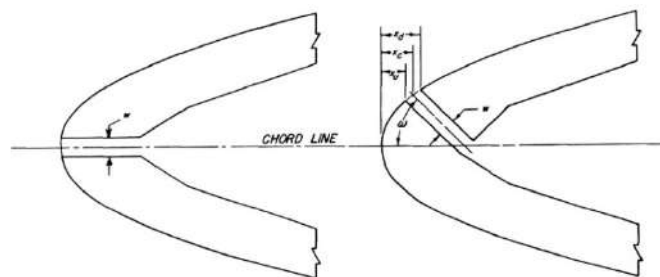


**Figure 2.1:** Airfoil with L.E. suction slot (McCullough and Gault, 1948).

**Anderson et al.** (1957) performed a study of flow control on an airplane (F-86F) with T.E. flaps, slat, and inflatable rubber boot on L.E. of the aerofoil (Fig. 2.2). The aerodynamic enhancement of the flap was increased by the inflatable rubber boot L.E. than the L.E. slat ( $C_l$  from 0.39 to 0.50). Comparing the blowing and suction L.E. flaps, the blowing flap influence the boundary layer twice as effective as L.E. suction flap in landing angles.

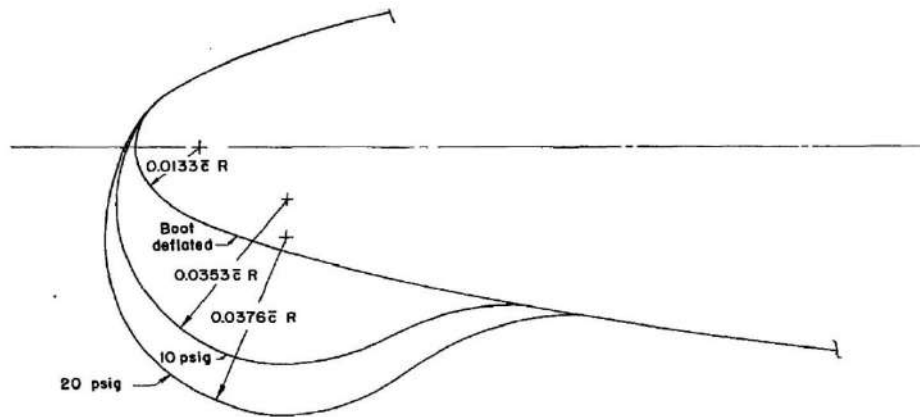


**Figure 2.2:** The swept wing with area suction ejector flap (Anderson et al. 1957).

**Tavella and Roberts** (1983) designed a wing (straight and swept) with blowing jets comes out from the tips near the leading edge using the slot at wingtips. Which helps increasing the effective span, injected at an angle will work as a control surfaces used for roll and lateral control of aircraft.

**Kupper and Henry** (2003) suggested the jet vortex generator than vane type VG and done a CFX simulation with the k- $\epsilon$  model. From the velocity plot vortex strength and size were analysed. The simulation and experiments show slight variation in vortex prediction. The simulation predicted weak vortex than experiment. The results disclosed that the jet VG not affecting the flow behaviour downstream.

**Ciuryla et al.** (2007) inspected the active control using synthetic jet actuators for separation and roll control on a small-scale prototype of Cessna182 (Fig. 2.3). Using synthetic jets, mounted in the wingtips, delays separation by 2 degrees whereas the maximum lift coefficient is increased by up to 15%. It was shown that synthetic jets can provide similar control authority as conventional

ailerons, where proportional control in pitch and roll was achieved for angles of attack larger than 6 degrees.

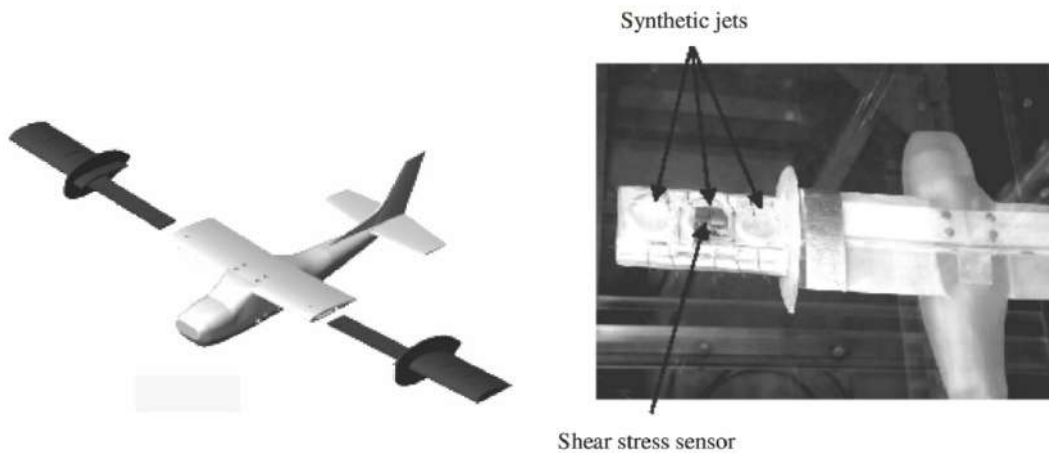


**Figure 2.3:** The synthetic jet actuators on Cessna182 model (Ciuryla et al. 2007).

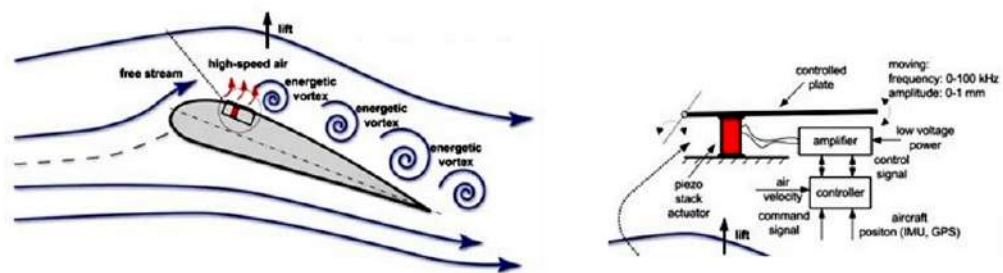


**Figure 2.4:** The Piezo-stack vortex generator on MAV delta wing (Mystkowski and Jastrzębski, 2013).

**Mystkowski and Jastrzębski** (2013) inspected Piezo-stack VG (small vibrating plates) installed on MAV (delta wing) (Fig. 2.4) for boundary-layer control. Due to the periodic vibration created by the VG flow separation got reduced.

**Tang et al.** (2014) experimented on the synthetic-jet-actuator (SJA) arrays (Fig. 2.5) for flow control which is located at  $0.23c$  and  $0.43c$  on wing. From the single SJA analysis It was obtained that the jet speed reaches a highest value among 400 Hz and 500 Hz, relates to actuator resonance frequency using hot-wire measurements. Force balance results showed that arrays are works well

with separation control enhancement and gives 27.4% raise in  $C_l$  and 19.6% fall in  $C_d$ .



**Figure 2.5:** The synthetic jet actuator arrays on wing (Tang et al. 2014).

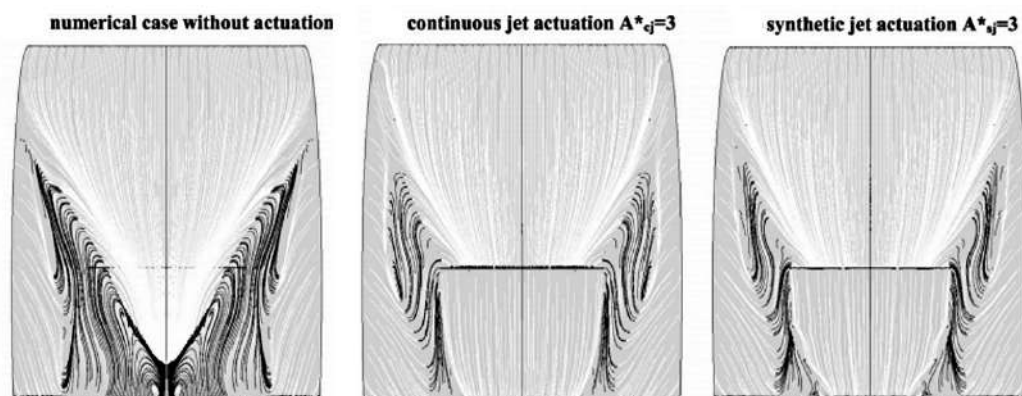


**Figure 2.6:** The synthetic and continuous jet actuators on cascade blade (De Giorgi et al. 2015).

**De Giorgi et al. (2015)** done a numerical simulation on Active flow control method applied on an airfoil and compressor cascade with SJA and CJA (Fig. 2.6). The synthetic jet actuators demonstrated desirable flow phenomena on separation control for both external and turbomachinery aerodynamics. The SJA showed two times the total pressure losses reduction than the CJA for cascade.

**Xu et al. (2015)** analysed a newly developed synthetic jet device with non-linear oscillation of the reciprocating piston actuator into the pipe is introduced and applied to control flow field of backward-facing step (Fig. 2.7). The optimum jet slot angle is 127.5 degrees and the optimum frequency is 35Hz. Sublayer fences are used to measure wall shear stress and silk threads provide auxiliary visual monitoring of the transient flow field.

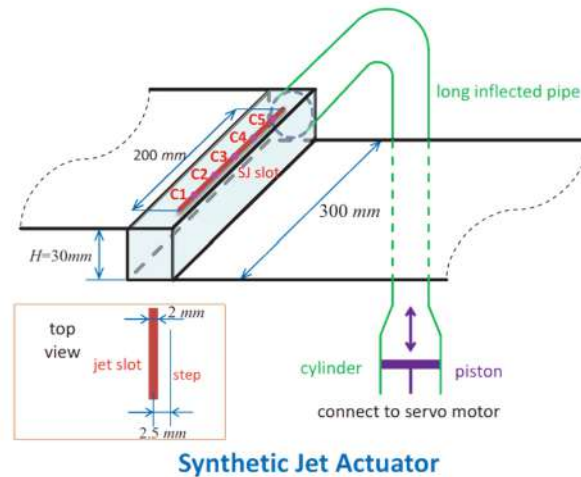


Figure 2.7: The synthetic jet actuators with backward-facing step (Xu et al. 2015).

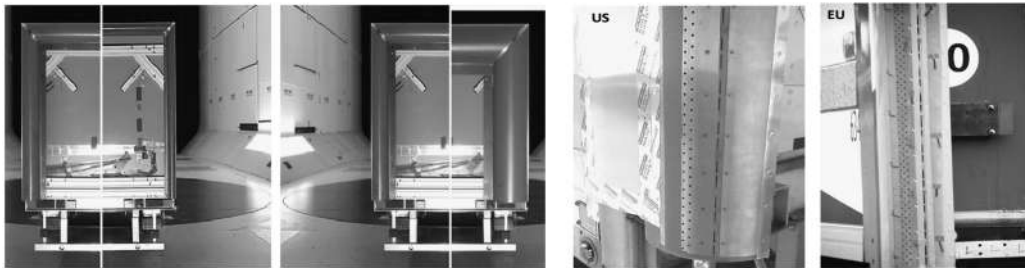
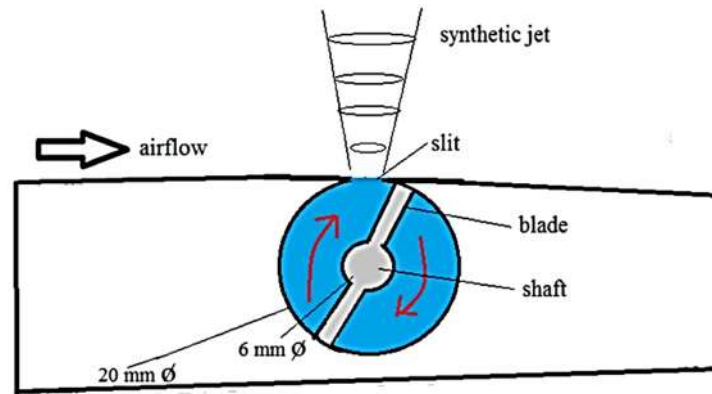


Figure 2.8: The active flow control on heavy ground vehicles (Seifert et al. 2015).

Seifert et al. (2015) examined the Active Flow Control on fuel savings of heavy vehicles (Fig. 2.8) by boosting the base pressure of large truck-trailer at highway speeds. A quarter cylinder add-on device with array Suction and unsteady blowing actuators is considered for study and found circular arc cover is not effective.

Arif et al. (2017) studied a dynamic flow control on NACA 2412 airfoil contains synthetic jet actuator (Fig. 2.9) which used a new method to produce the jet by rotating blade placed inside the cylinder which submerged within airfoil. different design parameters of rotating blade are discussed. The numerical and the experimental result shows the raise in  $C_l$  with growing angle of attack.



**Figure 2.9:** The synthetic jet actuators on NACA 2412 (Arif et al. 2017).

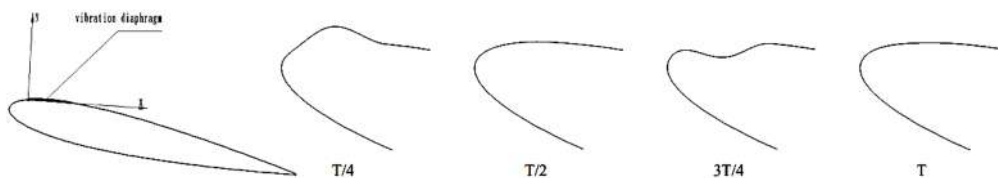


**Figure 2.10:** The NACA 0012 airfoil with L.E. vibrating diaphragm (Di et al. 2017)).

**Di et al.** (2017) tested the vibration diaphragm of  $0.1c$  length at suction side near L.E. on aerofoil (Fig. 2.10) for stall angle and  $Re=1.2 \times 10^5$ . The results indicated that the flow condition is affected by the amplitude and frequency of the diaphragm but varies with different stall angles. The maximum  $C_l$  happened at low frequency - 0.5, and maximum  $C_l/C_d$  happened at frequency 1 - 1.5 at  $16^\circ$ . And highest values (91.31%) are achieved at 0.015 amplitude and 1.4 frequency. It indicated as angles increase, the optimum amplitude increases but optimum frequency decreases up to certain angles, then keep the certain value 1.1 and wavers between 1.15–1.3.

**Beyhaghi and Amano** (2017) examined the effect of narrow drill channels (with different Length, width, angle) near the L.E. of NACA 4412 airfoil (Fig. 2.11) for  $1.6 \times 10^6$ . The drill allows air at L.E. and passes it to the bottom surface of airfoil, which raises the pressure on the lower side and gives the greater lift. It is determined that the thin and long drill channel with flow leaves parallel to the free stream on the lower side gives higher lift. To increase the benefit of slot at higher angles, drill slot should be moved to lower surface with some inclination

to the entry of slot. The average enhancement in  $C_l$  is by 8% for working range of AoA without substantial increase in drag.

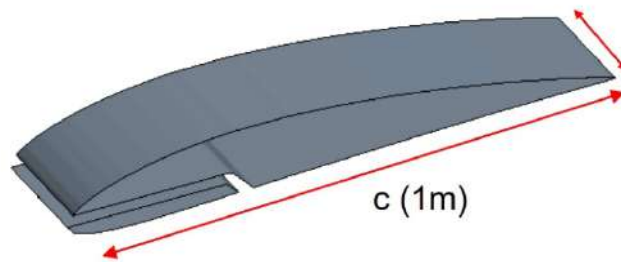


**Figure 2.11:** The NACA 4412 airfoil with L.E. narrow drill channels (Beyhaghi, and Amano, 2017).

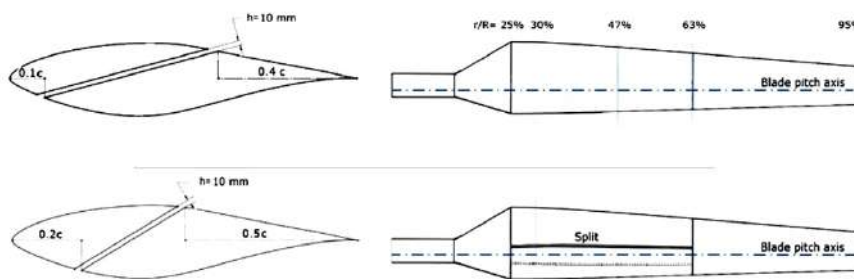


**Figure 2.12:** The HAWT with split blade (Moshfeghi et al. 2017).

**Moshfeghi et al.** (2017) modified the HAWT (S809 airfoil) (Fig. 2.12) by introducing the split along the span which connects upper and lower side in inclined angle in cross view. The parameters like split width, location, power coefficient, shaft torque, tip speed, and wind speed are taken for study. At low angles the injection location and angle play important role as it triggers separation to happen early and affect the flow. At high stall case, the split location does not have significant effect on flow. And found the split increases the total power at smaller tip speed.

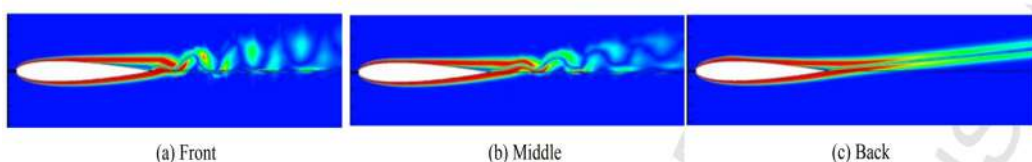


**Figure 2.13:** The NACA0012 airfoil with suction control (Zhang et al. 2017).

**Zhang et al.** (2017) studied the separation behavior of a NACA0012 airfoil (Fig. 2.13) for various Reynolds numbers and angles. The repression results of suction are examined considering of many factors. The variations in energy consumption and lift–drag ratio during the control process are used for evaluating the control effects. With the rise in suction coefficient ( $C_q$ ), the flow separation point shifts back to the trailing edge. The vortex shedding is fully suppressed when  $C_q \geq 0.01$ , and the flow field is steady and the lift–drag ratio increases first, reaches the highest value at  $C_q = 0.01$ , and then decreases. With the similar porosity, the hole thickness and the space among the adjacent holes have very small effect on the foil drag and lift–drag ratio.

**Siau and Bonnet** (2017) presented the transitory incidents happening during the spontaneous control of flow separation over a NACA0015 airfoil at an incidence angle of  $11^\circ$  and a chord Reynolds number of 1 million. The pressure transducers are in the detached area of the airfoil, which expands  $0.3c$  upstream of the trailing edge. To limit the flow, the fluid vortex generators are in a single span wise array situated  $0.3c$  after the L.E. The unsteady performance of the attachment procedure is also qualitatively examined through a  $0.3 \times 10^6$  Reynold number of visualizations. A reduction of the wake was detected when using the jets. Regarding the performance of the jet system,  $C_d$  was reduced by 37 percentage.

**Dghim et al.** (2018) inspected (using hotwire anemometry) the tip vortex control of rectangular wing (NACA 0012) with synthetic jet actuation (SJA) injected laterally from the square tip (Fig. 2.14) at  $Re. 8 \times 10^4$ . The synthetic jet produced by the low frequency actuator extended to longer distances so that wing tip vortex core region falls within the jet core and destroying the turbulent structures by well mixing and diffusivity of both flows at tip.



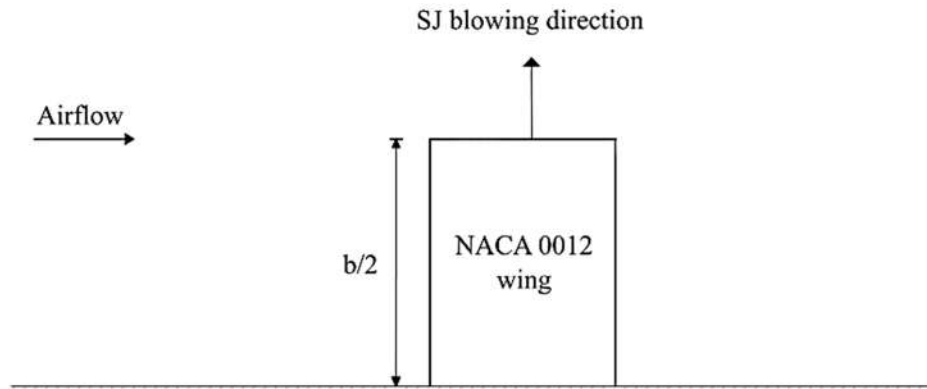


**Figure 2.14:** NACA 0012 wing with the lateral synthetic jet actuator (Dghim et al. 2018).

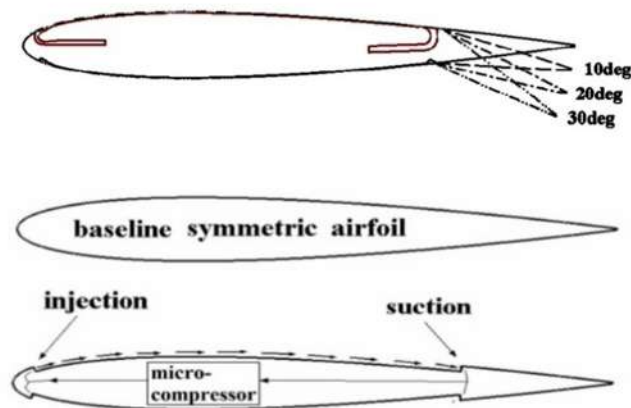


**Figure 2.15:** The NACA 0012 with injection and suction control (Zhang et al. 2018).

**Zhang et al.** (2018) investigated the effects Co-Flow Jet (CFJ) flow control with plain flaps and without flap. The CFJ airfoil is adapted from the NACA0012 airfoil (Fig. 2.15) by converting the upper surface downward by  $0.1\%C$ . A constant deflection angle of  $30^\circ$  is used. The lesser  $C_\mu$  value of 0.05 is the most cost effective to rise the lift coefficient. Simultaneously, it substantially reduces the drag by 67.17%. The CFJ airfoil without flap and jet injection shows the maximum  $C_l$  of 3.048 (raise of 114%) is attained at  $C_\mu=0.30$  with a decreased drag. The outcomes indicate that flapless control surface may be a realistic option.

**Xu et al.** (2020) studied the Co-flow Jet (injection and suction) on NASA hump (Fig. 2.16) to restrain flow separation at low energy expenditure. Optimal location for CFJ suction is at the location at which the hump surface slope reaches the least value, which gives the lowest energy intake. The minimum energy intake for the injection only case improves the separation control by 57%. The suction of the CFJ flow control is very beneficial. It uplifts the B.L. and makes the CFJ energy intake considerably lower than the injection only flow control.

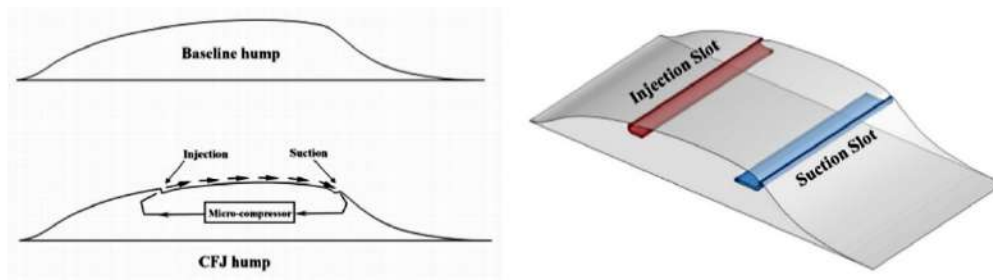


**Figure 2.16:** The NASA hump with injection and suction control (Xu et al. 2020).

## 2.2 Passive flow control:

### 2.2.1 Vortex generators

**Gyatt** (1986) analytically and experimentally studied the vortex generators array the Carter Model 25 horizontal axis wind turbine. counter rotating arrangement were tried on the inboard and outboard half-span, and on the entire blade. Parameters such as Spacing of distance of  $0.15c$ , span wise width of  $0.1c$ . length/ height ratio of 4, with a height  $0.05c - 0.1c$ , roughness strips on the leading edge were considered for the analysis. Results showed that increased in power output by 20% at 10 m/s wind speed and decrease in output at lower than 10m/s speeds. The outboard span position is effective compared to inner sections. The output is increased by 6% at 16 mph with full span position. The leading-edge roughness adversely affects the outputs of wind turbine. VGs effect on flow behaviour is like increment in the blade pitch angle.

**Griffin** (1996) studied the performance enhancement of the stall regulated wind turbine using VGs (Fig. 2.17). It was performed to increase the energy

production per annum and power output without affecting the loads of the turbine using vortex generators array. At low speed such as 8.5 m/s wind speed, the VG causes the drag penalties and loss in power output.

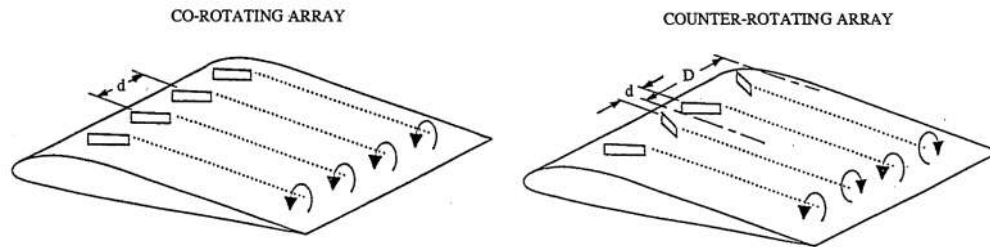


**Figure 2.17:** Different vortex generators arrangements (Griffin, 1996).

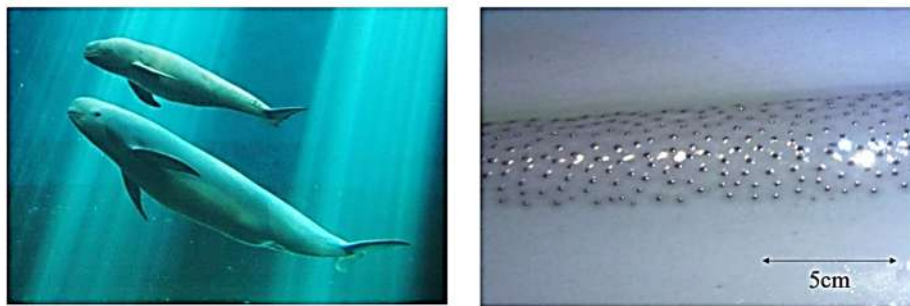


**Figure 2.18:** The vortex generator proposed for a marine use (**Brandner and Walker, 2001**).

**Brandner and Walker, (2001)** done a cavitation tunnel experimental investigation on a vortex generator proposed for a marine purpose (Fig. 2.18). flow visualisation on different parameters such as flow wake trajectory, cavitation, boundary layer profiles, forces and moments acting on the vortex generator in presence and absence of cavitating conditions. In moderate cavitation numbers, no noteworthy impact of cavitation on vortex generator's flow behaviour.

A vane type VG is attached on upper surface of wing. The axial vortex produced by the vortex generator eliminates the slow-moving flow near the wall, so that flow is attached further and improves the aerodynamic stalling. The fixed vane type VG act as a drag producing devices at low angle so effective only at high angles. To evade such problems, retractable vortex generators and low-profile vortex generators with the device heights less than 50% of the thickness of

boundary-layer has been considered. This elaborated analysis of a passive flow control method is presented by **Lin J.C. (2002)** ((Fig. 2.19).

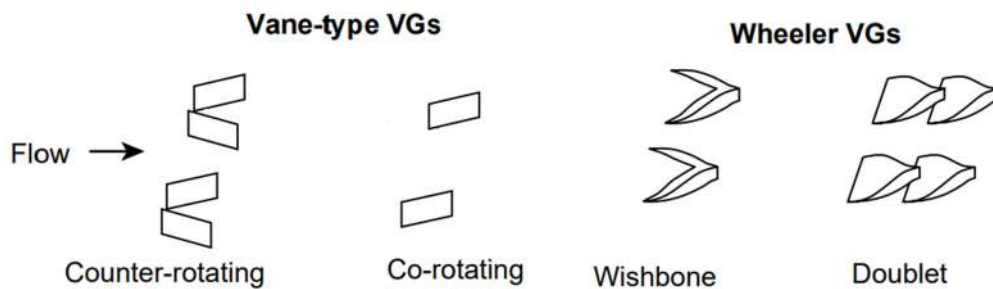


**Figure. 2.19:** Different types of low-profile Vortex generators (VGs) (Lin, 2002).

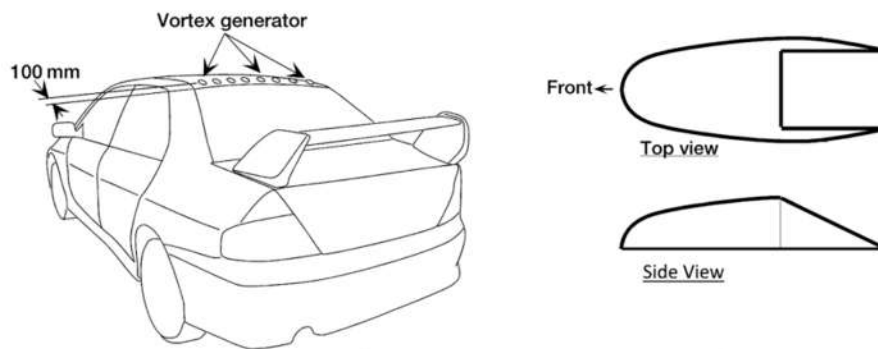
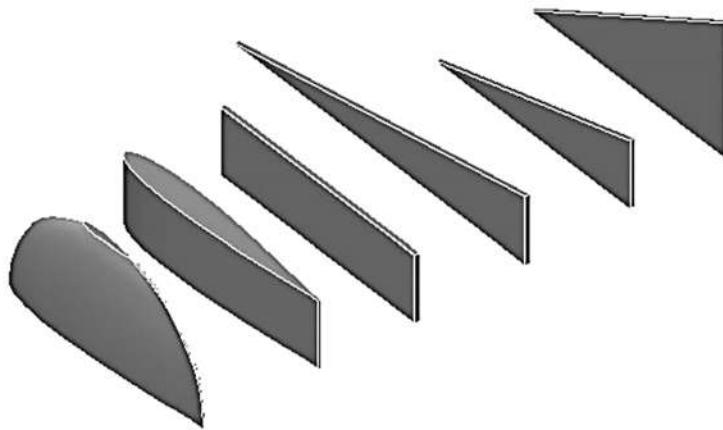


**Figure. 2.20:** Mitsubishi Lancer Evolution with VGs (Koike et al. 2004).

**Koike et al. (2004)** experimentally investigated Vortex generators (VGs) on sedan's rear window (Fig. 2.20) to improve the aerodynamic characteristics. It was observed that the vortex generator height should be equivalent to the B.L thickness (15mm to 25 mm) and should be arranged along the width of the car in row at 100 mm from the roof end. The distance between the vortex generator should be at intervals of 100 mm. the delta-wing-shaped vortex generator shows the better drag reduction than from bump-shaped vortex generator. It reduces the drag by 0.006 on the Mitsubishi LANCER EVOLUTION.

**Heyes and smith (2005)** done an experiment using PIV to control the tip vortex using a supplementary vortex generator (Fig. 2.21) at low Reynolds number of  $2.2 \times 10^5$ . The results demonstrated that vortex generated by both VG and wing tip merge within the length of 5 chord from trailing edge. Several vortex

generator geometries were tried. A triangular VG increased the vortex generation with minimum loss in lift. But a semi-circular VG increased the vortex core radius. high slenderness generator affecting the merging of vortices. So, small slenderness ratio VGs were suitable. The VGs angle of attack also played important role, angle increases effectiveness of circulation also increases. But stall at highest angles of attack which decrease the vortex strength.



Visual key to vortex generators.

**Figure 2.21:** Different vortex generator shapes (Heyes and smith, 2005).

**Velte et al.** (2007) studied Flow investigation of vortex generators installed on wing by stereoscopic PIV measurements has been executed at low speed ( $Re=20\ 000$ ). The vortex generators were arranged in span wise as a row, and set on a bump to create counter-rotating vortices. The investigation showed a vortex structure behind each VG which is extended to 10 device heights downstream to decrease the recirculation zone.

**Shan et al.** (2008) analyzed the low speed flow separation on symmetrical airfoil (NACA0012) set at an angle of  $6^\circ$  using vortex generators (Fig. 2.22). Different cases were taken such as noncontrolled case without VG, a controlled flow case with passive VG, and a controlled flow case with active VG. The results shown that the passive vortex generators moderately remove the separation, promotes the reattachment and reduced separation zone size by 80%. But active vortex generator completely removes the separation zone.

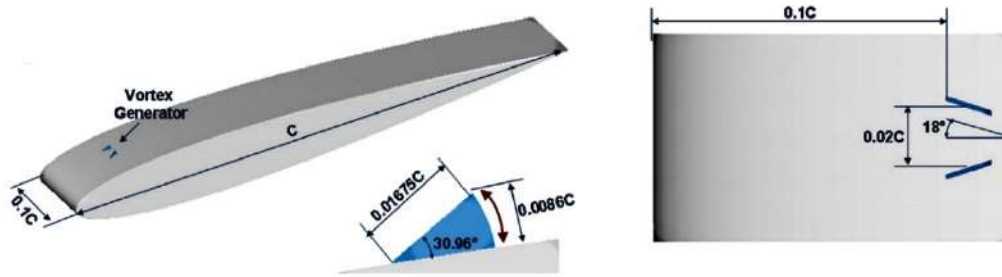


**Figure 2.22:** Vortex generator on NACA0012 airfoil (Shan et al. 2008).

**Bur et al.** (2009) conducted an experimental study to control the interaction of shock wave and a separated B.L in a transonic speed by vortex generator. Both co-rotating and counter-rotating vanes are used ahead of the shock (steady shock and oscillating shock). The span wise spacing of vanes found to be the important parameter for flow control. Small gaps between the vanes promote the merging of vortices and efficiently decrease the drag than the large gaps. Also, it is considerably reducing the shock oscillation.

**Lengani et al.** (2011) analysed “low profile VGs” on the control of the turbulent B.L detachment of full-size flat plate using Laser Doppler Velocimetry and a Kiel total pressure probe. Investigation was carried out with / without control device to study the parameters such as Velocity, pressure distributions, and Reynolds stresses. VG suppress the turbulent flow separation and large flow oscillations which causes the increase in total pressure loss of the base model. Losses for the controlled condition are reduced by 50% than uncontrolled separated case.

A numerical simulation study has been done by **Zhen et al.** (2011) using different stream wise locations  $\Delta X_{vg}/\delta$ , spacing  $\lambda/h$  and shape configurations to obtain the optimum parameters of passive VG in the enhancement of the aerodynamic behaviour of Aludra’s wing with NACA4415 airfoil. The VG with  $\Delta X_{vg}/\delta = 10$ , which is closer to separation baseline, was more effective in increasing  $C_{Lmax}$  by 6.3% than baseline case compared to  $\Delta X_{vg}/\delta = 16$ . The spacing of VGs  $\lambda/h$  has shown a significant effect on lift force enhancement of the wing. VG configuration with  $\lambda/h=7.5$  increased  $C_{Lmax}$  by 4% which was greater than VG with  $\lambda/h = 10$ . The rectangular shaped, curved-edge VG is

further efficient than the triangular shaped VG in increasing the lift force of the wing

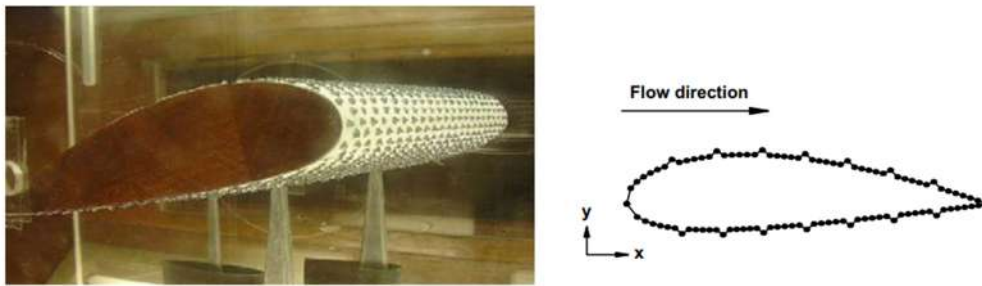


**Figure 2.23:** NACA 4424 airfoil with fouling (Khor and Xiao, 2011).

Khor and Xiao (2011) analysed the flow properties of NACA 4424 airfoil by incorporating fouling effect (small protrusions arranged in row and column) (Fig. 2.23) using CFD. The effect was simulated using std k-e model with standard wall equation and produces commonly acceptable results. It shows the capability of CFD that it can be used to analyse the fouling effects. Fouling effect affects the aerodynamic efficiency of NACA 4424 airfoil and reduces the L/D by 80% for lesser angles of attack. This increases the fuel consumption significantly. It is found that the increase in height of the fouling increases the pressure gradient gradually. But it is not affected by varying the densities of fouling.

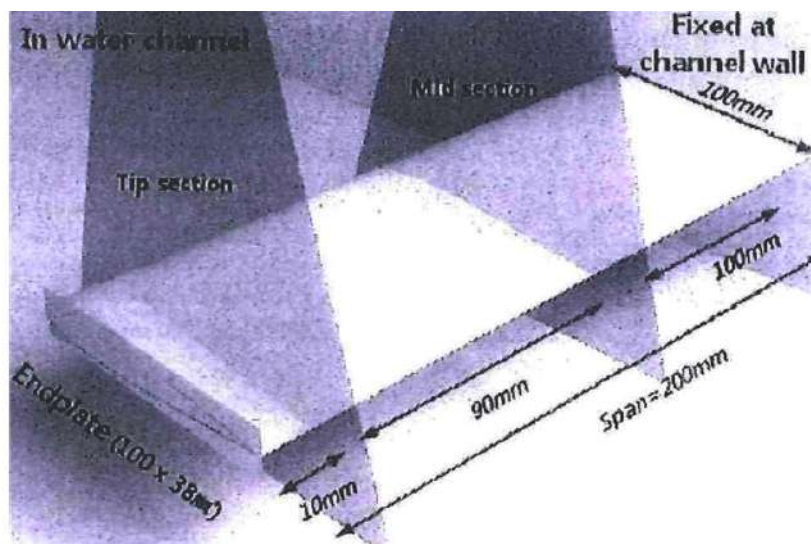


**Figure 2.24:** NACA 0018 foil with endplate (Gim and Lee, 2013).

**Gim and Lee (2013)** studied the endplate effect on tip vortex generation on NACA 0018 foil (Fig. 2.24) using PIV method using a circulating flow water tunnel at Reynolds number of  $Re=2.5 \times 10^4$ . The analysis carried out for two different angles of attack  $\alpha = 10^\circ$  and  $20^\circ$ . Endplate stops the flow to roll-up over the wing tip and it also reduces shear stress in the wake zone. The endplate effect is observed until the mid-span.

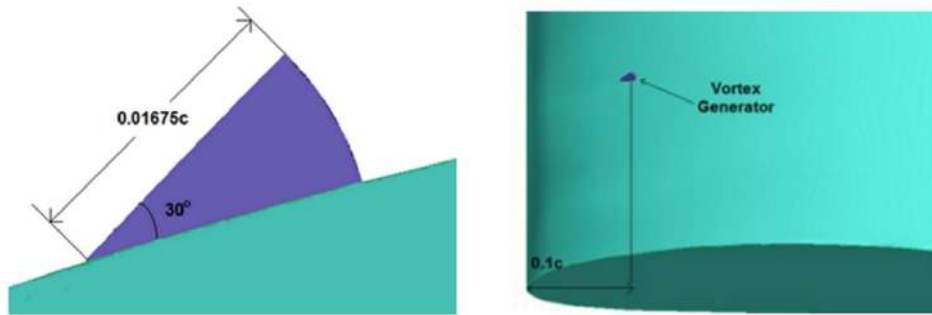


**Figure 2.25:** Vortex Generator on NACA 4412 (**Agarwal and kumar, 2014**).

**Agarwal and kumar (2014)** investigated the Vortex Generator flow Field on NACA 4412 (Fig. 2.25) at low Re. No. The vortex generated by the VG increases the lift at greater angles of attack, hence the staling angle of the airfoil is increased. The drag is reduced at greater angles of attack as the boundary layer remains attached on the airfoil for a greater part of airfoil when the VG is present on airfoil than when the VG is not there. The separation point moves aft on the airfoil due to VGs. VG enhances the airfoil's forces at greater angles of attack with slight reduction in performance at lesser angles of attack where the flow naturally remains attached on the airfoil surface.

**Gámiz et al. (2014)** studied the primary vortex generated by a rectangular VG on a flat plate with 5 different heights ( $h$ ) which are decided with reference to  $\delta$  which is the local boundary layer thickness. Heights varies as  $h = \delta$ ,  $h_1 = 0.8\delta$ ,  $h_2 = 0.6\delta$ ,  $h_3 = 0.4\delta$  and  $h_4 = 0.25\delta$ . For the simulation, following were considered,  $Re = 1350$ , inclination of the vane with respect to the flow direction  $\beta = 18.5^\circ$ . The results showed that the VG heights affects the vortex path and the case  $h_3$  is preferable VG configuration. Because it produces lesser drag with same vortex generation characteristics of larger heights VG. The case of  $h_4$



produces the strongest circulation at the trailing edge but rapidly decays in the flow direction.

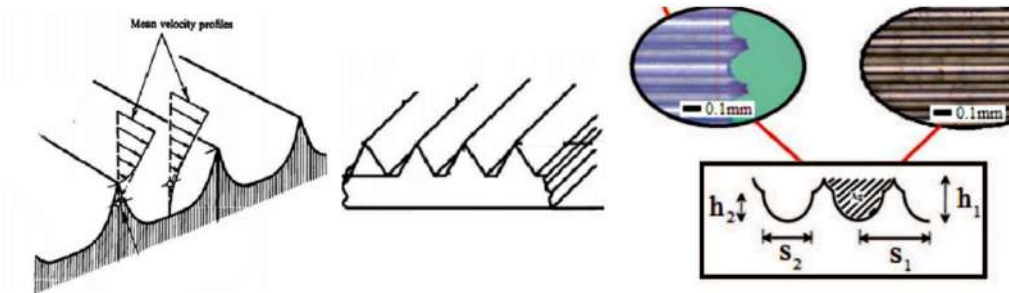


**Figure 2.26:** Serrate-Semi-Circular bio-inspired riblets (Saravi et al. 2014).

The effect of bio-inspired riblet (Serrate-Semi-Circular riblet - Fig. 2.26) surfaces on drag reduction and turbulent B.L. structure in wall-bounded flows is presented by Saravi et al. (2014). The design parameters riblets of  $s_1 = 19.5$ ,  $s_2 = 14$ ,  $h_1 = 10.5$ ,  $h_2 = 7.5$  and  $(A_g)^{1/2} = 11$  were taken for the analysis. Results shown that the reduction in drag was by 7% which is better than other existed riblet designs such as V and U-shaped. The design parameter groove cross section  $A_g$  plays vital role in flow control than riblet spacing  $S$ .

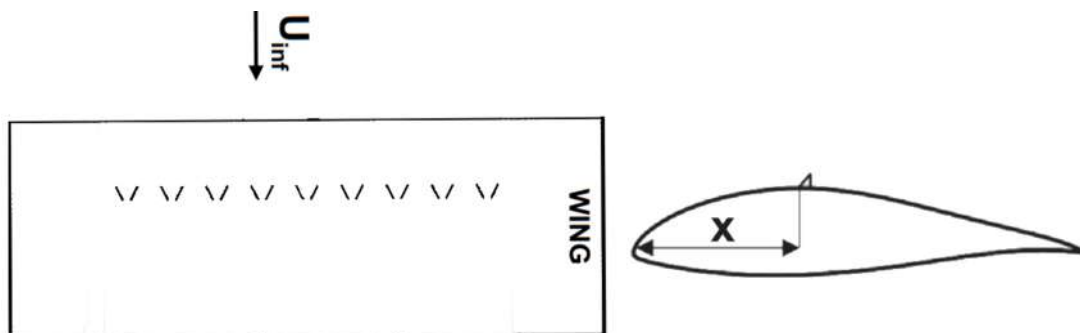


**Figure. 2.27:** The counter rotated triangular VG on wind turbine blade (Manolesos et al. 2015).

An experimental study of flow separation control on wind turbine blade airfoil (Fig. 2.27) was done by Manolesos et al. (2015). The triangular vortex generator which are counter rotated were considered for the study of three-dimensional flow separation. For a  $Re = 0.87 \times 10^6$ , Stall angle is increased by  $5^\circ$ , and lift increased before the stalling angle of  $15^\circ$ . It is observed that, 44% improvement in maximum lift, and 0.002 reduced in drag within the stalling

angle of attack. The effectiveness of the vortex generator is extended upto 37.2 times the vortex generator height because of the strong turbulent interaction between the two vortices. while further downstream (upto 47.2 VG heights) diffusion governs the flow.

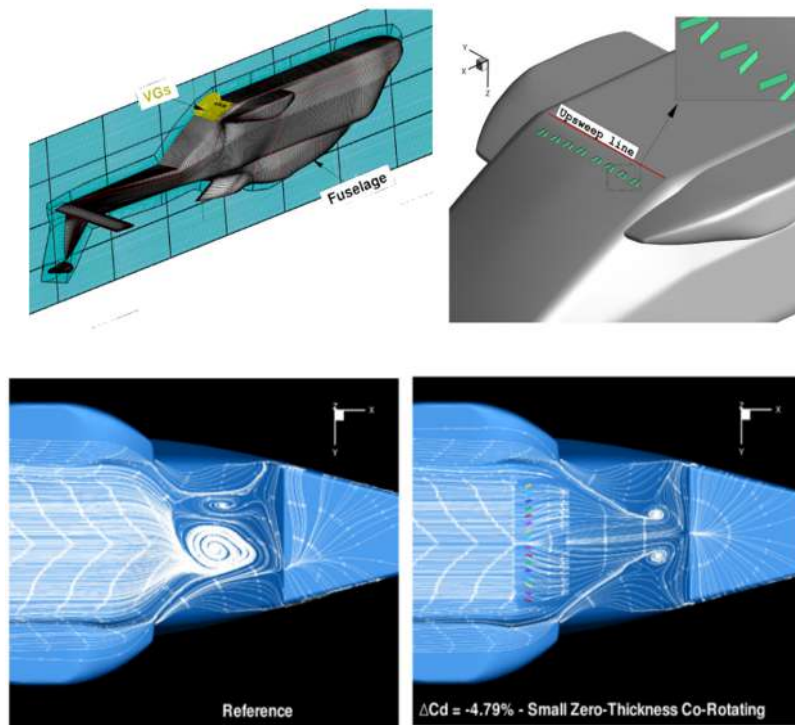


**Figure 2.28:** vortex generator on a heavy-class helicopter fuselage (**Gibertini et al. 2015**).

**Gibertini et al. (2015)** examined the effect of vortex generator's layout and position on helicopter drag using a model of helicopter fuselage (Fig. 2.28) (including backdoor/tail-boom junction). Methods used for analysis are pressure and load measurements and stereo PIV surveys. The back-ramp layout showed a maximum of 5% fuselage drag reduction.

**Haipeng et al. (2017)** shown that the aerodynamic features of S809 airfoil (Fig. 2.29) can be effectively improved using the vortex generators. It decreases the B.L thickness and delays the stall phenomenon. Compared to the single vortex generator, pair of vortex generator (double vortex generator) showed improvement in the flow separation delay and hence increase the aerodynamic efficiency of the airfoil S809.

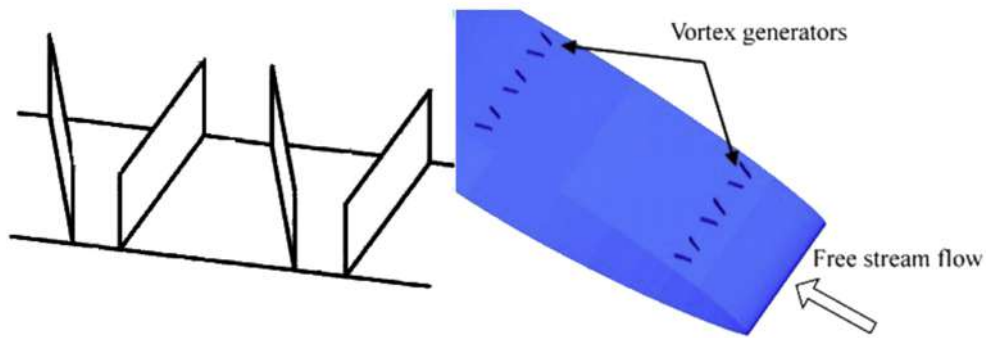


**Figure 2.29:** The double VG on S809 Airfoil (**Haipeng et al.** 2017).

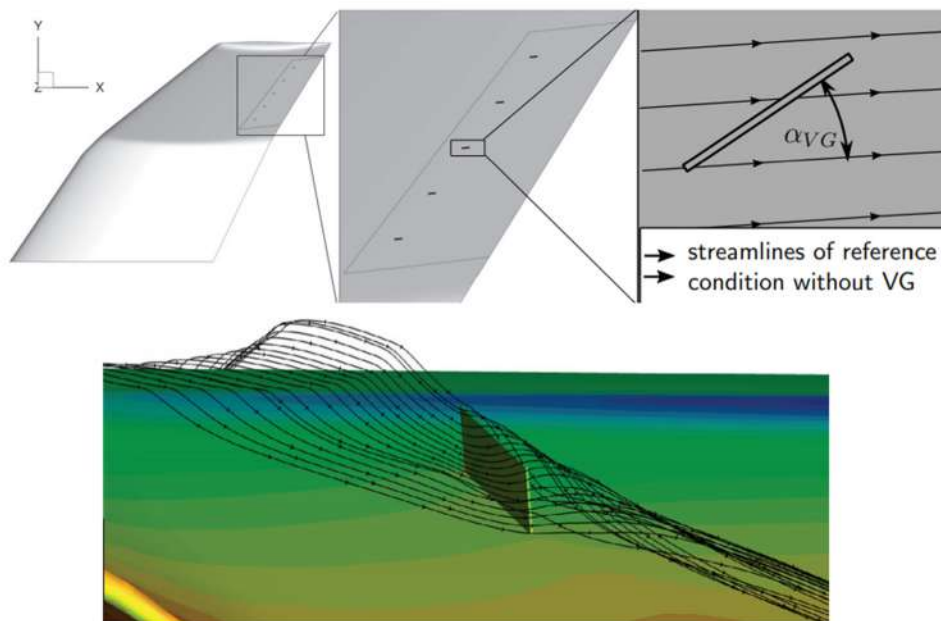


**Figure 2.30:** vortex generator on winglet control surface (**Brüderlin et al.** 2017).

**Brüderlin et al.** (2017) investigated the vane type vortex generators (VG) sited on the winglet control surface which is deflected at  $5^\circ$  (Fig. 2.30). Using the RANS simulations, it is found that the VGs are not effective at  $0^\circ$  deflection of control surface and effectively delays the flow separation when it is deflected to an angle.

**Sobhani et al.** (2017) introduced a cavity in VAWT blade's airfoil profile (Fig. 2.31) and simulated the using CFD with incorporating k-w SST turbulence. The different dimple geometrical parameters including shape, size, and location has been taken to enhance the turbine performance. The circular shaped dimple with

0.08c times the diameter located near leading edge (pressure side of airfoil) was found to be optimum. Compared to the reference airfoil, average efficiencies of the turbine are increased to 25% for airfoil with a cavity.

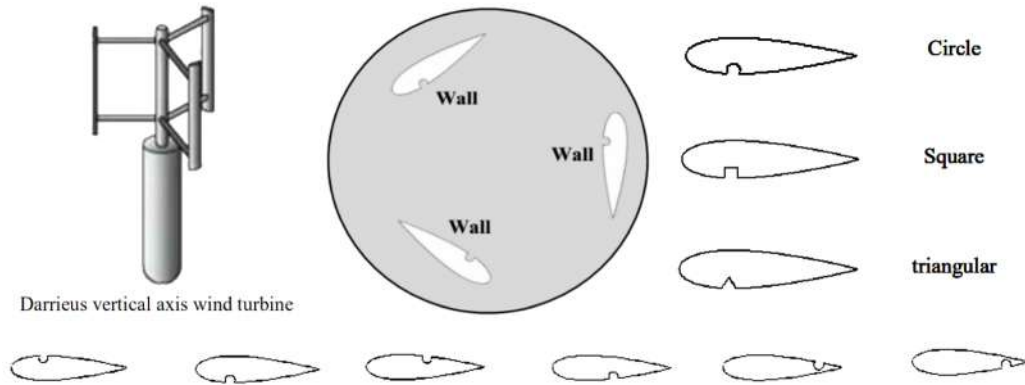


**Figure 2.31:** Dimples on Darrieus VAWT (Sobhani et al. 2017).

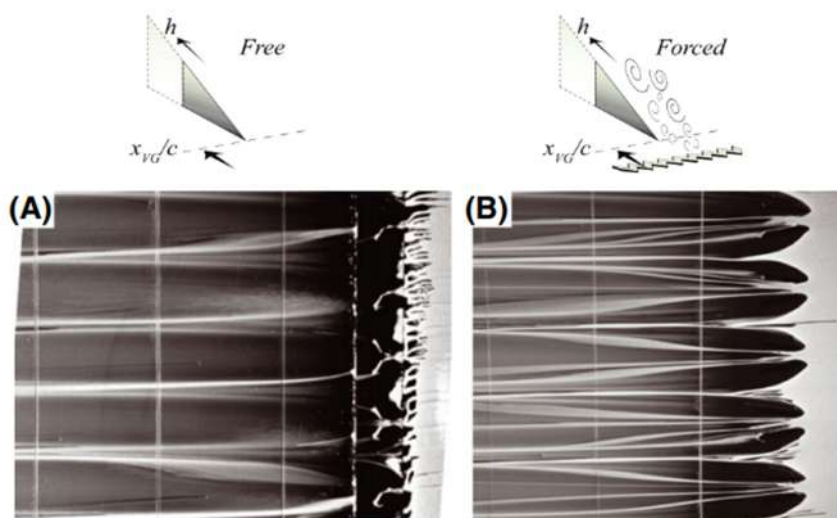


**Figure 2.32:** Vortex generator with free and forced flow conditions (Baldacchino et al. 2018).

**Baldacchino et al.** (2018) did an experiment with the help of Oil-flow visualizations on DU97-W-300 airfoil (Fig. 2.32) furnished with several VG designs at Reynolds number of  $2 \times 10^6$  and observed that the vortex-induced mixing control the separation using 41 separate VG designs, which includes different height, length, shape, angle, density and positions along chord wise and span wise. The VGs delay the stall with roughness effect. In stall region, VGs increases load fluctuations in the stalling condition.

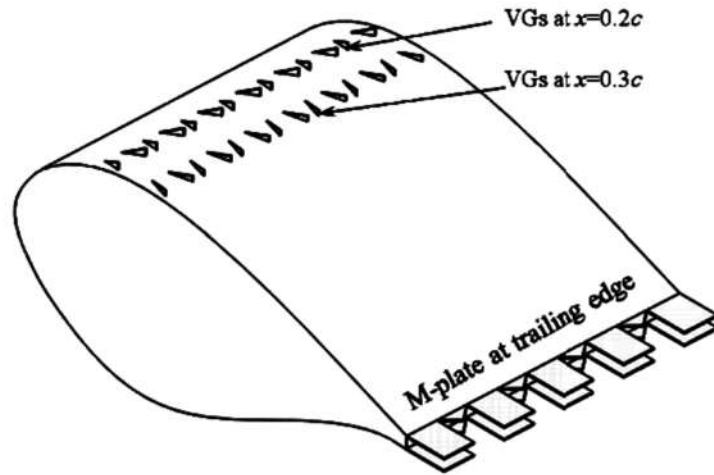


**Figure 2.33:** Wind turbine blade with vortex generators and M-plate (**Zhang et al. 2019**).

**Zhang et al. (2019)** studied 2 types of aerodynamic devices (vortex generators and M-type trailing-edge device (M-plate)) to modify the surface condition of thick airfoil (Fig. 2.33) and to analyse the flow separation phenomenon. The unsteady flow separation was studied at  $Re = 1.0 \times 10^6$ . And then, the effects of the accessories on the unsteady separation were studied. The results shown that the 3D B.L separation at larger angles of attack. Divergence appears near stall condition and scatters the results a lot. Study shown that the VGs works well on controlling the stall and divergence on the airfoil, but M-plate not controlled the divergence.

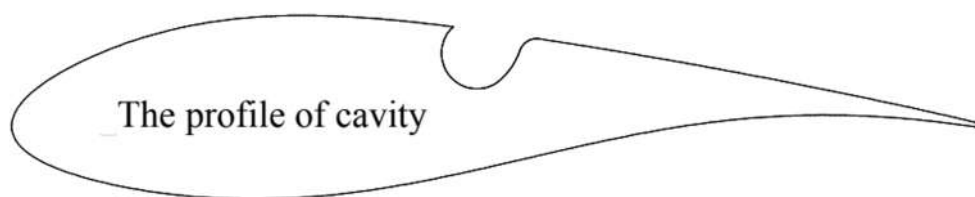


**Figure 2.34:** Riso\_B1\_18 airfoil with a cavity (**Fatehi et al. 2019**).

**Fatehi et al. (2019)** analysed the Riso\_B1\_18 airfoil with an optimized cavity shape (Fig. 2.34) using the transient numerical simulation. Even though it's not effective at low angles, the cavity trapeses the vortex well at high angles to prevent stall, fluctuations so that increases the lift-to-drag ratio as follows, 31% at AOA of  $14^\circ$  and 57% at AOA of  $20^\circ$ .

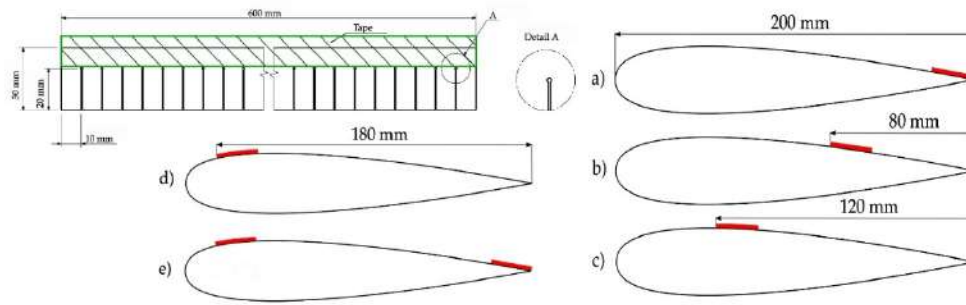


**Figure 2.35:** Flexible flaps on NACA0020 (Reiswich et al. 2020).

Reiswich et al. (2020) performed an experiment using force balance and smoke–wire visualization on a NACA0020 with elastic flaps (Fig. 2.35) of different positions(row) on the upper profile surface for  $Re = 2 \times 10^5$ . The results disclosed that flaps attached additionally increase area hence the drag coefficient (skin friction drag + pressure drag) also increased. And its effective in the deep stall region. flaps positioned at both ends (the leading and trailing edges) of the profile are preferable. The flow visualization captured the leaning flow near the with reduced size of the separated region due to the flaps.

### 2.3 Trailing Edge Devices

Lange and May (1948) studied the influence of L.E. flaps and split flaps on a rectangular wing (AR of 3.4 and circular-arc airfoil) (Fig. 2.36) flow behavior. The study included several L.E. lift enhancement devices and 0.2C length split flaps for  $Re. 2.9 - 8.4 \times 10^6$ .  $C_{lmax}$  of base wing (0.58) is increased by 1 for half-span (0.5b) split flaps ( $60^\circ$ ) by 1.24 for full span(1b) split flaps ( $60^\circ$ ).  $C_{lmax}$  increases by drooped-nose with the extensible L.E. flap, and round leading edge. And it is further increased by adding 0.5b split flaps ( $60^\circ$ ) with above configurations. The drag penalty due to split is reduced with the help of drooped-nose flap or extensible L.E. flap.

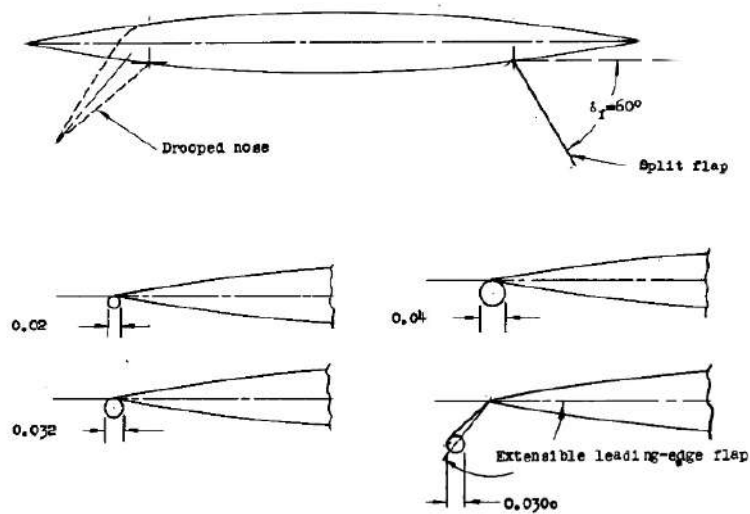


**Figure 2.36:** The L.E. flaps and split flaps on a rectangular wing (**Lange and May, 1948**).

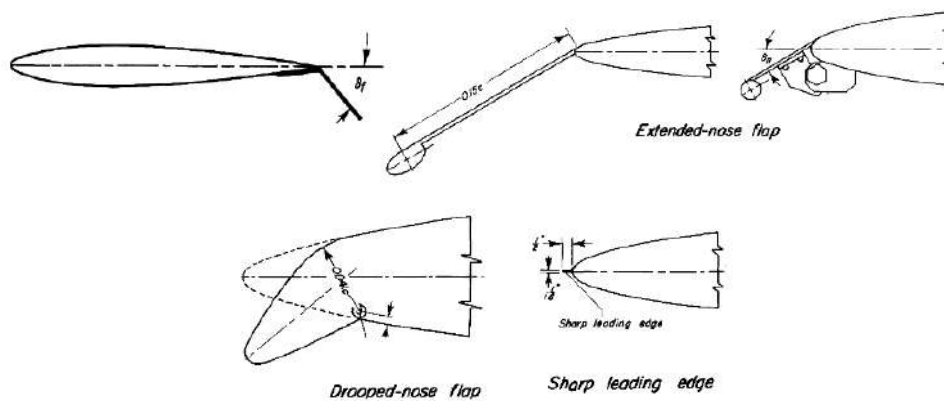


**Figure 2.37:** Different type of L.E. flaps on wing-fuselage combination (**Hopkins, 1949**).

**Hopkins** (1949) studied the aerodynamic features of wing-fuselage combination (sweep angle of  $63^\circ$  and AR of 3.5) at low speed using the, sharp L.E. flaps, drooped flaps, extended L.E. flaps, split flaps, and elevons (Fig. 2.37). The extended L.E. flap with full span has reduced the drag by double the times than the drooped flap with full span at the higher lift coefficients.

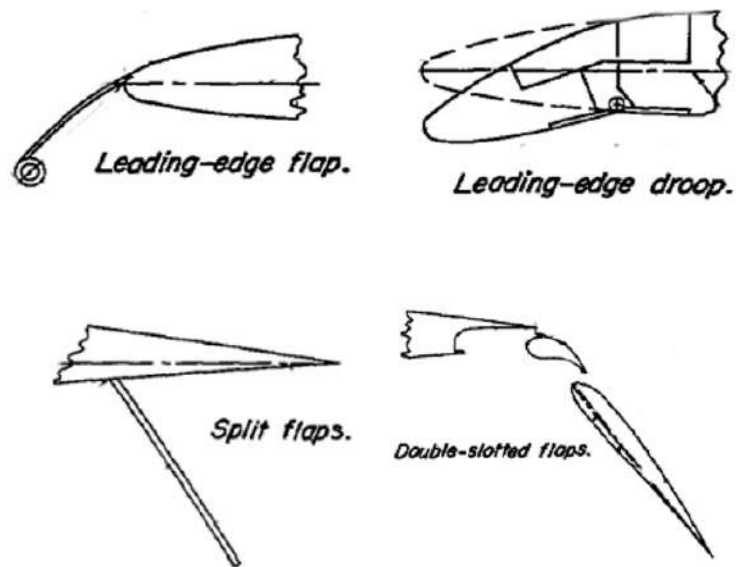


**Figure 2.38:** Different type of L.E. and T.E. flaps on sweptback wing (Salmi, 1950).

Salmi (1950) studied the stability characteristics of sweptback wing (sweep angle -  $47.7^\circ$ , AR - 5.1 and 6) with swappable tips (Fig. 2.38). Several flow control devices such as L.E. and T.E. flaps, wing fences, and roughness were included in the analysis at  $Re. 6.0 \times 10^6$ . The L.E. flaps and L.E. flaps (length 0.5b) with shortest-span T.E. flaps ( $< 0.400$ ) showed better stability characteristics than the drooped nose and lower than the double slotted flaps. The change in aspect ratio does not affect the results of flaps.

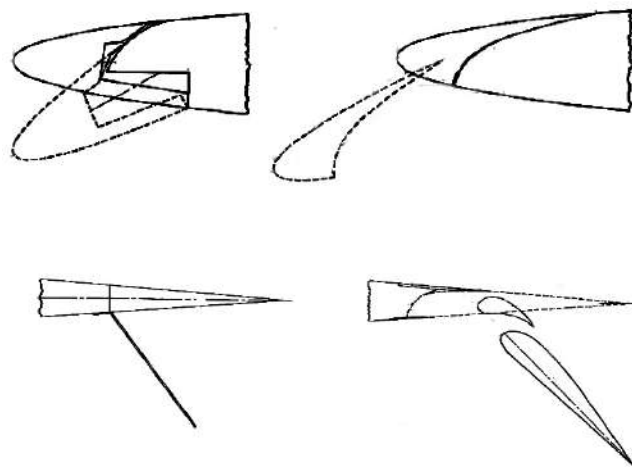


**Figure 2.39:** Different type of L.E. and T.E. flaps on NACA 64<sub>A</sub>010 (Kelly and Hayter, 1953).



An analysis by **Kelly and Hayter** (1953) on the NACA 64<sub>A</sub>010 with different L.E. slat, flap, split flap, and double-slotted flap (Fig. 2.39) for different Reynold number of 2, 4, 6, and 7 million. Optimum slat positions with and without 2 T.E. flaps were found. Expansion of L.E. slat and flap raise the  $C_{lmax}$  by 0.83 and 0.66. it also moves the aerodynamic centre to move forward to quarter chord point. **Hahne and Jordan** (1991) explored the lift characteristics of a business-jet aircraft wing (HSNLF (1)-0213 airfoil) with single-slotted flap. It showed that the single-slotted T.E. flap rises lift useful for takeoff and landing.

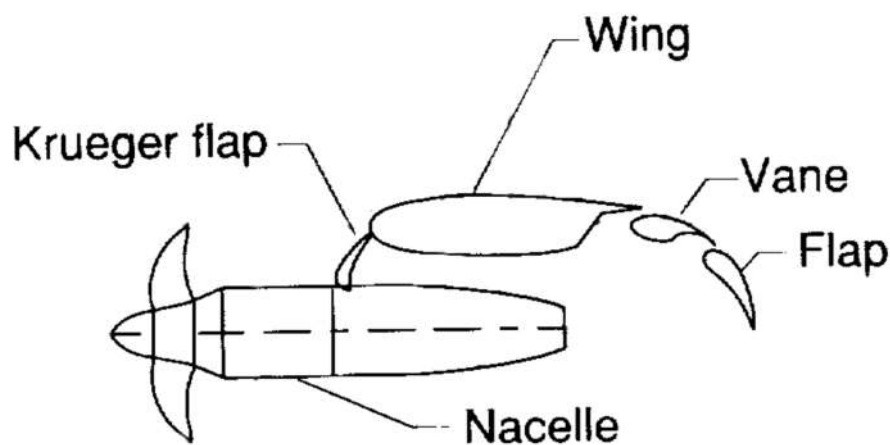


**Figure 2.40:** The wing-turboprop engine assembly with L.E. and T.E. flaps (Gentry et al. 1994).

**Gentry et al.** (1994) examined a wing-flaps placed on the wing-turboprop engine assembly (Fig. 2.40). Different propeller speeds, the propeller slipstream, nacelle positions and slopes were taken for the analysis. It's found that the slipstream accelerates the flow and increases the lift along with the increase in propeller speed and activated flaps. The effect of inclination of engine nacelle affects the forces more than the effect of nacelle positions. The decrease in nacelle increases the lift and its slope and showed best performance at larger angles with increase in drag.

**Jang et al.** (1998) did a study on NACA 4412 with Gurney flap. A thin plate with 0.01-0.03c length attached at lower side trailing edge was taken for study using INS2D. Gurney flap of 0.005c, 0.01c, 0.0125c, 0.015c, 0.02c, and 0.03c length flaps were analysed. Results showed few Gurney flaps boost the  $C_l$  with

insignificant rise in  $C_d$ . The flap with  $0.015c$  enhanced the  $C_l$  by 0.3 and achieved the lift with less angles (reduce the angle by  $3^\circ$ ).

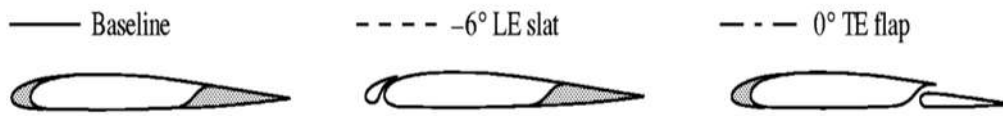


**Figure 2.41:** The Helicopter rotor blade with L.E. and T.E. flaps (Noonan et al. 2001).

Noonan et al. (2001) compared the single element airfoil in rotor blade tip region with slotted airfoils in the rotor blade tip (Fig. 2.41). 4 different rotor arrangements with different advance ratios in forward flight and hover was considered. Other boundary conditions were tip Mach - 0.627, attitude - 4000ft and T - 95°F. including base model, other models are rotor having forward-slotted airfoil with slat ( $-6^\circ$ , and  $-10^\circ$ ) and with aft-slotted airfoil flap ( $3^\circ$ ). The results showed that the airfoil having forward slot and slat ( $-6^\circ$ ) works well than other configurations on load allowances.

Troolin (2006) researched the flow structure of a NACA 0015 with T.E. Gurney flap (length of  $0.01c - 0.04c$ ) at  $Re = 2 \times 10^5$  using PIV method. 2 separate vortices (like the Kármán vortex shedding) interact downstream causes increase in lift slope. Li et al. (2007) experimented the Gurney flaps and divergent T.E. on a supercritical aerofoil at  $M = 0.7$  and  $Re = 3.15 \times 10^5$ . 4 different flap heights  $0.005c$ ,  $0.01c$ ,  $0.015c$  and  $0.02c$  are taken. The results exposed that the Gurney flaps had noteworthy impacts on aerodynamic features than divergent T.E., The Gurney flaps enhance the flow behaviour on base supercritical and the divergent T.E. airfoils.

Wang et al. (2008) did an analysis on the application of Gurney flap (Fig. 2.42). It's found that the flap should be at bottom surface T.E. with vertical position with height equal to the thickness of the B.L. Gurney flap rises the pressure in front hence in lower surface and enhance the forces acting on the model at subsonic speed. It also delays or remove the wake from upper surface due to

vortices generated by the flaps. After critical Mach, it moves the shock downstream and reduce the wave drag.

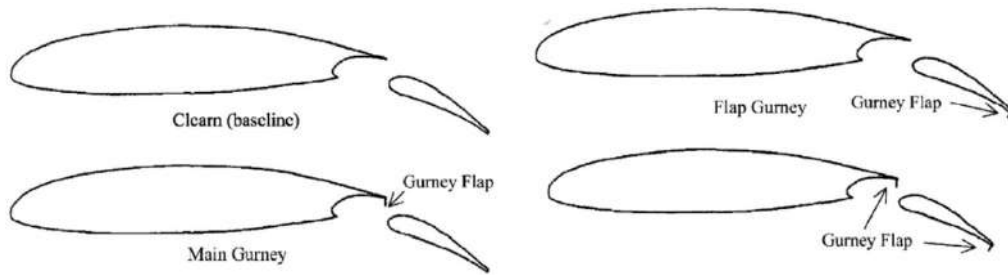


**Figure 2.42:** The single slotted airfoil with gurney flaps (Wang et al. 2008).



**Figure 2.43:** The slotted, Natural Laminar flow S103 airfoil (Somers, 2012).

Somers (2012) proposed the slotted S103 airfoil to obtain maximum lift / drag and compared with NASA NLF (1)-0215F (Fig. 2.43) experimentally at Reynolds numbers 3,6, & 9 x 10<sup>6</sup> and a Mach 0.1. The aft element with  $-1^\circ$  nose down and  $-0.0017c$  moved forward and  $-0.0017c$  downward. Results showed slotted airfoil has greater positive effect on forces than base model.

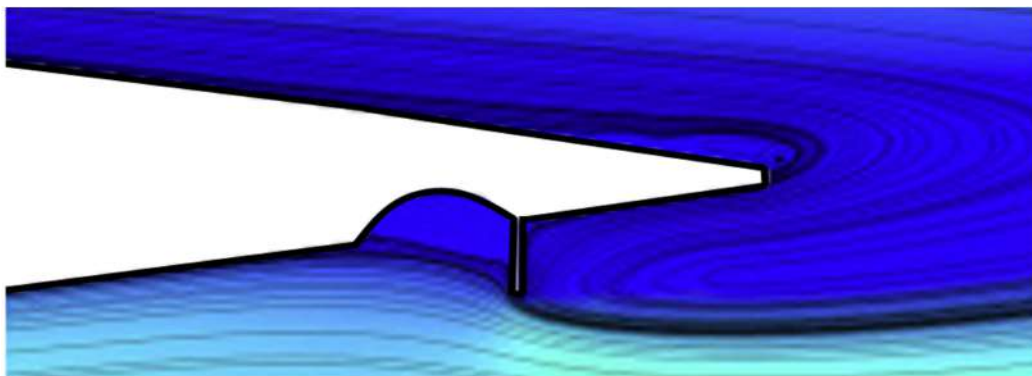


**Figure 2.44:** The semi-circular dimple and Gurney flap on NACA-0015 (Ismail and Vijayaraghavan, (2015).

Ismail and Vijayaraghavan (2015) modified the profile (dimple -circular arc and Gurney flap on bottom surface) of a NACA-0015 used in VAWT (Fig.

2.44). It focused on enhancement in torque and power produced by VAWT using Response Surface Approximation. The CFD analysis showed that the profile modifications enhance the tangential force for steady case by 35% and for oscillating case by 40%.

**Pastrikakis et al.** (2015) did a research on gurney flap placed on W3-Sokol rotor blade. The gurney flap with the heights of  $0.003c$ ,  $0.005c$ ,  $0.01c$ ,  $0.02c$  were placed from  $0.46R$  to  $0.66R$  at the trailing edge have been taken for analysis. The largest flap is more effective and its effect is further increased with elastic blades. **Sieradzki** (2016) demonstrated a single and the double Gurney flap (T-strip) on deflected aircraft stabilizer. Its showed that the both flap configurations improved the flow control at high deflection angle with little bit drag generation.

The suction slots positioned at different location on Wells turbine blade (Fig. 2.45) were studied by **Shehata et al.** (2017) under oscillating wave flow situations using CFD. The more no of suction slots postponed the stall without any external energy well than less no of slots. Different no of slots (2, 3, and 4) were taken on stall regime study. It is discovered that the blade with 3 suction slots at  $0.4c$ ,  $0.55c$  and  $0.9c$  gave highest torque coefficient. It about 26.7% before the stall and 51% after the stall.

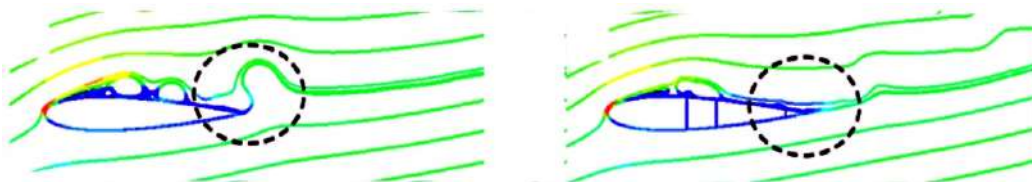


**Figure 2.45:** The suction slots on Wells turbine blade (**Shehata et al.** 2017).

**Lu et al.** (2017) analysed the T.E. flap which is flexible and has adjustable camber changing its shape from  $0.5c$  to end on GA (W)-2 airfoil (Fig. 2.46). In take-off angle  $8^\circ$ , variable profile T.E. flap raise  $C_l$  by 8% and  $C_l/C_d$  by 7% than the normal flap. In landing angle, it raises  $C_l$  at stall angle by 1.3%. In cruise angle, it raises the  $C_l/C_d$  with the maximum of 30%.

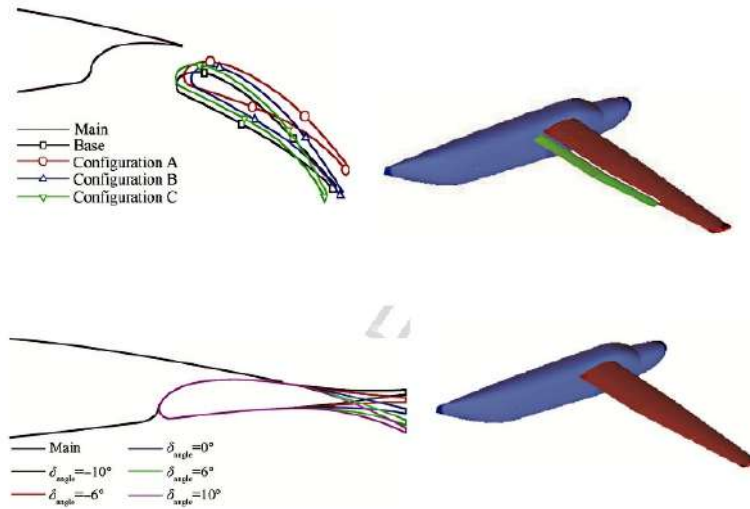


**Figure 2.46:** The wing with flexible and variable camber T.E. flap (Lu et al. 2017).

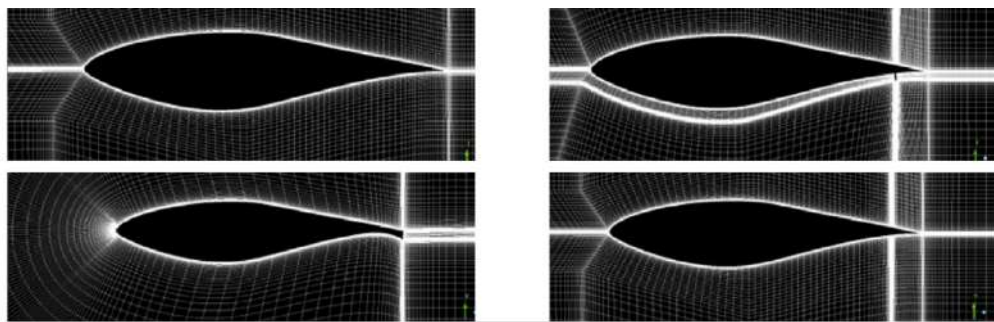


**Figure 2.47:** Different T.E. configuration on HAWT blade (Chen and Qin 2017).

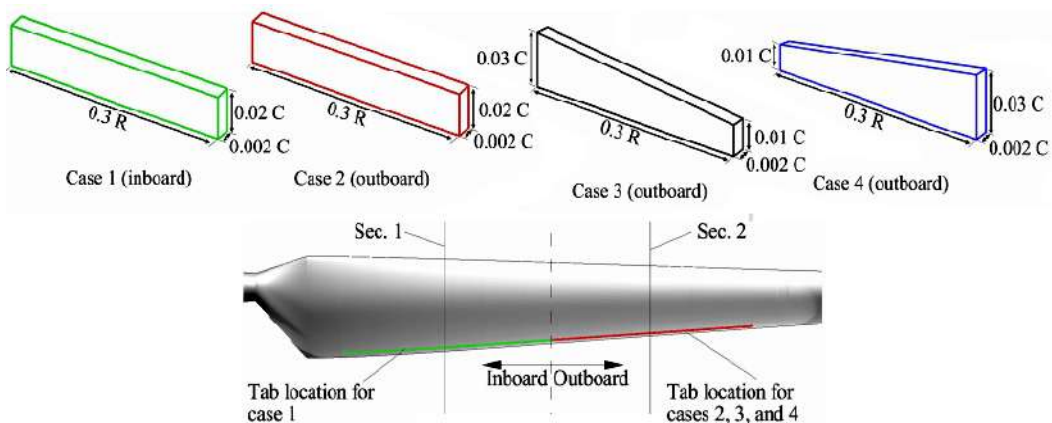


**Figure 2.48:** The micro tabs on HAWT blade (Ebrahimi and Movahhedi, 2018).

**Chen and Qin** (2017), examined T.E. flow control devices on HAWT (Fig. 2.47) for the speed of 5-15m/s. it includes micro tabs and micro jets at T.E. of the blade with rotating condition and the divergent T.E., And found that at lower flow speed, micro jet injected at 60 m/s is preferable and at higher flow speed 0.02c height micro tab is preferable for flow control.

**Ebrahimi and Movahhedi** (2018) did a 3D study on micro tabs placed on HAWT (NREL Phase VI) (Fig. 2.48). Different spanwise position and height of tabs were taken with fixed chordwise position (0.95c) on bottom surface. Results exposed that micro tabs near the tip have better control than tabs near the root but shows similar power output enhancement characteristics. It saved 17% of the wasted wind energy at low speeds.

## 2.4 Leading Edge Devices

**Weick and Wenzinger** (1932) experimentally tested Handley Page slots on a wing model with Clark Y airfoil (Fig. 2.49). various lengths (varied from 20 to 100% of the half span) of slots extended inward from tip of the wings were considered. roll damping characteristics was studied using different slot lengths. The maximum  $C_l$  and acceptable damping in roll for a range of angles of attack was produced by the optimum slot which is approximately 50 per cent of the half span.

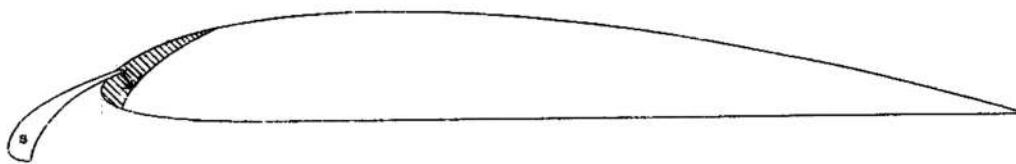


**Figure 2.49:** Handley Page slots on a wing model (**Weick and Wenzinger**, 1932).

**Bamber** (1939) tested several forms of fixed wing slot (slotted flap having a chord 25.66 percent of the air-foil chord) in a large-chord NACA 23012 airfoil. Flap at 55% with 40-degree deflection was practically ineffective for max lift coefficient. Leading edge flap with 0 degree deflected increases the max lift

coefficient by 0.65 and stall angle by 11 degree. Nose slot with 40 degree deflected increases the max lift coefficient by 0.4 and stall angle by 10 degree.

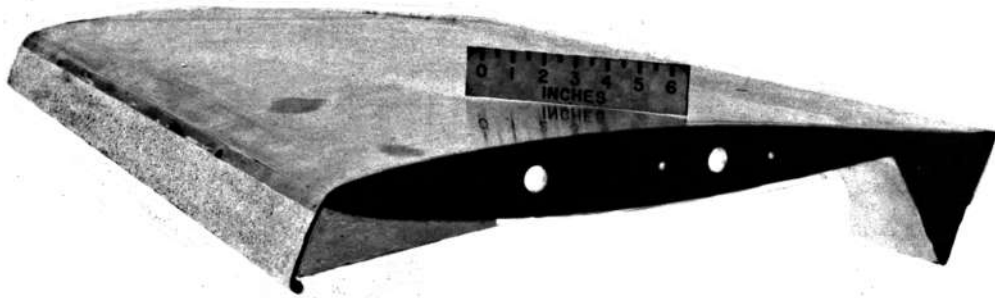


**Figure 2.50:** Airfoil with leading edge flap and split flap (Fullmer, 1947).

Fullmer (1947) inspected the high lift devices as follows, 0.1c length leading edge flaps, which are sliding from both upper and lower portion of an NACA 64<sub>1</sub>-012 airfoil (Fig. 2.50). And split flap at T.E. with 0.2c length. Both were attached and tested for  $Re$  of  $6 \times 10^6$ . Upper L.E. flap increases  $C_l$  and stall angle by 0.43 and 4 deg. And lower L.E. flap increases  $C_l$  and stall angle by 0.12 and 1.4 degree respectively. After 60 degree deflected T.E split flap deflected, Upper L.E. flap increases  $C_l$  and stall angle by 0.81 and 6.9 degree. And lower L.E. flap increases  $C_l$  and stall angle by 0.43 and 3.9 degree respectively. The upper L.E. flap and T.E flap gives maximum  $C_l$  of 2.98 for 16.2°.

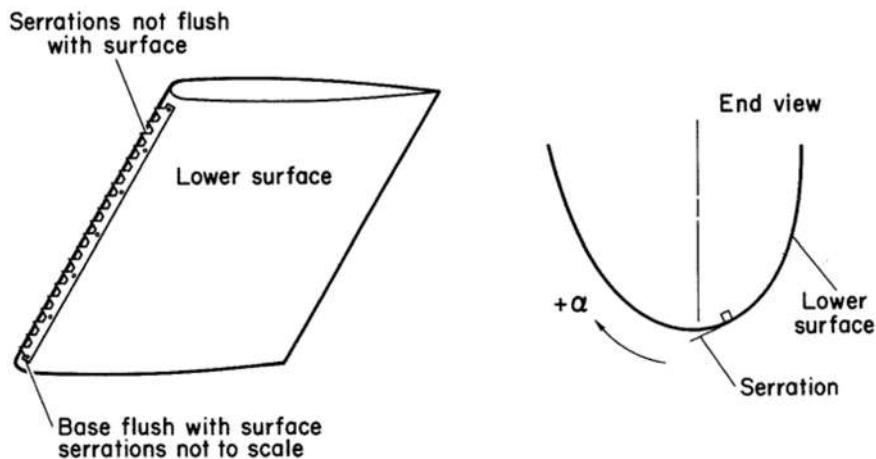


**Figure 2.51:** Airfoil with leading edge serrations (Soderman, 1972).

An investigation was done by Soderman (1972) on a NACA 66-012 with serrated strips (brass material) of various sizes and shapes on the leading edge (Fig. 2.51). The results showed, the maximum size serrations barricaded the

flow on suction side, and minimum size serration eliminated or delay the separation depends in the location on aerofoil at max angles. The optimum serration geometries are size of 0.10 cm to 0.50 cm, located below the chord line (0.95 cm) on leading edge.

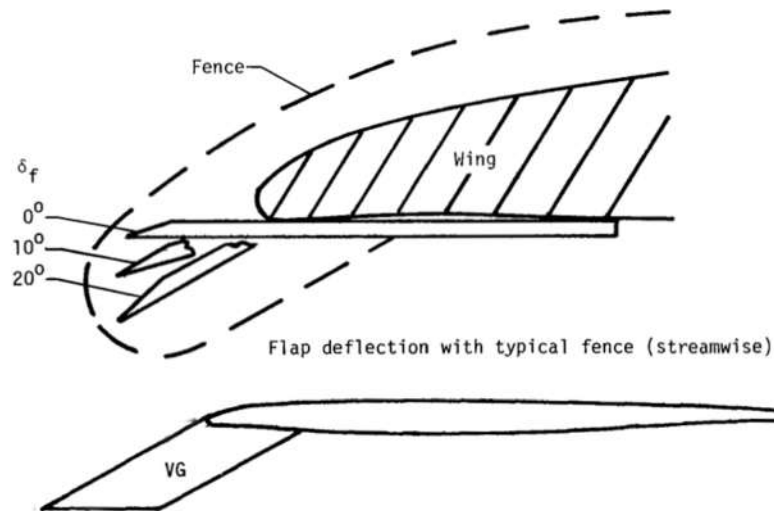


**Figure 2.52:** The leading-edge device on supercritical wing (Mann et al. 1983).

Mann et al. (1983) performed a test with the help of Fluorescent tufts on supercritical wing with leading-edge devices (Fig. 2.52) for to enhance maneuver. Wing geometrical parameters such as swept angle of  $45^\circ$  and AR of 3.28 are taken with the boundary conditions of Mach numbers of 0.60 and 0.85 and angles  $-0.5^\circ$  to  $22^\circ$ . Results showed, the sharp L.E. flaps work well with vortex generation and drag reduction. At 0.60 Mach, the effect of deflection of the flaps on drag control was more than the effect of increasing of flap. At 0.85 Mach, the effect of flap chord was more effective than a large chord deflection of flap in drag control. Also found vortilons attached under the wing also effective in flow control at 0.60 Mach and pitching moment was not affected much by any of the devices attached.

Ghaffari and Lamar (1985) did an analytical process to find the effect of Leading-Edge Extension (LEE) on thick delta wings with twist and camber (Fig. 2.53). 36 different shaped planforms were tested to find aerodynamic effectiveness. Results showed that the decrease in length of the LEE'S has best



effect on efficiency, regardless of the planforms. It is noticed that the fixed chord LEE was better than swept LEE device. But LEE satisfying the design criteria not having any effect on aerodynamic characteristics.

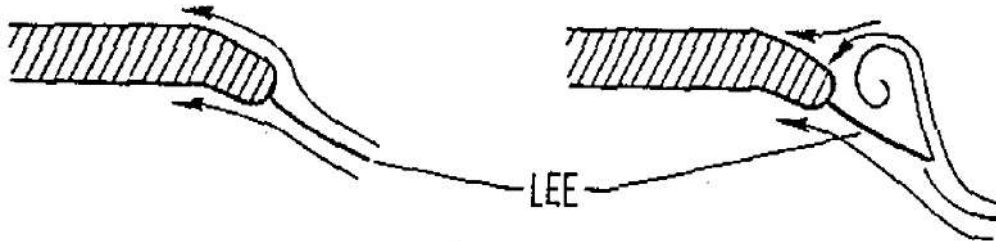


**Figure 2.53:** The leading-edge extension on thick delta wing (Ghaffari and Lamar, 1985).

**Chandrasekhara et al.** (2004) deflected the  $0.25c$  times of leading portion of an airfoil (Fig. 2.54) as drooped so that leading portion is at low incidence angle. Measured the flow properties at Mach numbers range of 0.2 to 0.4 with unsteady pressure transducer and found drooped reduce the dynamic stall with approx. 50% lesser pitching-moment and positive damping. Also, 75% decrement in drag than non-drooped airfoil. **Chandrasekhara et al.** (2004) also found 10% lift decrement due to drooped edge. And recovered the loss with the help of  $0.01c$  height of Gurney without increasing drag. **Chandrasekhara** (2010) also studied the effect of Gurney flap geometries (Gurney flaps of  $0.01c$ ,  $0.02c$  and  $0.03c$ ) on helicopter blade. And found that  $0.01C$  flap is effective to recover the loss in lift.

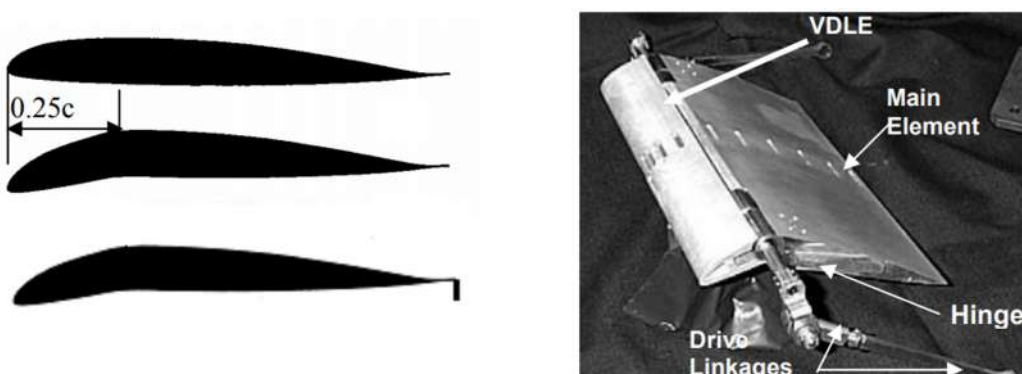


**Figure 2.54:** Airfoil with drooped leading edge and gurney flap (Chandrasekhara et al. 2004).

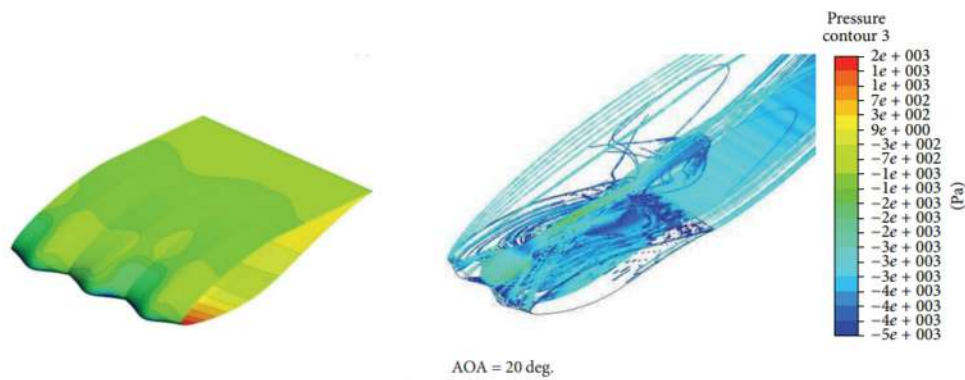


**Figure 2.55:** The wind turbine airfoil with leading edge bump (Asli et al. 2015).

Asli et al. (2015) analysed the bio inspired (Humpback Whales flippers) protuberances on nose of S809 airfoil (Fig. 2.55) at Reynolds number of  $10^6$ . The results exposed that the decrease in aerodynamic force (lift) for lesser incident angle because of flow disturbance by protuberances. But showed smooth stall trend at larger angle. The bumps acted as a vortex generator which creates high momentum vortex that prevent deep stall.

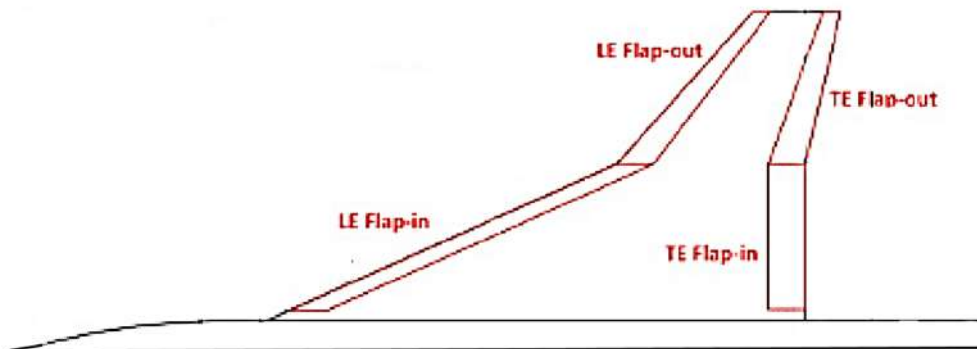


**Figure 2.56:** The cranked arrow wing with inboard L.E. flaps (Toyoda et al. 2015).

Toyoda et al. (2015) analysed a cranked arrow wing with inboard L.E. flaps (Fig. 2.56) for vortex generation and observed the non-linear flow due to separation and vortices formation. Choudhry et al. (2015) revealed the relation between separation bubbles, L/D and stall. It was detected that 9% reduction in bubble upgrade 17% in L/D, and 33% increase in stalling due to turbulence flow

transition promotion. It recommended the tripping devices in MAVs and wind turbines for early transition of flow.



**Figure 2.57:** The wavy leading edge on NACA 00012 (Serson et al. 2015).

Serson et al. (2015) analysed wavy leading edge on NACA00012 profile (Fig. 2.57) at a  $Re = 1000$ . Numerous wavelength and amplitude mixtures were taken for wave design. Most of the wavy combinations were adversely work on  $L/D$ , but eliminates the lift coefficient fluctuations. The minimum wavelength  $\lambda/c = 0.25$  had not affected the results. But  $\lambda/c = 0.5$  and  $1.0$  affects the aerodynamic efficiency( $L/D$ ) adversely. From the visualization's technique, it was found that flow tries to attach behind the waviness crest, detach behind the troughs.

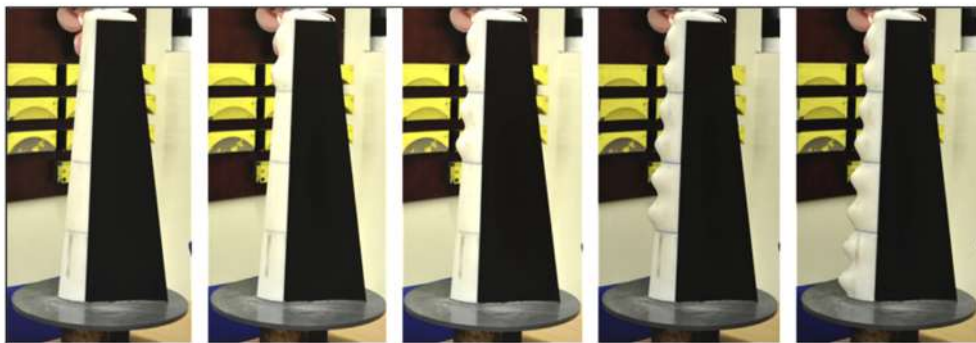


**Figure 2.58:** The L.E. tubercle on a S814 tidal turbine (Shi et al. 2016).

Shi et al. (2016) examined the Various tubercle design for a S814 tidal turbine (Fig. 2.58). It's found that it reduced the maximum lift value but increases the lift coefficients after stall situations. The full span tubercles amplify the lift and slightly increases the drag but overall, increases the aerodynamic efficiency (Maximum of 32% increased at 16 degree of angle of attack). But the effect reduces with reduction in length of the tubercle along the span of the wing. It also reduces the induced drag.

**Bahrff et al.** (2016) ran an experiment on an aeroacoustics using Krueger flap and conventional slat (Fig. 2.59). Changing the slat gap affected the noise, gap increases noise also increases. And closed gap showed high level of noise control. **Akaydin et al.** (2016) verified the effect of Krueger flap over a conventional slat for noise control (Fig. 2.60). The better flow acceleration in gap reduces the noise with same aerodynamic forces generation.

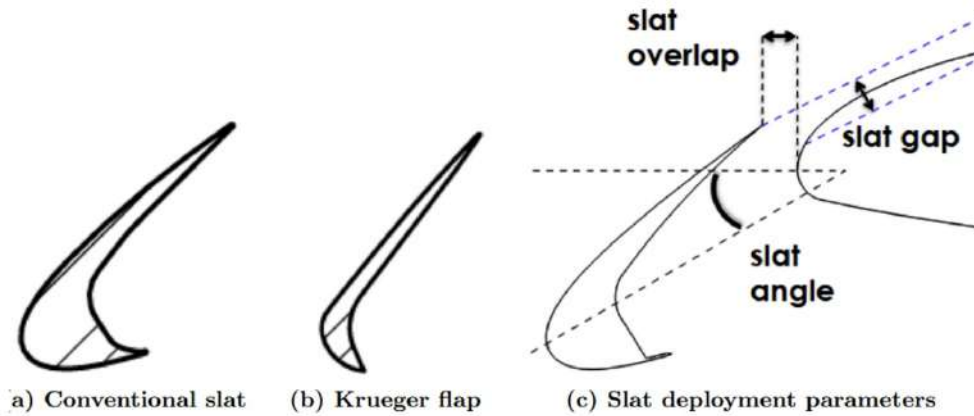


**Figure 2.59:** Airfoil with conventional slat and Krueger flap (**Bahrff et al.** 2016).

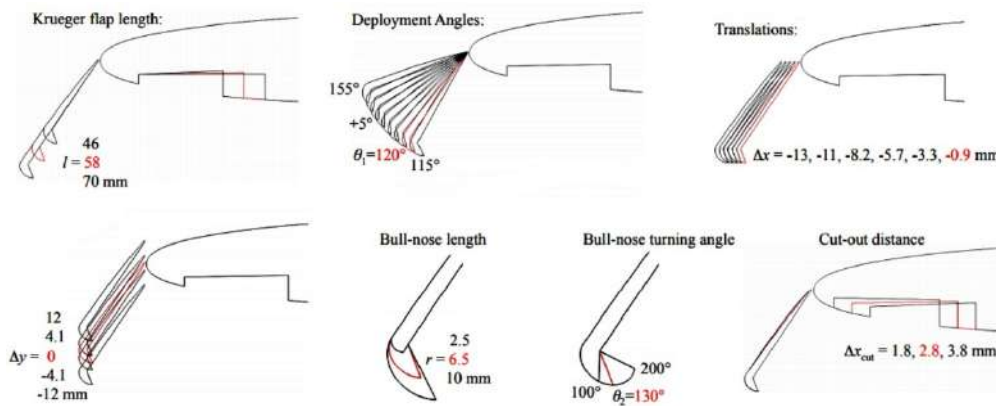


**Figure 2.60:** Airfoil with Krueger flaps (**Akaydin et al.** 2016).

**Zhou et al.** (2017) inspected the interference flow between a small plate placed near the L.E. of NACA4405 (Fig. 2.61) and Mach number effect on flow separation reduction. Study focused the parameters such as length, angle and position of plate. At Mach  $< 0.5$ , plate effectively reduce the detachment of flow and provide a relatively high  $C_l$  at large angle. At Mach  $> 0.5$ , plate showed less

amelioration in  $C_l$ . For the plate with  $L = 0.06c$ ,  $Y = 0.05c$  and  $\beta = 15^\circ$  at  $M = 0.4$ . the smooth attached flow pattern was found at angle  $< 10^\circ$ . But not enriched the performance of the airfoil. The separation bubble forms at angles  $(10^\circ - 18^\circ)$  for the airfoil suppressed by the small plate. At an angle  $22^\circ$ , bubble appears again and reduce the effect of plate.

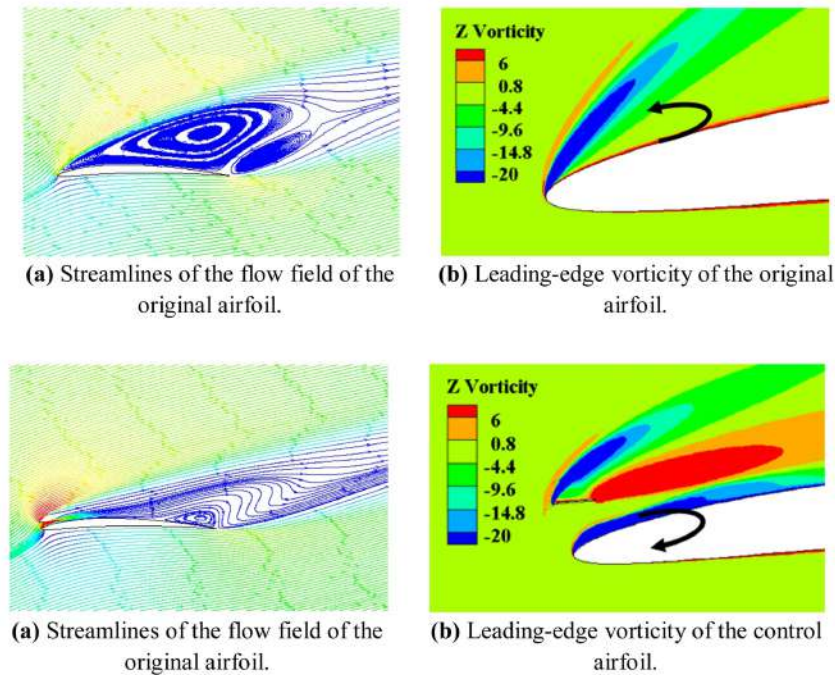


**Figure 2.61:** A small plate near the L.E. of NACA 4405 Airfoil (Zhou et al. 2017).

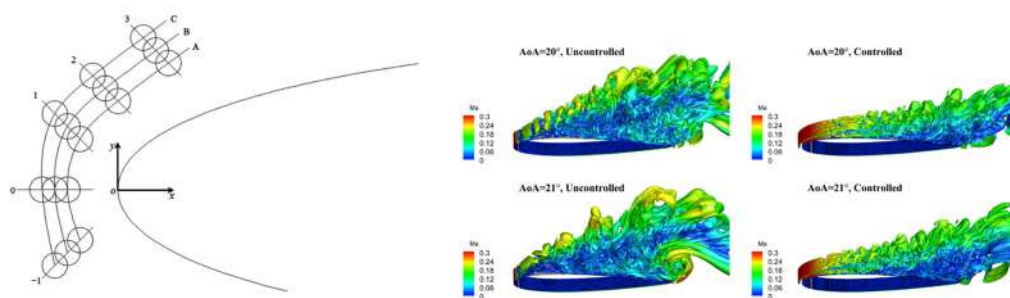


**Figure 2.62:** The micro cylinder on NACA 0012 airfoil leading edge (Luo et al. 2017).

Luo et al. (2017) considered a micro cylinder (Fig. 2.62) on the stalled airfoil (NACA 0012) at  $Re = 6 \times 10^6$  for numerical simulation using RANS and DDES simulations and varied the flow angles 16 to 23 degrees. 3 parameters were

taken for the analysis such as spacing, diameter and location of the micro cylinder. The smallest diameter ( $D/c= 0.01$ ) of the micro cylinder Boost the lift and  $L/D$  after fully separated condition (19deg).

**Aftab et al.** (2017) researched the effect of different tubercle leading edge (TLE - sinusoidal and spherical) on NACA 4415 (Fig. 2.63). Both designs reduce the aerodynamic efficiency but reduction by spherical TLE less than sinusoidal TLE. both TLE with tinier amplitude ( $0.025c$ ) tubercles showed better flow characteristics. The spherical TLE controls the leading-edge separation bubble than other base airfoil and sinusoidal airfoil at  $18^\circ$  AoA. The experimental study concludes that spherical TLE improves the  $C_{lmax}$  than the airfoil with VG above  $10^\circ$  AoA.

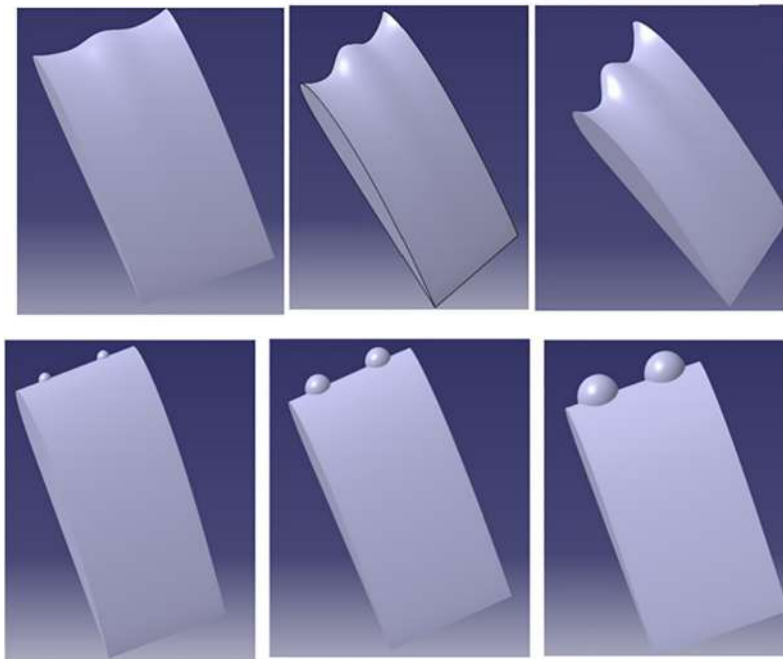


**Figure 2.63:** Airfoil with sinusoidal and spherical tubercle leading edge  
(**Aftab et al.** 2017).

**Turner et al.** (2017) investigated the airframe noise reduction on leading edge slat using the slat - cove filler (SCF) and slat gap filler (SGF). The flexible SCF fills the slat cove directs the flow properly without unsteadiness, so reduces the noise. The SGF blocks the gap flow using overleaf structure and increase the lift coefficient by increasing the camber which helps landing. Even though it

very complex mechanism it reduces the noise to a greater level. To solve this issue, Super elastic shape memory alloys can be proposed.

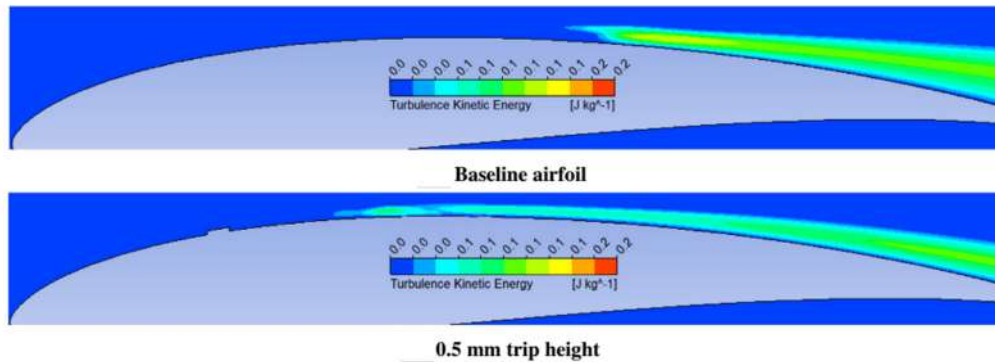


**Figure 2.64:** Airfoil with boundary layer trip (Sreejith and Sathyabhama, 2018).

Sreejith and Sathyabhama (2018) investigated the laminar separation bubble (LSB) formation on airfoil E216 (Fig. 2.64) using Transition  $\gamma$ - $Re\theta$  model at  $Re_c$  of  $10^5$ . The movement of LSB towards the leading edge was observed using velocity coefficient of pressure plot. Trip parameters of such as location - 0.1C and 0.17C, trip heights - 0.3 mm, 0.5 mm, 0.7 mm, 1 mm were taken for the analysis. And found that trip height of 0.5mm will be the maximum height for optimum flow improvements. Trip reduces/removes the LSB and increases the drag(D) by 15.48% and L/D by 21.62% for  $60^\circ$ .

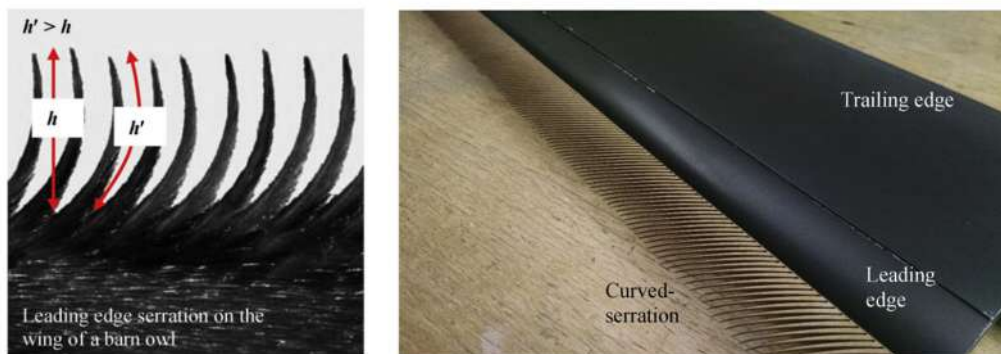


**Figure 2.65:** The leading-edge curved serrations on airfoil (Juknevičius et al. 2018).

Juknevičius et al. (2018) done a study of leading-edge serration on aero acoustics and aerodynamic performance of a symmetrical airfoil NACA 0008

(Fig. 2.65). The square grid is used to introduce the turbulence in flow. The optimum working the serration wavelength should be more and serration amplitude should be less. It was detected that it can either increase performance or reduce the noise. But both are not possible using single configuration. And found that highest amplitude and wavelength showed the significant improvement in both performance and noise reduction.

**Tong et al.** (2018) did a noise control analysis on wavy leading edge in turbulent flow using LES simulation at Re. of 26000 and 397000. 10 mm diameter rod was used to trip turbulence. The acoustic analogy method was used. The wavy leading edge showed enhancement in lift and drag with suppressed fluctuations. It due to the vortex pair from the peak. At 90° azimuth angle, noise reduced averagely by 9.5 dB due to wavy edge and effective at all azimuthal angles.

**Leknys et al.** (2018) inspected the influences of a thin trip wire placed near a leading-edge NACA 0012 airfoil (Fig. 2.66) at Reynolds number 20,000 which is under dynamic stall. The change in diameter of thin wire not having any impact on the flow separation because the flow is already in a high flow separation condition due to high angle, which makes airfoil behaves as a bluff body. It reduces the maximum lift and flow fluctuations. It was quantified that the trip wire not a possible mode of flow control.

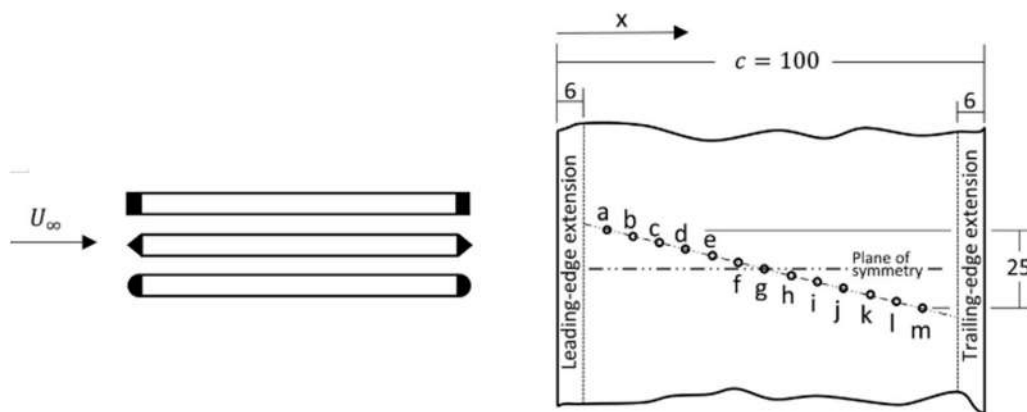


**Figure 2.66:** Leading edge vortex generators on pitching plate (**Leknys et al.** 2018).



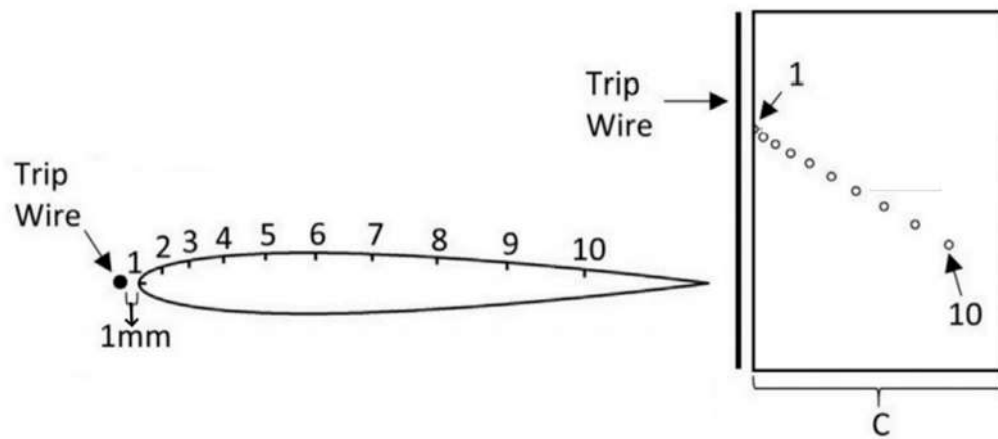


**Figure 2.67:** Airfoil with leading edge pitching plate (Leknys et al. 2018).

Leknys et al. (2018) examined the flapping wings and micro-aerial vehicle's stall behaviour using a pitching flat plate (Fig. 2.67) to control the flow. Three distinct designs (circular, square, and triangular) were attached on L.E. and T.E. The circular shape on both ends of wing shows better lift than other designs (square and triangular) with increasing rotation rate. But those attachments become inactive at high incident angles.

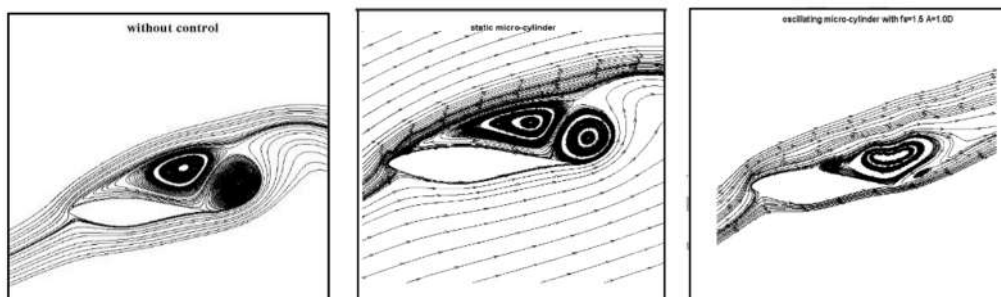


**Figure 2.68:** S809 airfoil with the oscillating micro cylinder (Shi et al. 2019).

Shi et al. (2019) simulated flow over a S809 airfoil with micro-cylinder (stationary and an oscillating condition) placed in front of the leading edge (Fig. 2.68) at a Reynolds number of  $1 \times 10^6$  for angles  $10^\circ$  to  $24^\circ$ . It was found that the oscillating cylinder delay the separation and increase the L/D by 88.21% at optimum condition than the stationary cylinder. It's also found that the similar effect of improvement cab be achieved by increasing the static cylinder about 4 times the initial diameter.

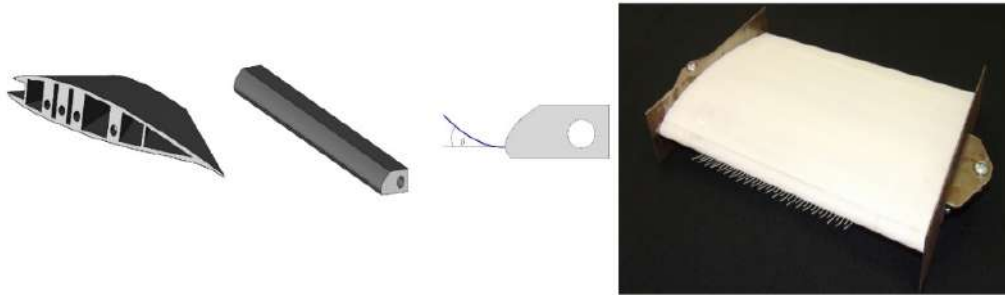


**Figure 2.69:** The leading-edge comb extensions on airfoil (Geyer et al. 2020).

Geyer et al. (2020) performed a noise-reducing experiment using leading edge comb-like extensions on low-speed airfoil (Fig. 2.69). And found it was effective at low frequencies than the high frequencies. The comb structure disrupts the large turbulent eddies into tinier ones and move away those eddies from surface. This causes reduction in pressure fluctuations. The maximum lift value is achieved at 6deg angle with straight projections having length of 0.0095 and distance of 0.019. and lift got affected adversely with increased spacing. But the maximum lift value is achieved at 12deg with curved projections having a length of 0.06 and distance of 0.019.

### Profile modifications

Kelly J. A (1950) conducted a wind-tunnel experiment on flow separation phenomenon using modifications to the leading-edge of the NACA 631-012 airfoil (Fig. 2.70). Increasing the leading-edge radii and camber enhanced the maximum lift without affecting stall behaviour. Increasing the leading-edge radii without changing camber revealed no enhancement on lift and stalling properties. The effect of leading-edge flap on max lift coefficient varies with different angle of attack. It is observed that the max lift coefficient increased upto 10° flap deflections, remains constant for 10° to 30° deflections, and decreased after that.

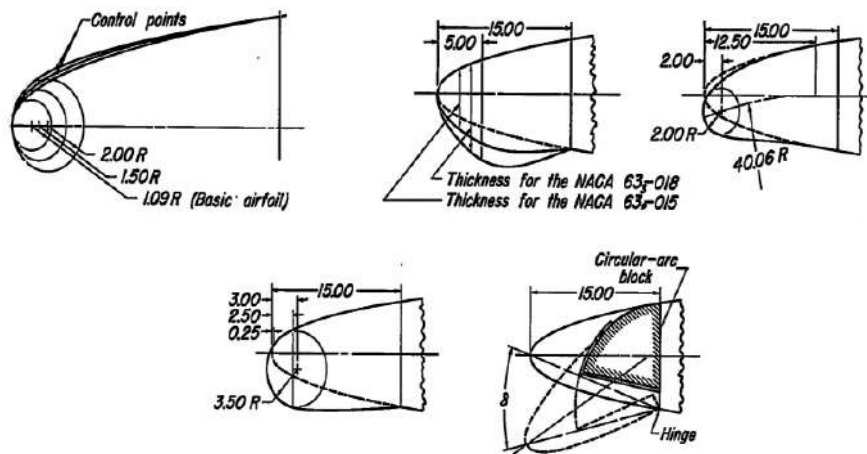


**Figure. 2.70:** The different leading-edge modifications on NACA 6-Series airfoil (Kelly J. A., 1950).

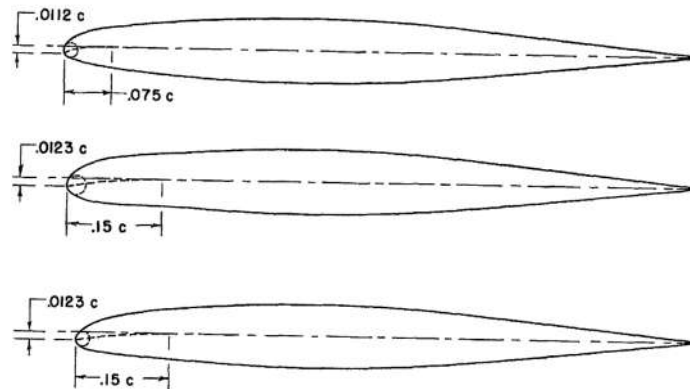


**Figure. 2.71:** The leading-edge profile modifications on NACA 6-Series airfoil (Maki and Hunton, 1956).

**Maki and Hunton** (1956) tested three different modified leading-edge regions of the NACA 64A010 airfoil (Fig. 2.71). It is found that the increment in low speed max lift coefficient and stalling angle with no increment in pitching moment and decrease in high-speed max lift coefficient upto Mach number of 0.65 because of compressibility effects. A modified section with 0.011c of nose radius and 0.15c of camber reduce the drag at high-speed.

**Merz and Hague** (1975) studied the alterations in the upper surfaces of NACA 64-2XX airfoils by varying the leading-edge thickness distribution and maximum thickness of the airfoil. Lift coefficient is increasing by increasing the thickness but not affected by the leading-edge profile modifications.

Adverse pitching moment increases with additional thickness and with increases in the leading-edge profile exponent. For a specified lift coefficient, adverse pitching moment is minimized by reducing the leading-edge profile exponent. Peak pressure for a certain lift coefficient can be considerably reduced by careful selection of the L.E additional thickness distribution exponent. For a given lift coefficient, adverse pitching moment is minimized by reducing the leading-edge profile exponent.



**Figure. 2.72:** The modified forward contour of NACA 641-212 airfoil (Hicks et al. 1975).

Hicks et al. (1975) modified forward contour of NACA 641-212 airfoil (Fig. 2.72) and tested at low speeds (Mach ranges 0.2, 0.3 and 0.4 and Reynolds number ranges 1.0, 1.5, 1.9, and  $3 \times 10^6$ ). It's found that maximum lift coefficient increases. Two different Modifications were considered, one is drooped leading-edge with increased leading-edge nose circle radius, and second one is increased thickness in front section upto 35% on upper surface without drooped. These modifications increased Maximum  $C_l$  by 30% and decreased the drag at high angle of attack. But at low and moderate angles, it showed 10% drag penalty and 30% pitching moment. The upper surface modifications not affect drag. The aerodynamic efficiency increased by 23% by upper-surface modification at  $M = 0.2$ .



**Figure. 2.73:** The upper-surface modifications on NACA 6-Series airfoil (Szalazek and Hicks, 1979).

Szalazek and Hicks (1979) analysed the  $C_{l_{max}}$  Improvement of Selected NACA 6-Series Airfoil using upper-Surface Modifications (Fig. 2.73). For upper surface modification, the airfoil thickness is increased upto max thickness of

airfoil. It indicates that the stall characteristics and climb performance are improved. and showed the maximum rise in lift coefficient at 14 degree of angle of attack.

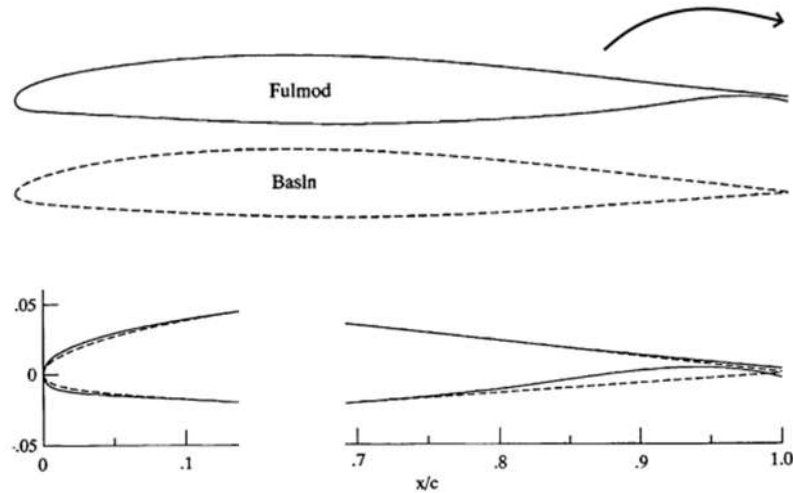


**Figure. 2.74:** The profile modifications at L.E. and T.E. of EA-6B airfoil (Allison et al. 1995).

Allison et al. (1995), modified and tested the airfoil at leading- and trailing-edge regions on a baseline wing-fuselage model (Fig. 2.74). The trailing-edge modification caused increase in the maximum lift coefficient. And leading-edge modification further increased it. This lift benefit was reduced at  $M=0.400$ . The effective angle of attack, lift and pitching moments increases because of the trailing-edge camber increment. but it causes additional drag at transonic Mach numbers due to viscous and wave drag.

Sankar et al. (2000) analyzed a drooped leading-edge on a base-line airfoil VR 12 (Fig. 2.75). Base line and drooped airfoils showed similar type of flow properties (such as attached flow, forces and moments) at lesser angles of attack ( $11^\circ+4^\circ$ ). The drooped airfoil showed slighter adverse pressure gradient and no stall at modest angles of attack ( $14^\circ+4^\circ$ ) but VR 12 airfoil showed a mild stall, with rise in drag and pitching moment. The drooped airfoil also stalled dynamically with lesser drag, pitching moments at higher angles of attack ( $21^\circ+4^\circ$ ).

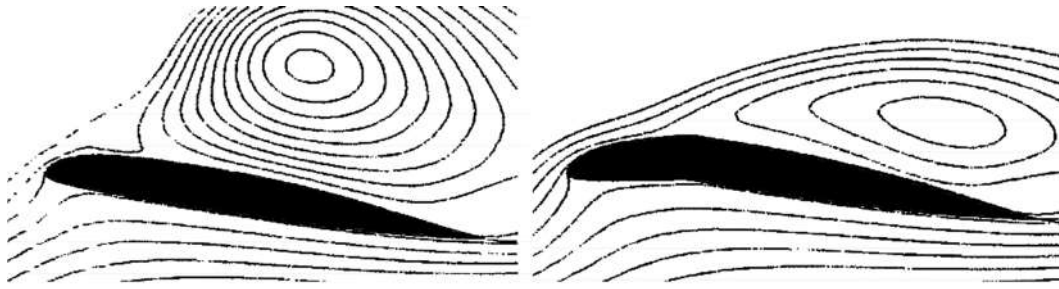


**Figure. 2.75:** The drooped leading edge airfoil (Sankar et al. 2000).

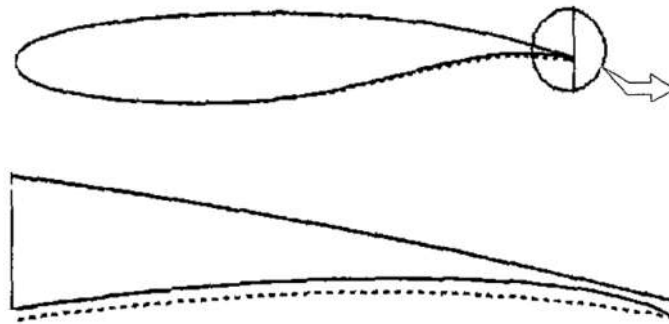


**Figure. 2.76:** divergent trailing edge DLBA 186 supercritical airfoil (Yoo, 2001).

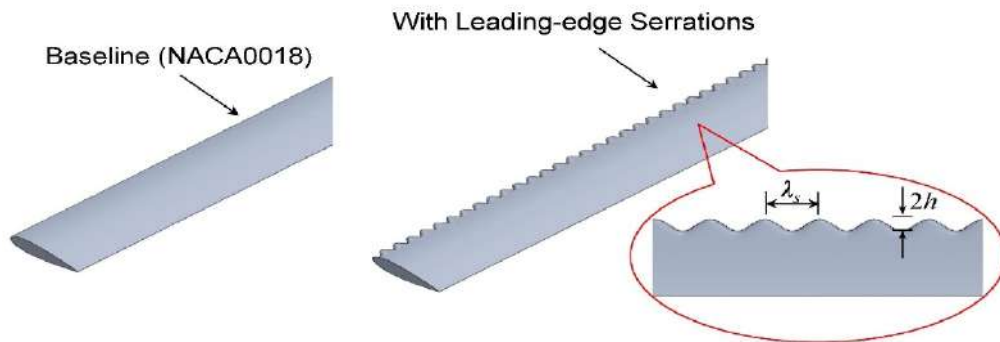


**Figure. 2.77:** Wing with and without L.E serrations (Wang and Zhuang, 2017).

**Yoo** (2001) performed a computational study on the divergent T.E. modification applied to a supercritical airfoil (DLBA 186) (Fig. 2.76). Baseline airfoil was modified as DLBA 283. Spalart-Allmaras one-equation turbulence model was used for simulation. The DTE model has reduced the strength of the shock and moved the shock position downstream, hence reduced the drag. Also, the recirculating flow region contribute to the lift. At low angles there is no

considerable increase in lift but drag reduced. Thus, the aerodynamic efficiency increases in transonic flow.

**Wang and Zhuang (2017)** studied the power performance at low TSRs of H-type Vertical Axis Wind Turbine ((Fig. 2.77) at different tip speed ratios and Reynolds number. To improve the performance, sinusoidal serrations on the L.E. were considered. At low tip-speed ratios and Reynolds number, dynamic stall occurs periodically. Hence, rotor torque, lift coefficient, and power output are reduced. The power output is improved for turbine with the sinusoidal serration (wave amplitude  $0.025c$  and the wavelength  $0.33c$ ) at low TSRs. The flow separation is significantly decreased for  $75^\circ$  to  $160^\circ$  azimuth angle with a positive torque generation.

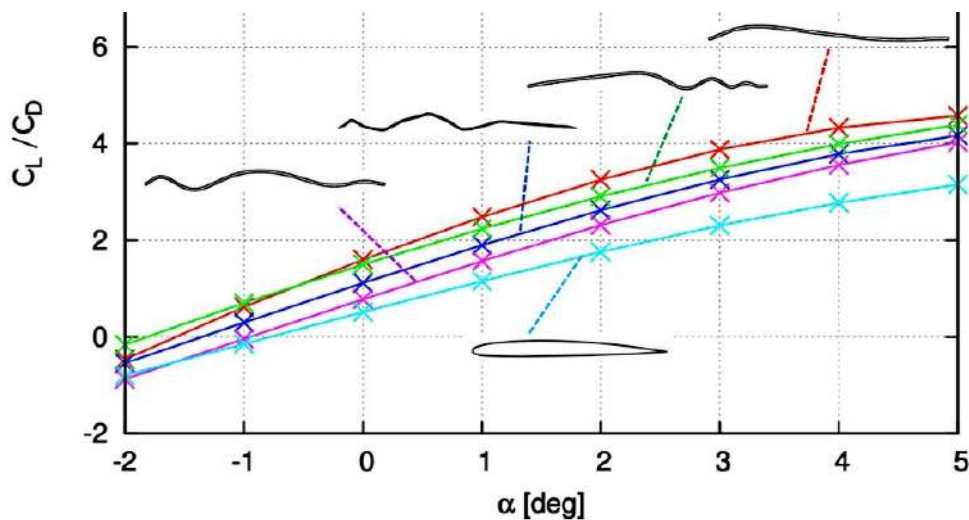


**Figure. 2.78:**  $C_L/C_d$  curve for different wavy airfoils (**Tang et al. 2020**).

**Tang et al. (2020)** studied the outcome of wavy leading edge on aerodynamic efficiency. 4 different wavy airfoil shapes are created using the NACA2408 airfoil (Fig. 2.78). The geometrical parameters such as count and width of waves were taken for the analysis. All 4 wavy designs showed increase in aerodynamic efficiency (lift increases and drag decreases) than NACA2408 airfoil profile. The addition of waves shape increases the surface area of the wing and increases the friction drag. It is also observed that the greater number of waves in wing lower the aerodynamic efficiency. Hence, for higher aerodynamic performance, the less count of waves is preferable.

## **2.5 Summary:**

From the above literature reviews on the flow separation control of airfoil/wing, the following conclusions are inferred.

The complexity in active flow control method's design and mounting mechanism makes them difficult to apply in existing aircraft wings. The low profile vortex generators are proved to be effective at high angles, and act as a drag device at low angles (cruise phase). For better flow control and aerodynamic efficiency, VGs position should be varied for different flow conditions i.e. angle of attack. And VG has to be retracted within the wing at cruising phase of the aircraft to avoid the additional flow disturbance and drag due to the VGs. The flow separation control by the profile modifications, and morphing of airfoil/wing involves complex design mechanisms, hence it is difficult to incorporate in the existing aircraft wing. Many flow control devices such as vortex generator were designed which are inspired by the marine mammals like whale fin, bump, tubercles, serrations, etc. and successfully proved its effectiveness in flow control only at high angles. It is also understood that the L.E. modifications on the wing such as drooped leading edge, wavy leading edge, attaching micro cylinder improves the aerodynamic efficiency only at high angles of attack and not within the operating range of angle of attack. It is inferred that the trailing edge modifications are less effective in flow separation control then the leading edge modifications. Thus this research focus on the passive flow control method using the leading edge modifications for flow separation control and drag reduction within the operating range of angles of attack without affecting the low angle cruising performance of aircraft wing.

## **2.6 Motivation and Objectives**

Most of the transport vehicle designs are inspired by the birds, marine mammals, and terrestrial animals. All those creatures have been evolving for a million of years by adapting for different atmospheric conditions in both internal and external structure. Hence, their external body shapes and structures are counted to be the most optimized aerodynamically. Most of the transport vehicle's designs and mechanisms are derived from the living creatures. The



recent researches on the aerodynamic optimization of automobiles particularly the aviation industry is based on the bio-inspired designs and mechanisms. The major objectives of the optimization in aviation design using the bio-inspired and bio-mimicry designs are flow separation control, drag reduction, and blade noise reduction, etc.

The bio-inspired designs play an important role in the aerodynamics to design the aircraft fuselage, wing, blades design, etc. Few examples are, the different types of winglets inspired by the birds to produce the minimum induced drag, such as Airbus's recent design concept which is inspired by the eagle winglet. The different leading edge designs such as wavy leading edge, vortex generators which are inspired by the marine mammal's parts such as whale fin, bump, tubercles, serrations, etc. The low noise turbine blade designs inspired by the owl's wing design (Justin and Peake 2020, Wang et al. 2019, Chen et al. 2019, Wagner et al. 2017). The recent extensive studies on the variable geometric surface wing, foldable wings, flopping wings, flexible wing control surfaces which are inspired by the birds, such as NASA's conceptual morphing aircraft. The high aspect ratio wings inspired by the sea birds. Bullet train's nose design inspired by the nose of the kingfisher bird. And the low drag car design inspired by the boxfish design (Kozlov et al. 2015).

The bio-inspired flow separation control method is an emerging field. Most of the bio-mimicking in aerodynamics is based on the wings, tails and flippers of various avian and aquatic species. No significant literature could be found on the mimicking of the nose of aquatic or avian species. The paper thus, proposes a new innovative leading-edge device, (which is inspired by the nose of cetacean species) for flow control, which is effective within the operating range of angles of attack. This simple and fixed leading-edge device gives better aerodynamic performance without adding complex retracting mechanism and its control. Bio-inspired nose with different nose length, nose depth, nose circle diameter and airfoils with different thickness, different camber, different camber location, different minimum pressure location, etc. will be considered for the analysis to understand the aerodynamic flow properties such as vortex formation, flow

separation, aerodynamic efficiency and moment. The main objectives of this study are as follows:

- a. To create a recirculation region (Axial vortices) on the leading edge of the airfoil using Forward facing step or Cavity (Bio inspired nose).**

Different bio-inspired nose designs (54 cases) have been numerically analysed on NACA2412 airfoil at low speed for different angle of attacks to find the optimum nose design (the porpoise nose).

- b. To find an optimal Bio Inspired Nose Design for Low subsonic speed airfoil**

The optimum nose design has been analysed on 22 different NACA 4 series airfoils and 10 different NACA 6 series with different thicknesses, camber, and camber locations, etc. at low speeds ( $M=0.05$ ) Re. No.  $1 \times 10^6$  and ( $M=0.13$ ) Re. No.  $3.1 \times 10^6$  for different angle of attacks to find the common optimum nose design for NACA 4 and 6 series airfoils.

The different spanwise length of porpoise nose on a finite wing have been analysed at ( $M=0.13$ ) Re. No.  $3.1 \times 10^6$  to find the optimum spanwise length of porpoise leading edge device.

- c. To find an optimal Bio Inspired Nose Design for High subsonic speed airfoil**

The optimum nose design has been analysed on NACA 6 series airfoils at high subsonic speeds ( $M=0.38$ ) Re. No.  $9 \times 10^6$ , ( $M=0.5$ ) Re. No.  $1.2 \times 10^7$  and ( $M=0.7$ ) Re. No.  $1.7 \times 10^7$  to find the effectiveness optimum nose design at high subsonic speed.

## CHAPTER 3

### RESEARCH METHODOLOGY

#### 3.1 Introduction to computational method

##### 3.1.1 Introduction to CFD

In computational fluid dynamics (CFD), the physical fluid flow problems are solved using the mathematical equations such as Navier-Stokes Equation, turbulence equations, etc. The governing equations are solved using the computer in the discretized form such as Finite Volume method. The important domains of CFD are Pre-processor (where geometry and mesh are generated and boundary conditions are applied), Solver (Includes the required governing equations, turbulence models and solver setting), and Post processor (the output of the simulations as contour, plots, etc.) as mentioned in figure 3.1. The CFD gives a wide-ranging of modelling abilities for a fluid flow with incompressible and compressible effect, laminar and turbulent flow conditions, and Steady or unsteady conditions as mentioned in figure 3.2.

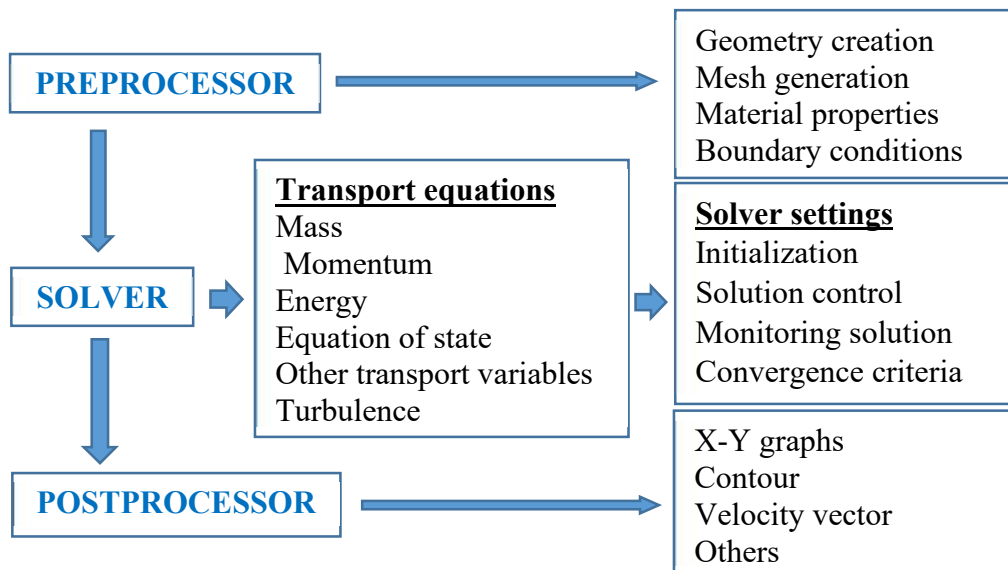


Figure 3.1 Main elements of CFD framework

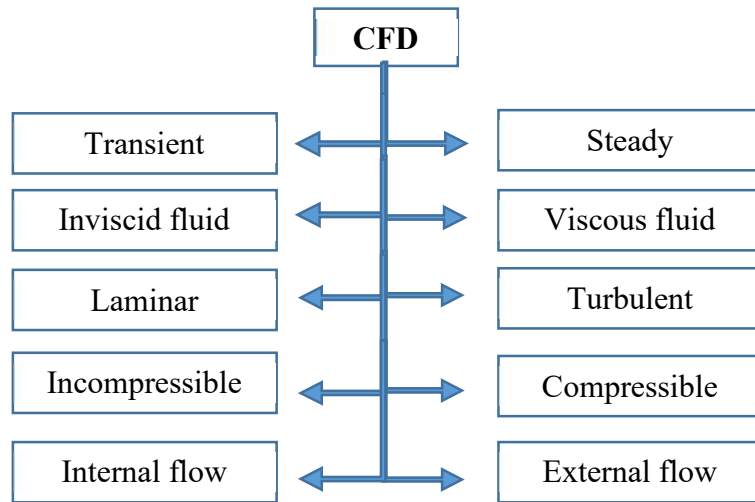


Figure. 3.2 Various flow physics in CFD

### Discretization

*General Scalar Transport Equation:*

ANSYS Fluent converts a general scalar transport equation to an algebraic equation using a control-volume-based technique which can be solved numerically. It is integrating the transport equation on each control volume, gives a discrete equation that expresses the conservation laws.

Discretization of the governing equations written in integral form for an arbitrary control volume  $V$  is given below (Eq. 3.1). Where,  $\rho$  is the density,  $\vec{v}$  is the velocity vector,  $\Gamma_\phi$  is the diffusion coefficient for  $\phi$ ,  $\nabla_\phi$  is gradient of  $\phi$ ,  $S_\phi$  is the source of  $\phi$  per unit volume, and  $\vec{A}$  is the surface area vector.

$$\int_V \frac{\partial \rho \phi}{\partial t} dV + \oint \rho \phi \vec{v} \cdot d\vec{A} = \oint \Gamma_\phi \nabla_\phi \cdot d\vec{A} + \int_V S_\phi dV \quad (3.1)$$

Discretization of above Equation on a given cell gives the following equation (Eq. 3.2). Where,  $N_{faces}$  is number of cell faces,  $\phi_f$  is value of  $\phi$  convected through the face,  $\rho_f \vec{v}_f \cdot \vec{A}_f$  is the mass flux through the face,  $\vec{A}_f$  is the area of the face,  $\nabla_{\phi_f}$  is the gradient of  $\phi$  at face,  $V$  is the volume and  $\frac{\partial \rho \phi}{\partial t} V$  is defined in temporal discretization.

$$\frac{\partial \rho \phi}{\partial t} V + \sum_f^{N_{faces}} \rho_f \vec{v}_f \phi_f \cdot \vec{A}_f = \sum_f^{N_{faces}} \Gamma_\phi \nabla \phi_f \cdot \vec{A}_f + S_\phi V \quad (3.2)$$

The discretized scalar transport equation contains the unknown scalar variable at the cell center as well as in neighbor cells. This non linear equation can be written in a linearized form as follows (Eq. 3.3). Where, the subscript nb refers the neighbor cells, and  $a_p$ , and  $a_{nb}$ , are the linearized coefficients of  $\phi$  and  $\phi_{nb}$ .

$$a_p \phi = \sum_{nb} a_{nb} \phi_{nb} + b \quad (3.3)$$

Applying the above equations for each cell will give a set of algebraic equations with a sparse coefficient matrix, and solved using a point implicit (Gauss-Seidel) linear equation solver in conjunction with an algebraic multigrid (AMG) method.

#### *Spatial Discretization:*

The spatial discretization of the Navier-Stokes equations means that the numerical approximation of the convective and viscous fluxes, and the source term. Three categories are finite difference, finite volume, and finite element. The finite volume method directly uses the conservation laws of the Navier-Stokes equations. It discretizes the governing equations by dividing the domain as a smaller control volume. The finite volume method is suited for complex geometries with both structured and unstructured grids. Two methods are used to define the shape and position of the CV. In cell centred scheme the flow properties are saved at centroids of the cell but in cell-vertex scheme the flow properties are saved at grid points. The accuracy is based on the scheme applied to estimate the fluxes. In central schemes, the average of conservative variable on left and right side of CV is used to find the flux at a side of a CV. In upwind scheme, the flux is derived from the conservative variable in a cell upstream. It distinguishes the upstream and downstream influences. ANSYS Fluent has the following upwind schemes: first-order, second-order upwind, power law, and QUICK. Compared to the upwind scheme, the central scheme needs less computing time, but upwind predicts the discontinuities and boundary layer

accurately. The limiter function is used to prevent the accidental switching in smooth flow conditions. But it needs more computational requirements. In first order upwind scheme, the cell center quantity is assumed to be the average value of the cell face quantity. In power law scheme, the face values are interpolated using the 1D convection-diffusion equation. In second order upwind scheme, cell face quantity is calculated using the multidimensional linear reconstruction approach. The quick scheme is constructed using a weighted average of second-order-upwind and central interpolations of the variable. It is accurate for the structured mesh with the cells aligned on the flow direction.

For the simulation, second-order upwind scheme is used, where the quantities at cell faces are computed using a multidimensional linear reconstruction approach. The higher-order accuracy is achieved through a Taylor series expansion of the cell-centered solution about the cell centroid. The face value is computed using the following expression (Eq. 3.4).

$$\phi_{f,SOU} = \phi + \nabla_{\phi} \cdot \bar{r} \quad (3.4)$$

where,  $\phi$  and  $\nabla_{\phi}$  are the cell-centered value and its gradient in the upstream cell, and  $\bar{r}$  is the displacement vector from the upstream cell centroid to the face centroid.

*Temporal Discretization:*

This method has more flexibility, because different approximation levels can be easily designated for the convective and the viscous fluxes, as well as for the time integration. When the method of lines is applied to the governing equations

$$\frac{d(\Omega \bar{M} \bar{W})}{dt} = -\dot{J} \quad (3.5)$$

where,  $\Omega$  is volume of CV and  $\dot{J}$  is the spatial discretization.  $\bar{M}$  represents the mass matrix.

In a cell-vertex scheme, the CV's average value of  $\bar{W}$  is related to the point values at interior and neighboring nodes. In the cell-centered scheme, the mass matrix is replaced by an identity matrix. For steady-state cases, the mass matrix

can be substituted by the identity matrix. Because the solution accuracy is governed only by the order of the residual. But the mass matrix is important for cell-vertex schemes in unsteady calculations.

For a static grid the time derivative is given by

$$\frac{\Omega \bar{M}}{\Delta t} \Delta \vec{v}^n = -\frac{\beta}{1 + \omega} \vec{v}^{n+1} - \frac{1 - \beta}{1 + \omega} \vec{v}^n + \frac{\omega \Omega \bar{M}}{(1 + \omega) \Delta t} \Delta \vec{v}^{n-1}$$

With 
$$\Delta \vec{v}^n = \vec{v}^{n+1} - \vec{v}^n \quad (3.6)$$

The  $n$  and  $(n + 1)$  represent the time levels,  $\Delta t$  represents the time step. The accuracy is depending on the following equation

$$\beta = \omega + \frac{1}{2} \quad (3.7)$$

Depending on the parameters  $\beta$  and  $\omega$ , it may either explicit ( $\beta = 0$ ) or implicit time-stepping schemes.

In Explicit Schemes, forward difference is used for the approximation of time derivative, and current time level is used for the evaluation of the residual. But it is stable only if related with a first-order upwind spatial discretization.

$$\Delta \vec{v}^n = -\frac{\Delta t}{\Omega} \vec{v}^n \quad (3.8)$$

In Runge-Kutta schemes (multistage time-stepping schemes), the solution is progressed in a number of stages and residual is estimated in-between states. In numerical simulations, the Explicit schemes are cheap (needs a small computer memory), but maximum time step is restricted due to the stability limitations. Mainly for viscous flows and highly stretched grid cells, the convergence will be slow. In steady-state solutions, the available convergence acceleration methodologies are local time-stepping, characteristic time-stepping, Jacobi preconditioning, implicit residual smoothing or residual averaging, e implicit-explicit residual smoothing, and multigrid method.

The Implicit Schemes, ( $\beta \neq 0$ ) is suitable for the unsteady flow simulation. Particularly, the 3-point implicit backward-difference scheme. In this case, the

scheme is mostly employed with dual time-stepping approach, where a steady-state problem is solved in pseudo-time at each physical time step.

$$\left( \frac{\Omega}{\Delta t} + \beta \frac{\partial \Phi}{\partial t} \right) \Phi^n = -\dot{S}^n \quad (3.9)$$

The term  $\frac{\partial \Phi}{\partial t}$  is the flux Jacobian. The expression in parenthesis is the implicit operator. If  $\beta$  is 1, which results in a 1st-order accurate temporal discretization. If  $\beta = 1/2$ , then A 2nd-order time accurate scheme.

For implicit schemes, larger time steps can be used, without hampering the stability of the time integration process. It has robustness and convergence speed. But it takes higher computational effort per time step or iteration. System of linear equations are solved using either a direct or an iterative method. , direct methods require a very high computational effort and a computer memory. The iterative method solves the equations using some iterative matrix inversion methodology with reduced iteration step and higher efficient. For structured grids, iterative methods like the alternating direction implicit scheme, the gauss-seidel relaxation scheme, and the lower- upper symmetric gauss-seidel are employed. for unstructured grids, the Gauss-Seidel relaxation scheme is used.

Gradients are required to generate scalar values at faces of cell, and calculate secondary diffusion and velocity derivatives terms. The following methods are used in Ansys fluent. the green-gauss theorem is used to calculate the gradient of the scalar at the cell center. Green-Gauss Cell-Based method calculate the Gradient using the arithmetic average values at the cell centers of neighboring cells. Green-Gauss Node-Based method calculate the Gradient using the arithmetic nodal average values on the face. The node-based method is very accurate than the cell-based method unstructured meshes, but it is more expensive. The Least Squares Cell-Based method assumes that the gradient varies linearly. It solves the minimization problem for the system to govern the gradient. the least-squares method accuracy on unstructured meshes is equivalent to the node-based method. But less expensive. Hence, Ansys fluent chosen this as the default method. In this method, the change in cell values



between cell  $c_0$  and  $c_i$  along the vector  $\Delta r_i$  from the centroid of cell  $c_0$  to cell  $c_i$ , can be expressed as

$$(\nabla\phi)_{c_0} \cdot \Delta r_i = (\phi_{c_i} - \phi_{c_0}) \quad (3.10)$$

Applying the above equations for each neighboring cell, the system can be obtained as follows (Eq. 3.11), where the  $[J]$  is the coefficient matrix that is purely a function of geometry.

$$[J](\nabla\phi)_{c_0} = \Delta\phi \quad (3.11)$$

The cell gradient  $(\nabla\phi_0 = \phi_x\hat{i} + \phi_y\hat{j} + \phi_z\hat{k})$  is determined by solving the minimization problem for the system of the non-square coefficient matrix in a least-squares sense. The above linear-system of equation is over-determined and can be solved by decomposing the coefficient matrix using the Gram-Schmidt process. This decomposition gives a matrix of weights  $(w_{i0}^x, w_{i0}^y, w_{i0}^z)$  for each cell. Therefore, the gradient at the cell center can then be computed by multiplying the weight factors by the difference vector  $\Delta\phi = (\phi_{c_i} - \phi_{c_0})$ ,

$$(\phi_x)_{c_0} = \sum_{i=1}^n w_{i0}^x \cdot (\phi_{c_i} - \phi_{c_0}) \quad (3.12)$$

$$(\phi_y)_{c_0} = \sum_{i=1}^n w_{i0}^y \cdot (\phi_{c_i} - \phi_{c_0}) \quad (3.13)$$

$$(\phi_z)_{c_0} = \sum_{i=1}^n w_{i0}^z \cdot (\phi_{c_i} - \phi_{c_0}) \quad (3.14)$$

Gradient Limiters or slope limiters, are employed on the second-order upwind scheme to stop oscillations, that occur in the flow (near shocks, discontinuities, etc.) The gradient limiters used in the ANSYS Fluent are: Standard limiter, Multidimensional limiter, and Differentiable limiter. the standard and multidimensional limiter are under the group of the non-differentiable form. The third limiter is under the group of a differentiable type of limiter. Fluent has

two limiting directions for these limiters. In cell to face limiting, the gradient is calculated at cell face centers. Which is the default method. in cell to cell limiting, the gradient is calculated among two adjacent cell centroids. The standard limiter is using the Minimum Modulus function to limit the solution overshoots and undershoots on the cell faces. The multidimensional is similar to the standard limiter. In the standard limiter, the limiting causes clipping in all directions and in other cells even the limiting is not needed. This causes unnecessary dissipation to scheme. But the multidimensional limiter, carefully examines and clips. Hence is less dissipative. In Differentiable Limiter, the solution continues to converge but the residuals are stalling. Hence it uses a smooth function to make the residuals to converge.

### **Turbulence models**

The idea of using fluid to extract/deliver the energy is not recent. Leonardo Da Vinci conducted countless experiments to envision fluid flow, conversing about vortex flow, vorticity, swirls, and eddies. Fluid flow is categorized into two main groups - laminar and turbulence - concerning the forces (inertial, viscous, etc.), and a transition region between them. In Laminar Flow, Fluid flows through a smooth path with no disturbance between adjoining paths. It is quite compatible to study laminar flow both numerically and experimentally. In Turbulent Flow, Fluid flows through a chaotic path that consist of eddies, swirls, and flow uncertainties. It is tough, almost impossible in some cases, to inspect turbulent flow both numerically and experimentally. Earlier, the classification of the type of fluid flow numerically was hard to apprehend. It was made easy after the development of Reynolds number, the dimensionless number that predicts static and dynamic properties of fluid such as velocity, density, dynamic viscosity, and length:

$$Re = \frac{\text{(inertial force)}}{\text{(viscous force)}} = \frac{\rho(\text{density}) * V(\text{velocity}) * L}{\text{(characteristic length)} / \mu \text{ (dynamic viscosity)}}$$

For internal flows, Reynolds number range for the laminar regime is  $\leq 2300$ , Reynolds number range for the Turbulent regime is  $> 4000$ . For external flow, Reynolds number range for the laminar to Turbulent regime is  $> 3 \times 10^5$ .

If inertial forces are domineering, the flow is turbulent. On the converse, if the viscous forces are domineering, the flow is laminar. It is usual to generate turbulence for a fluid with low viscosity, though it is uncommon for fluids with high viscosity. Aside from laminar behavior, turbulence comprises numerous hurdles, and thus needs arduous effort during experimental and numerical investigations. Turbulent flow is unsteady, irregular, three-dimensional, rotational and diffusive at high Reynolds numbers. Because of these discrepancies in turbulent flow, small-scale fluctuations appear in flow properties. Even though direct application of fluctuated values into the Navier-Stokes equation is possible, called a *Direct Numerical Solution (DNS)*, it needs a great amount of resources in terms of hardware, software, and human work. Therefore, an appropriate numerical model should be employed when modelling turbulent flow.

To choose a suitable model and simulate physical incident as precisely as possible, following steps are required. Examining the physical incident to understand the flow phenomenon. Investigating the literature to define an appropriate model. If literature is poor, trying some models simultaneously to get an exact prediction. In the validation process, optimizing the selected model. Application of the turbulence model into the numerical method is significant and makes a great change to the simulation results. At first, a brief examination must be carried out (which relates to the Reynolds number) to identify the type of fluid flow.

Many miscellaneous turbulence models are used to examine the motion of the fluid. But it depends on turbulent viscosity, and no general turbulence model is present yet. In general, turbulence models are categorized based on governing equation and numerical method used to calculate turbulent viscosity, for which a solution is required for turbulence. *Reynolds-averaged Navier-Stokes equations (RANS)* and *large eddy simulation equations (LES)* are the common ones that require a compatible amount of resources during examination against DNS. Beyond that, *Unsteady Reynolds-averaged Navier-Stokes (URANS)*, in which motion of the solid body or flow separation produces unsteady flow, has been largely applied. The key purpose of turbulence modelling is to prompt equations to predict the time-averaged velocity,

pressure, and temperature fields, without calculating the complete turbulent flow model as a function of time as in RANS and LES. It is needless to solve the Navier-Stokes equations for each value of fluctuation, as most engineering challenges do not require such a comprehensive solution. RANS model is based on mean values of variables for both steady state and dynamic flows (unsteady for URANS). The numerical simulation is powered by a turbulence model, which is randomly selected to find out the influence of turbulence fluctuation on the average fluid flow. The DNS directly applies the fluctuated values into the Navier-Stokes equation not including any turbulence model. The LES model is a typical turbulence model between DNS and RANS in which filtered Navier-Stokes equations are employed for large scale eddies. Demanding a modest amount of hardware, computational time, and human effort, RANS/URANS methods, and sub-models are favorably applied for various fluid dynamics problems. The application of LES is rare but likely in some cases, which specifically need more computational facilities compared to URANS/RANS.

### **Solver setting**

*Pressure-Based Solver:* It uses the projection method algorithm, where the velocity is derived by resolving a pressure correction equation which is obtained from the continuity and the momentum equations. The iterative method is utilized to resolve the governing equations (nonlinear and coupled) until to get the converged solution. Two algorithms are available in ANSYS Fluent. A segregated algorithm, and a coupled algorithm. For the pressure based solver, ANSYS Fluent provides four segregated types of algorithms: SIMPLE, SIMPLEC, PISO, coupled. The Steady-state calculations will generally use SIMPLE or SIMPLEC, while PISO is recommended for transient calculations. The coupled algorithm enables full pressure-velocity coupling. The steps involved in both algorithms are shown in figure 3.3 a and 3.3 b.

The Segregated algorithm solves the governing equations sequentially. Each governing equation are solved one after another. It's memory-efficient, as it stores one discretized equation in the memory at a time. Hence, it has relatively slow convergence. The coupled algorithm solves the momentum equations and

the pressure-based continuity equation simultaneously. And solves the remaining in segregated method. It has improved rate of convergence than the segregated algorithm. But it takes 2 times the memory as all equations is stored in the memory at a time.

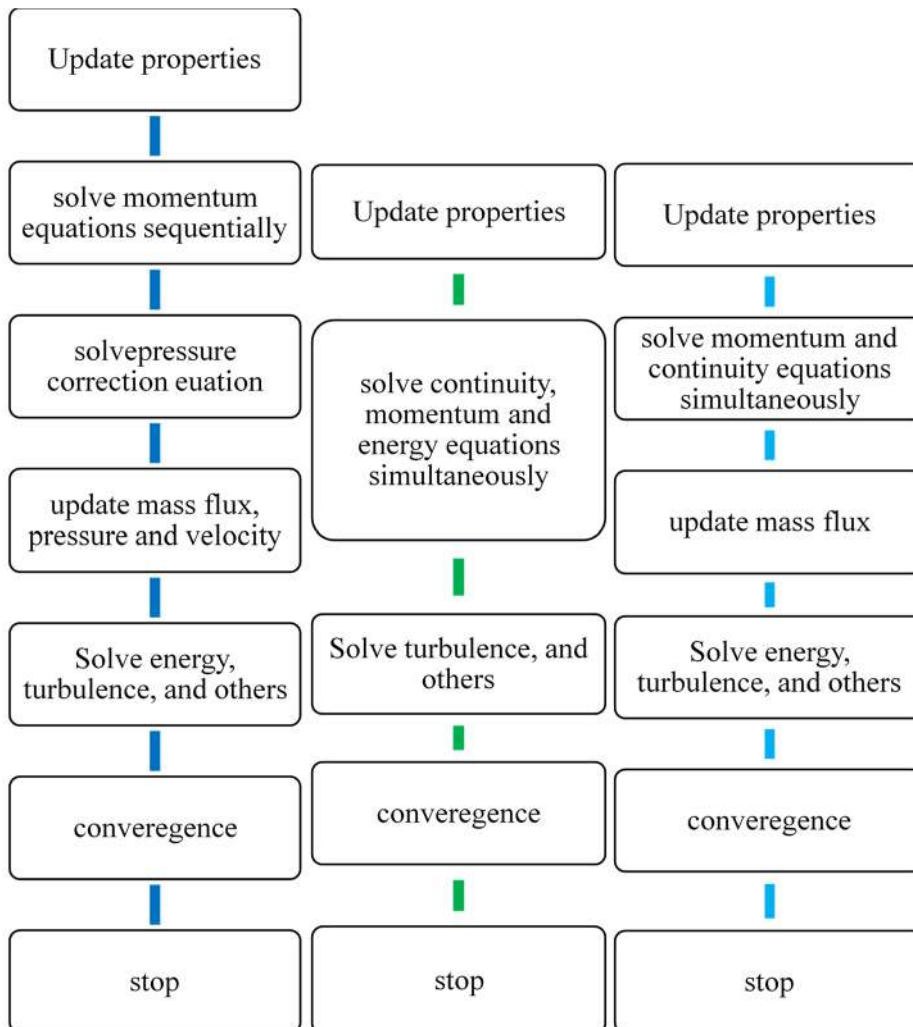


**Figure 3.3** a) A pressure based segregated algorithm, b) a pressure based coupled algorithm, c) a density based algorithm

*Density-Based Solver:* The density-based solver solves all the governing equations (continuity, momentum, and energy) simultaneously. And solves the remaining in segregated method. It needs several iteration loops to get the converged solution as it is a non-linear and coupled equations. These non-linear equations are linearized and then solved to get a flow-field property. The coupled equations are solved either using explicit formulation or implicit formulation. In implicit formulation, the unknown variable of each cell is

determined using both known and unknown values from neighboring cells. Hence, these equations are solved simultaneously. In explicit formulation, the unknown variable of each cell is determined using only existing values. Therefore, equations for the unknown value are solved one at a time. The steps followed in both algorithms are shown in figure 3.3 c.

### **Initial and Boundary Conditions**

The properly taken initial conditions are the essential point of all flow solver, because it will lead to the quicker simulations with improved convergence and faster iterations, also increases the solution accuracy. The divergence will occur if the initial conditions taken improperly. The initial conditions define the state of the fluid at time  $t = 0$  / at the first step of an iterative scheme. The ANSYS Fluent provides 12 types of boundary zone types for the flow domains such as velocity inlet, pressure inlet, mass-flow inlet, mass-flow outlet, pressure outlet, pressure far-field, outflow, inlet vent, intake fan, outlet vent, exhaust fan, and degassing. Mostly for external aerodynamics, the flow field properties such as freestream pressure, density and velocity values are used. The numerical domain is only a certain portion of physical domain with artificial boundaries such as the inlet, outlet, symmetry plane, etc. The boundary conditions should create the same physical domain condition as close as possible. the inlet and outlet boundaries should not be closer to the object taken for the analysis to get the accurate solution. for the Navier-Stokes equations, noslip boundary condition is used between the object wall and the fluid flow. The relative velocity is assumed to be zero ( $u = v = w = 0$  at the surface). The standard sea level conditions are considered as the initial conditions for most of the external aerodynamic simulations.

### **Mesh Topology**

The fine quality mesh is important for accuracy and convergence of computation of turbulent flows. The aspect ratio (stretching of a cell  $< 35:1$ ), Smoothness (changes in adjacent cells), Skewness (compared to equilateral cell  $< 0.95$ ). Generally, the quadrilateral/triangular cells will be generated in 2D

meshes, and hexahedral, tetrahedral cells are generated in 3D meshes. Mesh topology can be further classified into structure mesh, unstructured mesh and hybrid mesh. Structured meshes are preferable in most of the cases as it takes lesser number of cell count and simulation time and cost. In structured mesh topology, different mesh patterns such as H- Type, C-Type, and O-Type patterns can be generated for flow over the airfoil. But it will be a time-consuming process if the geometry is complex. So unstructured meshes are used for the complex geometries which creates the fine meshes around the body to be simulated and coarse meshes towards the domain boundary. Which takes less time to create but generate more cell counts for accurate CFD simulations.

In H-Type mesh, fine cells are crowded at the L.E and T.E. Its suitable for the thin airfoil with sharp L.E and T.E. For an airfoil with curved leading edge, it needs more splits at the leading-edge curvature to accurately capturing the profile. Its unnecessarily creates the refined meshes in the upstream of the airfoil. In C-Type mesh is an improved mesh type of H-type, which captures the L.E curvature without singularities. C-type mesh pattern avoids the upstream fine meshes. But it creates in the downstream of the airfoil T.E. but it helps to capture the separation of boundary layer, trailing wakes etc. its most suitable for the sharp T.E. airfoils. Mostly the computational domain will have longer portion after the T.E. of the airfoil. So, the fine meshes unnecessarily increase the total mesh counts and solver time and cost.

In O-type mesh almost overcomes the disadvantages of the H and C-type grids. It creates the fine mesh around the airfoil without creating the fine meshes in the upstream and downstream of the airfoil. So, this grid has the lowest number of cells than the H-type and C-type patterns. It creates distorted cells for sharp T.E. airfoils, which affect the accuracy of CFD computations. Hence, its preferable to go with the C-type grid, even though its expensive. In unstructured mesh, fine meshes wrapped around the body and coarse meshes for remaining portion of the domain. It's like the O -Type topology. so, it creates distorted cells at the trailing edge. To get the wake region behind the body, separate

refined zone is required behind the body, which increase the cell counts and simulation time.

### 3.1.2 Governing equations of CFD

The behavior of fluid particles is determined by the basic conservation laws such as continuity, momentum, and energy equations. It shows the total changes in flow properties inside the control volume (CV). The flux is due to the convective transfer and molecular motion.

#### The continuity equation

The law of mass conservation states that the mass cannot be generated nor destroyed in a fluid system. Consider a control volume  $\Omega$  with flow velocity  $\vec{v}$ , density  $\rho$ , unit normal vector  $\vec{n}$ , and elemental surface area  $dS$ . For the flow leaves the CV where the unit vector points out, the inflow is considered as negative and outflow is considered as positive. Then the integral form of continuity equation is written as

$$\frac{\partial}{\partial t} \int_{\Omega} \rho d\Omega + \oint_{\partial\Omega} \rho(\vec{v} \cdot \vec{n}) dS = 0 \quad (3.15)$$

First term is the time rate of change of mass inside the CV, and second term is the convective flux across the surfaces.

#### The momentum equation

The newton's second law states that the change in momentum cause the force acting on a CV. Two forces on a CV are body forces ( gravitational, buoyancy, centrifugal forces, and electromagnetic forces) and surface forces (due to pressure and shear stress distribution). the integral form of momentum equation is written as

$$\frac{\partial}{\partial t} \int_{\Omega} \rho \vec{v} d\Omega + \oint_{\partial\Omega} \rho \vec{v} (\vec{v} \cdot \vec{n}) dS = \int_{\Omega} \rho \vec{f}_e d\Omega - \oint_{\partial\Omega} P \vec{n} dS + \oint_{\partial\Omega} (\vec{\tau} \cdot \vec{n}) dS \quad (3.16)$$

Where  $p$  is the pressure component and  $\vec{\tau}$  viscous stress tensor. First term is the change in momentum with respect to time, second term is convective flux tensor, third term is body force, last two terms are the surface force.



### The energy equation

The first law of thermodynamics states that the change in total energy is due to the rate of work done and net heat flux on CV. The total energy per unit mass ( $E$ ) is equal to the sum of internal energy per unit mass ( $e$ ) and kinetic energy per unit mass ( $\frac{|\vec{v}|^2}{2}$ ). the integral form of energy equation is written as

$$\begin{aligned} \frac{\partial}{\partial t} \int_{\Omega} \rho E d\Omega + \oint_{\partial\Omega} \rho E (\vec{v} \cdot \vec{n}) dS \\ = \oint_{\partial\Omega} k(\nabla T \cdot \vec{n}) dS + \int_{\Omega} (\rho \vec{f}_e \cdot \vec{i} + \dot{q}_h) d\Omega - \oint_{\partial\Omega} p(\vec{v} \cdot \vec{n}) dS \\ + \oint_{\partial\Omega} (\vec{\tau} \cdot \vec{v}) \cdot \vec{n} dS \end{aligned} \quad (3.17)$$

Where  $k$  is the thermal diffusivity coefficient,  $T$  - absolute static temperature,  $\dot{q}_h$  is the time rate of heat transfer per unit mass. The first term is rate of change of energy, second term is convective flux, third term is diffusive flux, fourth term is heat sources due to time rate of heat transfer per unit mass and rate of work done by the body forces. Last term is rate of work done by surface forces. Using the enthalpy and energy relation the energy equation is written as

$$H = h + \frac{|\vec{v}|^2}{2} = E + \frac{P}{\rho} \quad (3.18)$$

$$\begin{aligned} \frac{\partial}{\partial t} \int_{\Omega} \rho E d\Omega + \oint_{\partial\Omega} \rho H (\vec{v} \cdot \vec{n}) dS \\ = \oint_{\partial\Omega} k(\nabla T \cdot \vec{n}) dS + \int_{\Omega} (\rho \vec{f}_e \cdot \vec{v} + \dot{q}_h) d\Omega \\ + \oint_{\partial\Omega} (\vec{\tau} \cdot \vec{v}) \cdot \vec{n} dS \end{aligned} \quad (3.19)$$

Where  $\vec{\tau}$  is the stress tensor, and in cartesian coordinates is written as

$$\vec{\tau} = \begin{bmatrix} \tau_{xx} & \tau_{xy} & \tau_{xz} \\ \tau_{yx} & \tau_{yy} & \tau_{yz} \\ \tau_{zx} & \tau_{zy} & \tau_{zz} \end{bmatrix} \quad (3.20)$$

The components of viscous stress tensor are defined below (equ 3.12 to 3.17), where  $\lambda$  is the 2nd viscosity coefficient, and  $\mu$  is the dynamic viscosity coefficient.

$$\tau_{xx} = \lambda \left( \frac{\partial u}{\partial x} + \frac{\partial v}{\partial y} + \frac{\partial w}{\partial z} \right) + 2\mu \frac{\partial u}{\partial x} \quad (3.21)$$

$$\tau_{yy} = \lambda \left( \frac{\partial u}{\partial x} + \frac{\partial v}{\partial y} + \frac{\partial w}{\partial z} \right) + 2\mu \frac{\partial v}{\partial y} \quad (3.22)$$

$$\tau_{zz} = \lambda \left( \frac{\partial u}{\partial x} + \frac{\partial v}{\partial y} + \frac{\partial w}{\partial z} \right) + 2\mu \frac{\partial w}{\partial z} \quad (3.23)$$

$$\tau_{xy} = \tau_{yx} = \mu \left( \frac{\partial u}{\partial y} + \frac{\partial v}{\partial x} \right) \quad (3.24)$$

$$\tau_{xz} = \tau_{zx} = \mu \left( \frac{\partial u}{\partial z} + \frac{\partial w}{\partial x} \right) \quad (3.25)$$

$$\tau_{yz} = \tau_{zy} = \mu \left( \frac{\partial v}{\partial z} + \frac{\partial w}{\partial y} \right) \quad (3.26)$$

### The Navier-Stokes equations:

It describes the mass, momentum and energy exchange across the boundary in a CV. The general form of conservation law for a vector quantity is written in Eq. 3.27, where  $\vec{U}$  is the vector quantity,  $\vec{F}_C$  is the convective flux tensor,  $\vec{F}_D$  is the diffusive flux tensor,  $\vec{Q}_v$  is the volume sources, and  $\vec{Q}_s$  is the surface sources.

$$\frac{\partial}{\partial t} \int_{\Omega} \vec{U} \, d\Omega + \oint_{\partial\Omega} [(\vec{F}_C - \vec{F}_D) \cdot \vec{n}] \, ds = \int_{\Omega} \vec{Q}_v \, d\Omega + \oint_{\partial\Omega} [\vec{Q}_s \cdot \vec{n}] \, ds \quad (3.27)$$

The above equation can be written together with continuity, momentum and energy equation as

$$\frac{\partial}{\partial t} \int_{\Omega} \vec{W} \, d\Omega + \oint_{\partial\Omega} \vec{F}_C - \vec{F}_v \, ds = \int_{\Omega} \vec{Q} \, d\Omega \quad (3.28)$$

Conservative variables  $\vec{U}$ , the convective flux tensor  $\vec{F}_c$ , the diffusive flux tensor  $\vec{F}_D$ , the volume sources  $\vec{Q}_v$ , and the surface sources  $\vec{Q}_s$  consists the following components.

$$\vec{U} = \begin{bmatrix} \rho \\ \rho u \\ \rho v \\ \rho \omega \\ \rho E \end{bmatrix}; \vec{F}_c = \begin{bmatrix} \rho v \\ \rho uV + n_x P \\ \rho vV + n_y P \\ \rho wV + n_z P \\ \rho HV \end{bmatrix}; \vec{F}_D = \begin{bmatrix} 0 \\ n_x \tau_{xx} + n_y \tau_{xy} + n_z \tau_{xz} \\ n_x \tau_{yx} + n_y \tau_{yy} + n_z \tau_{yz} \\ n_x \tau_{zx} + n_y \tau_{zy} + n_z \tau_{zz} \\ n_x \Theta_x + n_y \Theta_y + n_z \Theta_z \end{bmatrix};$$

$$\text{And } \vec{Q}_s = \begin{bmatrix} 0 \\ \rho f_{e,x} \\ \rho f_{e,y} \\ \rho f_{e,z} \\ \rho \vec{f}_c \cdot \vec{v} + \dot{q}_h \end{bmatrix} \quad (3.29)$$

Where,

$$\Theta_x = u\tau_{xx} + v\tau_{xy} + \omega\tau_{xz} + k\frac{\partial T}{\partial x}$$

$$\Theta_y = u\tau_{yx} + v\tau_{yy} + \omega\tau_{yz} + k\frac{\partial T}{\partial y}$$

$$\Theta_z = u\tau_{zx} + v\tau_{zy} + \omega\tau_{zz} + k\frac{\partial T}{\partial z}$$

The Navier-Stokes equations have five equations (5 variables  $\rho, \rho u, \rho v, \rho \omega, \rho E$ ) with seven unknown variables ( $\rho, u, v, \omega, E, p, T$ ). Hence it needs two more equations such as thermodynamic equation which relates the pressure, density and temperature, internal energy or the enthalpy. And equation relates viscosity coefficient and the thermal conductivity coefficient. The following are the commonly used equations.

For calorically perfect gas, the equation of state is

$$P = \rho RT \quad (3.30)$$

The enthalpy equation is

$$h = C_p T, \text{ where } R = C_p - C_v; \gamma = \frac{C_p}{C_v} \quad (3.31)$$

The pressure equation is

$$P = (\gamma - 1)\rho \left[ E - \frac{u^2 + v^2 + \omega^2}{2} \right] \quad (3.32)$$

The Sutherland equation is

$$\mu = \frac{(1.45T^{3/2})}{T + 110} \cdot 10^{-6} \quad (3.33)$$

If temperature is 288k, then  $\mu = 1.78 \cdot 10^{-5} \text{ kg/ms}$

viscosity coefficient and the thermal conductivity coefficient relation is

$$k = C_p \frac{\mu}{Pr} \quad (3.34)$$

Where the Prandtl number is constant ,  $Pr = 0.72$ .

### 3.1.3 Governing equations of turbulence models:

The Turbulence models available in ANSYS – Fluent software are Spalart-Allmaras model,  $\kappa - \epsilon$  models (Standard, RNG, and Realizable),  $\kappa - \omega$  models (Standard, SST), Transition  $\kappa - \kappa l - \omega$  model, Transition SST model, and Re. stress models (RSM). The DES and LES model are available only in 3D flows. All the models have its own significant accuracy depends on the physics of the flow, computational resources, time and cost. As the number of equations involved in the models increases, its accuracy and computational expenses are increasing. To predict the complex turbulent flows, fine meshes are required in near-wall (NW) (small  $y^+$ ) than for laminar flows. Treatment of wall boundaries need fine grids and more computer resources. The standard or non-equilibrium wall functions (fully developed flow condition is assumed), the  $y^+$  should be 30 -300, and 30 is desirable. The small  $y^+$  cannot account the low-Re. No. effects, it reduces the accuracy and convergence. And in enhanced wall treatment used to resolve laminar sublayer  $y^+$  should be =1 with at least 10 cells within the NW region. the non-equilibrium wall function is used for complex flows like separation, reattachment, etc. In the NW region is divided as follows, the innermost layer is viscous sublayer, which is almost laminar. The outer layer is fully-turbulent layer. The interim region between both regions.

The NW modelling influences the numerical solutions. For the better prediction of turbulent core flows, the  $\kappa - \varepsilon$ , RSM, and LES model are used. The Spalart-Allmaras and the  $\kappa - \omega$  models is applicable to both low-Re. No. models as well as high-Re. No. models. The two approaches in modelling of NW region are wall functions and NW modelling. In wall functions, the inner region is not undertaken. Instead the semi-empirical formulas are linked the with fully-turbulent region. In NW modelling, the inner region is determined with a fine mesh upto the wall. In 2D URANS method, the required average grid size is  $10^5$  and number of time steps  $10^{3.5}$ . and in 3D URANS method, the required average grid size is  $10^7$  and number of time steps  $10^{3.5}$ .

In most high-Re. No. flows, the wall function approach, rapidly changing solution variables in inner region does not resolved. So, it is economical and reasonably accurate. The NW models are used in the low-Re. No. effects (inner region).

The  $\kappa - \varepsilon$  model is a high-Re. No. model ( $30 < y^+ > 300$ ), determines a turbulent length and time scale based on transport equations for the turbulence kinetic energy ( $\kappa$ ) and turbulence dissipation rate ( $\varepsilon$ ) with the assumption of fully turbulent flow, and negligible molecular viscosity effect.

$$\frac{\partial}{\partial t}(\rho k) + \frac{\partial}{\partial x_i}(\rho k u_i) = \frac{\partial}{\partial x_j} \left[ \left( \mu + \frac{\mu_t}{\sigma_k} \right) \frac{\partial k}{\partial x_j} \right] + G_k + G_b + \rho \varepsilon - Y_M + S_k \quad (3.35)$$

$$\frac{\partial}{\partial t}(\rho \varepsilon) + \frac{\partial}{\partial x_i}(\rho \varepsilon u_i) = \frac{\partial}{\partial x_j} \left[ \left( \mu + \frac{\mu_t}{\sigma_\varepsilon} \right) \frac{\partial \varepsilon}{\partial x_j} \right] + C_{1\varepsilon} \frac{\varepsilon}{k} (G_k + C_{3\varepsilon} G_b) - C_{2\varepsilon} \rho \frac{\varepsilon^2}{k} + S_\varepsilon \quad (3.36)$$

$$\mu_t = \rho c_\mu \frac{k^2}{\varepsilon} \quad (3.37)$$

Where,  $G_k$  and  $G_b$  - turbulence kinetic energy generation due to mean velocity gradients, and buoyancy.  $Y_M$  - fluctuating dilatation.  $C_{1\varepsilon} = 1.44$ ,  $C_{2\varepsilon} = 1.92$  and  $C_{3\varepsilon}$  (1 if main flow parallel to gravity and 0 for perpendicular to the

gravity) are constants.  $\sigma_\kappa = 1.0$  and  $\sigma_\varepsilon = 1.3$  are the turbulent Prandtl numbers,  $C_\mu = 0.09$ ,  $S_\kappa$  and  $S_\varepsilon$  are user-defined source terms.

The standard  $\kappa - \omega$  model incorporates the effect of low-Re. No. effects, compressibility, and shear flow. And valid for wall-bounded and free shear flows. The std  $\kappa - \omega$  model transport equations (using turbulence kinetic energy ( $\kappa$ ) and the specific dissipation rate ( $\omega$ )) as follows.

$$\frac{\partial}{\partial t}(\rho k) + \frac{\partial}{\partial x_i}(\rho k u_i) = \frac{\partial}{\partial x_j} \left[ \Gamma_\kappa \frac{\partial k}{\partial x_j} \right] + G_\kappa - Y_\kappa + S_\kappa \quad (3.38)$$

$$\frac{\partial}{\partial t}(\rho \omega) + \frac{\partial}{\partial x_i}(\rho \omega u_i) = \frac{\partial}{\partial x_j} \left[ \Gamma_\omega \frac{\partial \omega}{\partial x_j} \right] + G_\omega - Y_\omega + S_\omega \quad (3.39)$$

In these equations,  $G_\kappa$  and  $G_\omega$ ,  $\Gamma_\kappa$  and  $\Gamma_\omega$  and  $Y_\kappa$  and  $Y_\omega$  - generation, effective diffusivity, and dissipation due to turbulence for  $\kappa$  and  $\omega$ , respectively.  $S_\kappa$  and  $S_\omega$  are user-defined source terms. The constants are:

$$\alpha_\infty^* = 1, \alpha_\infty = 0.52, \alpha_0 = \frac{1}{9}, \beta_\infty^* = 0.09, \beta_i = 0.072, R_\beta = 8, \quad (3.40)$$

$$R_k = 6, R_\omega = 2.95, \zeta^* = 1.5, M_{i0} = 0.25, \sigma_\kappa = 2.0, \sigma_\omega = 2.0 \quad (3.41)$$

The shear-stress transport (SST)  $\kappa - \omega$  model blend the  $\kappa - \omega$  to NW region and the  $\kappa - \varepsilon$  model to far field. It has the conversion of  $\kappa - \varepsilon$  to a  $\kappa - \omega$  model. it shows steady variation from the std  $\kappa - \omega$  models in the low region to a high-Re. No.  $\kappa - \varepsilon$  model in top region of boundary layer. The SST  $\kappa - \omega$  model shows better accuracy for adverse pressure gradient flows, airfoils, and shock.

The SST  $\kappa - \omega$  model is like the std  $\kappa - \omega$  model:

$$\frac{\partial}{\partial t}(\rho k) + \frac{\partial}{\partial x_i}(\rho k u_i) = \frac{\partial}{\partial x_j} \left[ \Gamma_\kappa \frac{\partial k}{\partial x_j} \right] + \tilde{G}_\kappa - Y_\kappa + S_\kappa \quad (3.42)$$

and

$$\frac{\partial}{\partial t}(\rho\omega) + \frac{\partial}{\partial x_i}(\rho\omega u_i) = \frac{\partial}{\partial x_j} \left[ \Gamma_\omega \frac{\partial \omega}{\partial x_j} \right] + G_\omega - Y_\omega + D_\omega + S_\omega \quad (3.43)$$

Here,  $\bar{G}_k$  and  $G_\omega$ ,  $\Gamma_k$  and  $\Gamma_\omega$ , and  $Y_k$  and  $Y_\omega$ -generation, effective diffusivity, and dissipation due to turbulence of  $k$  and  $\omega$ , respectively.  $D_\omega$ - cross-diffusion term.  $S_k$  and  $S_\omega$  are user-defined source terms. The constants are:

$$\sigma_{k,1} = 1.176, \sigma_{\omega,1} = 2.0, \sigma_{k,2} = 1.0, \sigma_{\omega,2} = 1.168 \quad (3.44)$$

$$\alpha_1 = 0.31, \beta_{i,1} = 0.075, \beta_{i,2} = 0.0828 \quad (3.45)$$

The SAS model include von Karman length-scale (VKL scale) to turbulence scale equation. This permits SAS model to dynamically change to settled forms in a URANS analysis, and gives LES performance in unsteady flow. And shows std RANS abilities in stable flow.

The SST-SAS model is based on transforming Rotta's approach to  $\kappa - \omega$  (SST).

$$\frac{\partial}{\partial t}(\rho k) + \frac{\partial}{\partial x_i}(\rho k u_i) = \frac{\partial}{\partial x_j} \left[ \left( \mu + \frac{\mu_t}{\sigma_k} \right) \frac{\partial k}{\partial x_j} \right] + G_k - \rho c_\mu k \omega \quad (3.46)$$

and

$$\begin{aligned} \frac{\partial}{\partial t}(\rho\omega) + \frac{\partial}{\partial x_i}(\rho\omega u_i) = \frac{\partial}{\partial x_j} \left[ \left( \mu + \frac{\mu_t}{\sigma_\omega} \right) \frac{\partial \omega}{\partial x_j} \right] + \alpha \frac{\omega}{k} G_k - \rho\beta\omega^2 + Q_{SAS} + (1 - \\ F_1) \frac{2\rho}{\sigma_{\omega,2}} \frac{1}{\omega} \frac{\partial k}{\partial x_j} \frac{\partial \omega}{\partial x_j} \end{aligned} \quad (3.47)$$

SAS source term  $Q_{SAS}$  - turbulence eddy frequency  $\omega$ .  $\sigma_{\omega,2}$  is the  $\sigma_\omega$  value for the SST model. The SAS approach proposed by Menter introduce the VKL scale ( $L_{vk}$ ), in the turbulence equations.  $L_{vk}$  - the ratio of the 1<sup>st</sup> / 2<sup>nd</sup> derivative of the velocity vector ( $k=0.41$ ).

### 3.1.4 Force Coefficients

The aerodynamic forces and moments on the body are due to only two basic sources pressure and shear stress distribution. Both pressure ( $P$ ) and shear stress ( $\tau$ ) have dimensions of the forces per unit area. Pressure acts normal to the surface and shear stress acts tangential to the surface. The net effect of pressure and shear stress distributions integrated over the complete body surfaces is a resultant aerodynamic force ( $R$ ) and moment ( $m$ ) on the body. The resultant force is inclined rearward from the vertical. It is not perpendicular to the chord line. The resultant force can be resolved into two components such as Lift and drag with respect to freestream flow direction. Or it can be resolved into Normal force and Axial force with respect to the airfoil chord line as mentioned in the Fig 3.4.

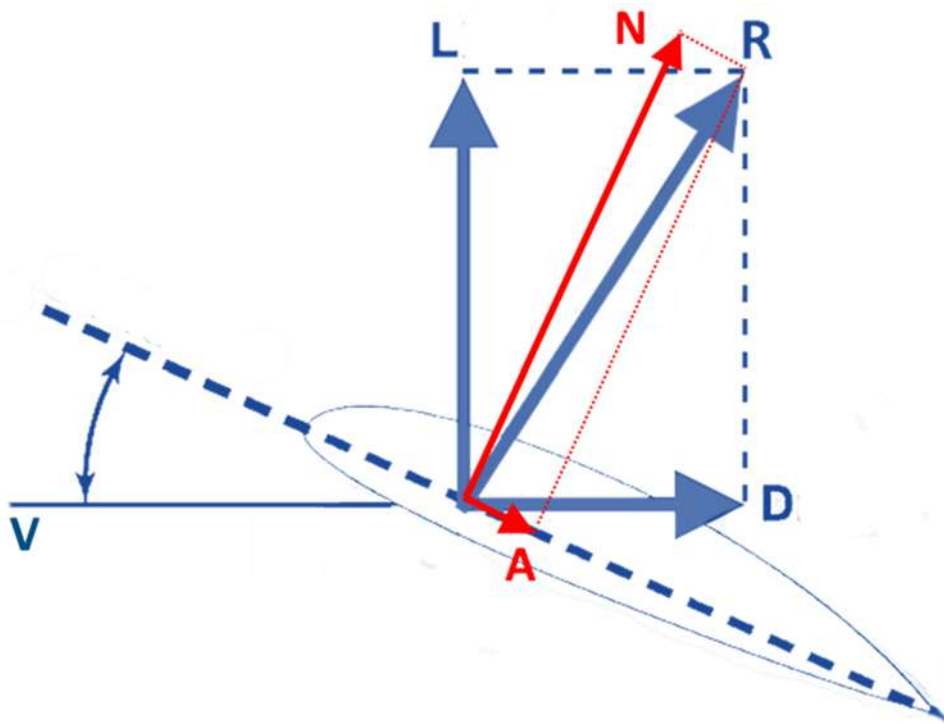


**Figure. 3.4:** Forces acting on an airfoil

The lift is a component of resultant force perpendicular to freestream velocity. The drag is a component of resultant force parallel to freestream velocity. The normal force is a component of resultant force perpendicular to airfoil chord line. The axial force is a component of resultant force parallel to airfoil chord line. Primes symbol denotes force per unit span.



$$L' = N' \cos \alpha - A' \sin \alpha \quad (3.48)$$

$$D' = N' \sin \alpha + A' \cos \alpha \quad (3.49)$$

The lift and drag force are written in terms of normal and axial forces as equation 3.48 and 3.49. The normal force and axial forces are easy to calculate as it is determined with reference to the airfoil chord. The pressure and shear stress components are resolved with respect to the airfoil chord to find normal force, axial force, and moment about leading edge from the pressure and shear stress distributions as mentioned in equation 3.50-3.52.

$$N' = \int_{LE}^{TE} -P_u \cos \theta dS_u - \int_{LE}^{TE} \tau_u \sin \theta dS_u + \int_{LE}^{TE} P_l \cos \theta dS_l - \int_{LE}^{TE} \tau_l \sin \theta dS_l \quad (3.50)$$

$$A' = \int_{LE}^{TE} -P_u \sin \theta dS_u + \int_{LE}^{TE} \tau_u \cos \theta dS_u + \int_{LE}^{TE} P_l \sin \theta dS_l + \int_{LE}^{TE} \tau_l \cos \theta dS_l \quad (3.51)$$

$$M'_{LE} = \int_{LE}^{TE} P_u \cos \theta x dS_u + \int_{LE}^{TE} \tau_u \sin \theta x dS_u - \int_{LE}^{TE} P_l \cos \theta x dS_l + \int_{LE}^{TE} \tau_l \sin \theta x dS_l - \int_{LE}^{TE} P_u \sin \theta y dS_u + \int_{LE}^{TE} \tau_u \cos \theta y dS_u + \int_{LE}^{TE} P_l \sin \theta y dS_l + \int_{LE}^{TE} \tau_l \cos \theta y dS_l \quad (3.52)$$

From the coordinate points of an airfoil, slope at different location on the airfoil can be found as in equation 3.53 - 3.55.

$$dx = ds \cos \theta \quad (3.53)$$

$$dy = -(ds \sin \theta) \quad (3.54)$$

$$S = c(1) \quad (3.55)$$

The coefficients are largely used in aerodynamic study rather than forces, moments and other properties like pressure and shear stress. So that calculations are valid for real time model and scaled down model.

$$C_l = \frac{L'}{q_\infty C}; \quad C_d = \frac{D'}{q_\infty C}; \quad C_n = \frac{N}{q_\infty C}; \quad C_a = \frac{A'}{q_\infty C} \quad (3.56)$$

$$C_p = \frac{P-P_\infty}{q_\infty}; \quad C_f = \frac{\tau}{q_\infty} \quad (3.57)$$

$$C_{P_l} = \frac{P_l-P_\infty}{q_\infty}; \quad C_{P_u} = \frac{P_u-P_\infty}{q_\infty} \quad (3.58)$$

$$C_l = C_n \cos \alpha - C_a \sin \alpha \quad (3.59)$$

$$C_d = C_n \sin \alpha + C_a \cos \alpha \quad (3.60)$$

$$C_n = \frac{1}{c} \left[ \int_0^c (C_{P_l} - C_{P_u}) d\kappa + \int_0^c \left( C_{f_u} \left( \frac{dy}{dx} \right)_u + C_{f_l} \left( \frac{dy}{dx} \right)_l \right) dx \right] \quad (3.61)$$

$$C_a = \frac{1}{c} \left[ \int_0^c \left( C_{P_u} \left( \frac{dy}{dx} \right)_u - C_{P_l} \left( \frac{dy}{dx} \right)_l \right) d\kappa + \int_0^c (C_{f_u} + C_{f_l}) dx \right] \quad (3.62)$$

$$C_{m_{LE}} = \frac{1}{c^2} \left[ \int_0^c (C_{P_u} - C_{P_l}) x dx + \int_0^c \left[ C_{f_u} \left( \frac{dy}{dx} \right)_u + C_{f_l} \left( \frac{dy}{dx} \right)_l \right] dx + \int_0^c \left[ C_{P_u} \left( \frac{dy}{dx} \right)_u + C_{f_u} \right] y dx + \int_0^c \left[ -C_{P_l} \left[ \frac{dy}{dx} \right]_l + C_{f_l} \right] y dx \right] \quad (3.63)$$

### 3.2 Geometric modelling

The leading-edge profile of NACA series airfoils has been modified as a bio-inspired nose design which are inspired by the cetacean species (Figure 3.5) by incorporating a forward-facing step and a cavity/backward facing step.

- The forward-facing step creates the low-pressure region due to multiple acceleration of flow on the upper surface at low angle of attack.
- The cavity / backward facing step creates the vortex and low-pressure region on the upper surface to delay the flow separation at high angle of attack.

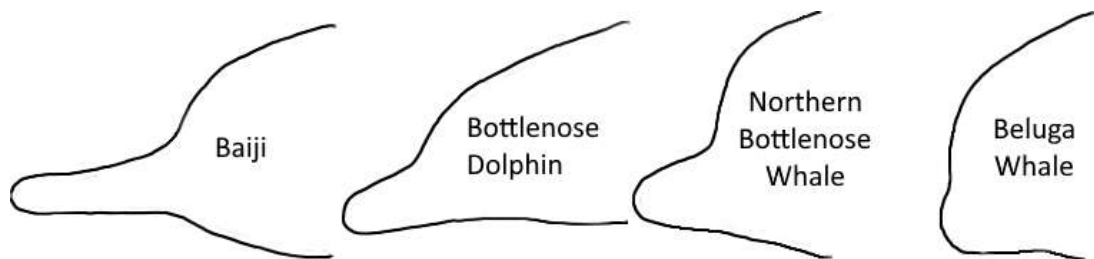


**Figure 3.5** Different nose shapes of Cetacean species

#### Steps:

1. The different bio- inspired nose shapes inspired by the cetacean species have been analysed computationally at low speed using a reference airfoil NACA 2412 to understand the aerodynamic behaviour. The camber line is taken as a reference line to draw the grid and different nose designs. From the analysis the optimum nose design has been found.
2. The different bio- inspired nose designs created with reference to the camber line have been analysed with different NACA 4 series airfoils including both symmetrical and unsymmetrical airfoils to find the optimum nose design which gives better aerodynamic performance for all NACA 4 series airfoils.

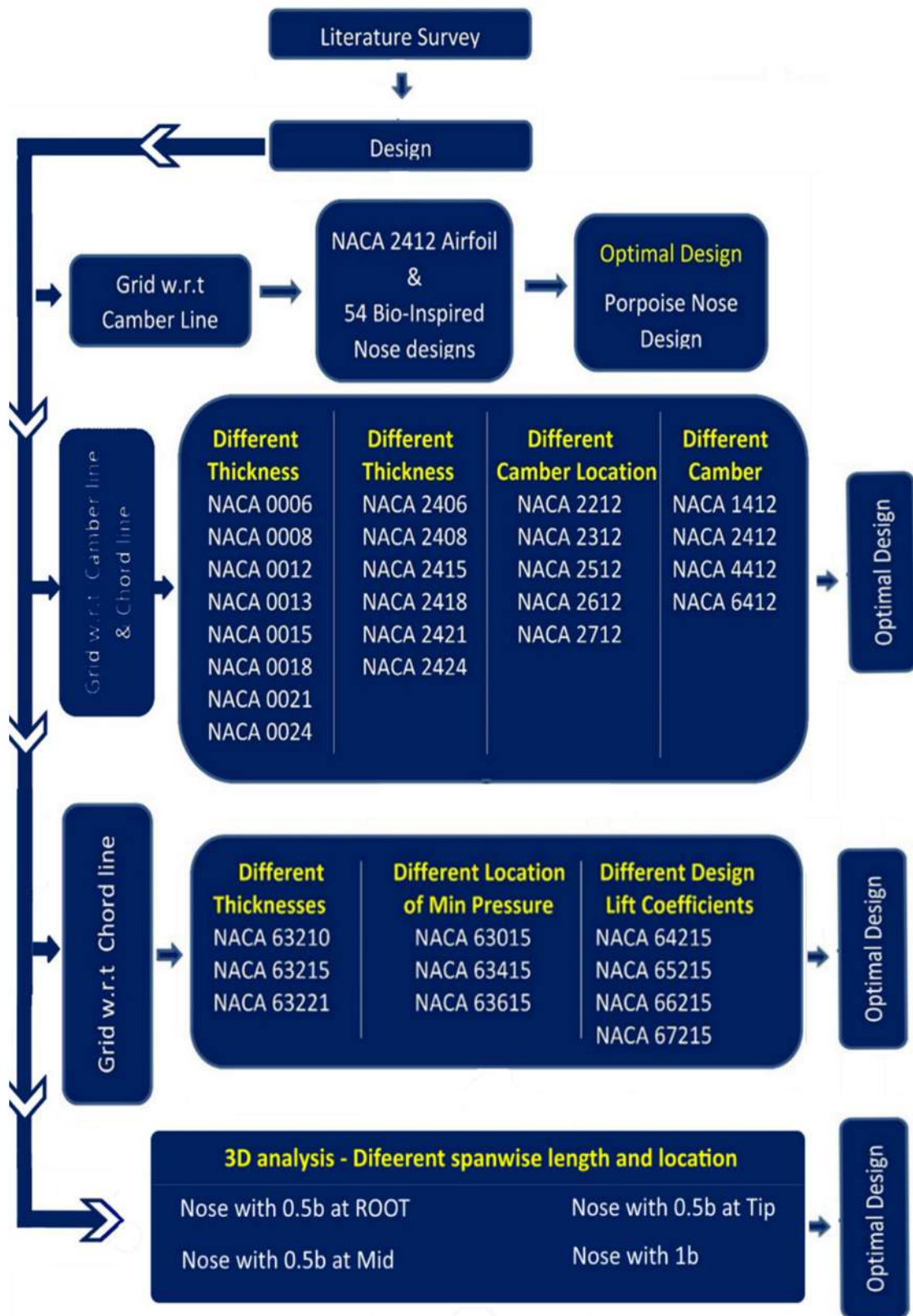
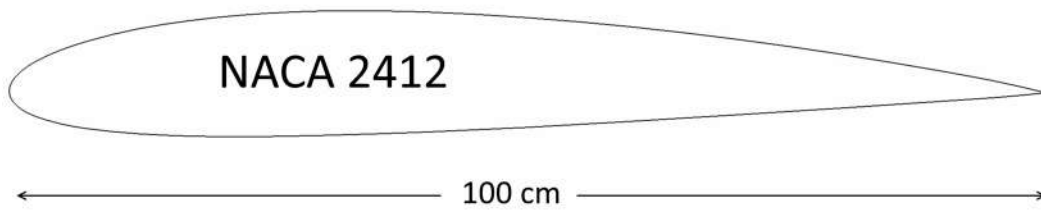


Figure 3.6 Methodology flow chart

3. The different bio- inspired nose designs created with reference to the chord line have been analysed with different NACA 4 series airfoils. Because, finding the camber line for all the unsymmetrical airfoils is a tedious process. In addition, the highly cambered thick airfoils have the highly deflected camber line near the leading edge of the airfoil. This distorts the nose shape by deflecting it downwards and affects the aerodynamic performance adversely.
4. The optimum nose design created using the chord line and camber line shows similar aerodynamic behaviour. Because the optimum nose design is very close to the leading edge. So, chord has been taken as a reference line to design the nose for further analysis.
5. The optimum nose design has been analysed on different NACA 6 series airfoils for low subsonic speed. And found one common optimum nose design for all NACA 4 and 6 series airfoils.
6. The effect of optimum nose design at high subsonic speeds has been analysed using NACA 66215 airfoil.
7. The optimum nose design with different spanwise length and position along the 3D finite wing has been analysed at low subsonic speed.

### **3.2.1 Design of bio-inspired nose on NACA 2412 airfoil.**

The bio-inspired nose designs with different nose length, different depth cavity have been chosen for the analysis to check the aerodynamic behaviour on flow separation control. To create different bio-inspired nose designs, NACA 2412 airfoil with a chord of 100 cm has been chosen as a reference model as shown in Figure 3.7. A square grid is created with reference to the camber line of the airfoil as shown in Figure 3.8. This grid is created near the lower portion of airfoil leading edge with the circles of different diameter drawn at different locations (marked as A to R).



**Figure 3.7** NACA 2412 airfoil

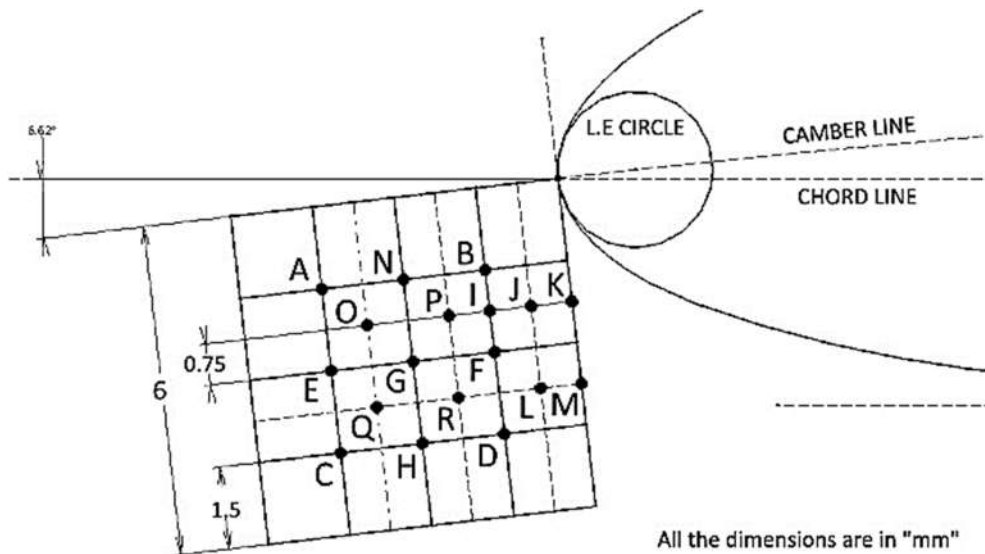


**Figure 3.8** Square grid created with respect to camber line

Totally 54 bio-inspired nose designs were created for the computational analysis. The square grid length is equal to half of the maximum thickness of NACA 2412 airfoil and the circles with diameters of 1 mm, 2mm, and 3 mm were considered for the analysis. The diameter of the bio-inspired nose has been changed from minimum 1% of chord to maximum equal to the airfoil leading edge circle diameter. To create the cetacean species nose shapes, an ellipse is used to join the nose circle and upper surface of the airfoil which is tangent to both. And another tangent line is used to join the nose circle and lower surface of the airfoil as shown in Figure 3.9. Using this design methodology, 54 bio-inspired nose designs have been created using NACA 2412 airfoil. These bio-inspired nose designs for NACA 2412 airfoil have been designed using CATIA V5 software.

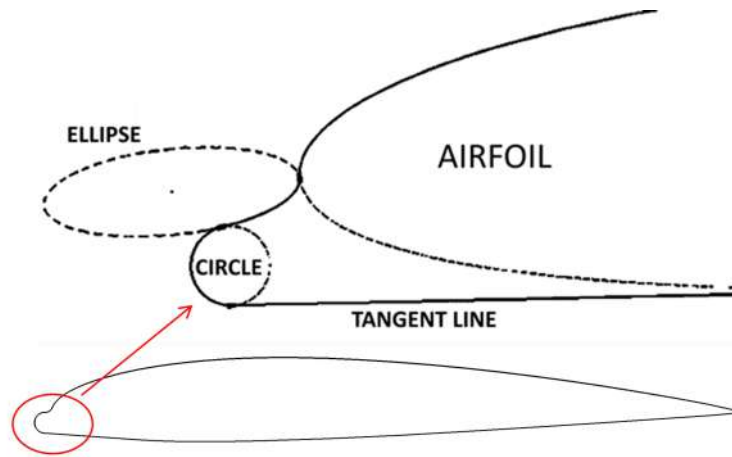
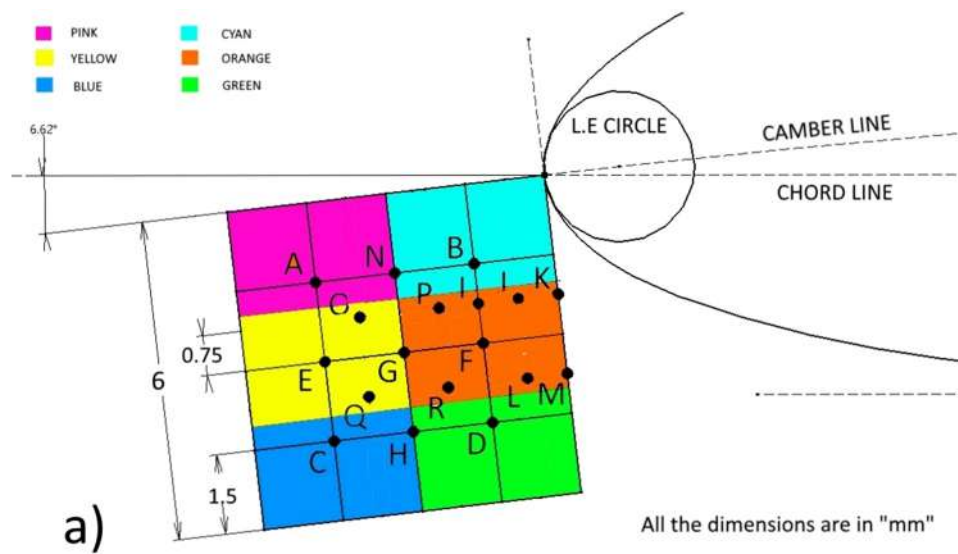


**Figure 3.9** NACA 2412 airfoil with bio-inspired nose design



a)

All the dimensions are in "mm"

b)

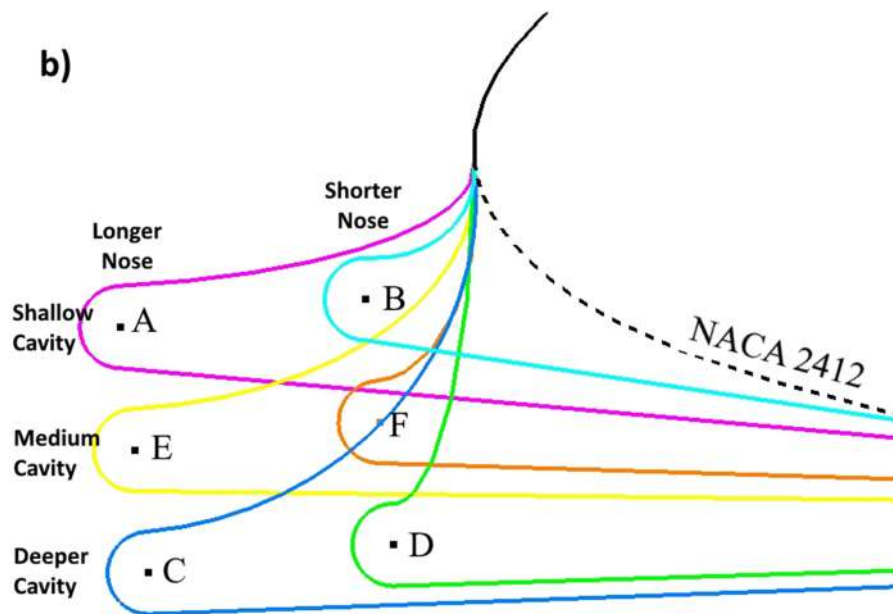


**Figure 3.10** NACA 2412 airfoil with different bio-inspired nose designs

Six regions are focused on the grid which are inspired by the various cetacean species as shown in Figure 3.10a and 3.10b.

- The pink region creates longer nose with shallow cavity (NACA 2412 A - Rough-toothed dolphin).
- The cyan region creates shorter nose with shallow cavity (NACA 2412 B - Bottlenose dolphins).
- The yellow region creates longer nose with medium depth cavity (NACA 2412 E - Spinner dolphin).
- Orange region creates shorter nose with medium depth cavity (NACA 2412 F - Beluga whale).
- The blue region creates longer nose with deeper cavity (NACA 2412 C - Indus dolphin). and
- The green region creates shorter nose with deeper cavity (NACA 2412 D - Northern bottlenose whale).

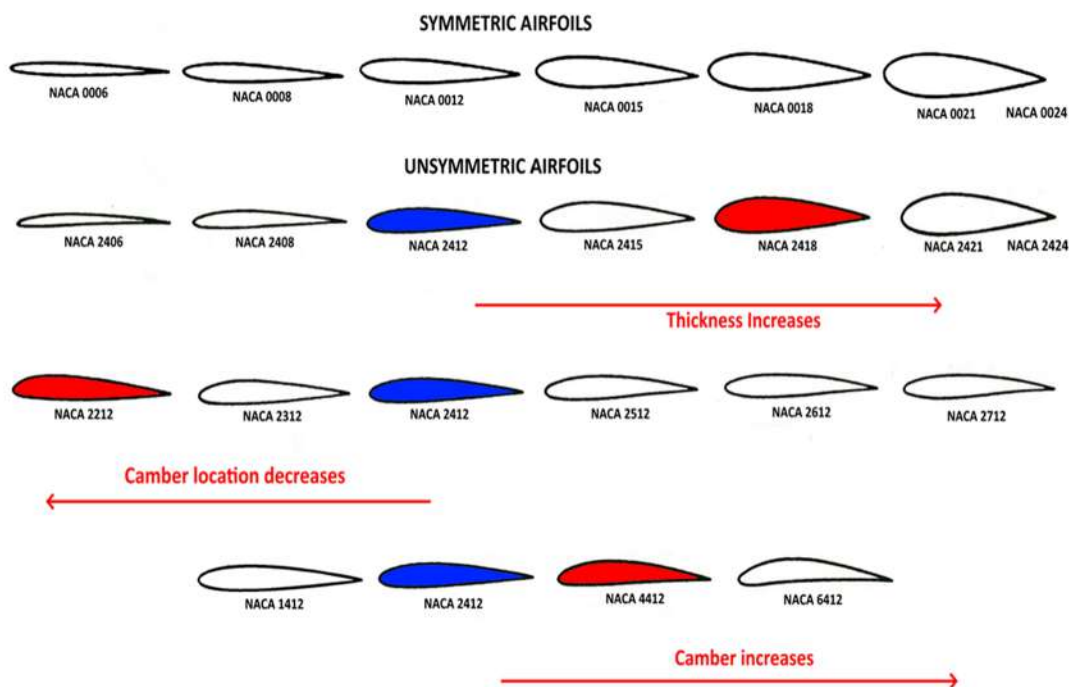


**Figure 3.11** NACA 4 series airfoils of different thickness, camber, and camber location.



The optimum bio inspired nose design has been tested on 22 different NACA 4 series airfoils as shown in Figure 3.11 (Jacobs et al. – 1933), and 10 different NACA 6 series airfoils with different thicknesses, different camber, and different camber locations to understand the effect of different airfoil geometry on the performance of bio-inspired nose on flow separation control as follows.

### **3.2.2 Design of bio-inspired nose on NACA 4 series Airfoils.**

From the computational analysis done on 54 modified NACA 2412 airfoil with different bio-inspired nose designs (Figure 3.10a and 3.10b), the optimum bio-inspired design was found. The optimum nose design matches with aquatic marine mammal “Porpoise” nose design. This optimum nose design having shorter length and medium depth cavity (depth - 2.25 % of chord, nose length - 0.75 % chord, and nose diameter – 2 % chord).

22 NACA 4 series airfoils with different thicknesses, different camber, and different camber locations have been taken for the low speed computational analysis to understand the effectiveness of different airfoil geometry on the performance of bio-inspired nose as follows.

NACA 4 series Symmetrical airfoils of different thickness such as NACA 0006, NACA 0008, NACA 0012, NACA 0015, NACA 0018, NACA 0021, and NACA 0024. NACA 4 series Unsymmetrical airfoils of different thickness such as NACA 2406, NACA 2408, NACA 2412, NACA 2415, NACA 2418, NACA 2421, and NACA 2424.

NACA 4 series Unsymmetrical airfoils of different camber such as NACA 1412, NACA 2412, NACA 4412, and NACA 6412. NACA 4 series Unsymmetrical airfoils of different location of camber such as NACA 2212, NACA 2312, NACA 2412, NACA 2512, NACA 2612, and NACA 2712.

Different nose designs are created using grid points with different diameter. Figure 3.12 shows the bio inspired nose design of different diameters created on NACA 2418 and 2424 airfoils. Same design methodology is used for other NACA 4 series airfoils. Two square grids with a length equal to the half of the

airfoil thickness are drawn as shown in Figure 3.13. One is with respect to airfoil camber and another with respect to chord.

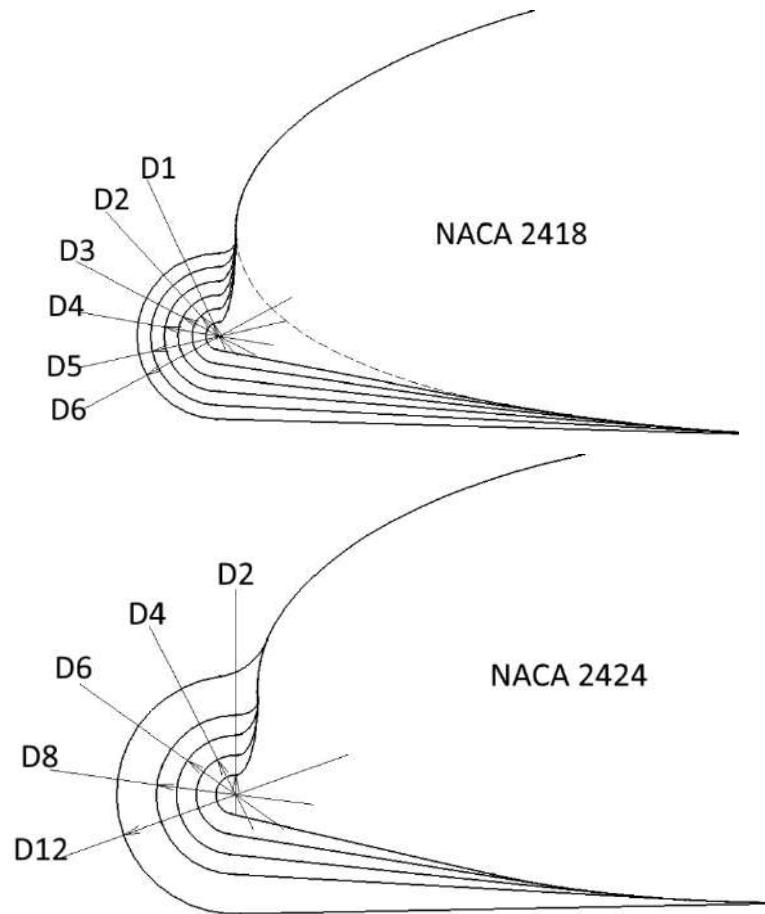


**Figure 3.12** Airfoils with bio-inspired nose designs of different diameters

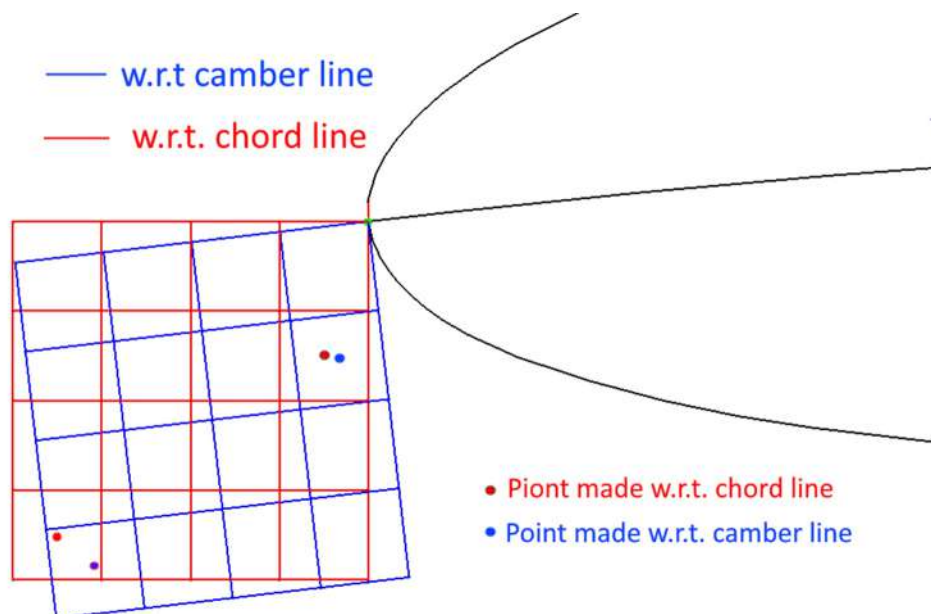


**Figure 3.13** Grid drawn with reference to chord and camber line of airfoil

Bio-inspired nose designs created using the grid drawn with respect to the airfoil camber line marked as NACA 2412 – J2 (J-position on the grid, 2 – diameter of nose circle), nose designs created using the grid drawn with respect to airfoil chord line marked as NACA 2412 – CJ2 (C-chord, J-position on the grid, 2 – diameter of nose circle).

It is found that the porpoise nose design (airfoil nose having shorter length and medium depth (i.e. depth - 2.25 % of chord, nose length - 0.75 % chord, and nose diameter – 2 % chord) created with reference to the airfoil chord line is easy to design and shown better aerodynamic behaviour for all the NACA 4 series airfoils of different geometries. Hence, for the further analysis on the NACA 6 series airfoils, the optimum porpoise nose design created using the chord line has been considered.

### **3.2.3 Design of bio-inspired nose on NACA 6 series Airfoils.**

10 different NACA 6 series airfoils have been considered for the low-speed computational analysis, to find the effect of optimum nose design on flow separation control. The most used NACA 6 series airfoils are chosen for the analysis as follows.

NACA 6 series unsymmetrical airfoils of different thicknesses such as NACA 63210, NACA 63215, and NACA 63221. NACA 6 series unsymmetrical airfoils of different location of the minimum pressure such as NACA 63015, NACA 63215, NACA 63415, and NACA 63615. NACA 6 series unsymmetrical airfoils of different design lift coefficients such as NACA 63215, NACA 64215, NACA 65215, NACA 66215, and NACA 67215.

### **3.2.4 Bio – Inspired nose on finite wing**

The three-dimensional computational analysis has been done to find the optimum spanwise length and position of porpoise nose on finite wing with NACA 2412 airfoil, as mentioned in the Figure 3.14 and 3.15. A finite wing of span 350mm with C-grid domain was used for the 3D simulation.

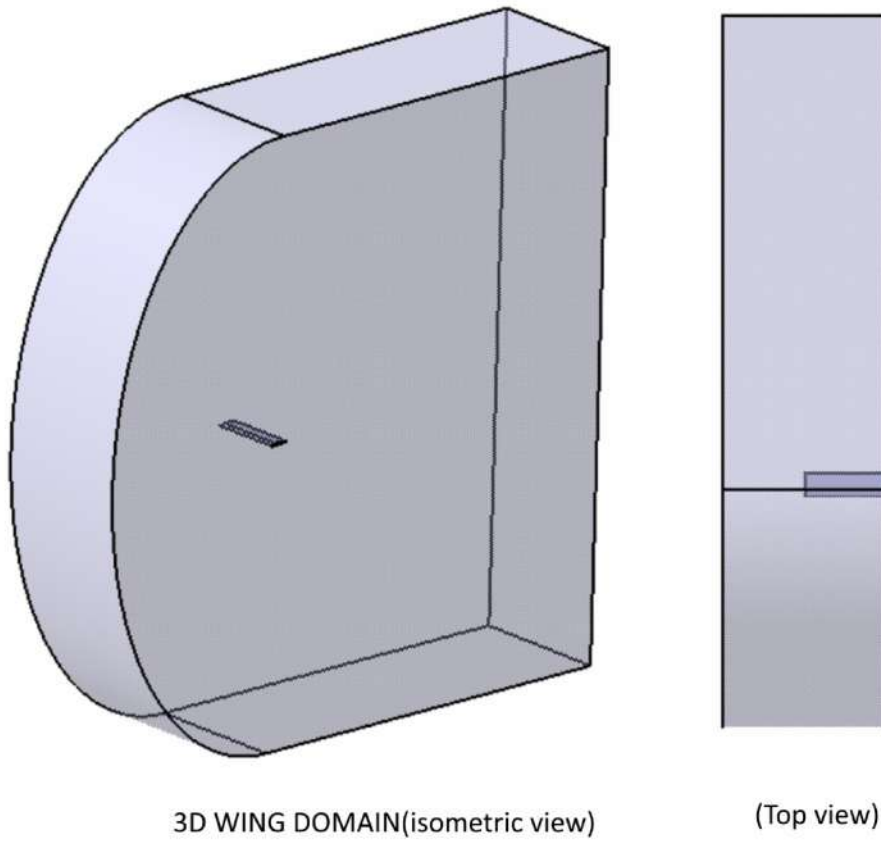


**Figure 3.14** C-Domain with finite wing.

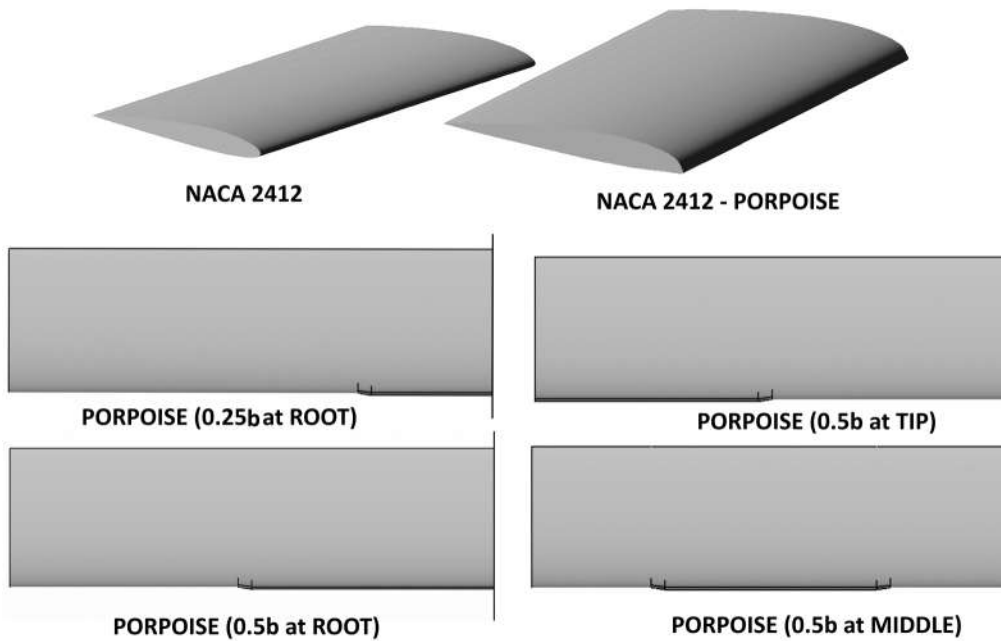


**Figure 3.15** Finite wing (with NACA 2412 airfoil) with different leading-edge configurations.

Domain thickness was taken as twice as the wingspan and horizontal and vertical length of domain was taken more than 10 times the airfoil chord around the airfoil. It is to avoid the interference between wall and the wing tip flows. The finite wing with porpoise nose of different spanwise length and location has been designed (Figure. 3.15). Nose with spanwise length of 100%, 50%, and 25% of finite wingspan ( $1b$ ,  $0.5b$ , and  $0.25b$ ) and positions such as root, mid portion, and tip of finite wing were considered.

### **3.3 Boundary conditions and Solver settings**

The two-dimensional computational analysis has been done on different NACA 4 and 6 series airfoils at different angles of attack and different subsonic speeds such as Re. No. of  $1 \times 10^6$  ( $M=0.05$ ), Re. No. of  $3 \times 10^6$  ( $M=0.13$ ), Re. No.  $9 \times 10^6$  ( $M=0.38$ ), Re. No. of  $12 \times 10^6$  ( $M=0.5$ ) and Re. No. of  $17 \times 10^6$  ( $M=0.7$ ). The three-dimensional computational analysis has been done on finite wing at Re. No. of  $3 \times 10^6$  ( $M=0.13$ ). A uniform velocity inlet condition was given at the semi-circular wall, a pressure outlet with sea level pressure value was given on vertical wall, and a symmetry condition was given on horizontal walls of the domain. No slip wall condition was used for airfoil.

The pressure-based solver is generally used for incompressible and mildly compressible flows. And The density-based solver is used for high-speed compressible flows. Both approaches differ in the way that the continuity, momentum, energy and species equations are solved. For low Reynolds number flow analysis, pressure based solver has been used. And for high Reynolds number flow simulation, density based solver has been used where the compressibility effects are predominant. For low angles of attack ( $\alpha < 6^\circ$ ), the steady flow analysis has been done along with the SST  $k-\omega$  - model. For high angles of attack ( $\alpha > 6^\circ$ ), transient analysis has been done along with the  $k-\omega$  SAS (Scale-Adaptive Simulation) model. The SST  $k-\omega$  - models is designed to avoid the freestream sensitivity of the standard  $k-\omega$  model, by combining elements of the  $\omega$  equation and the  $\varepsilon$  equation. It is typically better at predicting adverse pressure gradient boundary layer flows and separation. Curvature correction is used to include the curvature effects in eddy-viscosity models. Production limiter is used to avoid the excessive buildup of turbulent kinetic energy

generation in the stagnation regions. The SAS (Scale-Adaptive Simulation) modeling approach is based on the introduction of the von Karman length scale into the turbulence equations. The inclusion of this term allows the model to adjust its length scale to already resolved scales in the flow and thereby provide a low enough eddy viscosity to allow the model to operate in ‘LES’ mode.

The energy equation has been included in the simulation. It ensures that the coupling between the flow velocity and the static temperature correctly incorporated. And temperature is computed from the energy equation. The constant operating pressure condition with 101325 Pa has been taken for the simulation. Operating pressure is important for incompressible ideal gas flows as it directly governs the density. In low-Mach-number compressible flow, the overall pressure drop is small compared to the absolute static pressure, and can be significantly affected by numerical round off. Operating pressure is significant for low-Mach-number compressible flows because of its role in avoiding round off error problems. Hence, appropriate operating pressure should be set.

The materials and their physical properties (density, viscosity, etc.) are important to set. The default condition such as aluminum with density 2719 kg/m<sup>3</sup>, Specific heat of 871 j/kg-k, and thermal conductivity of 202.4 w/m-k has been used for the airfoil / wing model. The air is taken as a fluid with density as ideal gas, Specific heat of 1006.43 j/kg-k, and thermal conductivity of 0.0242 w/m-k, viscosity as Sutherland, molecular weight of 28.966 kg/kgmol for the simulation.

For Incompressible flow, the density is calculated using the ideal gas is given below (Eq. 3.64). Where, R is the universal gas constant,  $M_w$  is the molecular weight of the gas,  $P_{op}$  is the operating pressure.

$$\rho = \frac{P_{op}}{\frac{R}{M_w} T} \quad (3.64)$$

For compressible flow, the density is calculated using the ideal gas is given below. Where,  $P_{op}$  is the operating pressure, P is the local relative pressure.

$$\rho = \frac{P_{0p} + P}{\frac{R}{M_w} T} \quad (3.65)$$

The viscosity is defined as a function of temperature using the Sutherland's law with three coefficients as mentioned in Eq. 3.66. Where,  $\mu$  is the viscosity in kg/m-s,  $T$  is the static temperature in K,  $\mu_0$  is reference value in kg/m-s,  $T_0$  is the reference temperature in K,  $S$  is Sutherland constant in k. For air at moderate temperatures and pressures,  $\mu_0 = 1.716 \times 10^{-5}$  kg/m-s,  $T_0 = 273.11$  K, and  $S = 110.56$  K are taken. The Sutherland's viscosity law resulted from a kinetic theory using an idealized intermolecular-force potential is

$$\mu = \mu_0 \left[ \frac{T}{T_0} \right]^{3/2} \frac{T_0 + S}{T + S} \quad (3.66)$$

The Velocity inlet boundary conditions are used to define the velocity and scalar properties of the flow at inlet boundaries. For the velocity inputs, the velocity magnitude and direction has been chosen instead of default method (velocity magnitude normal to the boundary), as the inlet is of semicircular shape. To define the flow angle of attack, X, Y and Z direction flow components have been defined in cartesian coordinate system. The proper selection of reasonable boundary conditions at the inlet is must to compute the initial values of  $k$  and  $\omega$  in the whole domain. The initial values are specified at the inlets in terms of Turbulent Intensity and Turbulent Viscosity Ratio. The typical values of turbulent Intensity lie in the range of 1-10%. A turbulence intensity of  $\leq 1\%$  is considered to be low and  $\geq 10\%$  is considered to be high. Hence, the default value for medium turbulence intensity ( $I = \frac{u'}{u_{avg}}$ ) of 5% has been taken for the analysis. The typical values of turbulent Viscosity Ratio lie in the range of 1-100. For most of the external flows, turbulent Viscosity Ratio ( $\frac{\mu_t}{\mu}$ ) is very small. And set between 1 to 10. For internal flows, large values up to 100 are used. The default value for the turbulent viscosity ratio is set to 10. The Pressure outlet boundary conditions are used to define the static pressure at flow outlets. The zero gauge pressure is defined at the pressure outlet to get the standard sea level conditions.

Wall boundary conditions are used to bound fluid and solid regions. For viscous flows, the no-slip boundary condition is set by default for shear condition, with zero roughness height which indicates a smooth wall. No slip condition means, the fluid sticks to the wall and moves with the same velocity as the wall, if it is moving. Hence, Stationary wall with no-slip condition is used for airfoil / wing model in the analysis.

The first-order discretization commonly gives better convergence than the second order scheme. However, it gives less accurate results, notably on tri/tetra meshes. Hence, second order scheme is used for the simulation. For low angles of attack, steady analysis with pressure based solver is used along with a SIMPLEC algorithm. Because the increased under-relaxation can be applied and more quick converged solution can be obtained. The least squares cell based method was used for the calculation of the gradient of variables. The Second order upwind method is used to compute the density, momentum, turbulent kinetic energy, specific dissipation rate, and energy. For high angles of attack, the unsteady analysis with density based compressible solver is used along with implicit solution formulation and Roe-FDS flux scheme. The second order implicit transient formulation was used. The least squares cell based method was used for the calculation of the gradient of variables. Second order upwind method is used to compute the turbulent kinetic energy and specific dissipation rate. The simulation with a time step size of  $1^{-6}$  second was used. As the angle of attack increases, the flow becomes unsteady. So, force coefficient fluctuates from maximum to minimum values. Hence, the mean force coefficient was considered for the plots.

### **3.4 Mesh Independence Study for 2D analysis**

The Mesh independence study has been done for standard NACA 2412 airfoil with different mesh elements and turbulence models. For the computational analysis, a C-grid domain as shown in Figure 3.16 was taken with a diameter of 12.5 times chord and horizontal length behind the airfoil of 20 times chord. The boundary conditions such as velocity inlet, wall with no-



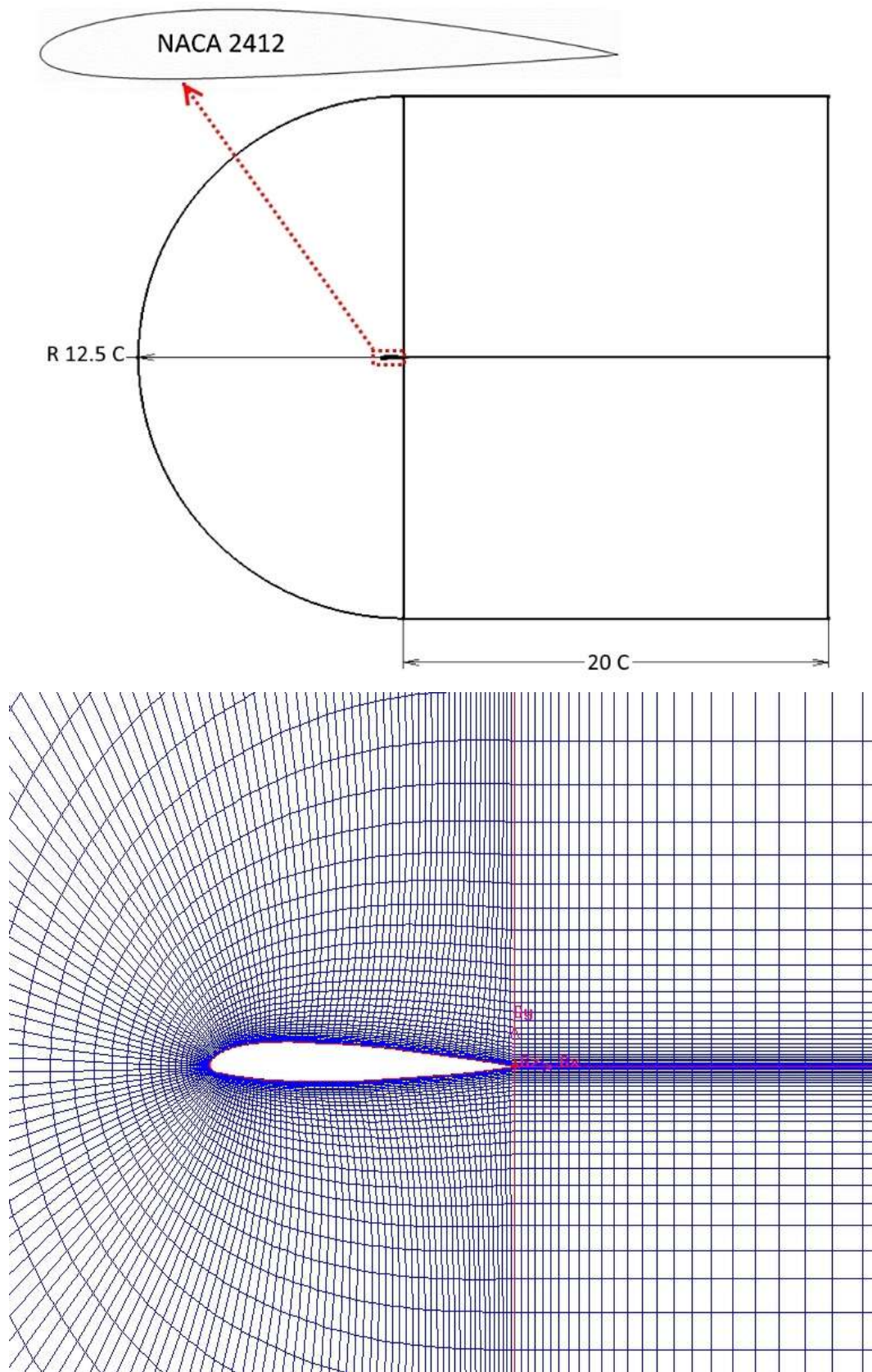
slip condition (airfoil) and the pressure outlet with the relative zero pressure was taken for the simulation.

The computational domain (figure 3.16) has been further divided into a multiple block near the airfoil to ensure the finer mesh near the airfoil. Number of divisions on airfoil surface, first cell height from airfoil surface, number of blockings around the airfoils, different turbulence models, different time steps, etc. were varied for the mesh independence study. The divisions on airfoil leading edge are crowded.

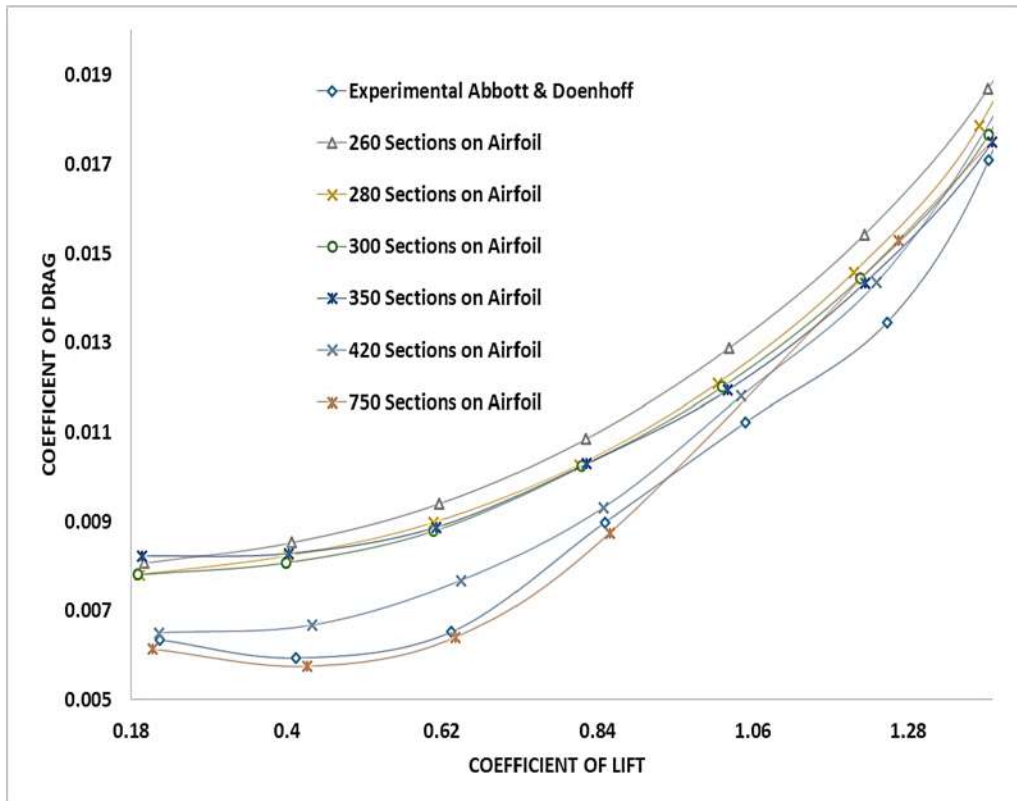
To capture the boundary layer, the proper height of the first grid adjacent to the airfoil surface is set by taking  $y^+$  less than 1.0. Different turbulence models have been incorporated in the simulation such as  $k-\epsilon$  standard, realizable  $k-\epsilon$ ,  $k-\omega$  SST, transition SST, and  $k-\omega$  SAS. Initially the most used turbulence model  $k-\omega$  – SST has been taken for mesh independence study to analyze the effect of different mesh divisions on airfoil surface and different  $y^+$  values on the force coefficient predictions.

Figure 3.17 shows that the variation in drag coefficient as the number of mesh division on the airfoil varies. There was a negligible variation in lift, but drag coefficient affected a lot by the number mesh divisions taken on the airfoil profile. In all the cases, number of mesh division is crowded near the leading edge where the flow properties change at high rate. The mesh division count of 750 (orange colour curve with asterisk markers) taken on the airfoil surface showed better prediction on drag coefficient especially at low angles of attack.

Further, the first cell height has been varied over the airfoil. The  $y^+$  value was varied from 1 to 0.1. The simulation results for 8-degree angle of attack are tabulated as shown in table 3.1. It is found that the force coefficient values are matching with the experimental values for the  $y^+$  value equal to 0.1. Hence, the number of mesh divisions of 750 on airfoil surface and  $y^+$  value of 0.1 have been finalised for the further computational analysis.



**Figure 3.16** Computational domain and mesh



**Figure 3.17** Coefficient of drag of NACA 2412 airfoil for different no of sections on airfoil at Reynolds Number of  $3 \times 10^6$

**Table 3.1** Coefficient of lift and drag of NACA 2412 at 8-degree angle of attack and Reynolds Number of  $3 \times 10^6$  for different  $Y^+$  values.

Angle of attack (Deg)	Total sections on Airfoil	$Y^+$ Values	$C_l$	$C_d$
8	750	< 1	1.069752	0.010507
8	950	< 1	1.0699	0.0106
8	750	= 0.1	1.063542	0.011093
8	Experimental Abbott & Doenhoff		1.0600	0.0116

Different two-equation turbulence models such as realizable  $k-\varepsilon$ ,  $k\omega - SST$ ,  $k\omega - SAS$  and transition SST, were used for the experimental validation of the numerical scheme used in the research. Figure 3.18 - 3.19 show that, at low angles of attack ( $0^\circ \leq \alpha \leq 6^\circ$ ), all three models (Transition SST,  $K\omega - SST$ ,  $K\varepsilon - Realizable$ ) predicts the same lift coefficient where the flow is merely steady. The  $K\omega - SST$  and Transition SST predict the drag coefficient value which is near equal to the experimental value, but  $K\varepsilon - Realizable$  model overpredicts the drag coefficient value. At high angles of attack ( $8^\circ \leq \alpha \leq 18^\circ$ ), all the turbulence models predict different values of lift coefficient. The  $K\varepsilon - Realizable$  predicted the lift coefficient values that are in good agreement with the experimental values but failed to predict the drag value properly. The Transition SST and  $K\omega - SST$  turbulence models underpredicts the lift values but predicts the drag value properly.

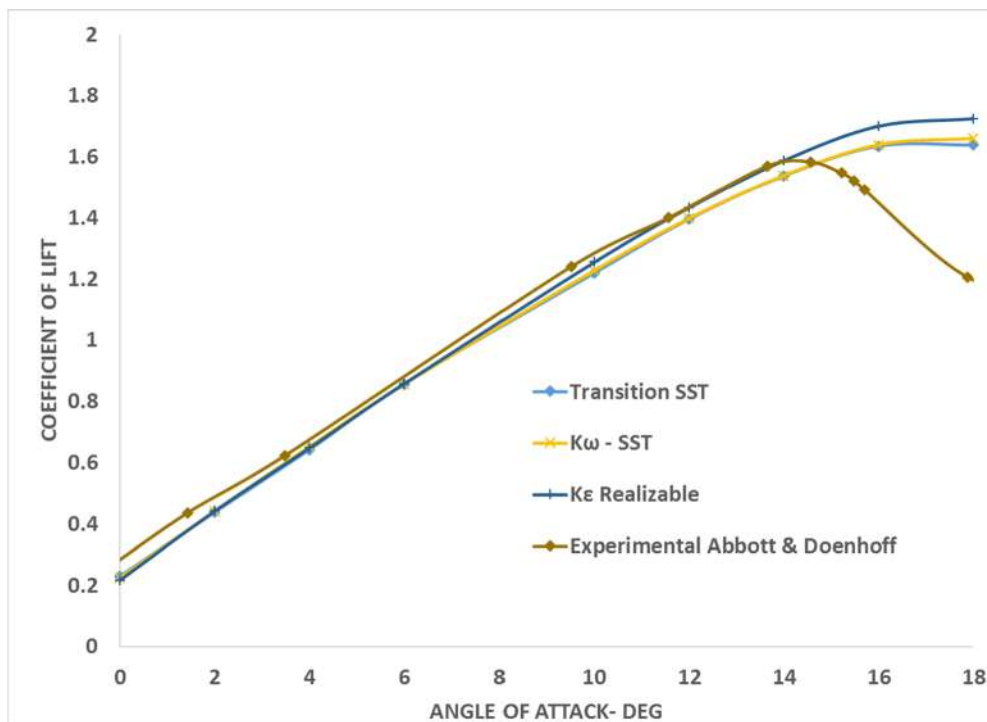


**Figure 3.18** Coefficient of lift of NACA 2412 airfoil for different turbulence model at Reynolds Number of  $3 \times 10^6$

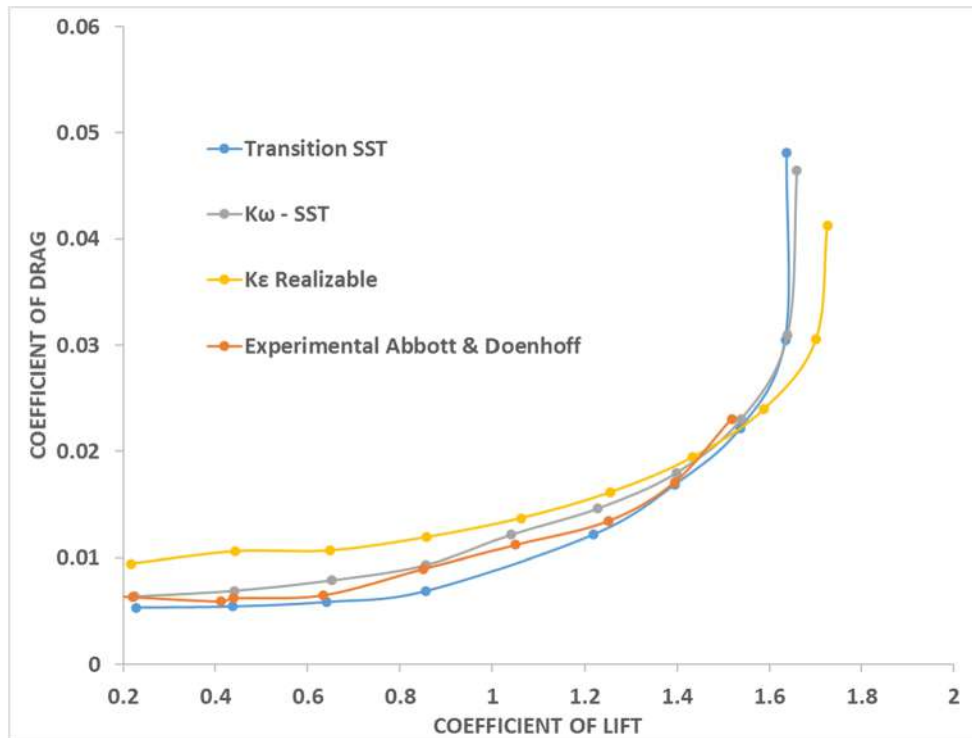


**Figure 3.19** Coefficient of lift and drag of NACA 2412 airfoil for different turbulence model at Reynolds Number of  $3 \times 10^6$

From the above analysis, it is found that the steady flow analysis incorporating  $K\omega - SST$  model predicts the force coefficients properly at low angle of attacks ( $\leq 6^\circ$ ) and predicts less lift coefficient at high angle of attack as the flow becomes unsteady.

The unsteady analysis has been done for different turbulence models at 10-degree angle of attack and Reynolds Number of  $3 \times 10^6$  as mentioned in the table 3.2. It showed that the SAS (Scale-Adaptive Simulation) gives better prediction of lift at high angle of attack with unsteady analysis than SST models. The coefficient of forces predicted by the  $K\omega - SAS$  model are well matching with the standard experimental values. Hence, the unsteady analysis incorporating the  $K\omega - SAS$  turbulence model was chosen for high angle of attack ( $\geq 8^\circ$ ) even though it consumes more computational time and cost. At a high angle of attack, due to the unsteady behaviour, the time averaged force coefficient value has been used.

**Table 3.2** Coefficient of lift and drag of NACA 2412 at 10-degree angle of attack and Reynolds Number of  $3 \times 10^6$  for different turbulence models.

Angle of Attack (Degree)	Turbulence Models	$C_l$	$C_d$
10	TRANSITION SST	1.2324	0.0136
10	$K\omega$ – SST	1.2276	0.0147
10	TRANSITION SST SAS	1.2434	0.0112
10	TRANSITION SST IDDES	1.2743	0.0147
10	$K\omega$ – SAS	<b>1.2478</b>	<b>0.0136</b>
10	Experimental Abbott & Doenhoff	<b>1.2500</b>	<b>0.0136</b>

Hence, the steady state analysis with  $K\omega$  – SST model is used for low angle of attack, which saves computational time and cost while the unsteady analysis with  $K\omega$  – SAS model is used for high angle of attack for better predictions.

### 3.4.1 Solver Validation for 2D analysis

The 2D analysis has been carried out on NACA2412 airfoil at a Reynolds number of  $3 \times 10^6$ . The mesh is refined very fine to ensure  $y^+$  less than 1, so that flow phenomena inside the boundary layer can be predicted properly. Density based compressible flow solver was used for transient analysis. The second order implicit transient formulation was used. The least squares cell based method was used for the calculation of the gradient of variables. Second order upwind method is used to compute the turbulent kinetic energy and specific dissipation rate. The simulation with a time step size of  $1^{-6}$  second was used. As the angle of attack increases, the flow becomes unsteady. So, force coefficient fluctuates from maximum to minimum values. Hence, the mean force coefficient was considered for the plots. A uniform velocity inlet condition was given at the semi-circular wall, a pressure outlet with sea level

pressure value was given on vertical wall, and a symmetry condition was given on horizontal walls of the domain. No slip wall condition was used for airfoil. Number of divisions on airfoil surface, first cell height from airfoil surface, number of blockings around the airfoils, different turbulence models, different time steps, etc. were varied for the mesh independence study. The  $k\omega$  – SST model (Rezaeiha et al.2019, Sun et al. 2021, Lei et al. 2013, Menter 1994) was used for low angle of attack, which saves computational time and cost. And  $k\omega$  – SAS model (Zheng et al. 2016, Meana-Fernández et al. 2019, Kim et al. 2020, Liu et al. 2018, Vakiliipour et al. 2021, Egorov and menter 2008) was used for high angle of attack. Computational results (using  $k\omega$  – SST &  $k\omega$  – SAS) are compared and matched with the experimental values of NACA2412 airfoil (Abbott et el. (1949)) (Figure 3.20 and 3.21). The numerical simulations accurately predicts the lift and drag coefficients of NACA 2412 over a wide range of angles of attack wherein the experimental and numerical lift curve and drag polar overlap one another up to stalling angle. Some deviation in lift and drag coefficients is observed in the post stall regimes as can be seen in Figs. 3.20 and 3.21. Maximum differences of 5% and 4% are observed in the lift and drag coefficients at angles of attack of  $20^\circ$  and  $16^\circ$  respectively. These deviations are well within acceptable limits within the imitations of computational fluid dynamics (Yagiz et al. 2012, Gao et al. 2015). The deviation in force coefficient values observed after a stalling angle is due to the failure of the two-equation turbulence models to accurately predict the transition and flow unsteadiness at high angles of attack. A descent example can be found in the numerical work of Lian and Shyy. wherein, even a transition turbulence model is found fails in capturing the stall accurately, in the validation studies (Lian and Shyy (2007)). The current work however, focus on the aerodynamic performance enhancement in the pre-stall regime and the numerical methodology can be trusted based on the current validation study.

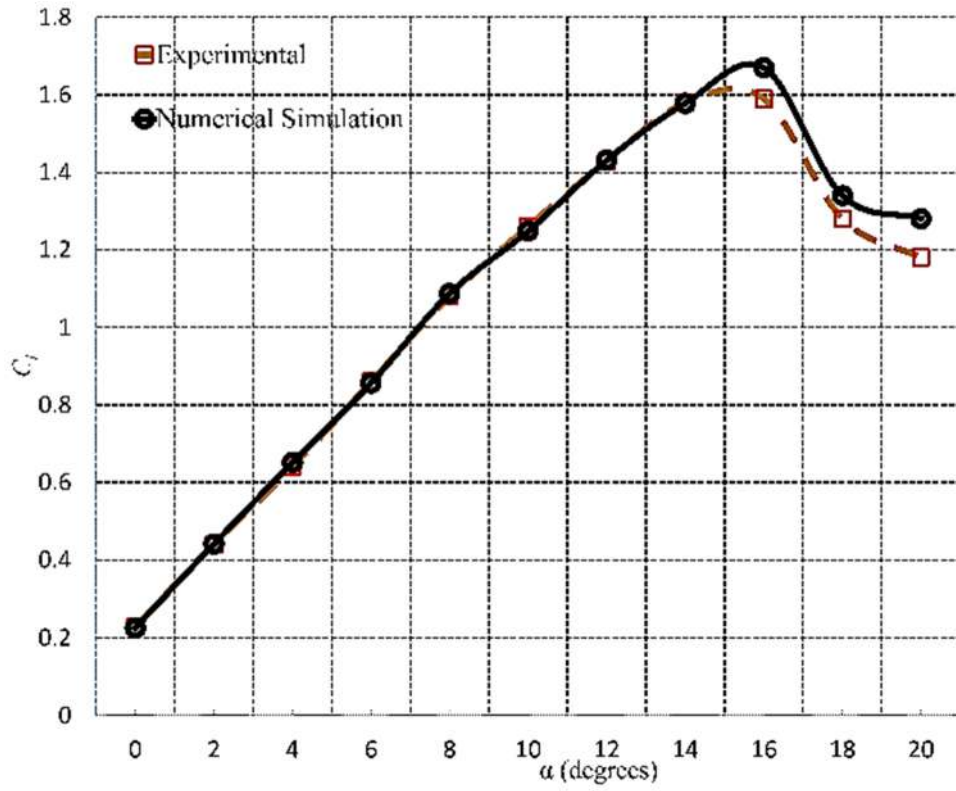


**Figure 3.20:** Coefficient of lift of NACA 2412 airfoil at  $Re = 3 \times 10^6$

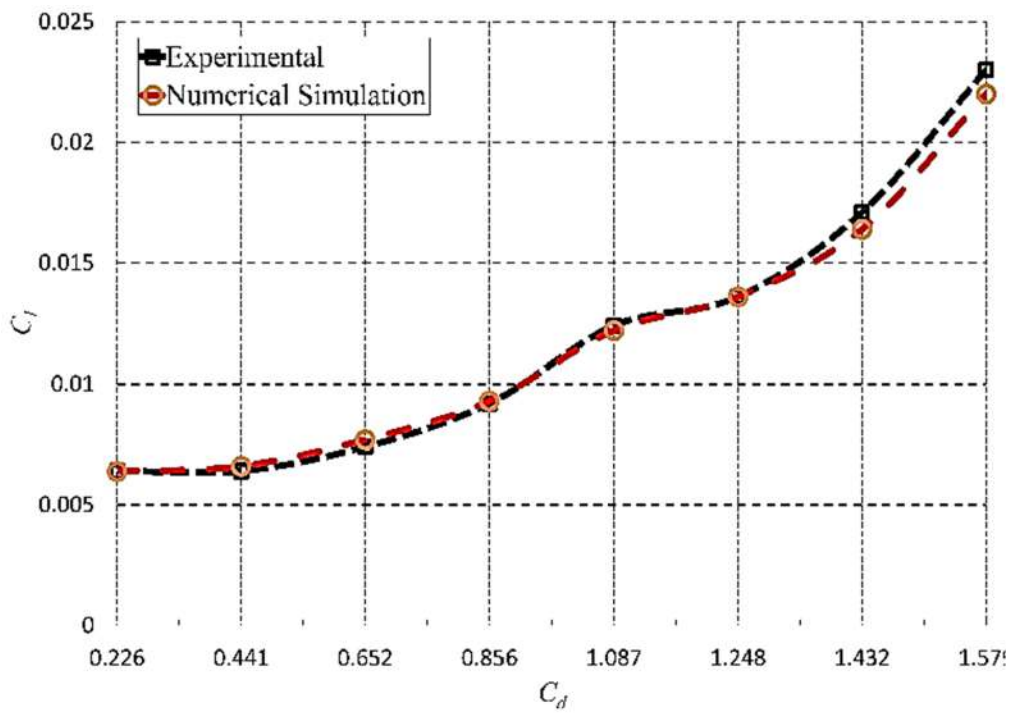


**Figure 3.21:** Drag polar curve of NACA2412 at  $Re = 3 \times 10^6$ .



### 3.5 Mesh Independence Study for 3D analysis

The 3D C-grid domain designed using CATIA was considered for the analysis (Figure. 3.14). Structured mesh was created with proper blocking method using ICEM-CFD meshing software as mentioned in the Figure 3.22. The wing was divided at  $0.1C$  to create the blocks for meshing as mentioned in Figure 3.23. The number of mesh divisions are varied on chordwise length of wing as mentioned in the table 3.3. The leading-edge portion and trailing edge portions were crowded to predict the flow changes and flow separations properly. In the leading-edge portion along chord, mesh divisions were varied from 100 to 500 counts, and in remaining portion along chord, the divisions were varied from 50 to 300 counts. In the wing span direction, the divisions were varied from 80 to 250 counts. Depends upon the leading edge spanwise length and position, the number of blocks were varied along the span direction in mesh generation.

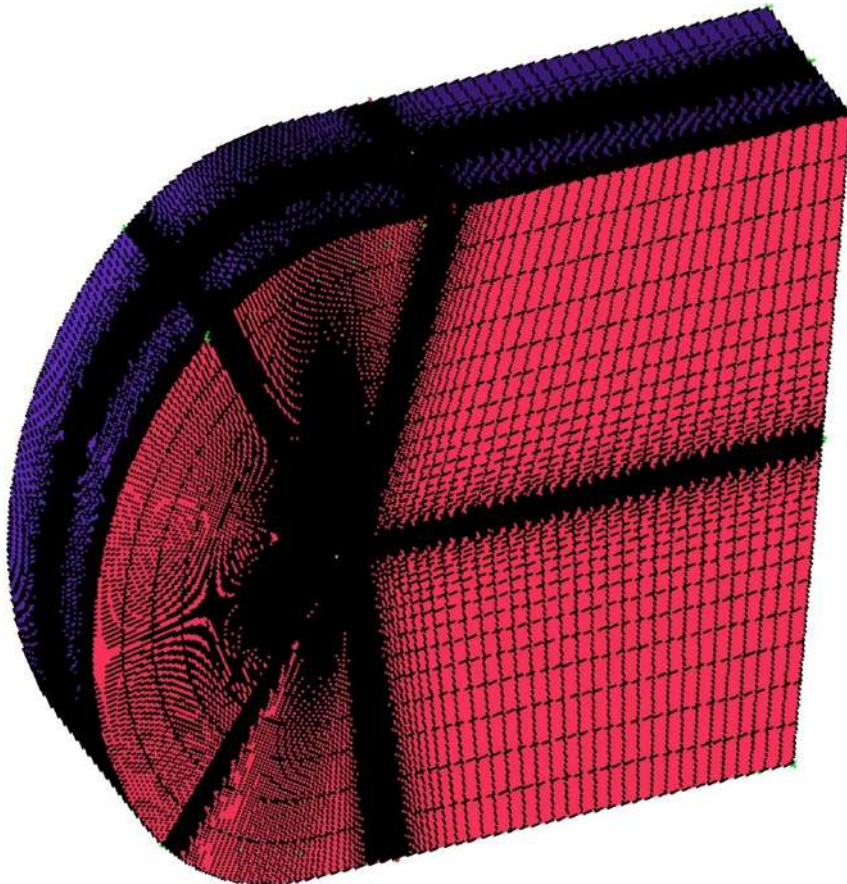


**Figure 3.22** 3D C- Domain with structured mesh.

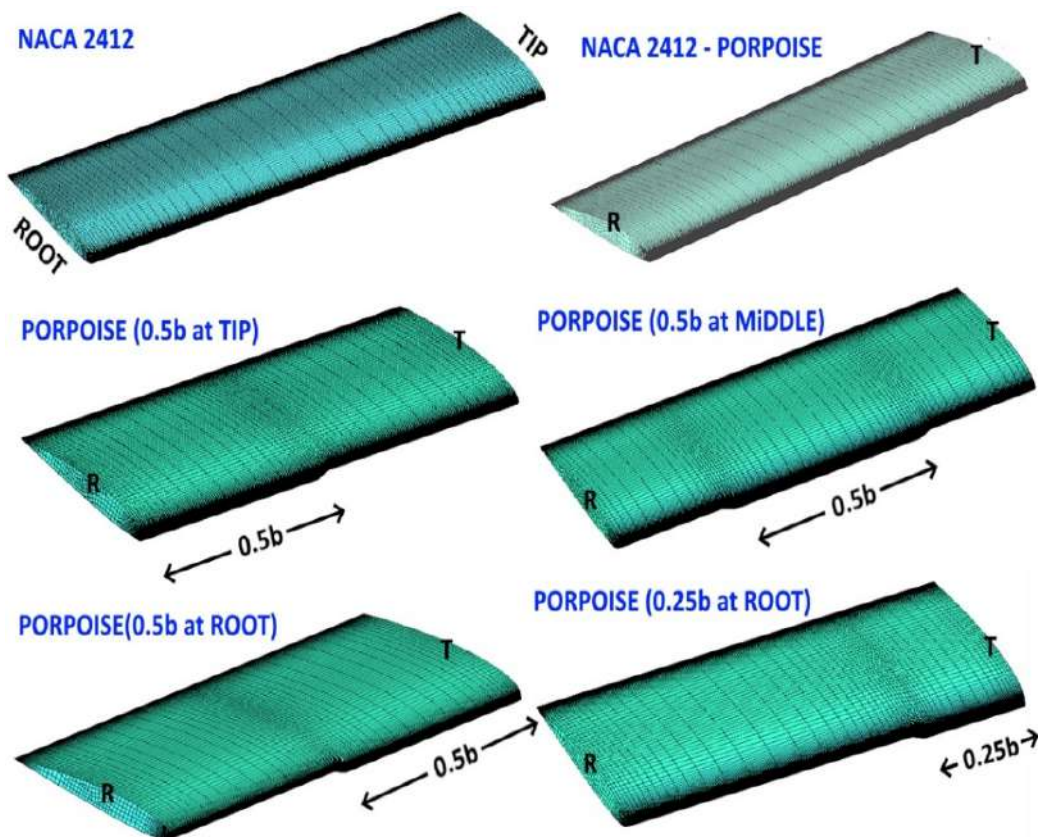
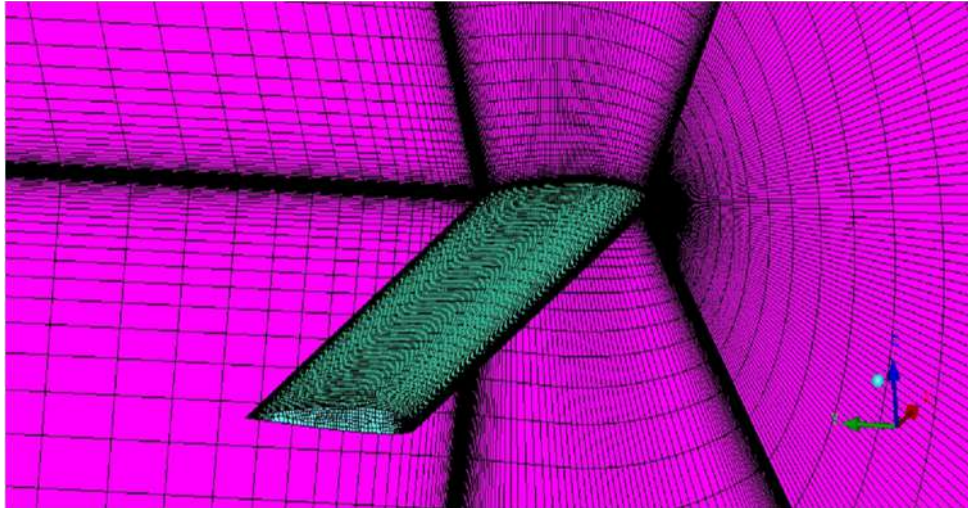


**Figure 3.23** The structured mesh of interior of the 3D C- Domain and different finite wing configurations.

For mesh independency study, the unsteady flow simulation with  $k-\omega$  – SST model and the wing at  $6^\circ$  angle of attack and Re No. of  $3 \times 10^6$  were considered. The mesh counts were varied from 2.2 million to 10.5 million (Table 3.3). It was found that the lift and drag coefficient, and ratio of lift to drag coefficient

not varied much after the 2.2 million mesh cell counts. So, the unsteady flow analysis with 2.2 million mesh cell counts was considered for three-dimensional analysis studies.

**Table 3.3** The coefficient of lift and drag values for wing of different mesh cell counts.

<b>Division on airfoil L.E. region</b>	<b>Division on airfoil Mid and T.E. region</b>	<b>Division along span</b>	<b>Total cell counts in million</b>	<b>C<sub>L</sub></b>	<b>C<sub>D</sub></b>	<b>C<sub>L</sub>/C<sub>D</sub></b>
100	50	80	1.5	0.577	0.03127	18.4
<b>100</b>	<b>100</b>	<b>80</b>	<b>2.2</b>	<b>0.574</b>	<b>0.02985</b>	<b>19.2</b>
100	100	150	3.0	0.574	0.02992	19.2
300	150	150	6.5	0.574	0.02988	19.2
300	150	250	10.0	0.575	0.02990	19.2
200	300	150	8.8	0.575	0.02993	19.2
300	300	150	10.3	0.574	0.02994	19.2
400	200	150	8.5	0.572	0.02999	19.1
500	250	150	10.5	0.577	0.03025	19.1
STEADY			<b>2.2</b>	<b>0.5738</b>	<b>0.02985</b>	<b>19.220</b>
UNSTEADY			<b>2.2</b>	<b>0.5745</b>	<b>0.02989</b>	<b>19.217</b>

### 3.5.1 Grid convergence index (GCI):

The grid convergence study does the similar work as grid refinement study. The series of grid refinement to find the optimal mesh for simulation is grid refinement study. But grid convergence study verifies the convergence of simulations based on Richardson's extrapolation as presented by Roache. It shows the consistency of the solutions and error percentage of convergence for

different grids. Three stage mesh conditions are more accurate to find the convergence and asymptotic range of convergence.

The order of convergence  $P_{oc}$  is calculated for the three solutions (Slater et al. 2000). If the grid refinement ratio  $r$  is constant, then  $P_{oc}$  is given by

$$P_{oc} = \frac{\ln\left(\frac{f_3 - f_2}{f_2 - f_1}\right)}{\ln(r)} \quad (3.67)$$

If the grid refinement ratio  $r$  is not constant between the grid levels ( $r_{1,2} \neq r_{2,3}$ ), then  $P_{oc}$  is given by (Stern et al. 2001) (Page no – 798)

$$P_{oc} = \frac{\ln(\epsilon_{2,3} / \epsilon_{1,2})}{\ln(r_{1,2})} + \frac{1}{\ln(r_{1,2})} [\ln[r_{2,3}^{P_k} - 1] - \ln[r_{1,2}^{P_k} - 1]]$$

$$\epsilon_{2,3} = f_3 - f_2$$

$$\epsilon_{1,2} = f_2 - f_1 \quad (3.68)$$

the above equation must be solved iteratively for  $P_{oc}$ .

Richardson extrapolation is used to find the solution for the zero grid spacing (Slater et al. 2000)

$$f_{exact} = f_1 + \frac{(f_1 - f_2)}{(r^p - 1)} \quad (3.69)$$

The discrete solutions  $f$ , grid refinement ratio is:  $r = h_2 / h_1$ , grids of spacing  $h_1$  and  $h_2$  with  $h_1$  being the finer (smaller) spacing.

Effective Grid Refinement Ratio is used when the user is not sure about the mesh (finer or coarser grid), also be used for unstructured grids (Longest and Vinchurkar, 2007).

$$r = \left(\frac{N_f}{N_c}\right)^{1/D} \quad (3.70)$$

where  $N$  - total grid points,  $D$  - flow domain dimension.

Estimated fractional error  $E$  (Roache 1994)

$$E = \epsilon / (r^p - 1) \text{ and } \epsilon = (f_2 - f_1) / f_1 \quad (3.71)$$

where  $\epsilon$  - relative error measure of property

The **GCI** for the fine grid is defined below (Slater et al. 2000) (Roache 1998).

$$GCI = \frac{F_s |(f_2 - f_1)/f_1|}{(r^p - 1)} \quad (3.72)$$

$$GCI = F_s E$$

The **GCI** for the coarser grid is (Roache 1998)

$$GCI = \frac{F_s |(f_2 - f_1)/f_1| r^p}{(r^p - 1)} \quad (3.73)$$

$$GCI = F_s E r^p$$

Where  $F_s$  – factor of safety, to compare 2 grids  $F_s = 3.0$ , and to compare 3 or more grids  $F_s = 1.25$  are recommended.

The **GCI** should be within the asymptotic range. To verify that the GCI values are within the asymptotic range of convergence

$$\frac{GCI_{2,3}}{(r^p * GCI_{1,2})} \cong 1 \quad (3.74)$$

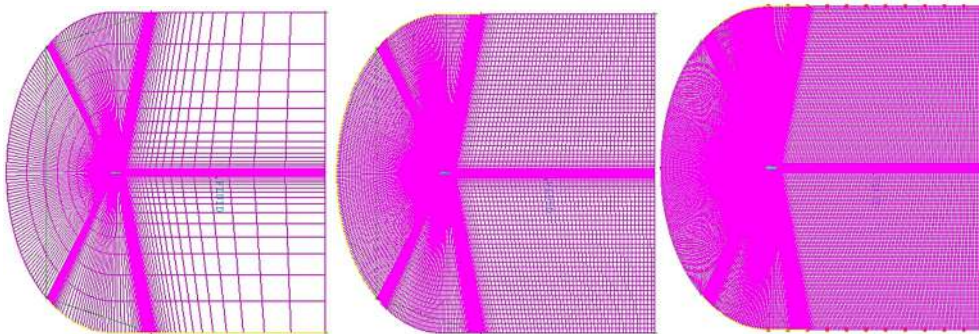


**Figure 3.24.** The computational domain with coarse, medium and fine meshes.

In the Grid convergence index(GCI) for the three dimensional flow analysis has been done. Three different grid levels (figure 3.24) are considered for The Grid convergence index (GCI) calculation such as 1.0 million (coarse mesh), 2.2 million (medium mesh) and 4.4 million (Fine mesh). Using the constant grid refinement ratio ( $r$ ) = 1.3, the corresponding  $p$ ,  $GCI_{2,3}$ ,  $GCI_{1,2}$ , Asymptotic range of convergence are tabulated in table 3.4 for three different grid levels. The plot of  $C_L / C_D$ , and  $C_D$  with varying grid spacings are compared with the solution for the zero grid spacing calculated by Richardson extrapolation (Fig.

3.25). its shows that the grid convergence index for different grid levels is less than 1%, and the asymptotic range of convergence is equals to 1 for  $C_L/C_D$ . Form this mesh study, it was found that the lift and drag coefficient, and ratio of lift to drag coefficient shows the negligible variation after the 2.2 million mesh cell counts. Hence, 2.2 million mesh cell counts were considered for the simulation.

**Table 3.4:** GCI and Asymptotic range of convergence for  $C_L$  and  $C_L / C_D$  with varying grid spacings with a constant refinement ratio of 1.3

Total cells in million	$C_L$	Order of convergence ( $P_{oc}$ )	GCI 2,3	GCI 1,2	Asymptotic range of convergence	Solution for the zero grid spacing
1.0 Coarse	0.5732	1.28	0.38	0.272	1.00087	0.575
2.2 Medium	0.5739					
4.4 Fine	0.5744					
Total cells in million	$C_L/C_D$	Order of convergence (p)	GCI 2,3	GCI 1,2	Asymptotic range of convergence	Solution for the zero grid spacing
1.0 Coarse	19.1706	1.28	0.37	0.270	1.00086	19.252
2.2 Medium	19.194					
4.4 Fine	19.2107					

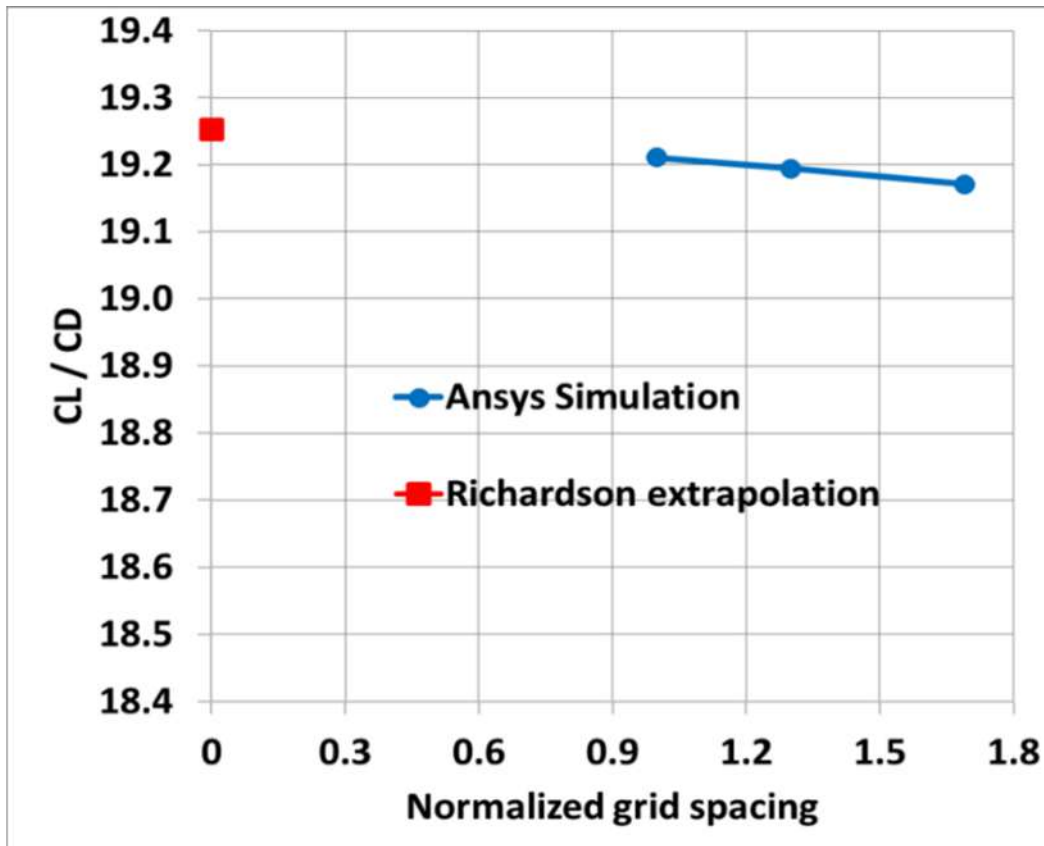


**Figure 3.25.** The plot of  $C_L / C_D$  with varying grid spacings.

### 3.6 Experimental Validation for 2D analysis

For validation, low speed wind tunnel experiment has been done for an optimised design (Figure. 3.27a and 3.27b) - the porpoise nose (shorter length and medium depth i.e., depth - 2.25 % of chord, nose length - 0.75 % chord, and nose diameter – 2 % chord). Experiment was done using SRM IST – KTR low subsonic wind tunnel with 0.6m x 0.6m test section size and designed for a maximum of 50 m/s test section velocity (Figure. 3.26a). The 32-port pressure scanner (Fig. 3.27c) is used to measure the differential pressure between the ports on the infinite wing model (Figure. 3.26b) and ports on the pressure scanner which is opened to atmospheric conditions. The infinite wing model with 0.153m x 0.6m reference area is moulded using composite materials with pressure ports on both upper and lower surfaces. The tubes connected to the pressure ports are taken from one side of the model. From the pressure distribution of an airfoil, coefficient of pressure and forces (normal force, axial

force, lift, and drag forces) have been calculated using the formulae (Eq. 3.60 – 3.62) mentioned in the section 3.1.5 (force coefficient).



**Figure 3.26 a)** SRM IST – KTR low subsonic wind tunnel with pressure scanner setup. **b)** Infinite wing model inside the test section.



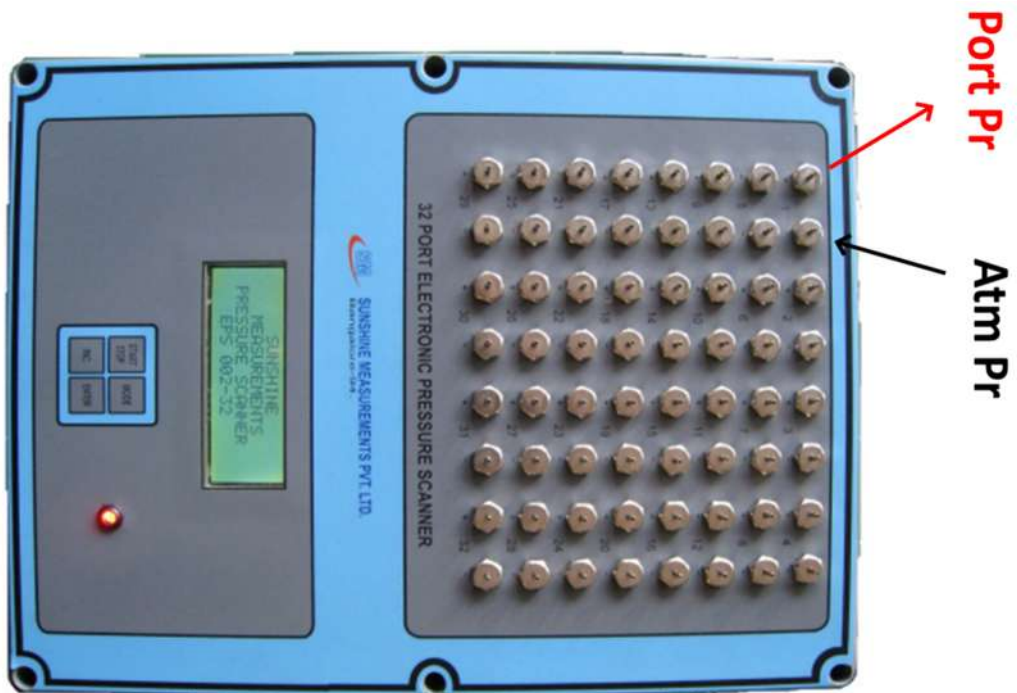
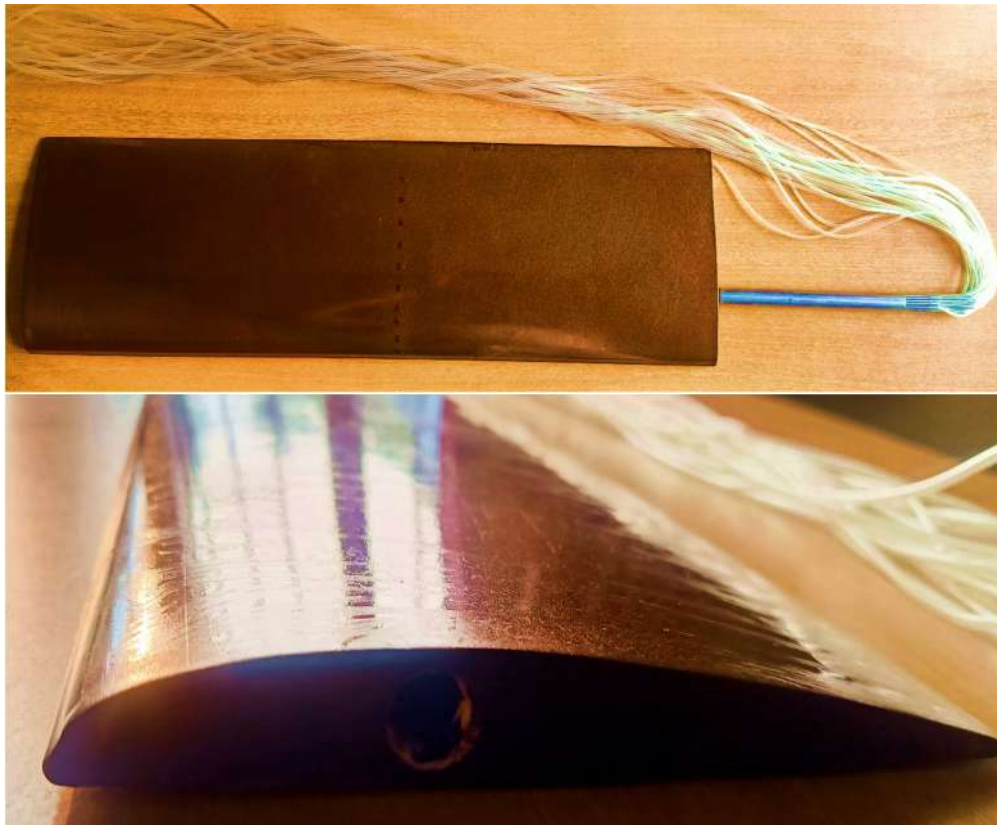


**Figure 3.27** Top view(a), and side view (b) of infinite wing model with porpoise nose airfoil. and (c) Pressure scanner.

The experiment has been conducted for Reynolds number of  $1.9 \times 10^5$  for different angles of attack. The domain, mesh, turbulence models mentioned in the section 3.2.3 (Mesh Independence Study for 2D analysis) has been used for this experimental validation study. The Figure 3.28a and 3.28b show the comparison of ANSYS simulation and experimental analysis results (normal force, axial force, lift and drag coefficient) of Porpoise airfoil. The Figure 3.29a and 3.29b show the comparison of computational results and experimental results (Pressure coefficient -  $C_p$ ) of Porpoise airfoils at 6 degree and 12-degree angles of attack. The curve shows that the computational methodology taken for the study is in good agreement with the experiment results upto the stalling angle. Results show some deviation in the lift (approx. 3%). At low angles of attack, shear stress contributes majority of portion to forces acting on an airfoil. But experimentation takes only pressure components to calculate the forces acting on an airfoil. Hence variation in drag is found between simulation and experiment. And the infinite wing model is small, so, a greater number of pressure ports could not be taken over the airfoil particularly near the nose. This affects the coefficient of pressure distribution near the nose of the airfoil. The flow changes that occurred on the nose are not captured properly because of inadequate pressure ports on the nose. And Most RANS turbulence models fail to capture the stall accurately due to the sensitivity of the flow separation towards turbulence intensity and Reynolds number. Due to the failure of the two-equation turbulence models to accurately predict the transition and flow unsteadiness at high angles of attack, some deviation in force curves is observed after a stalling angle.

The Figure 3.30 shows the comparison of computational results (lift and drag coefficient) of NACA 2412 and Porpoise airfoils at  $1.9 \times 10^5$ . The porpoise airfoil shows an enhancement in aerodynamic efficiency than conventional NACA 2412 airfoil. The effectiveness of bio inspired nose on flow separation control is increases with increasing angles of attack.

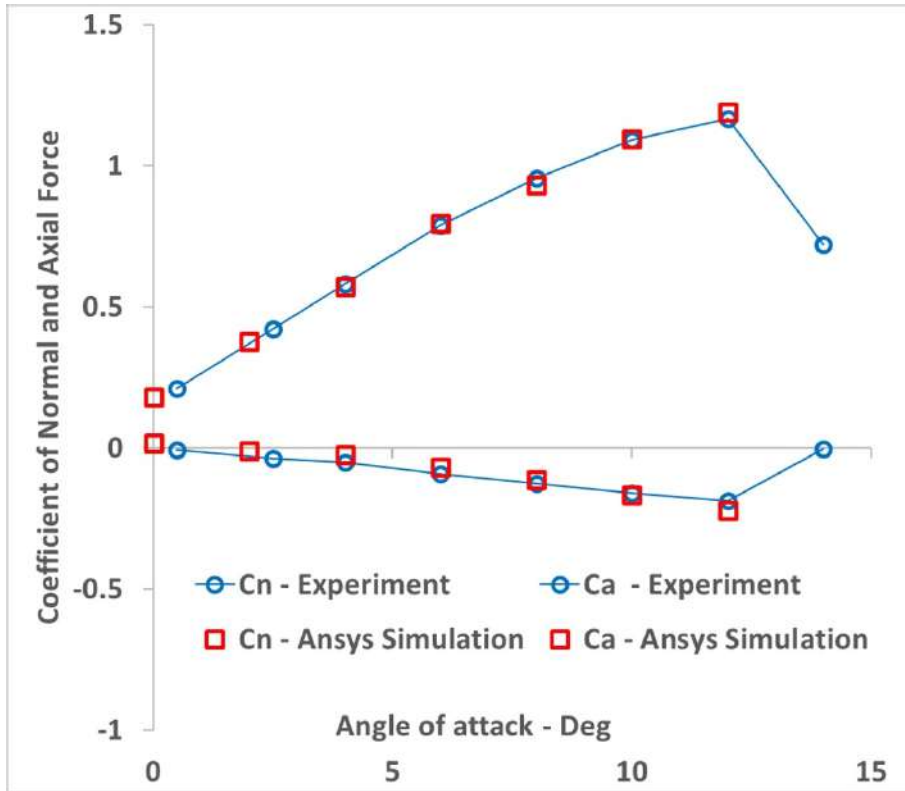


Figure 3.28 a) Coefficient of normal and axial force of Porpoise airfoil

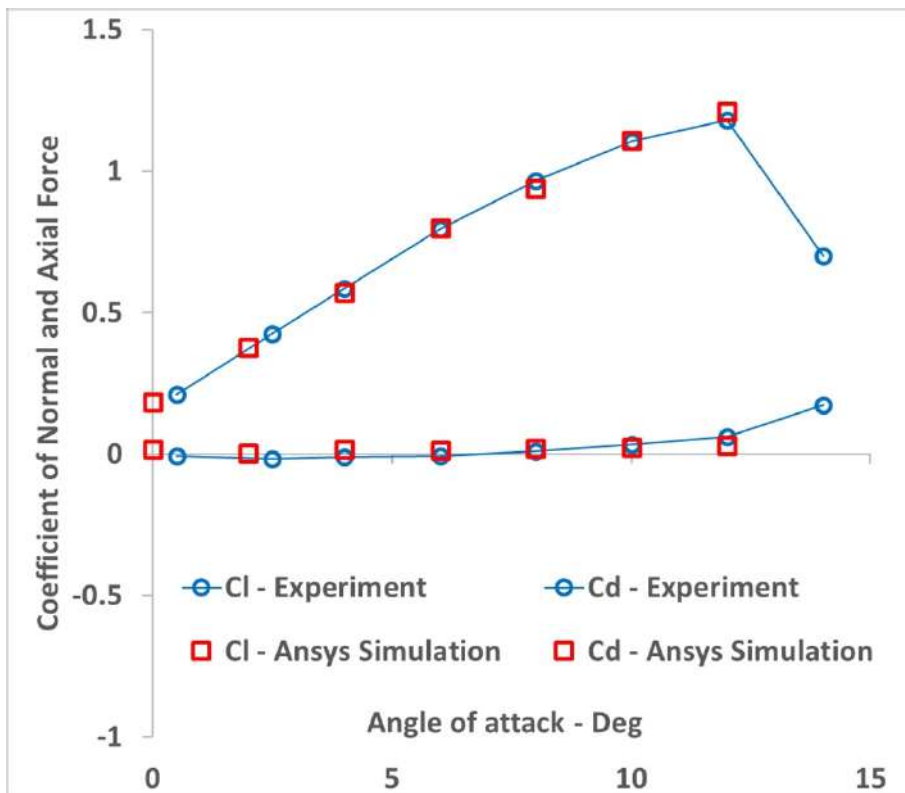


Figure 3.28 b) Coefficient of lift and drag of Porpoise airfoil at  $Re. 1.9 \times 10^5$

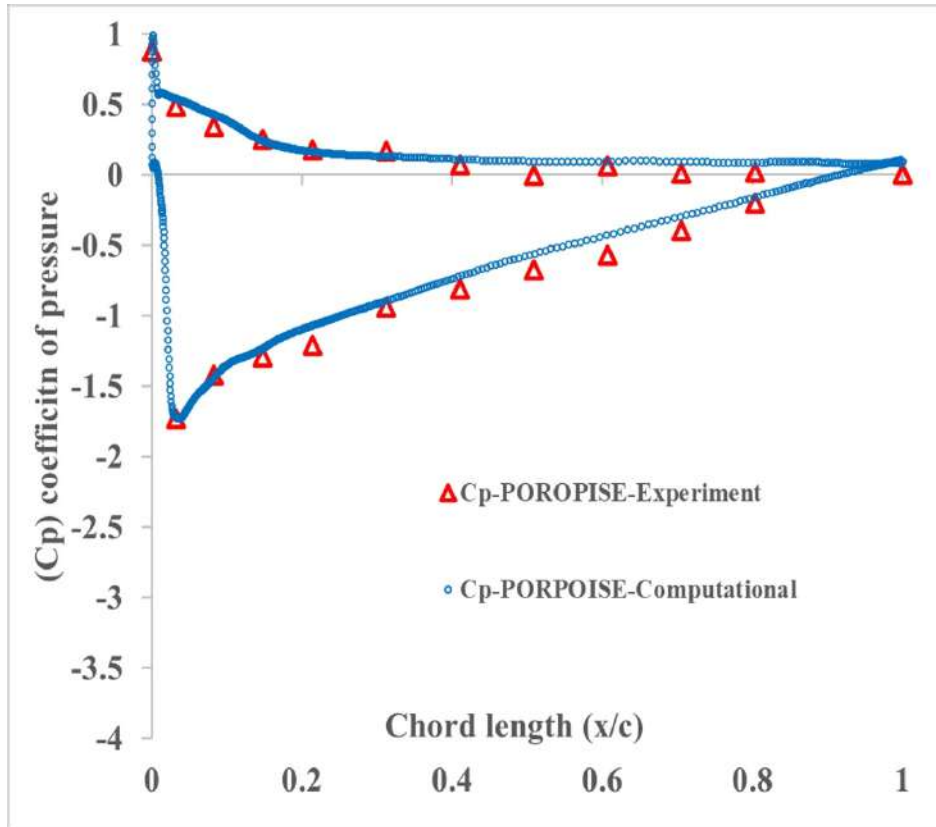


Figure 3.29 a)  $C_p$  distribution on Porpoise airfoil at 6 deg angle

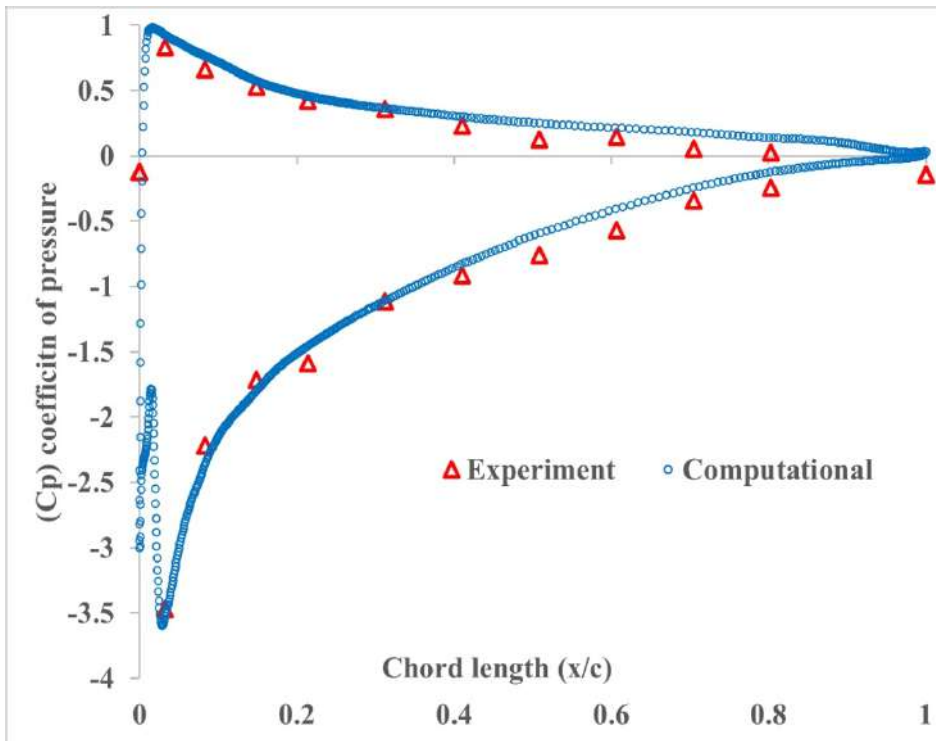
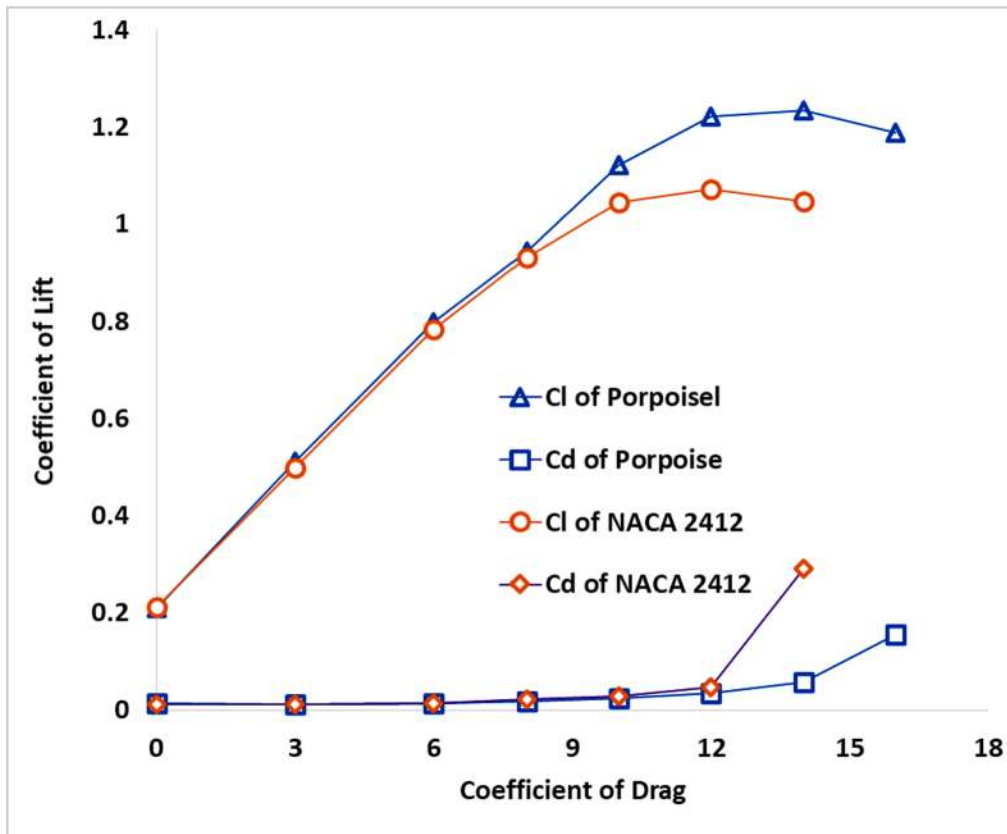


Figure 3.29 b)  $C_p$  distribution on Porpoise airfoil at 12 deg angle.



**Figure 3.30** Coefficient of lift and drag of NACA 2412 and Porpoise airfoil

## **CHAPTER 4**

### **RESULTS & DISCUSSIONS**

#### **4.1 Low speed analysis on NACA airfoils**

##### **4.1.1 Optimum Bio-Inspired nose for NACA 2412 airfoil**

NACA 2412 airfoil has been modified with the bio-inspired nose (54 cases) and analysed using Ansys – Fluent at low speed. The effect of nose geometries such as nose length and depth on the drag contribution has been analysed and found as follows. Figure 4.1 shows the variation of drag at different angle of attack for base airfoil (NACA 2412) and bio – inspired NACA 2412 airfoils. The bio – inspired airfoils having different nose length varies from minimum of 0.75% chord to maximum of 3.75 % of chord with a fixed cavity depth (medium depth – 2.25% of chord) have been tested. It is observed from the Figure 4.1, that the shorter nose forms optimum forward-facing step at low angle of attack ( $0^\circ - 6^\circ$ ) and optimum backward facing step at high angle of attack ( $6^\circ - 16^\circ$ ) which allows multiple acceleration over the nose. This increases the kinetic energy of the near wall flow on the upper surface. Thus, decreasing the drag and increasing the aerodynamic efficiency at all angle of attack. There is no noticeable change in the lift.

It is also observed that the longer nose forms forward facing step which increases the aerodynamic efficiency ten times higher than the shorter nose at low angle of attack. This is due to the movement of stagnation point to the lower surface and extending the low-pressure region on the upper surface as shown in Figure 4.3 (E.g. NACA 2412 – A1 at  $4^\circ$ ). But this longer nose decreases the aerodynamic efficiency at high angle of attack due to the flow separation originating from it, as shown in Figure 4.3 (E.g., NACA 2412 - A1 at  $16^\circ$ ). This results in drastic increase of drag and drastic decrease of lift. It is inferred that

as length of the nose decreases, aerodynamic efficiency increases at all angle of attack.

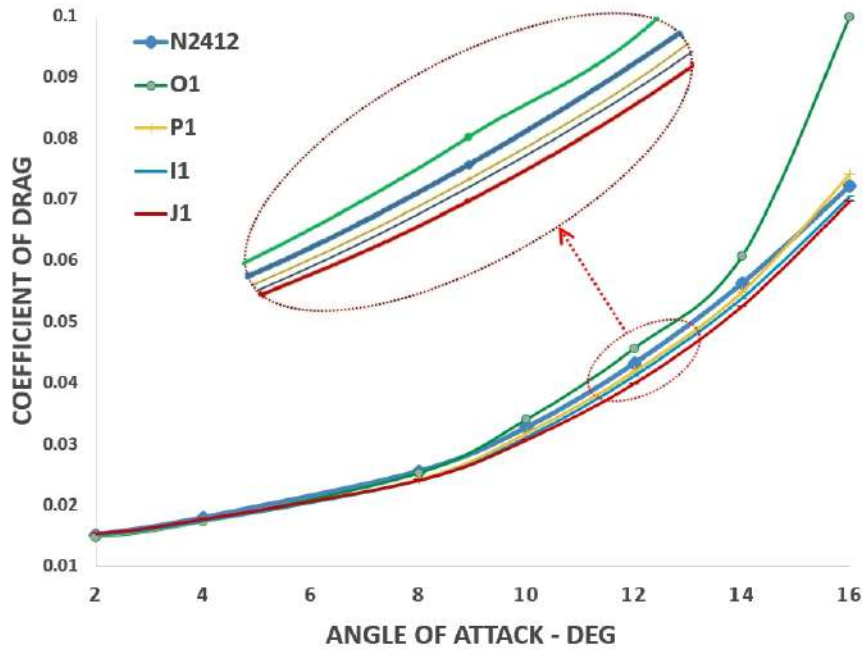


Figure 4.1  $C_d$  graph for NACA 2412 airfoils with different nose length

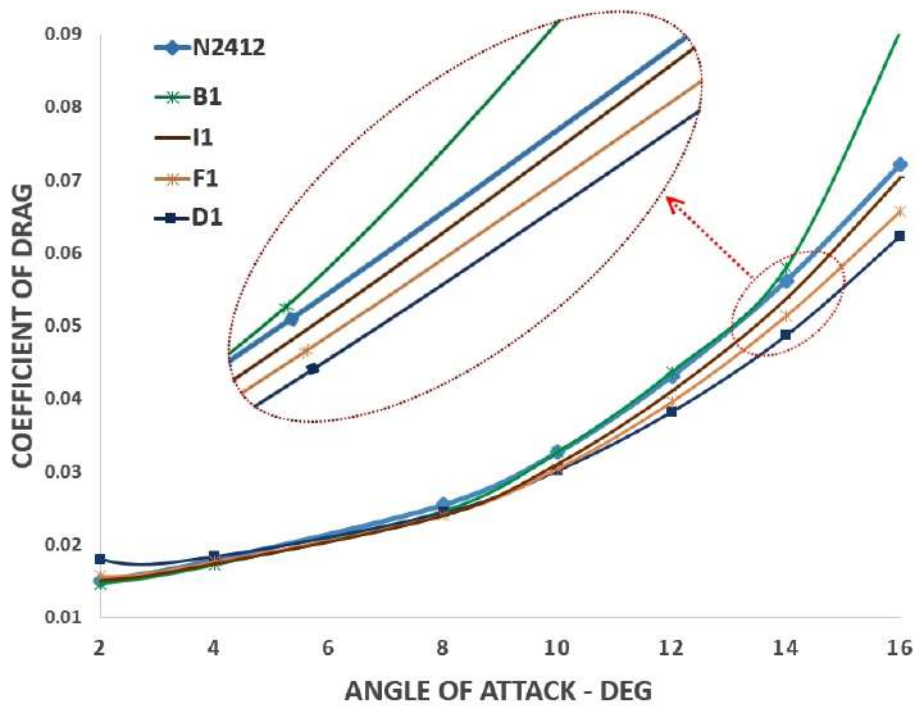
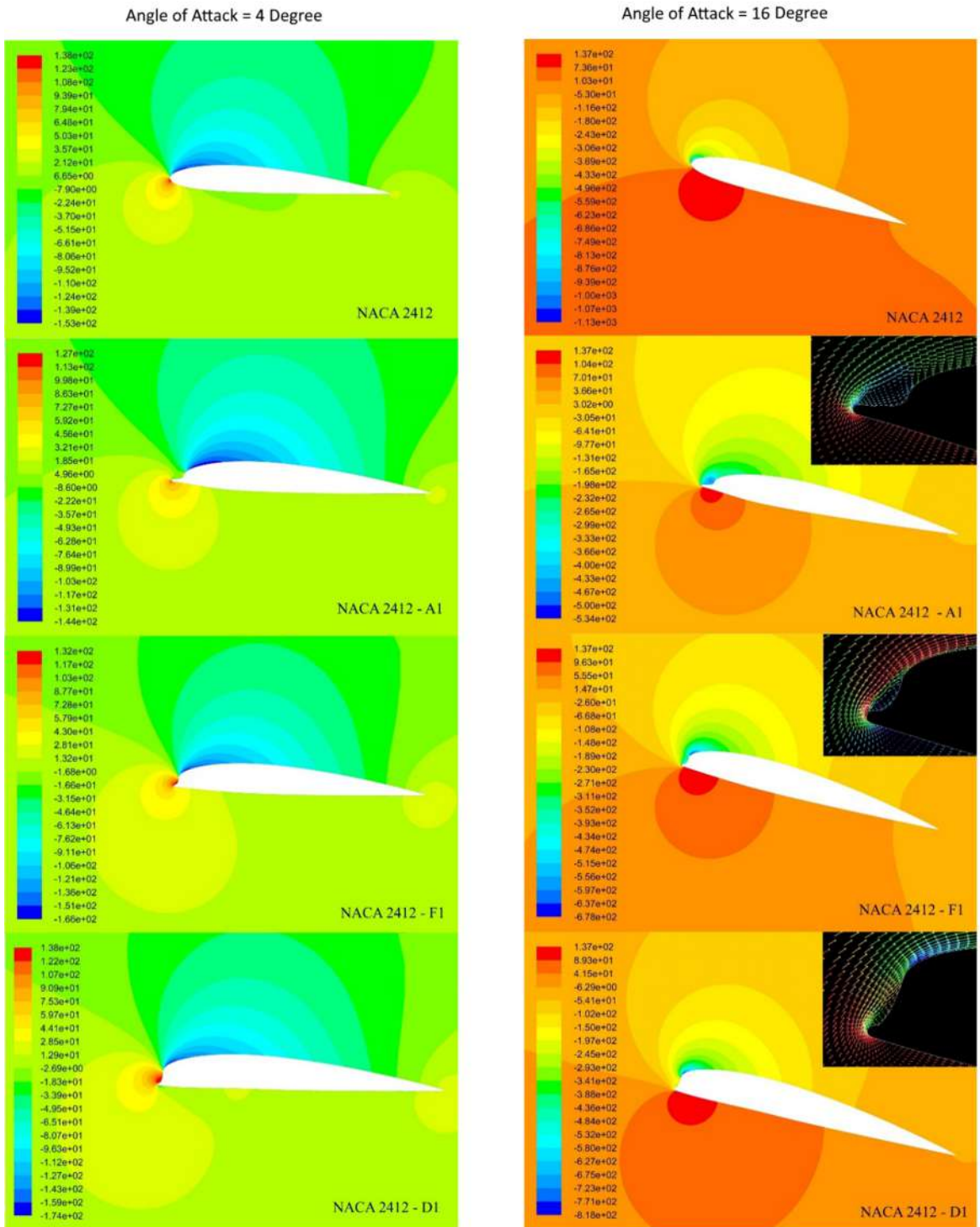


Figure 4.2  $C_d$  graph for NACA 2412 airfoil with different nose cavity depth



**Figure 4.3** Pressure contour of NACA 2412 and modified airfoil at  $4^\circ$  and  $16^\circ$  angle of attack.

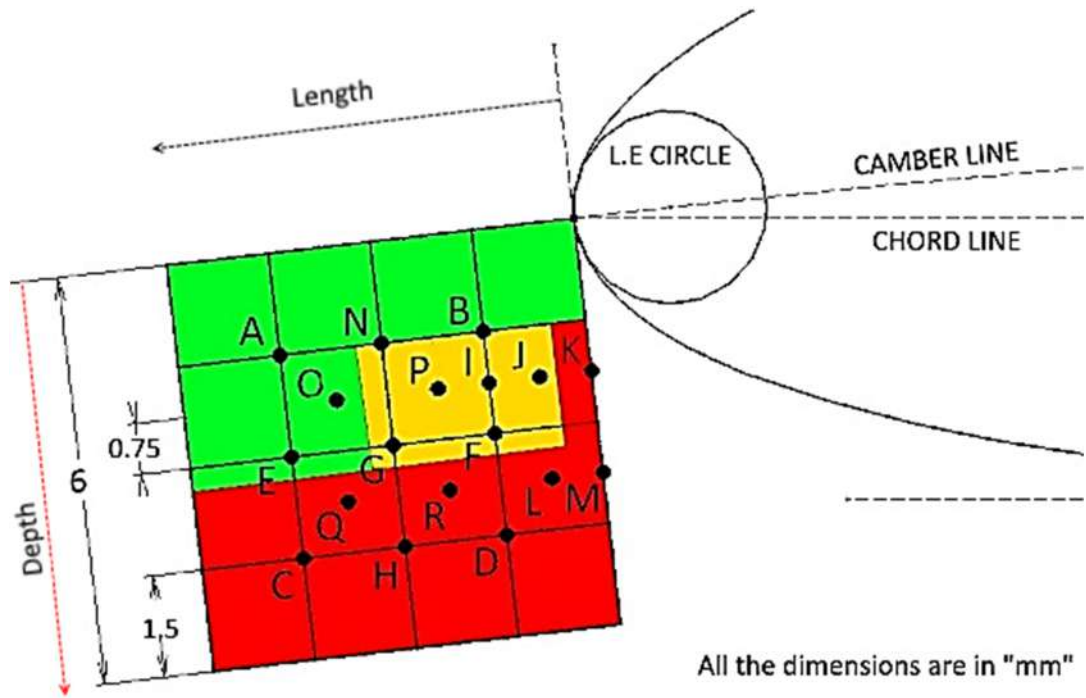


Figure 4.2 shows the variation of drag at different angle of attack for base airfoil (NACA 2412) and bio – inspired NACA 2412 airfoils. The bio – inspired airfoils have different cavity depth varies from minimum of 1.5 % of chord and maximum of 4.5 % of chord with a fixed nose length (shorter length – 1.5 % of chord) have been tested.

It is observed that the deeper cavity nose increases the aerodynamic efficiency at high angle of attack ( $\geq 8^\circ$ ) by creating the axial vortices and induces multiple acceleration of flow as shown in the Figure 4.3 (NACA 2412 - D1 at  $16^\circ$ ). But it increases the drag at low angle of attack. This is due to the movement of stagnation point to the upper surface and thus reducing the pressure difference as shown in Figure 4.3 (NACA 2412 – D1 at  $4^\circ$ ).

It is also observed that the shallow cavity nose decreases the aerodynamic efficiency at high angle of attack ( $\geq 8^\circ$ ). It fails to create vortices and multiple acceleration therefore flow separates from the nose. But it increases the aerodynamic efficiency at low angle of attack by forming the forward-facing step. It is inferred that the medium depth cavity nose (2.25c) gives better aerodynamic efficiency than the base airfoil at all angle of attack.

Based on the aerodynamic performance at different angle of attack, the six regions are further grouped into three cases as shown in the Figure 4.4. The green shaded grids represent airfoil with shallow cavity and longer/shorter nose (Case 1), the yellow shaded grids represent airfoil with medium depth cavity and shorter nose (Case 2), and the red shaded grids represent airfoil with deeper cavity and longer/shorter nose (Case 3).



All the dimensions are in "mm"

Figure 4.4 NACA 2412 airfoil with grid.

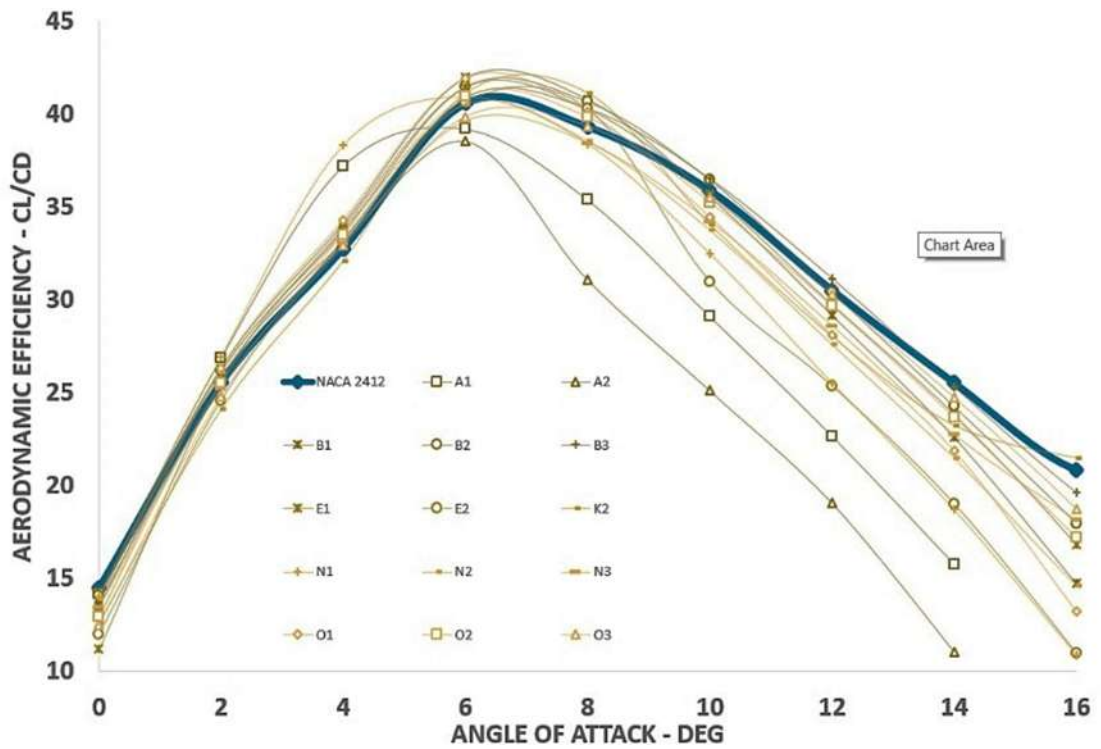


Figure 4.5  $C_l / C_d$  graph for NACA 2412 and bio-inspired nose airfoils with shallow cavity

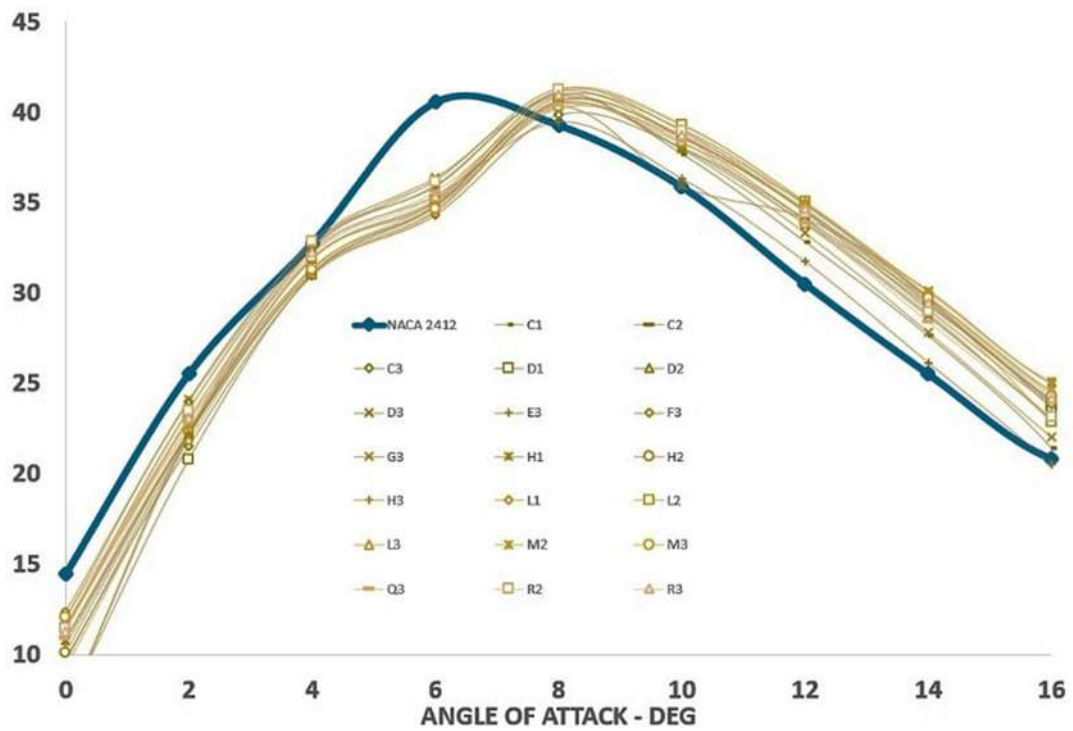


Figure 4.6  $C_l / C_d$  graph for NACA 2412 airfoils with deeper cavity.

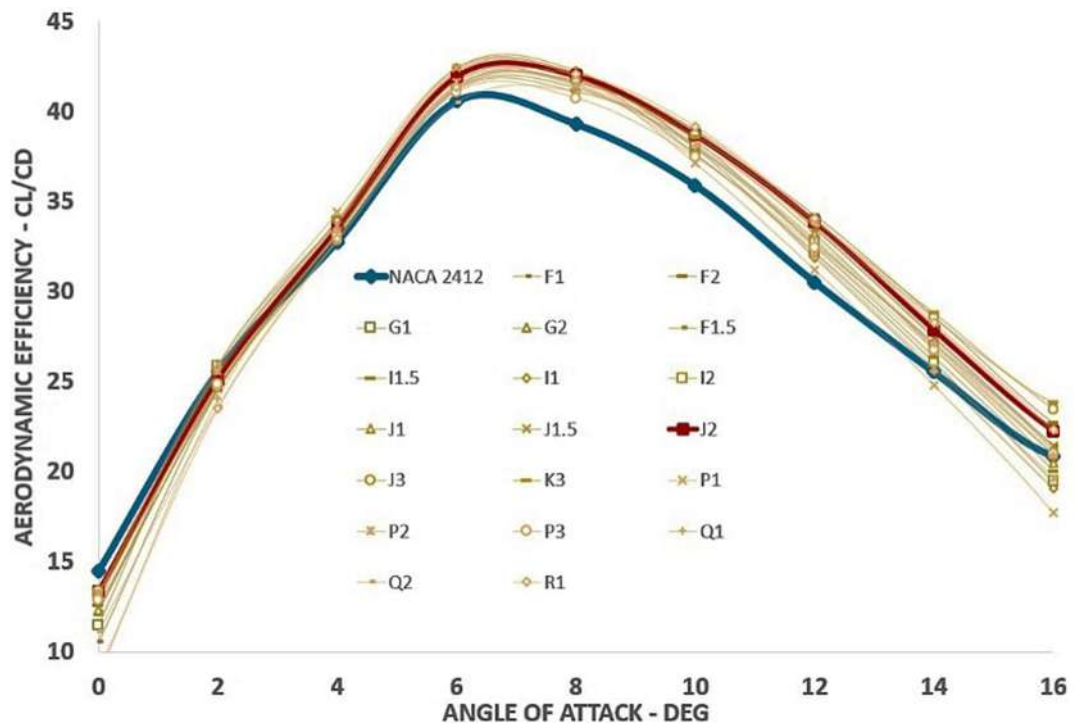
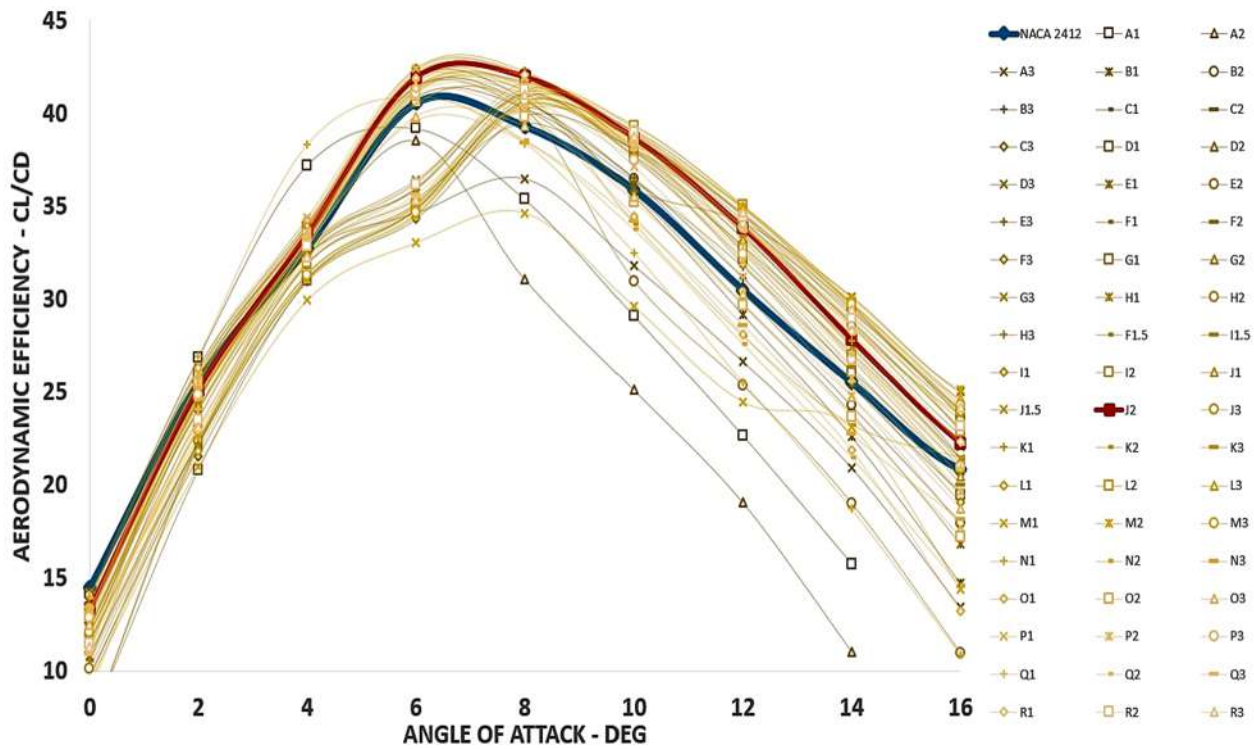
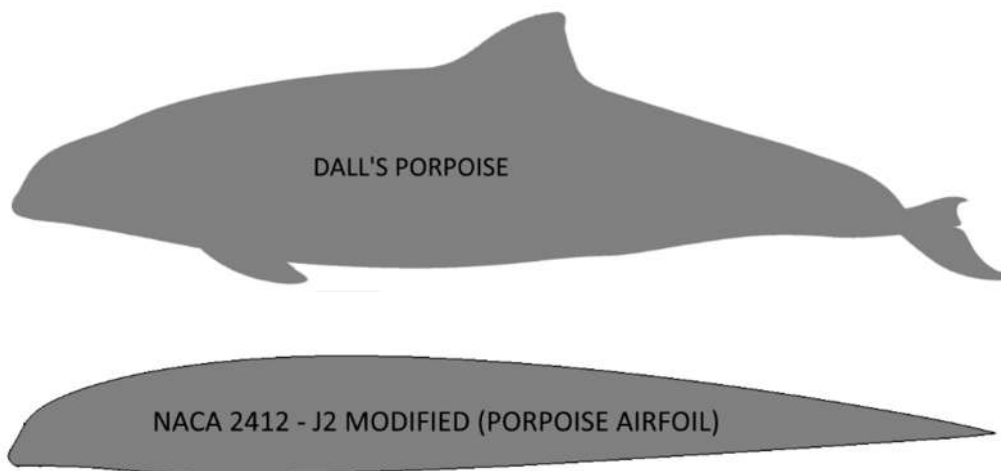


Figure 4.7  $C_l / C_d$  graph for airfoils with shorter nose and medium depth cavity



**Figure 4.8**  $C_l / C_d$  graph for NACA 2412 and bio-inspired nose airfoils



**Figure 4.9** The Dall's porpoise and modified NACA 2412 – J2 airfoil.

As discussed earlier, shallow depth cavity improves the aerodynamic efficiency only at low angle of attack (Figure 4.5) and deeper cavity improves the

aerodynamic efficiency only at higher angle of attack (Figure 4.6). Medium depth and shorter nose airfoils (yellow region) show the better aerodynamic performance at all angle of attack than the base airfoil (Figure 4.7). Figure 4.8 shows the aerodynamic performance of all the bio- inspired NACA 2412 airfoils compared with NACA 2412. And optimum nose design (NACA 2412 - J2: Cavity depth - 2.25 % of chord, nose length - 0.75 % chord, and nose diameter – 2 % chord) is highlighted in red colour.

It is found that the airfoil with medium depth and shorter nose shows noticeable increase in aerodynamic efficiency than NACA 2412 airfoil. The NACA 2412 – J2 nose design was further modified at upper and lower surfaces by the inspiration of fastest cetacean species - The Dall's porpoise (Figure 4.9). The upper part of the nose was flattened and the lower part of the nose length was reduced to match with the Dall's porpoise (Figure 4.10).

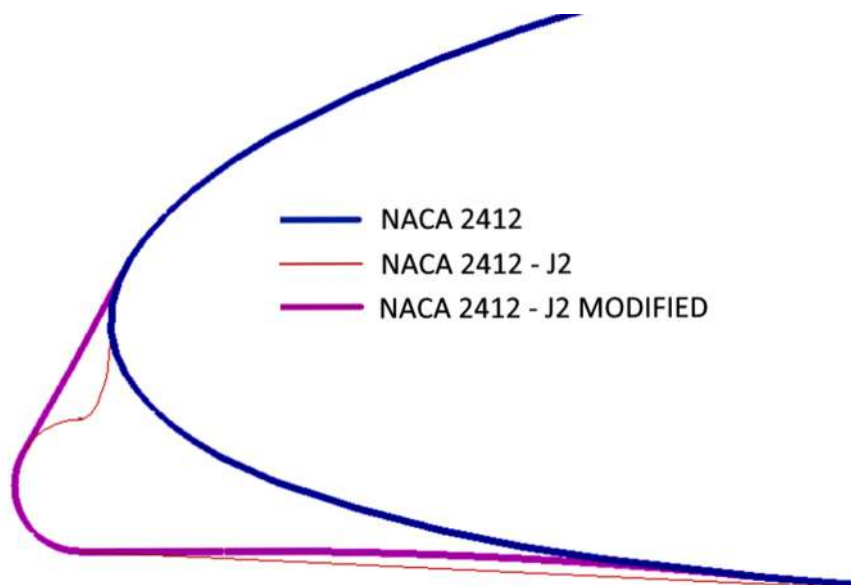


**Figure 4.10** Nose profiles of NACA 2412 – J2 and Porpoise airfoil.

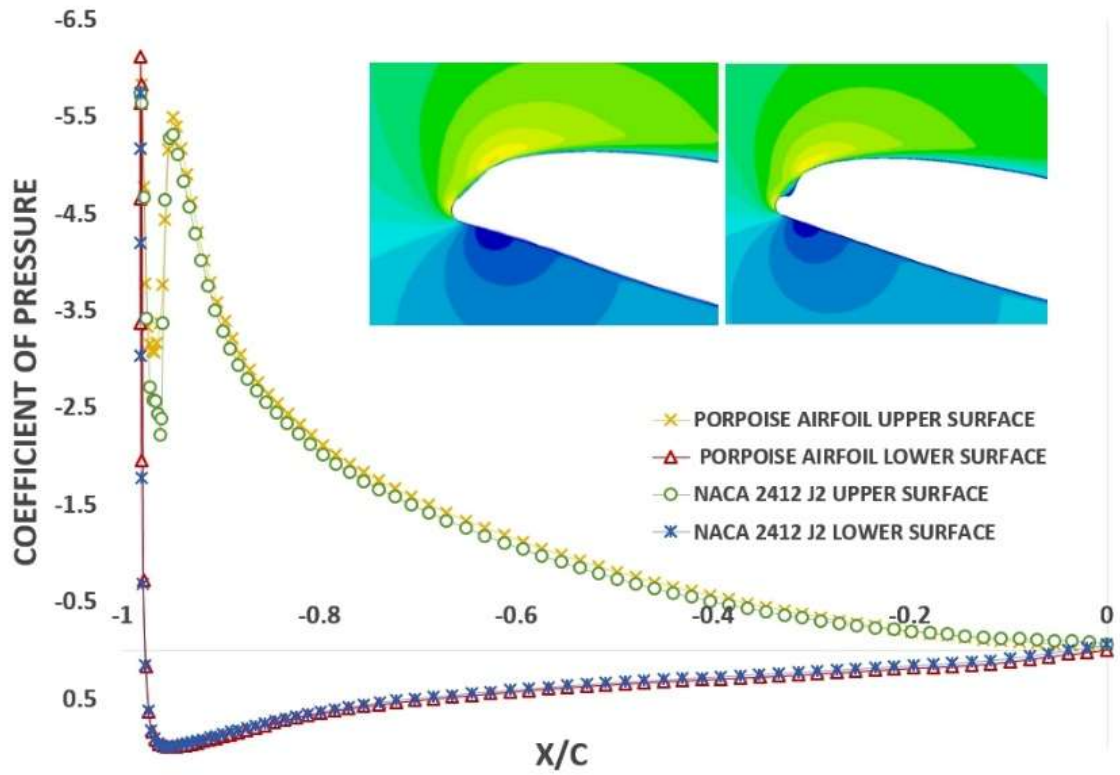


Figure 4.11  $C_p$  distribution of NACA 2412 – J2 and Porpoise airfoil.

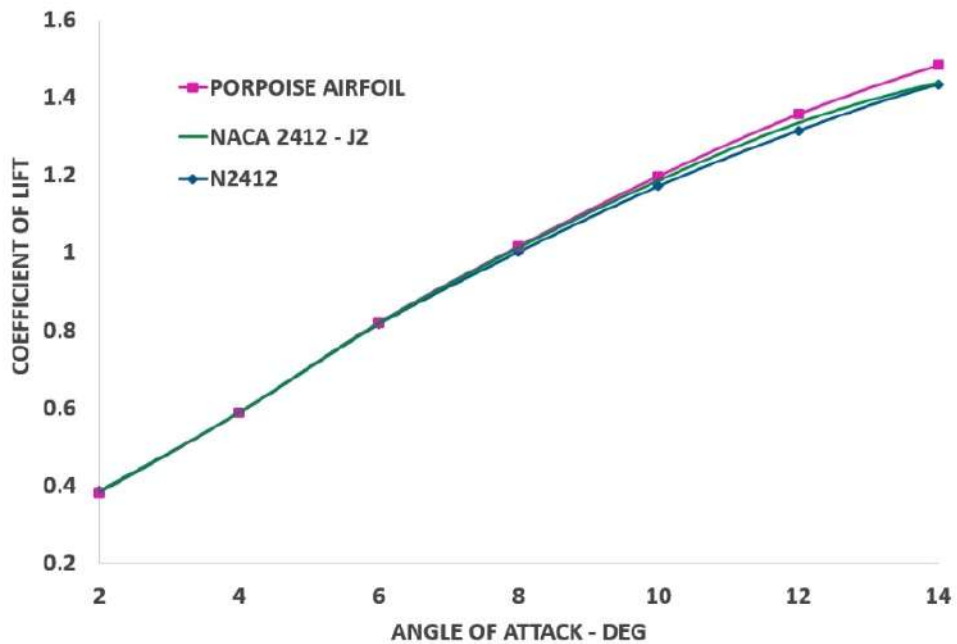
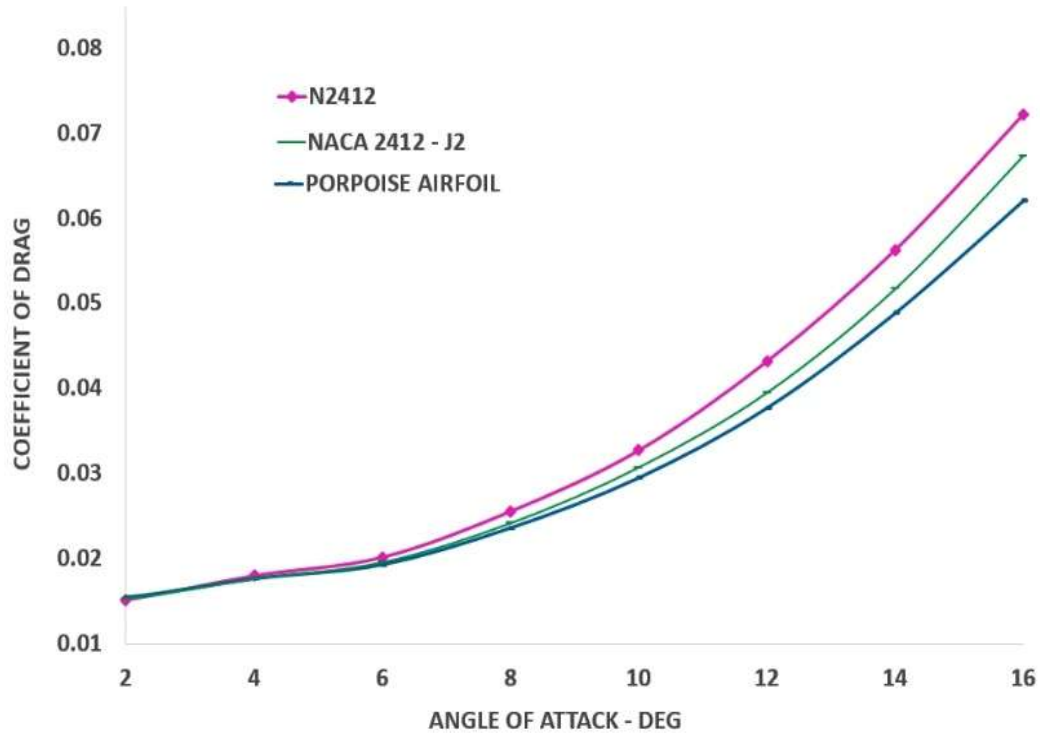
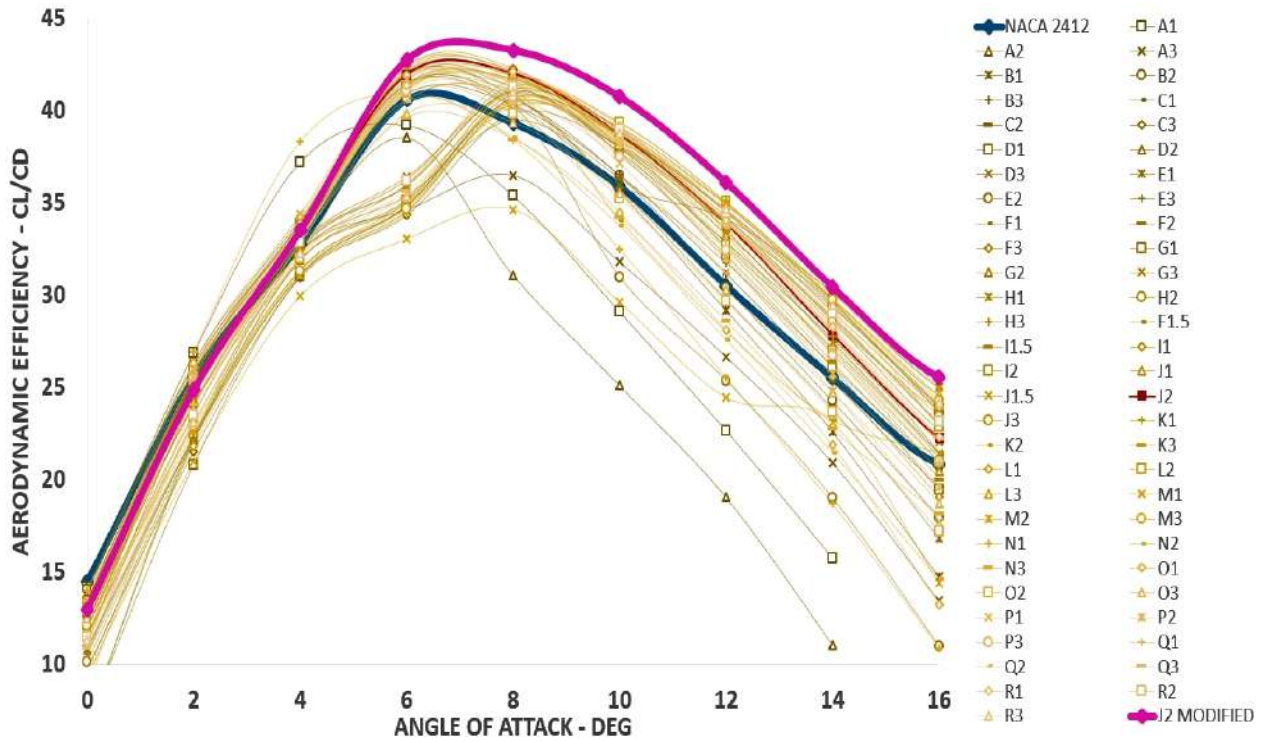


Figure 4.12  $C_l$  graph for NACA 2412 – J2 and Porpoise airfoil.



**Figure 4.13**  $C_d$  graph for NACA 2412 – J2 and Porpoise airfoil.

Figure 4.12 and Figure 4.13 show that for the porpoise airfoil, lift increases and drag decreases with increase in angle of attack than the NACA 2412 – J2 airfoil. The maximum decrease in drag coefficient is 14% with an average decrease of 6.5%. The maximum increase in lift coefficient is 5.3% with an average increase of 1.8%. And the maximum increase in aerodynamic efficiency is 22.4% with an average increase of 8.6%. This is due to the better acceleration on the upper surface which increases the minimum pressure than the NACA 2412 – J2 airfoil as shown in Figure 4.11. The attached flow on the porpoise airfoil nose deflected to the higher angle thus increase the acceleration to the maximum value compared to the NACA 2412 – J2 airfoil. Figure 4.14 shows the aerodynamic efficiency of all modified NACA 2412 airfoils. And porpoise airfoil  $c_l/c_d$  curve is highlighted in pink colour. For the porpoise airfoil, the rate of increase of aerodynamic efficiency is proportional to the increasing angle of attack.



**Figure 4.14** Comparison of  $C_l / C_d$  graph for NACA 2412 and porpoise airfoil with bio – inspired nose airfoils.

#### 4.1.2 Effect of Bio inspired nose design on NACA 4 series airfoils

In the previous analysis, the optimum bio inspired nose design (PORPOISE) was found for NACA 2412. Further analysis has been done to check the possibilities of finding a universal nose design, which gives optimum aerodynamic performance for all NACA 4 series airfoils. The nose geometrical parameters (such as nose length, nose depth, and nose diameter) and airfoil geometrical parameters (such as thickness, camber, and camber location) were varied in the analysis.

Figure 3.7 shows the NACA airfoils chart, where NACA 2412 has been taken as a reference. Concerning that, other airfoils of different geometries were chosen. The increase in the airfoils thickness, increase in the airfoils camber, and decrease in the airfoils camber location will move the optimum nose circle downwards. So, the nose depth changes from medium to deep, which fails at a low angle of attack as discussed in NACA 2412 results. Among 22 NACA 4 series airfoils, the results of NACA 2418 (maximum thickness), NACA 4412



(maximum camber), and NACA 2212 (minimum camber location) (highlighted by red colour in Figure 3.7) are discussed. The above analysis was done for the different nose designs such as, the long nose with a shallow cavity design created using 'A' point, shorter nose with a deeper cavity airfoil created using 'D' point, and shorter nose with a medium depth cavity airfoil created using 'F' & 'J' points.

It is found that the flow behaviour is in good agreement with the NACA 2412 results (Figure 4.8). The length and depth of the bio-inspired nose play the important role to change the aerodynamic performance of the airfoil than the diameter of the nose circle. The grid point "J" which was used to design the optimised nose lies closer to the baseline airfoils leading edge, so it is at almost same location for both the square grids and shows the similar results in the analysis.

Figure 4.15 shows that, the increase in airfoil thickness from 2412 to 2418, have not affected the bio inspired nose performance and gives the similar flow behaviour as on NACA 2412. The optimised nose design (porpoise) increases the L/D within the operative range of angle of attack ( $> 4^\circ$ ) than the baseline airfoil. And shows no increment in the L/D value for less than  $4^\circ$  angle of attack.

Figure 4.16 and Figure 4.17 show that, for a decrease in the location of camber from 2412 to 2212, and an increase in camber from 2412 to 4412, the optimised nose design shows an increment in L/D value above  $4^\circ$  angle of attack. The L/D values are reduced at angles of attack less than  $4^\circ$ , as compared to the baseline airfoil. It is because the increase in the camber or decrease in the camber location, increases the nose cavity depth. So, the stagnation point moves to the upper surface and reducing the pressure difference. In addition, it affects the streamline profile of the airfoils lower profile.

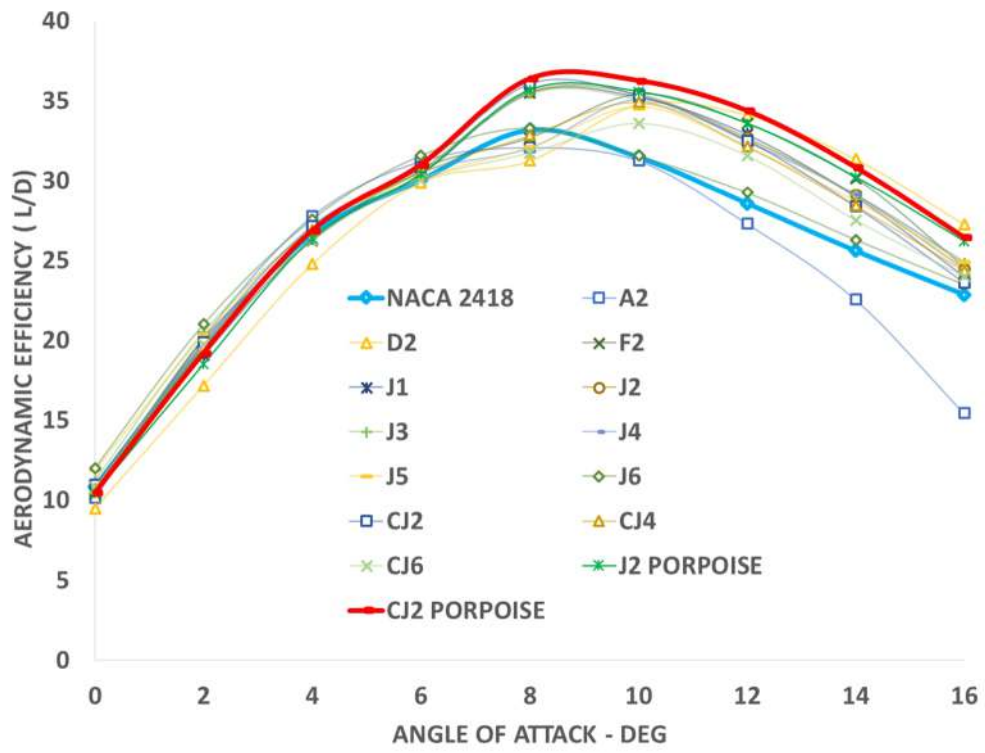


Figure 4.15  $C_l / C_d$  graph for NACA 2418 and bio-inspired nose airfoils.

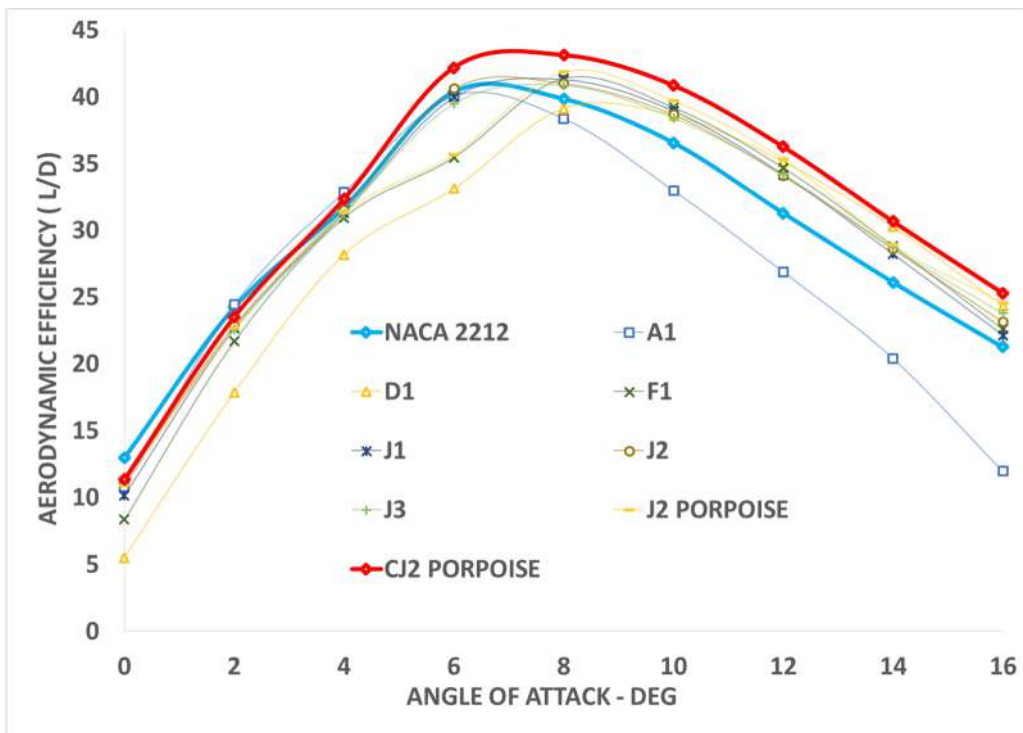
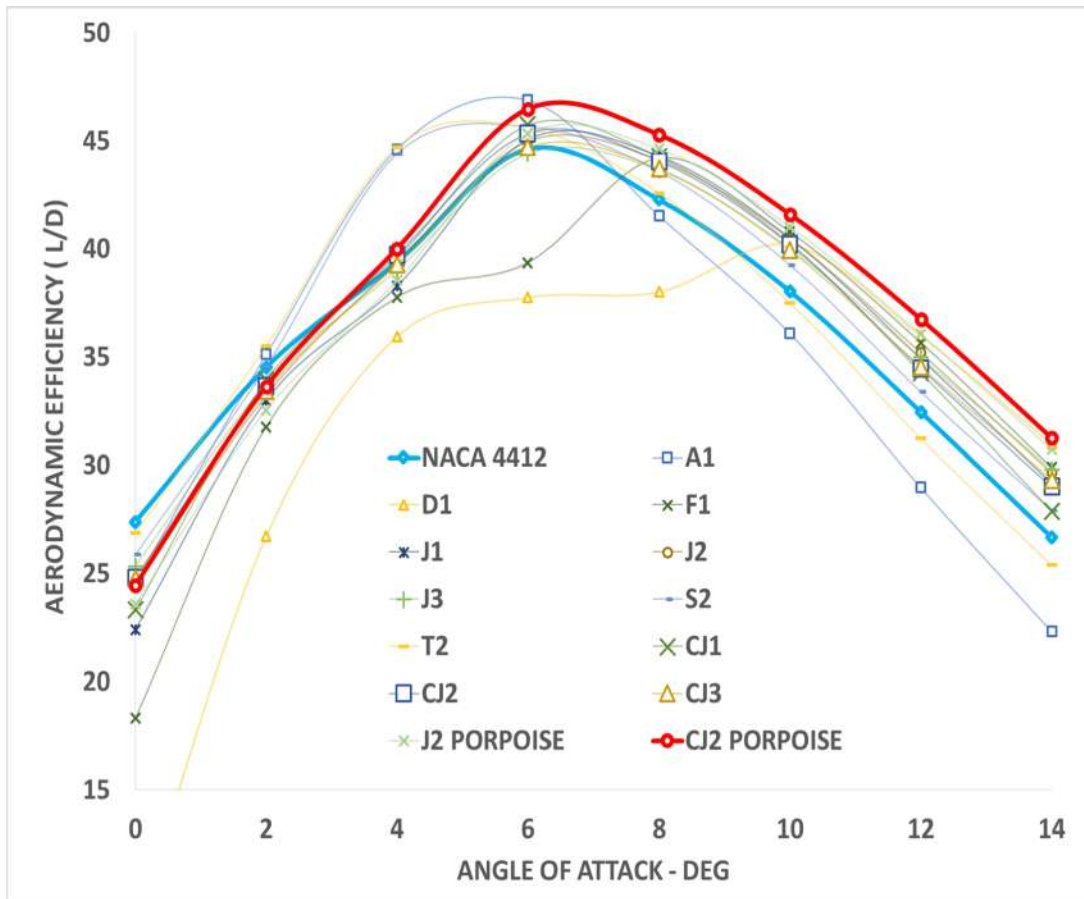


Figure 4.16  $C_l / C_d$  graph for NACA 2212 and bio – inspired nose airfoils.



**Figure 4.17**  $C_l / C_d$  graph for NACA 4412 and bio – inspired nose airfoils.

The diameter of the nose circle is increased with the increasing airfoil thickness (as mentioned in Figure 4.18a) to check their effect on the increment of the kinetic energy of the flow over the nose. Figure 4.18b shows that the nose diameter upto 3% chord does not show much variation in pressure distribution and minimum pressure. However, the bigger diameter nose (5% & 6% of the chord) affects the lower profile of airfoils near the leading edge. Also reduces the acceleration of flow over the nose, hence reduces the minimum pressure on the upper surface as mentioned in Figure 4.18b. From the analysis, the range of nose circle diameter that works better for different thicknesses of the airfoil have been found (Table 4.1).

**Table 4.1** Range of optimum nose circle diameter

Thicknesses of The Airfoil	Nose Circle Diameter	Optimum Nose Circle Diameter
Upto 12% of chord	2% chord	2% chord
13% to 21% of chord	2% to 3% of chord	
Above 21% of chord	2% to 4% of chord	

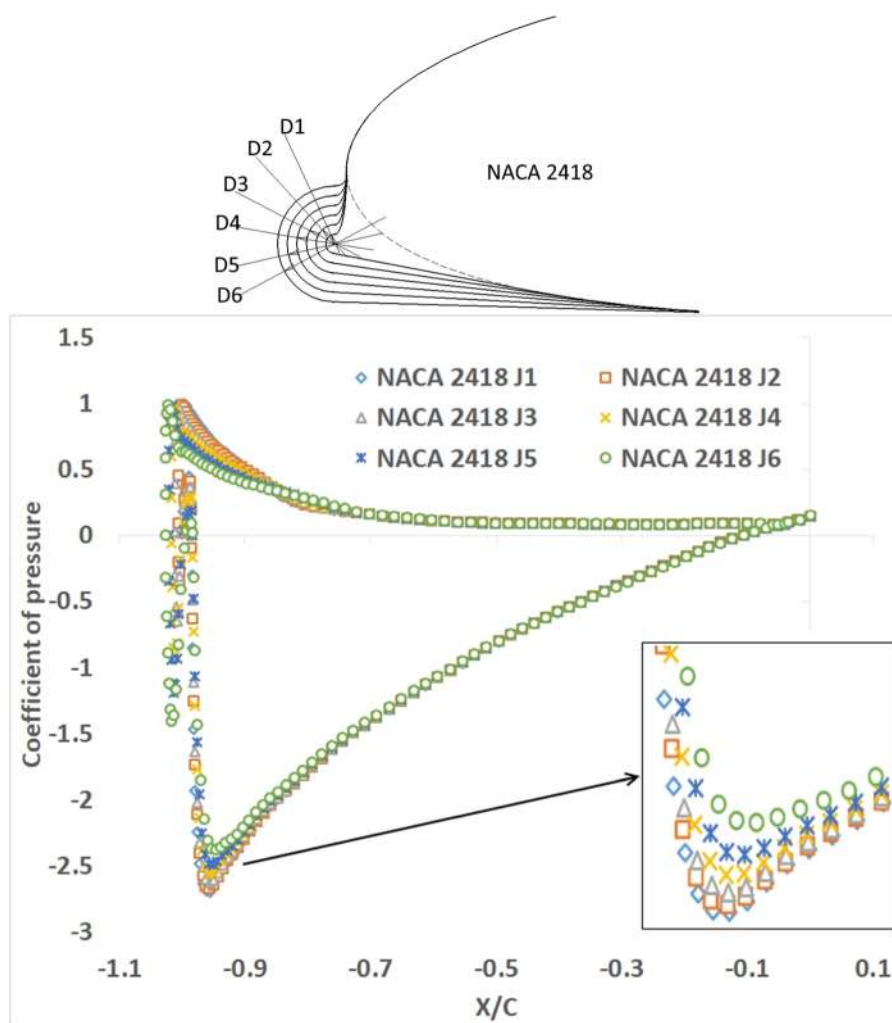


**Figure 4.18** a) Different nose profiles and b)  $C_p$  distribution of NACA 2418 airfoil with bio-inspired nose of different nose circle diameters.

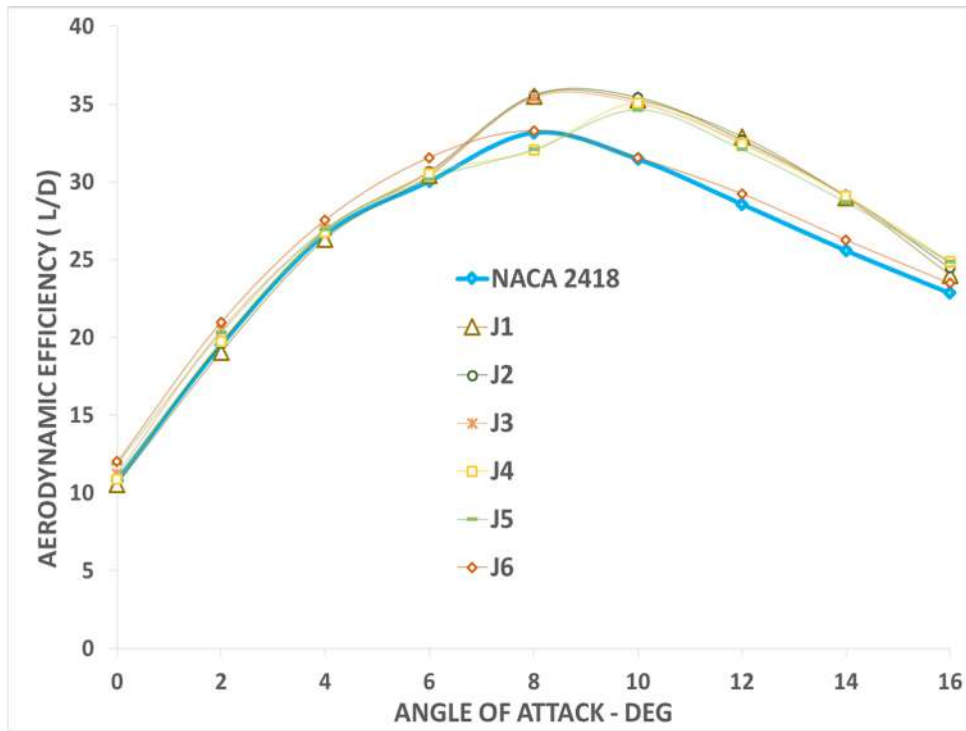


**Figure 4.19a**  $C_l / C_d$  graph for NACA 2418 and its bio – inspired nose airfoils.

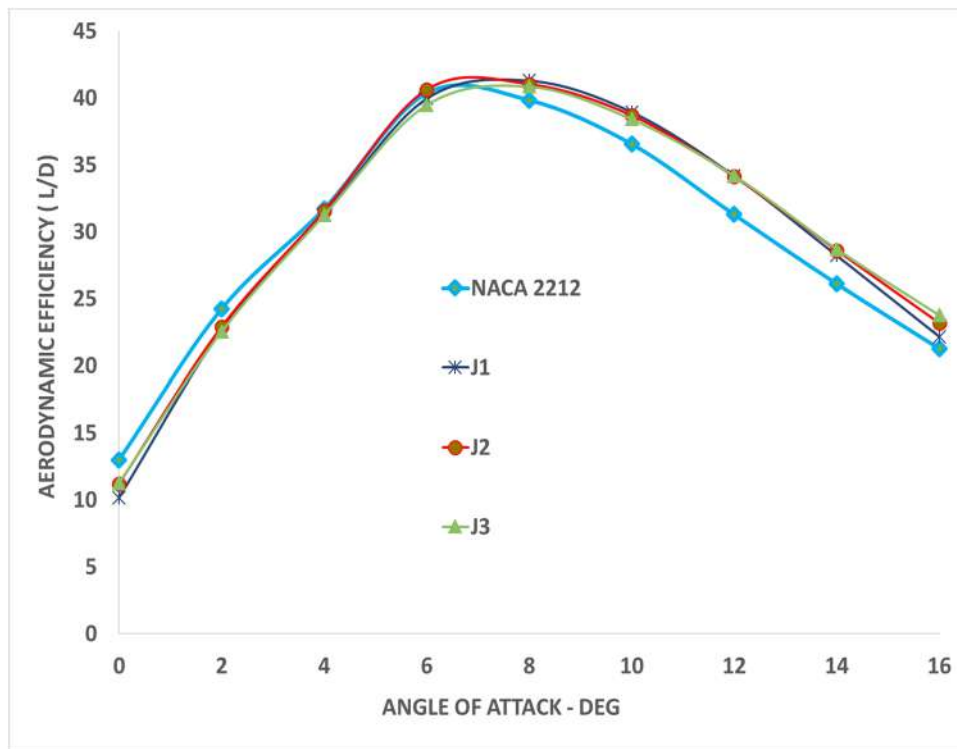


**Figure 4.19b**  $C_l / C_d$  graph for NACA 2212 and its bio – inspired nose airfoils.

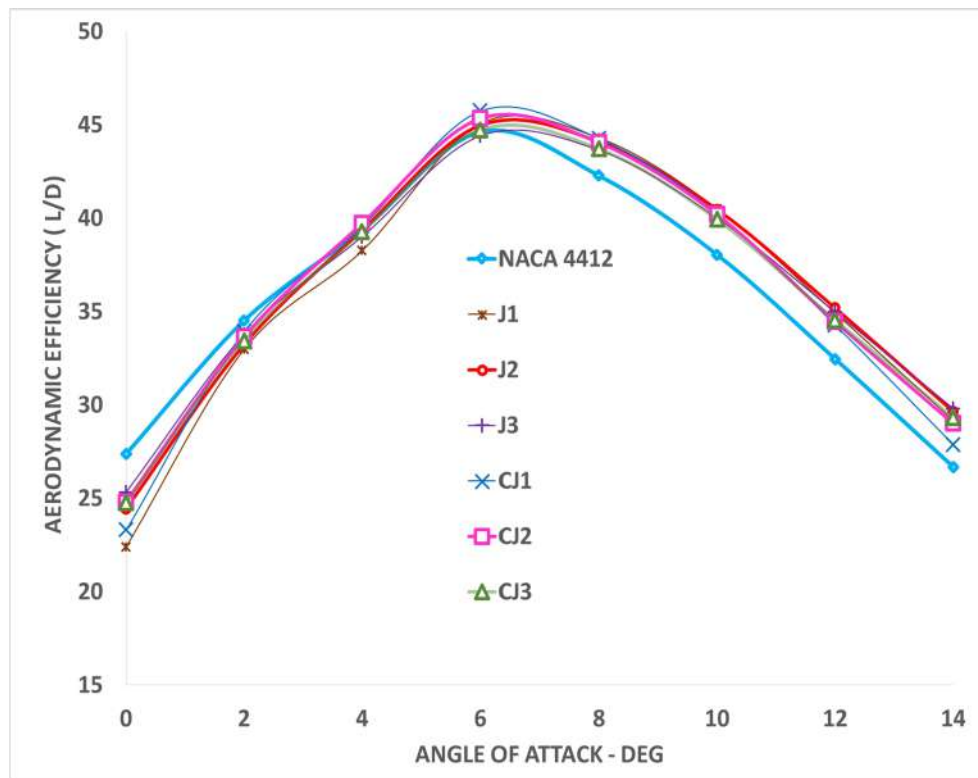


**Figure 4.19c**  $C_l / C_d$  graph for NACA 4412 and its bio – inspired nose airfoils.

Therefore, it is recommended that a bio-inspired nose with diameter 2% of a chord can be used for all NACA airfoils irrespective of its thickness, camber and camber locations as shown in the Figure 4.19a-4.19c. Therefore, fixing the nose diameter (2% of a chord) helps to achieve the universal leading-edge device that can be mounted in any existing aircraft with NACA series airfoils.

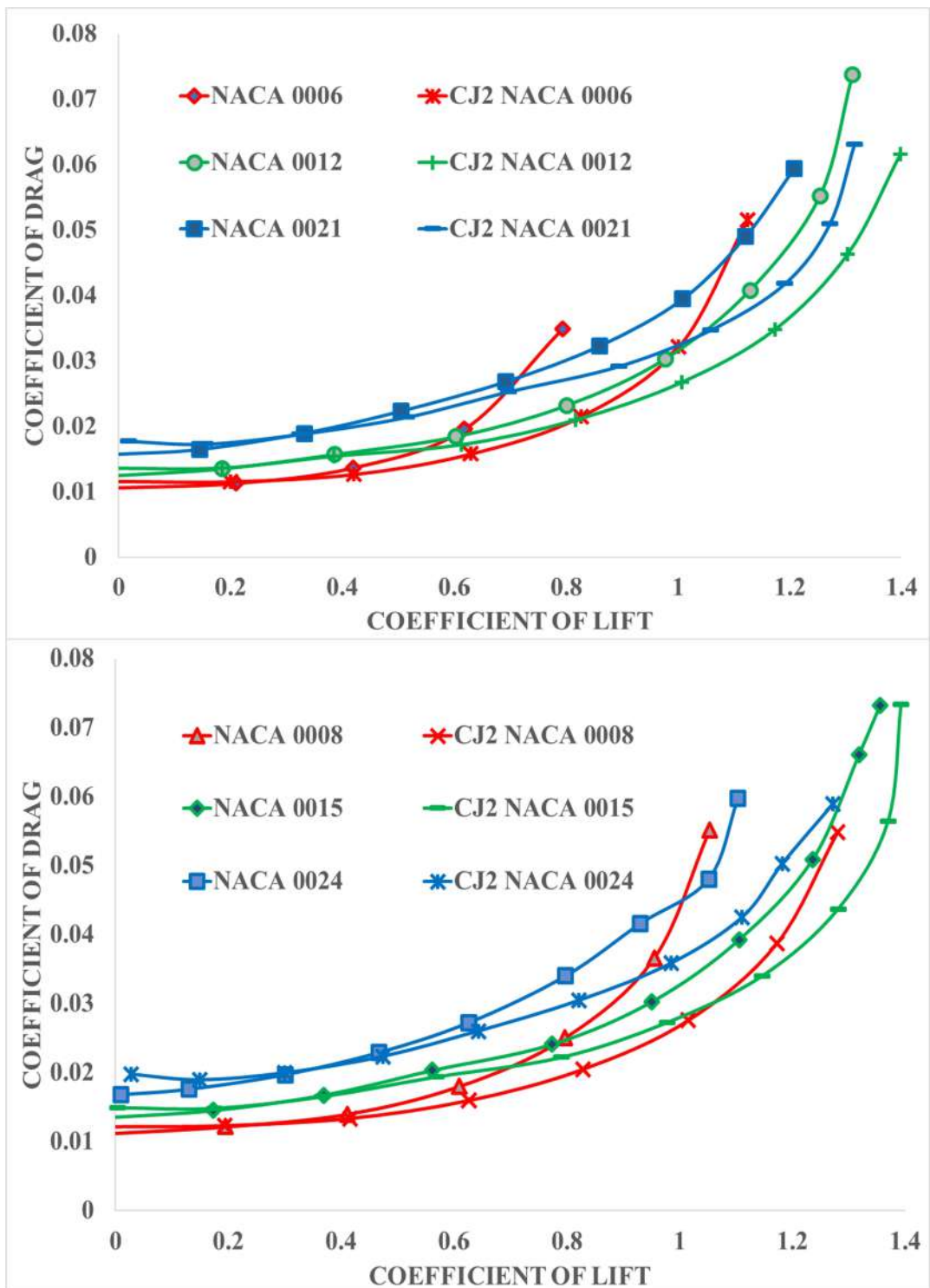
From the above analysis, it was inferred that the Porpoise nose design (shorter nose with medium depth cavity: Cavity depth - 2.25 % of chord, nose length - 0.75 % chord, and nose diameter – 2 % chord) shows better aerodynamic performance irrespective of different airfoil geometries of NACA 4 series airfoils. Therefore, the porpoise design created using ‘J’ point with respect to the airfoil chord line is taken for further studies. It is because the J point is near to the airfoil leading edge, so it lies almost at the same location for both square grids drawn with respect to the camber line and chord line. In addition, it is easy to determine the airfoil chord line than to find the camber line.

Further study is done on NACA symmetrical aerofoils with thickness varied such as 6%, 8%, 12%, 15%, 18%, 21% & 24% of chord, and the results are

shown in the following Figures 4.20 and 4.21. For better clarity of the plot, only 6 different thicknesses results are plotted in each Figure out of 7 different thicknesses. The Figure 4.20 shows that, at a low angle of attack, increasing the thickness of the airfoil increases the drag by increasing the wake thickness behind the airfoil. And at high angle of attack, increasing the thickness of the airfoil decreases the drag because of the attached flow on the rounded nose (Coanda effect). The Figure 4.21 shows that the maximum lift coefficient is increasing for increasing thickness, and reaches the maximum value at 12% of the chord. Then it is decreasing for further increase in thickness.

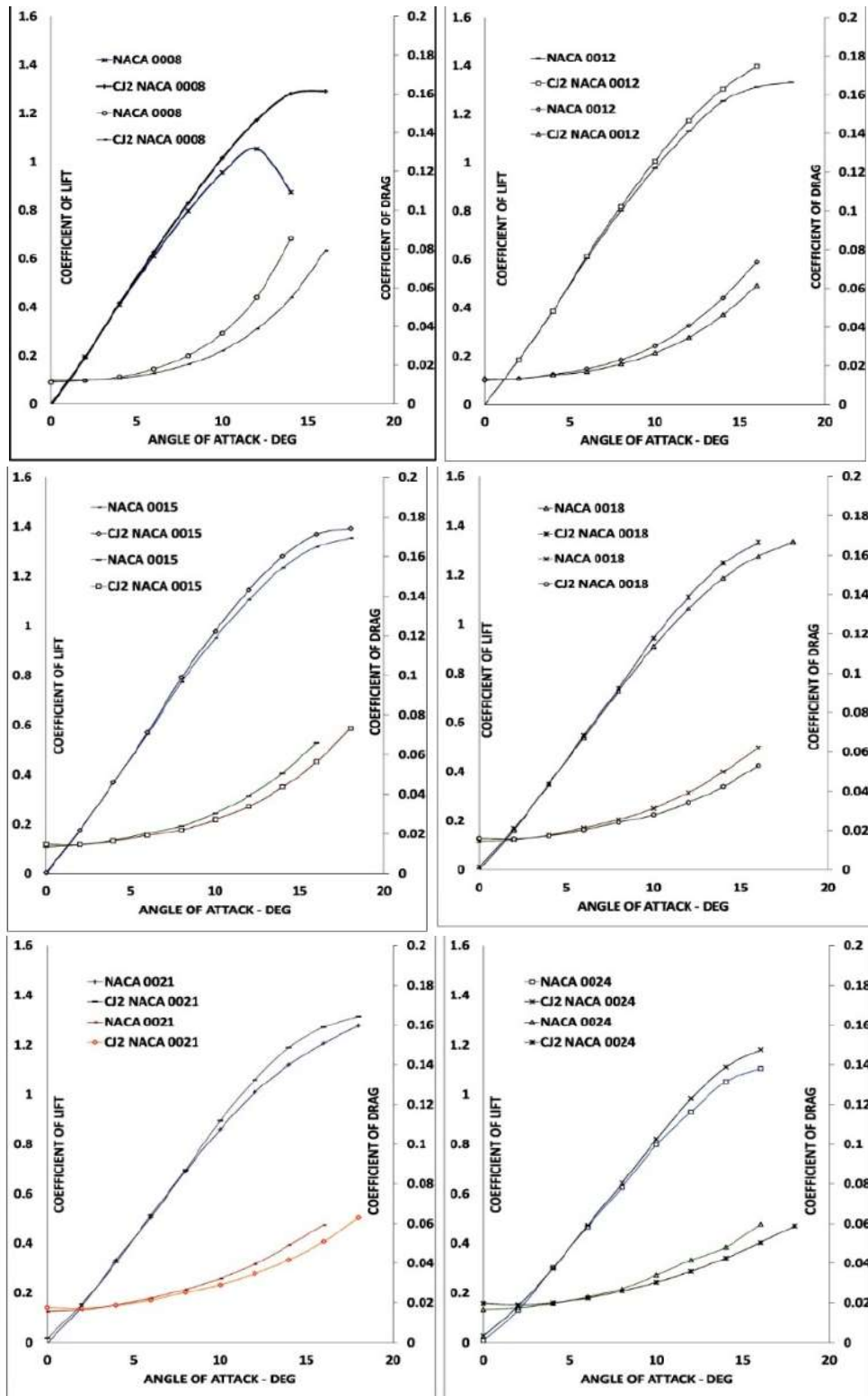
From the Figure 4.20 & 4.21, it is shown that the bio-inspired nose improves the aerodynamic efficiency of the airfoils with a different thickness within the operating range of angle of attack and shows the greatest improvement at a high angle of attacks. The effect of bio inspired nose design is maximum for low thickness airfoils. The porpoise nose design increases the acceleration and kinetic energy of flow over the upper surface, which results in a high lift and low drag compared to conventional NACA 0006 airfoil. Therefore, the thin airfoils maximum lift coefficient and operative range of angle of attack are increased with a reduction in drag value than the NACA airfoil, which is shown by red colour drag polar curves (Figure 4.20).

The drag polar curve shows, the NACA 0008 – Porpoise airfoils drag polar curve (red colour with cross markers) falls below the drag polar curve of NACA 0015 airfoil (green colour with diamond markers). It indicates that the NACA 0008 – Porpoise airfoil produces more or less the same lift as NACA 0015 airfoil but with less drag. It is inferred from the analysis that, instead of thick airfoils, thin airfoils with porpoise nose design can be used to get maximum aerodynamic efficiency.

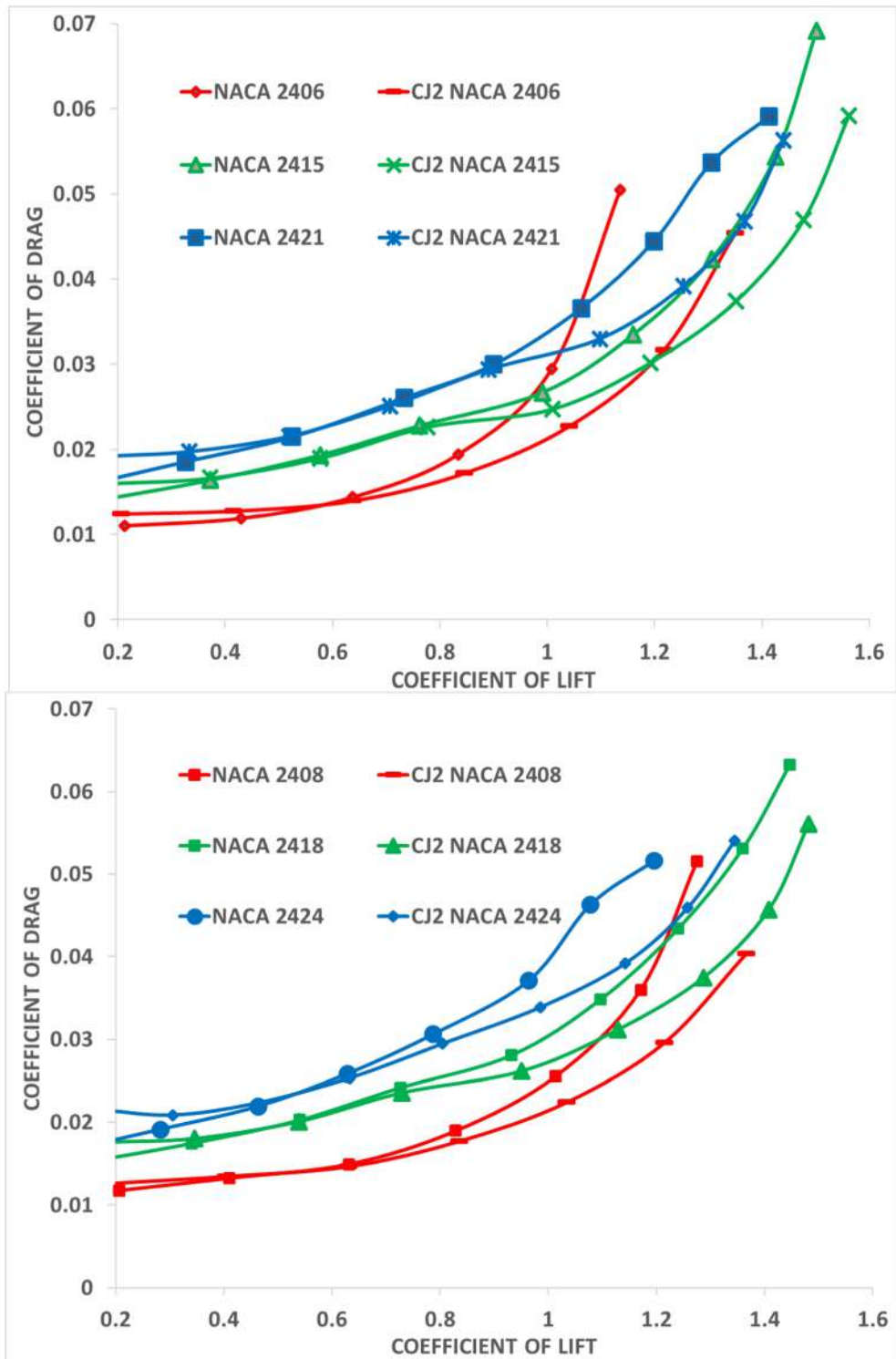


**Figure 4.20** Drag polar of NACA 4 series symmetric airfoils of different thickness (6%, 8%, 12%, 15%, 21% & 24% of chord) and its modified airfoils.





**Figure 4.21**  $C_l$  and  $C_d$  of NACA 4 series symmetric airfoils of different thickness (8%, 12%, 15%, 18%, 21% & 24% of chord) and its modified airfoils.



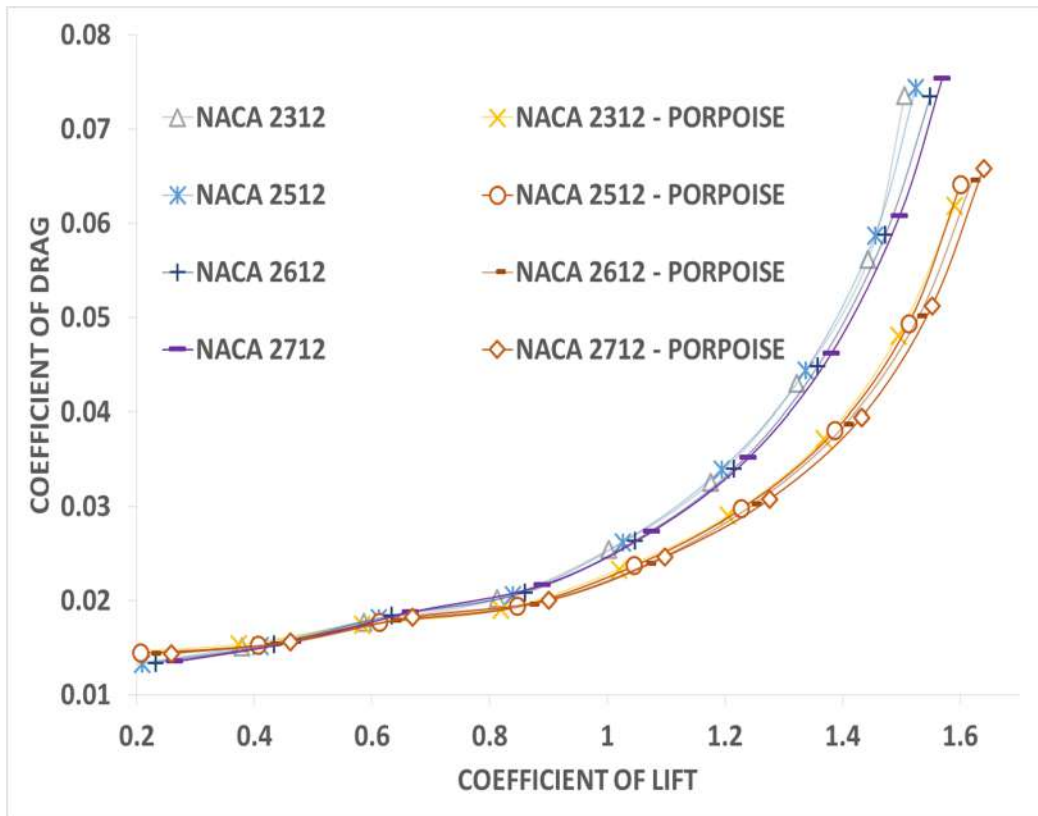
**Figure 4.22** Drag polar of NACA 4 series unsymmetrical airfoils of different thickness (6%, 8%, 15%, 18%, 21% & 24% of chord) and its modified airfoils.

Figure 4.22 shows the drag polar plot for NACA (24XX) airfoils with different thickness and its modified porpoise airfoils. It shows the same flow behaviour as NACA 4 series symmetrical airfoils, except an increase in maximum lift coefficient because of an increase in camber (4% of the chord). Compared to the conventional NACA 2415 airfoil, the NACA 2406 airfoil with porpoise nose design gives the less drag at low angles of attack, and shows more or less the same aerodynamic behaviour as NACA 2415 airfoil at high angles of attack. Similarly, the NACA 2408 shows better aerodynamic performance than NACA 2418.

Figure 4.23 shows the drag polar curve of NACA 2X12 series airfoils, with the location of the maximum camber, varies from 0.3c to 0.7c. The movement of maximum camber location towards the trailing edge shows more improvement in the lift at a low angle of attack than at a high angle of attack. Because of the movement of the camber location, the attached flow region extends on the airfoils upper surface at a low angle of attack.

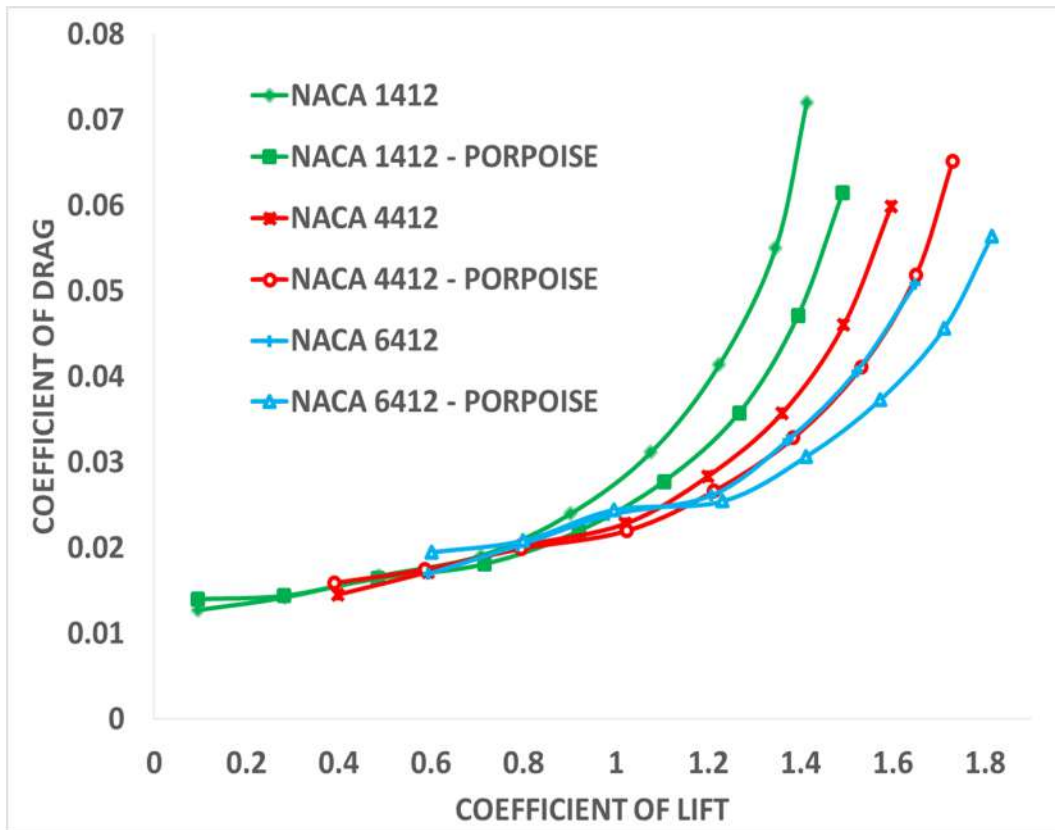
However, flow separates near the leading edge of the airfoil at a high angle of attack. Therefore, airfoils rear portion modification does not affect the flow behaviour. Moving the airfoils maximum camber location rearward with constant camber and thickness, have not affected the porpoise nose design and shows similar flow behaviour as NACA 2412 reference airfoil.

Figure 4.24 shows the drag polar curve of NACA X412 series airfoils, with maximum camber varies from 1% to 6% of chord. As the camber increases, the airfoil maximum lift coefficient and drag coefficient increases. Therefore, the curves are shifted to the right side in the plot. For these airfoils, porpoise nose design shows the more or less same improvement in aerodynamic efficiency (L/D) within the operative range of angle of attack.



**Figure 4.23** Drag polar of NACA 4 series unsymmetrical airfoils of different camber location (30%, 50%, 60%, & 70% of chord) and its modified airfoils.

However, at a low angle of attack, increasing the camber pushes the porpoise nose downwards and increases the depth of the nose cavity. Therefore, the stagnation pressure moves to the upper surface and reduces the pressure difference and lift of the airfoil. So, the porpoise nose design decreases the aerodynamic efficiency at a low angle of attack ( $<4^\circ$ ). It is also found that the addition of porpoise nose with NACA airfoil improves the aerodynamic performance and matched with other NACA airfoils. The NACA 4412 airfoil with porpoise nose shows similar aerodynamic performance as NACA 6412. Hence, the addition of porpoise nose can also be used instead of morphing of airfoil or wing to alter the aerodynamic behaviour of airfoil or wing upto certain extend.



**Figure 4.24** Drag polar of NACA 4 series airfoils of different camber and its modified airfoils.

#### 4.1.3 Effect of Bio inspired nose design on NACA 6 series airfoils

The drag polar curve of NACA 6 series airfoils (632XX) with different thickness and the respective porpoise nose airfoils is shown in Figure 4.25. It shows similar flow behaviour as on NACA 4 series unsymmetrical airfoils, except the reduction in drag force. And the NACA 63210 shows better aerodynamic performance than NACA 63221. Figure 4.26 shows the drag polar curve of NACA 6 series airfoils (63X15) with different design lift coefficient and its porpoise nose airfoils. Changing the design lift coefficient on NACA 6 series shows the similar flow phenomena as changing the maximum camber of NACA 4 series airfoils. And the NACA 63415 airfoil with porpoise nose shows similar aerodynamic performance as NACA 63615.

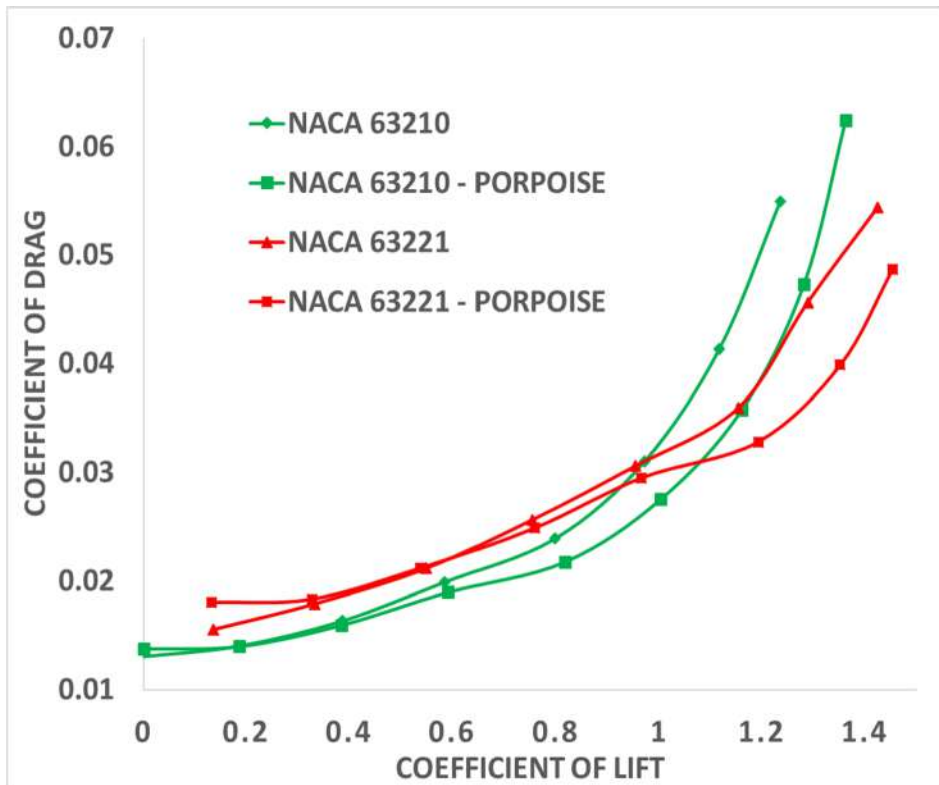


**Figure 4.25** Drag polar of NACA 6 series airfoils of different thickness

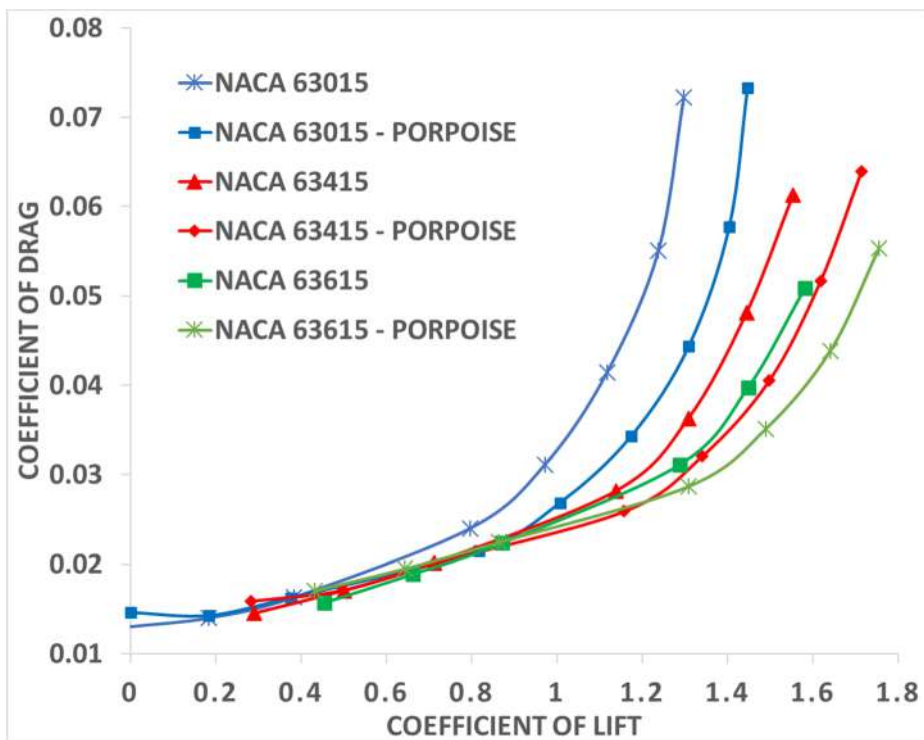


**Figure 4.26** Drag polar of NACA 6 series airfoils of different design lift coefficient

Drag polar Curves are shifted to right because of increase in lift coefficient with negligible increase in drag coefficient. It is inferred that, the increment in lift coefficient on NACA 63X15 series airfoils can be done by the addition of porpoise nose instead of changing the airfoil geometry (without increasing the drag).

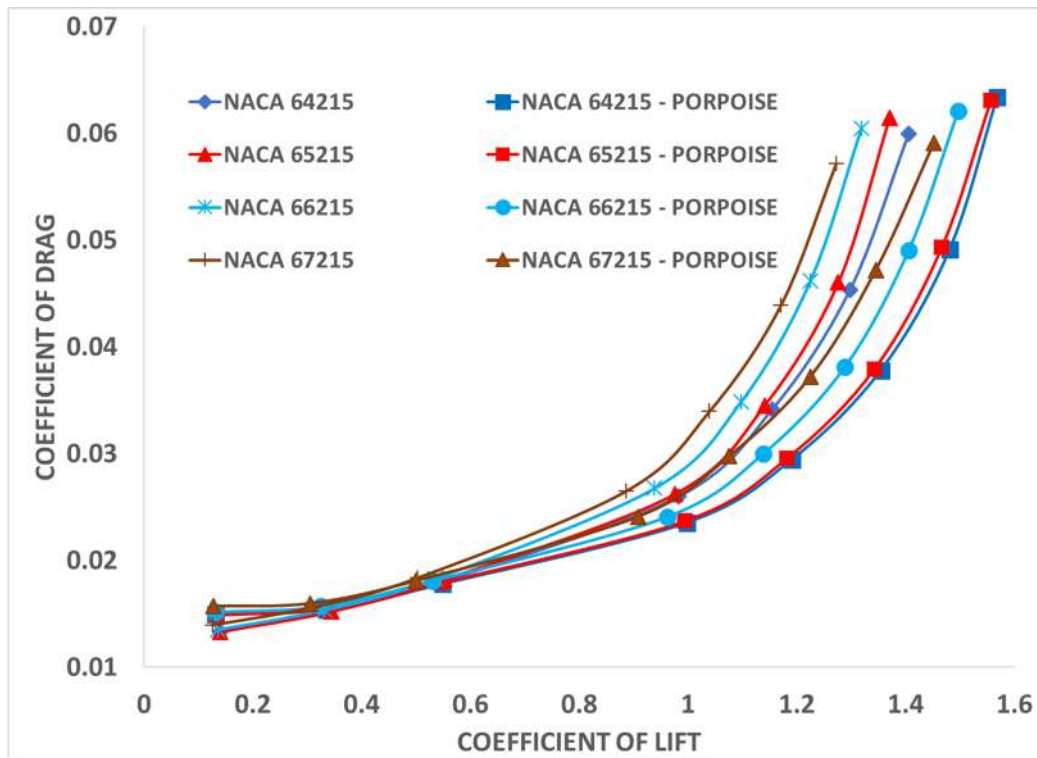


**Figure 4.27** Drag polar of NACA 6 series airfoils of different min pressure location

Figure 4.27 shows the drag polar curve of NACA 6 series airfoils (6X215) with different minimum pressure location and its porpoise airfoils. Moving the location of minimum pressure rearward on NACA 6 series shows the similar flow phenomena as changing the maximum camber location of NACA 4 series airfoils. Drag polar Curves are shifted to right side due to the increase in lift coefficient with a little increase in drag. As the location of minimum pressure moves rearward, acceleration of flow and lift is decreasing. Adding nose to the NACA 67215 airfoil (most rearward position of minimum pressure - 0.7c), improves its aerodynamic characteristics, and drag polar curve matches with the NACA 64215 airfoil (location of minimum pressure on 0.4c). It shows that, instead of changing the geometrical parameters of the airfoils, addition of

porpoise nose improves the aerodynamic characteristics of the conventional airfoils. It is inferred from the above analysis that the optimum bio-inspired nose design inspired by the cetacean family's porpoise marine mammal gives better results for all NACA 4 and 6 series airfoils irrespective of its geometry. Compared to wing morphing mechanisms that requires complex geometry modification, the addition of simple leading-edge device (porpoise nose) is more desirable to enhance the aerodynamic performance.

## **4.2 High subsonic speed analysis on NACA airfoils**

### **4.2.1 Optimum Bio-Inspired nose for NACA 2412 airfoil**

The computational analysis of NACA 2412 and optimised NACA airfoil (Porpoise) at Re. No. of  $3 \times 10^6$  for different angles of attack ( $0^\circ$ - $20^\circ$ ) has been done with very fine mesh elements. The comparison of coefficient of lift and drag for conventional NACA 2412 airfoil and Porpoise airfoil (Figure 4.28) shows increment in the aerodynamic efficiency (lift increases and drag decreases) for increasing angle of attack. It was found that the porpoise nose has no effect on flow behaviour at low angles of attack upto  $6^\circ$ , and it enhances the aerodynamic efficiency at high angles of attack ( $>6^\circ$ ). The maximum enhancement is achieved after stalling angle (66.5% and 54.4% increment in L/D at  $18^\circ$  and  $20^\circ$  angle of attack respectively) as shown in Figure 4.29.

The Figure 4.30 shows the flow properties of NACA 2412 and Porpoise airfoil at  $16^\circ$  angle of attack. It shows the extended low-pressure region on upper surface and reduced suction peak pressure for porpoise airfoil than base airfoil. The shear stress distribution shows the downstream movement of separation point from  $0.84c$  to  $0.88c$  (Figure. 4.31a), which is the reason for the less wake thickness and drag shown in turbulent intensity contour (Figure. 4.31b). The streamline pattern with velocity contour (Figure 4.31c) shows the reduced wake thickness and eddies behind the porpoise airfoil at  $18^\circ$  than the base airfoil, hence gives maximum increment in aerodynamic efficiency.



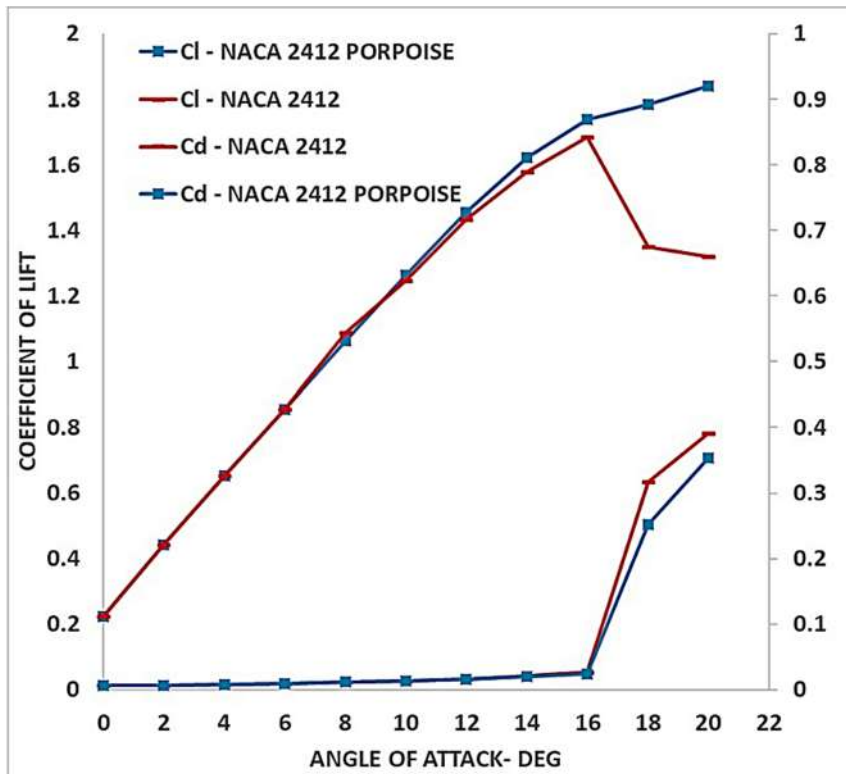


Figure 4.28 Force coefficients of NACA 2412 and Porpoise airfoil at  $Re. 3 \times 10^6$ .

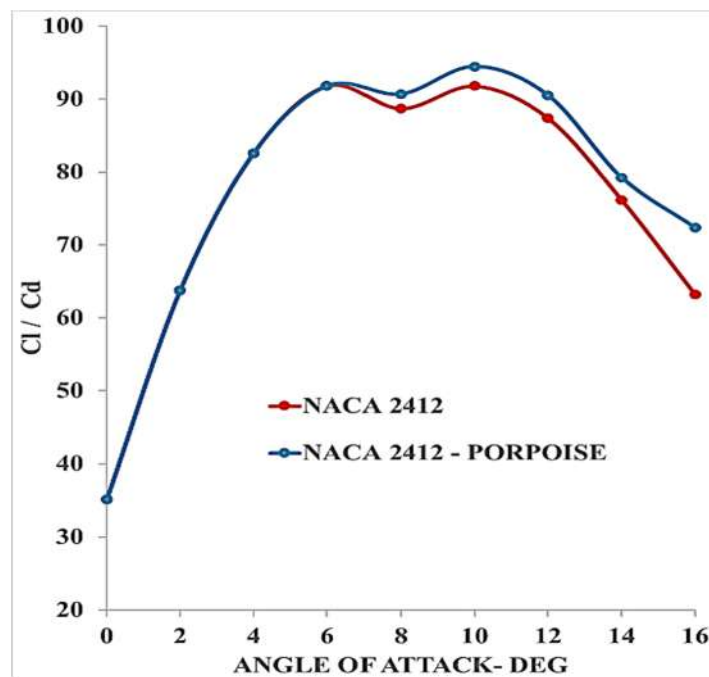
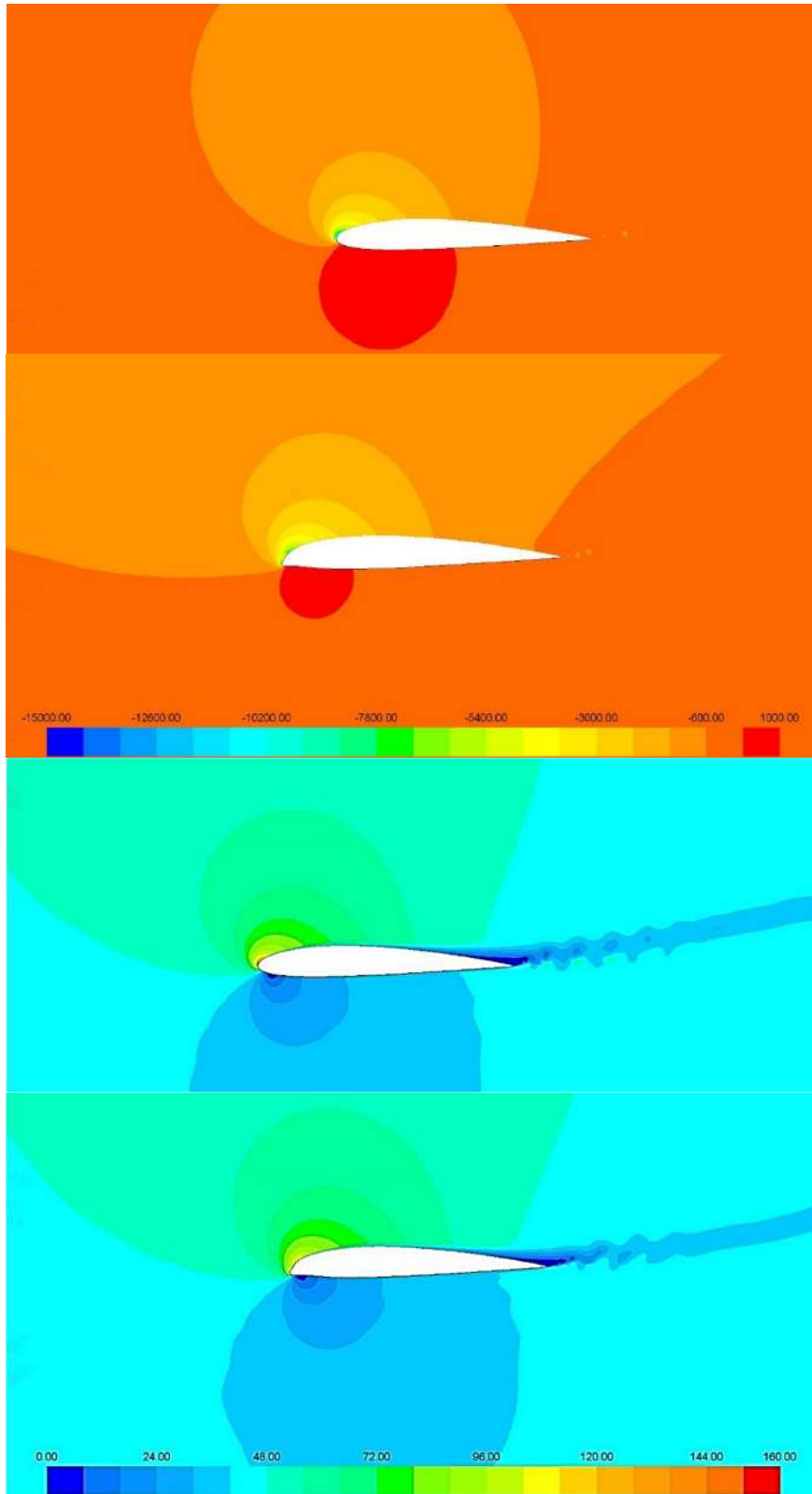
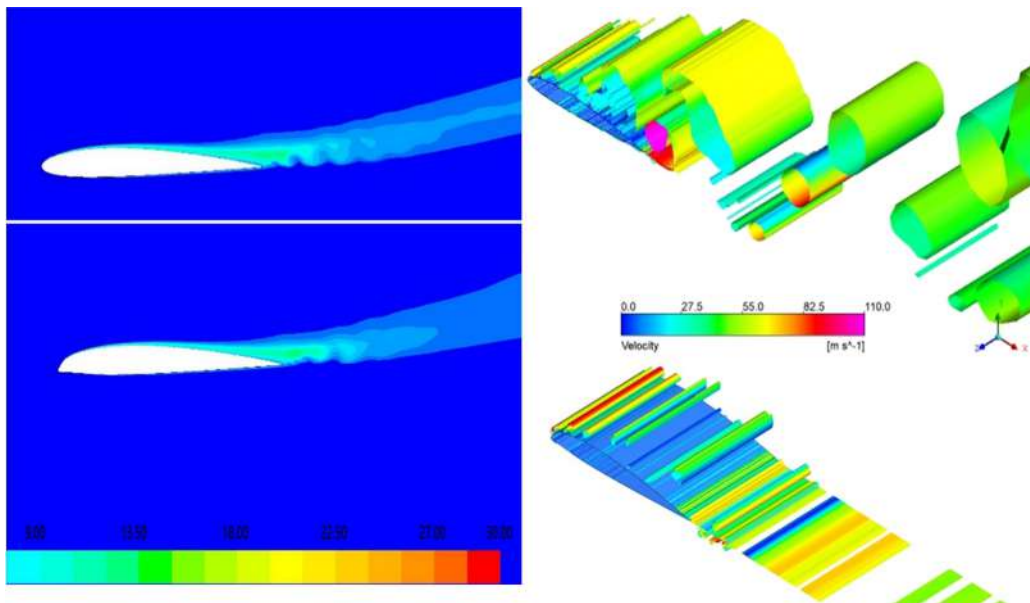
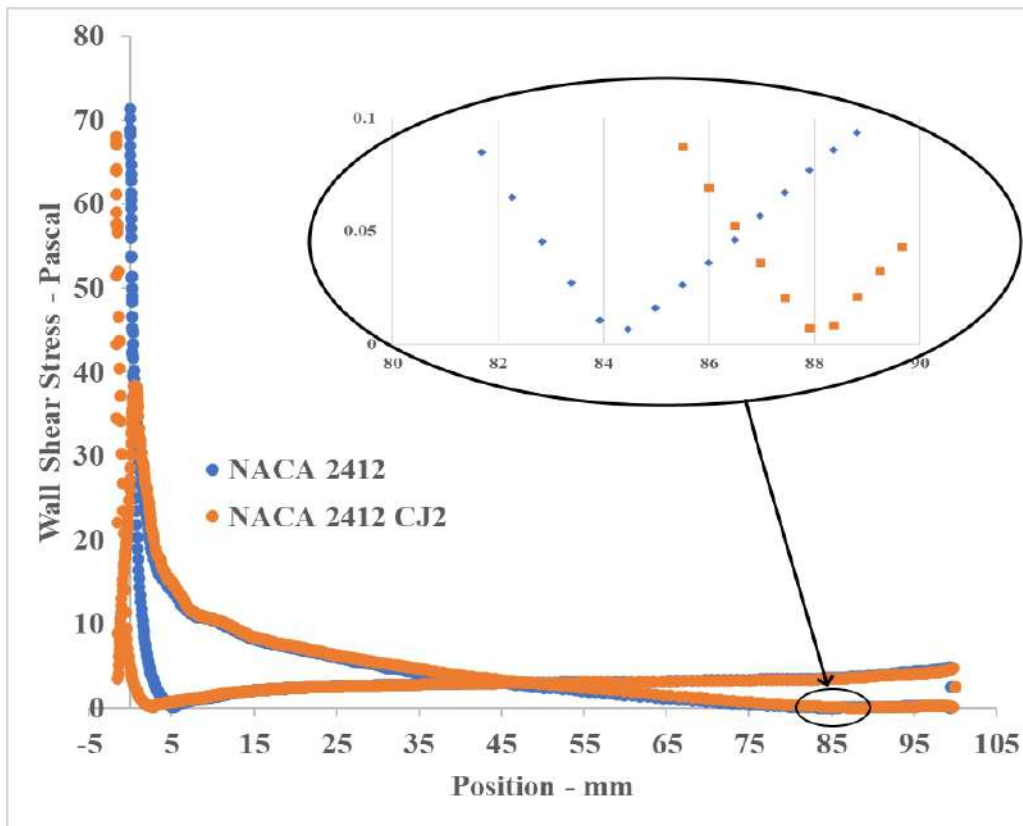


Figure 4.29  $C_l/C_d$  of NACA 2412 and Porpoise airfoil at  $Re. No. of 3 \times 10^6$ .



**Figure 4.30** a) Pressure and b) Velocity contours of airfoils at  $16^\circ$ .



**Figure 4.31 a)** Shear stress distribution **b)** turbulent intensity of NACA 2412 and Porpoise airfoils at 16°, **c)** Velocity distribution(Q-Criterion) of NACA and Porpoise at 18°.

#### 4.2.2 Optimum Bio-Inspired nose for NACA 66215 airfoil

The computational analysis of NACA 66215 and modified porpoise airfoil at Re. No. of  $9 \times 10^6$  for different angles of attack ( $3^\circ$ - $18^\circ$ ) has been done. The Figure 4.32 shows the increase in lift and decrease in drag for porpoise nose airfoil within the operating range of angle of attack without affecting the pitching moment significantly. As the angle of attack increases, the flow becomes unsteady. So, force coefficient fluctuates from max to min values. Hence, the mean force coefficient is taken for the plot. As a result, plot shows the less lift coefficient value after 9 deg angle of attack for conventional NACA 66215 airfoil. The increment in  $C_l/C_d$  is 1.44%, 77.7%, and 66.9% for  $6^\circ$ ,  $12^\circ$  &  $18^\circ$  angles respectively. As the Reynolds number increases, the effectiveness of porpoise nose also increases and hence, the increment in  $C_l/C_d$  is higher.

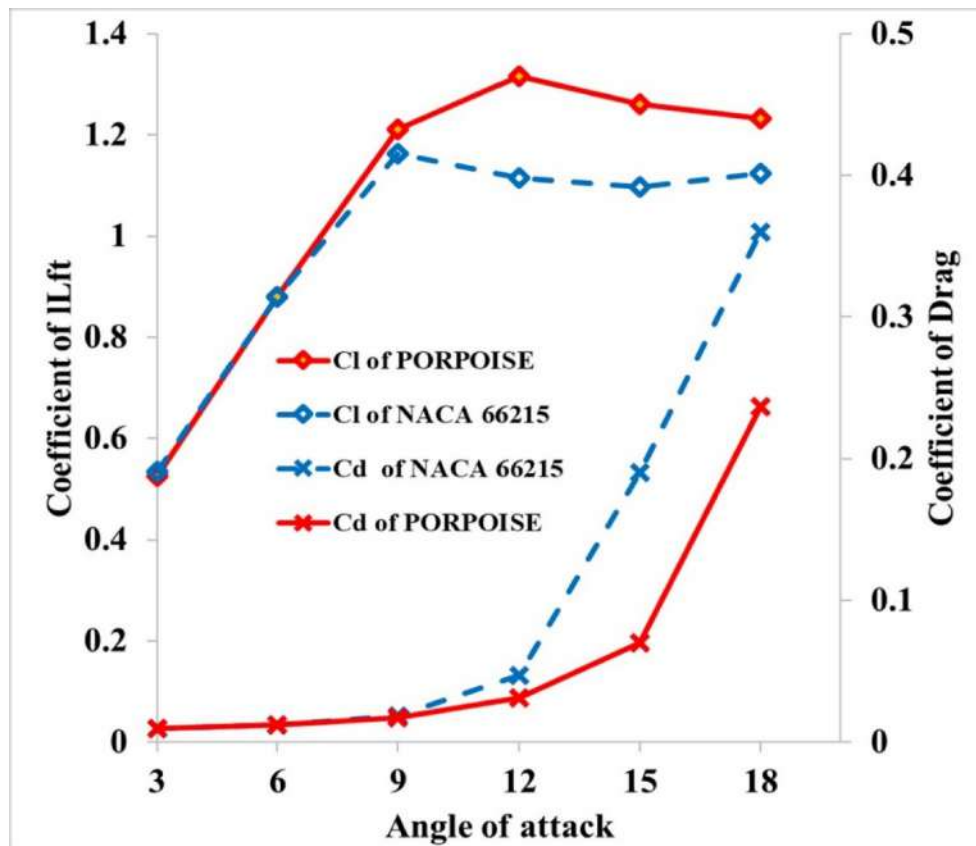
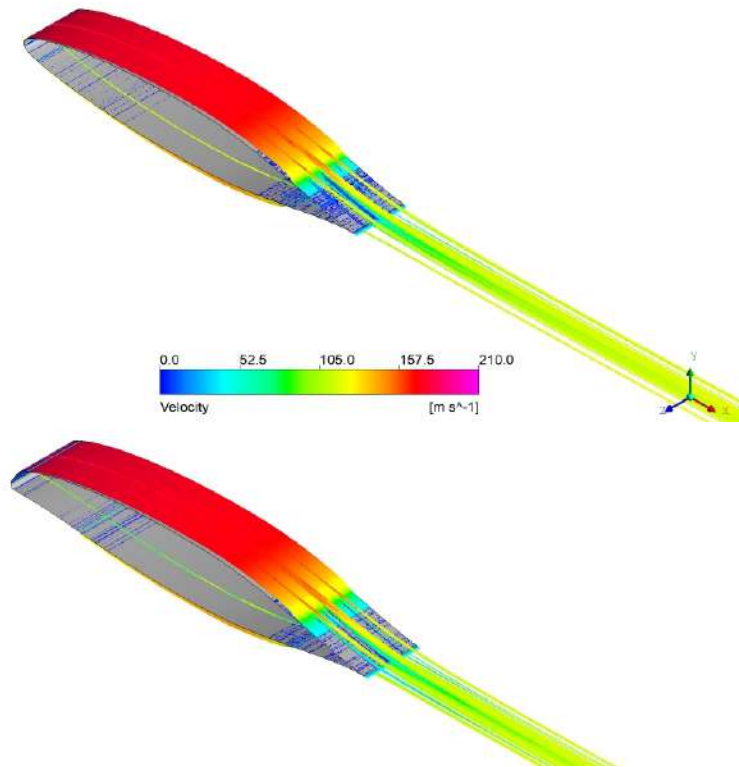
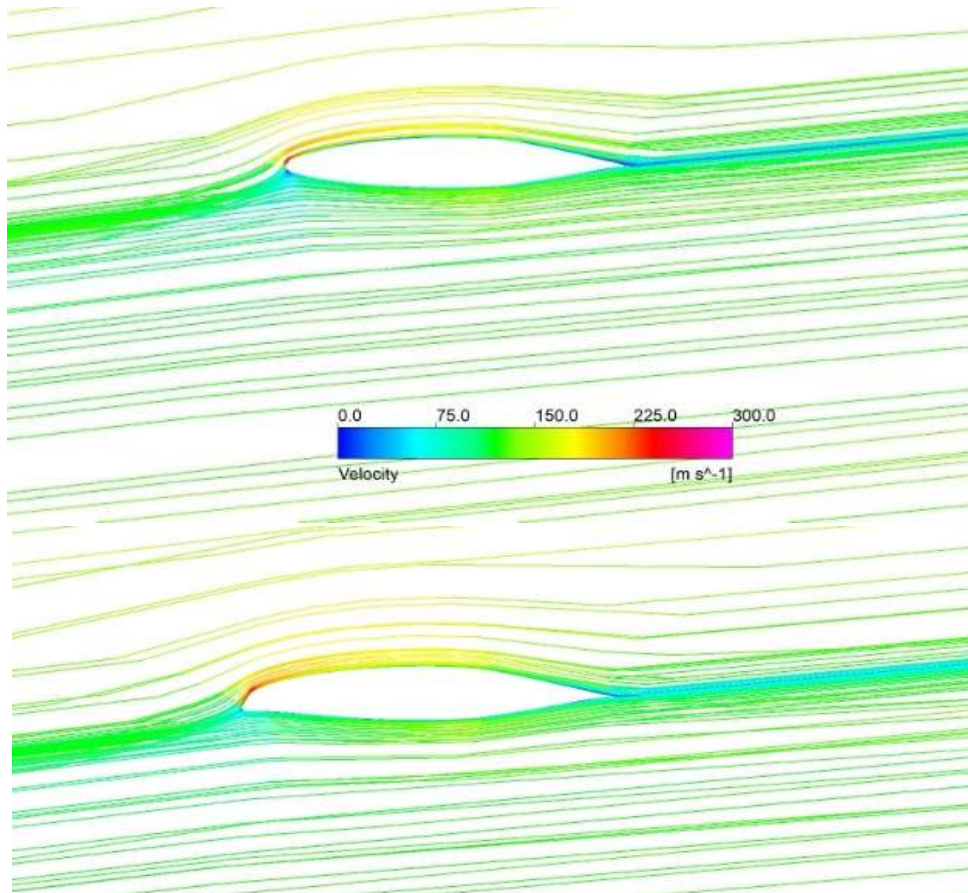


Figure 4.32 Lift & drag coefficient of NACA and porpoise airfoils at Re.  $9 \times 10^6$ .



**Figure 4.33** Streamline pattern with velocity distribution of airfoils at  $3^\circ$ .

The Streamline pattern and velocity distribution of both NACA 66215 and porpoise airfoil at low angle of attack  $3^\circ$  (Figure 4.33) show that, both airfoils give similar flow patterns and show same force coefficient values (Figure. 4.32). The Figure 4.34 shows the streamline pattern with velocity distribution over a NACA and porpoise airfoils at  $6^\circ$  angle. The extended yellow region on the porpoise airfoil shows an increase in flow acceleration and extended low-pressure region on the upper surface but almost similar type of trailing edge flow behaviour as NACA 66215. There is no noticeable difference in turbulent kinetic energy distribution of porpoise airfoil than base airfoil( Fig. 3.5a). As a result of better acceleration, the shear stress distribution of porpoise airfoil shows the little upward shift in the curve than NACA airfoil with the little peaks (orange colour line with circular markers) near the leading edge of porpoise airfoil as shown in Figure 4.35b. Hence porpoise airfoil shows little improvement in aerodynamic efficiency by 1.44%.



**Figure 4.34** Streamline pattern with velocity distribution of airfoils at  $6^\circ$ .

For high angle of attack i.e., at  $12^\circ$  (Fig. 4.37), porpoise airfoil shows multiple acceleration on the nose profile and extended low pressure region on the upper surface (increases the lift), and reduced wake region (decreases the drag). The shear stress distribution (orange colour line with circular markers) shows higher upward shift in curve near leading edge and downstream shift (from 70% of chord to 77% of chord) of zero shear stress point (separation point) near the trailing edge for the porpoise airfoil than base airfoil (Fig. 4.36). It also shows the less turbulent kinetic energy for porpoise airfoil than base airfoil. After stalling angle of attack ( $18^\circ$ ), porpoise nose shows better flow acceleration and flow attachment on the flat face of porpoise nose. This suppresses the large separated region on the airfoil (Fig. 4.38). Hence it increases the low-pressure region and lift, and reduces the wake region and drag. However, NACA 66215 shows flow separation from the nose of the airfoil with larger wake region.

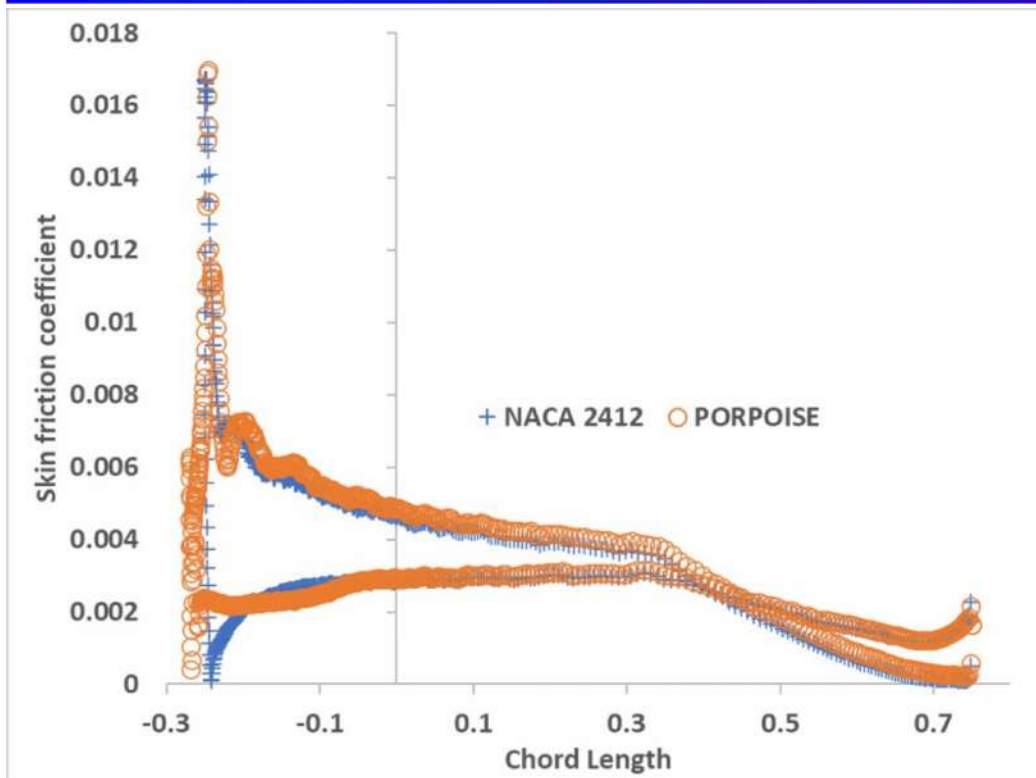
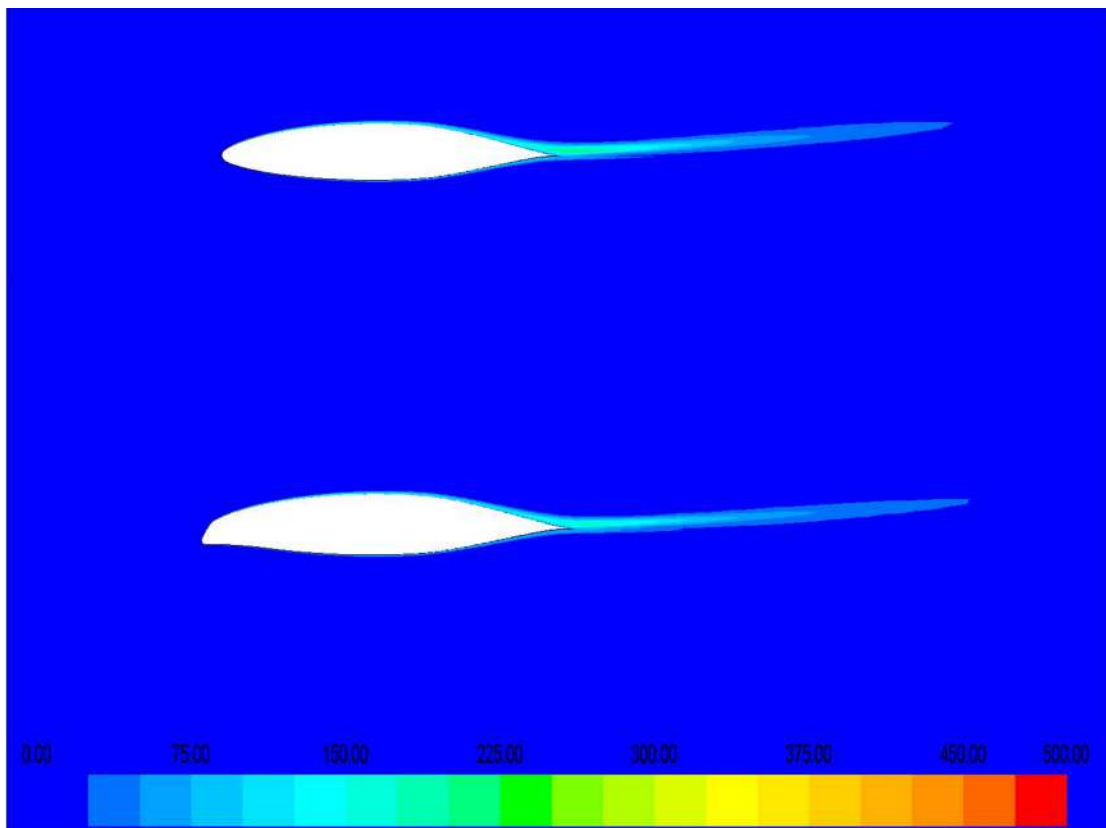


**Figure 4.35** a) Turbulent kinetic energy and b) Shear stress distribution of NACA 2412 and Porpoise airfoils at 6°.

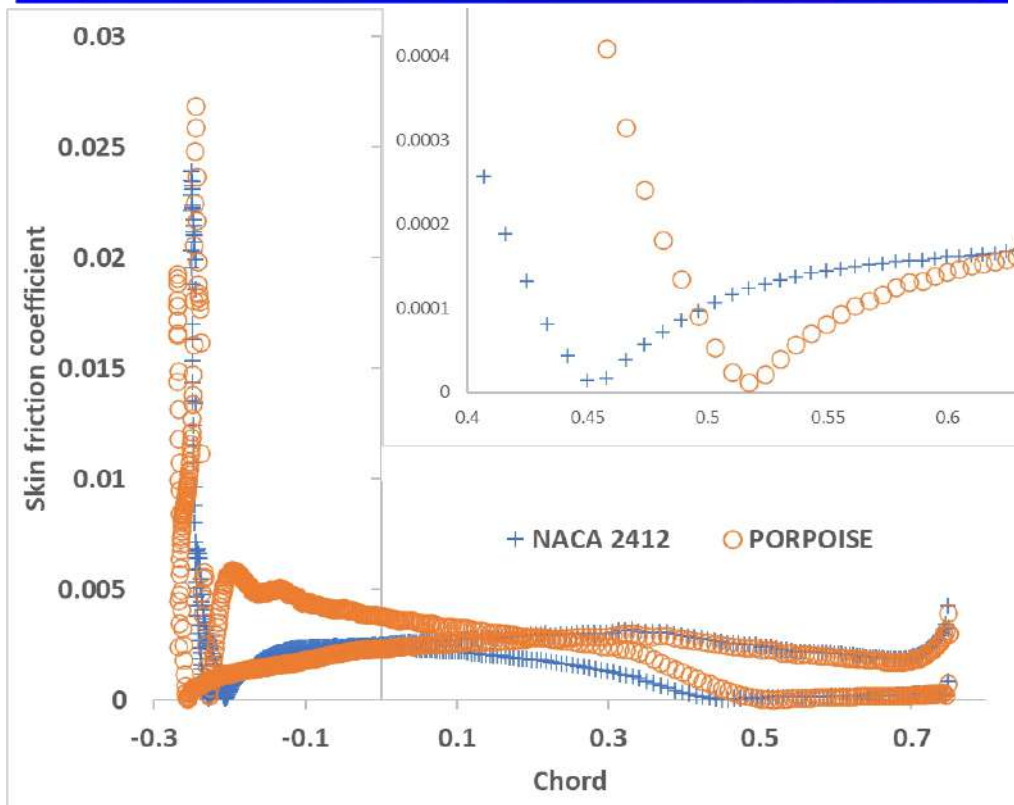
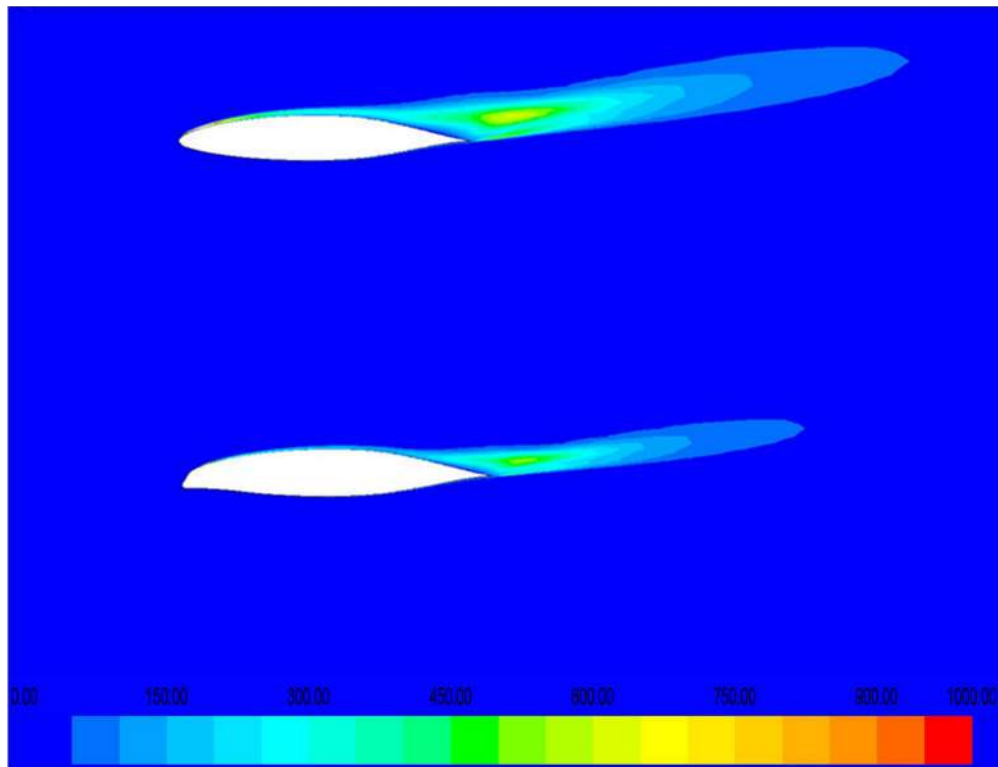


**Figure 4.36** a) Turbulent kinetic energy and b) Shear stress distribution of NACA 2412 and Porpoise airfoils at 12°.



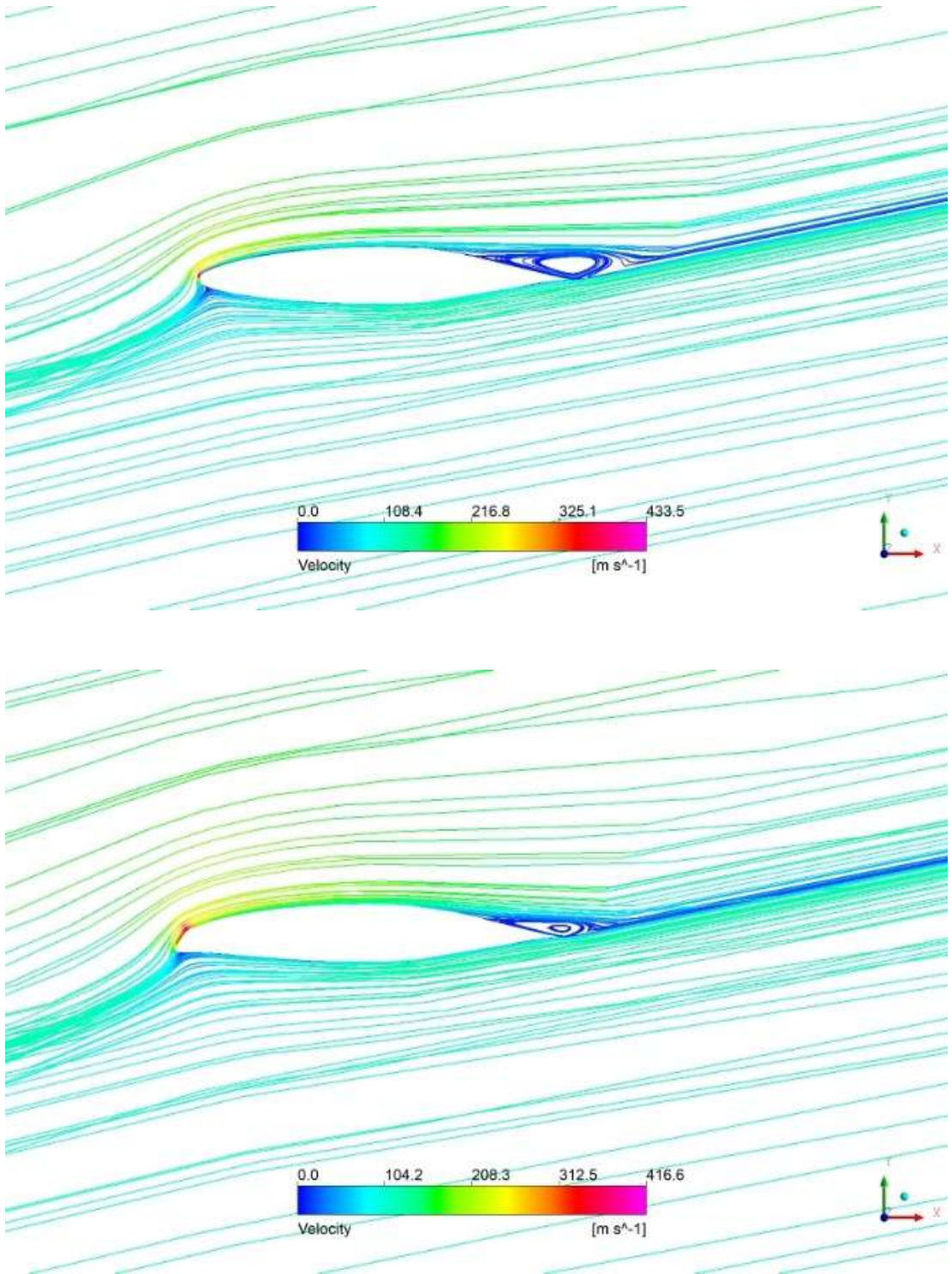


**Figure 4.37** Streamline pattern with velocity distribution of airfoils at 12°.

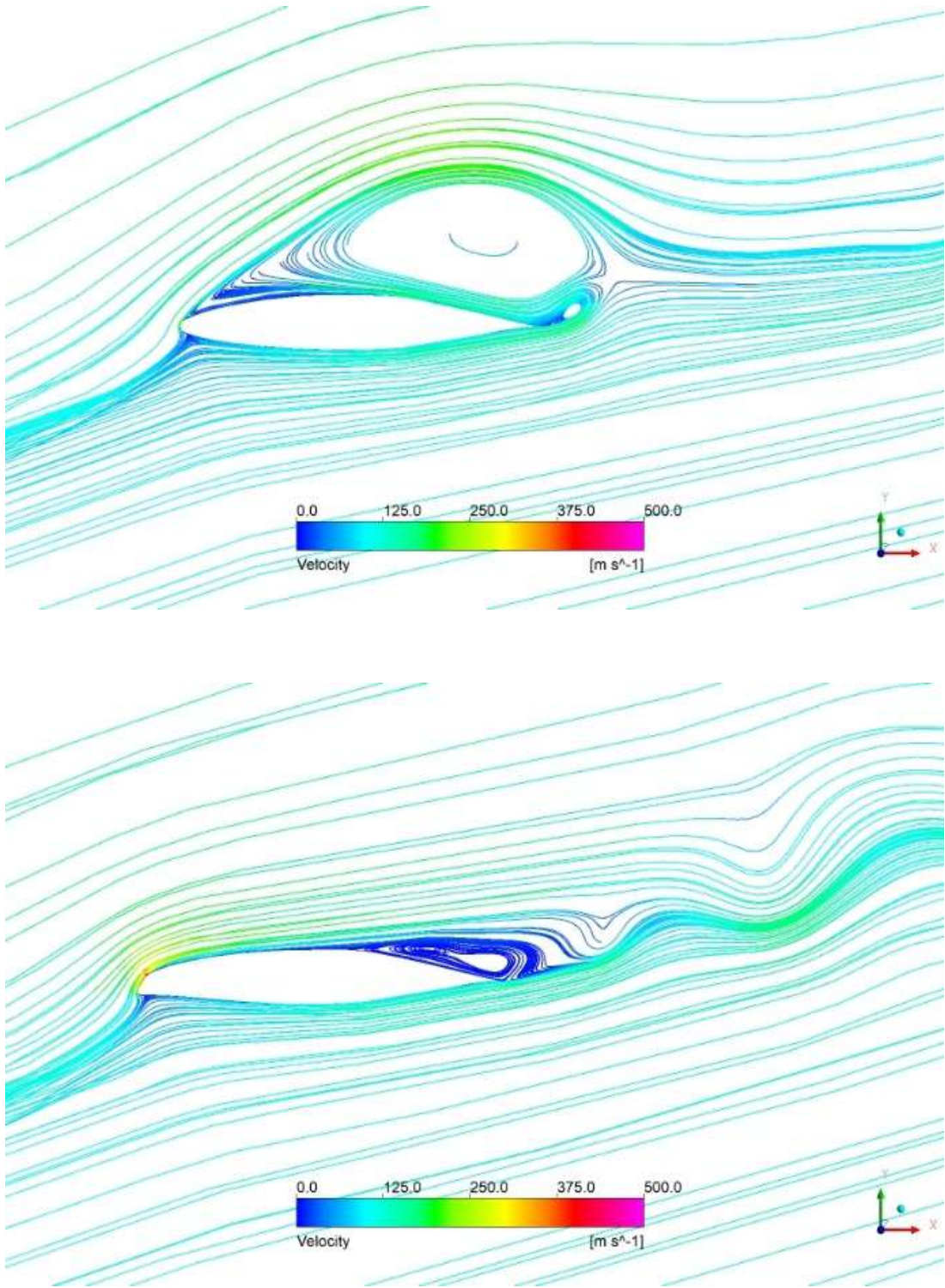


**Figure 4.38** Streamline pattern with velocity distribution of airfoils at 18°.

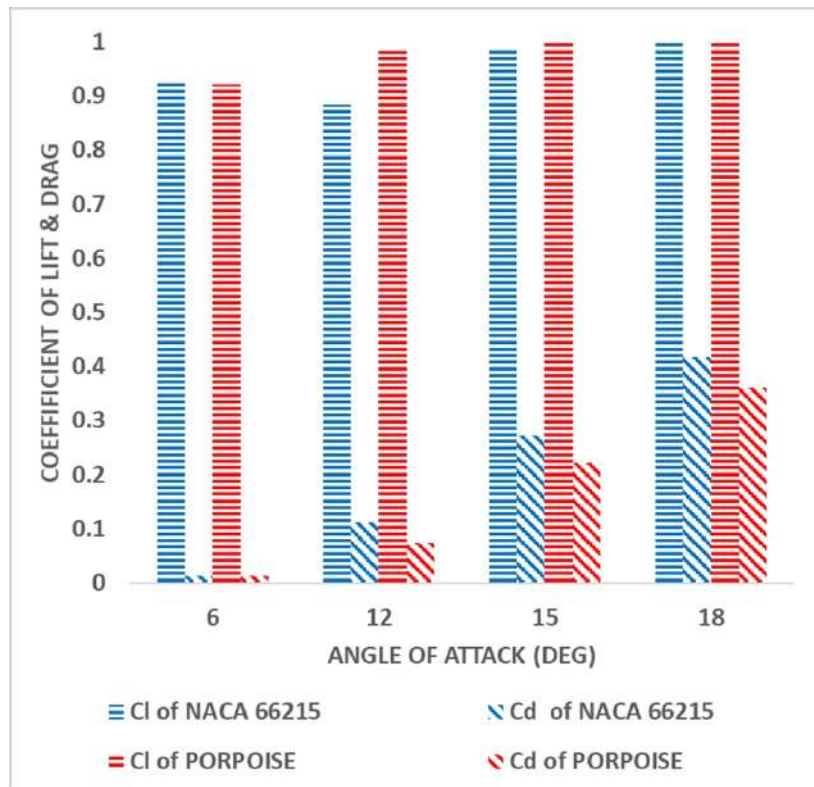


**Figure 4.39** Lift and drag coefficient of airfoils at Re.  $12 \times 10^6$ .

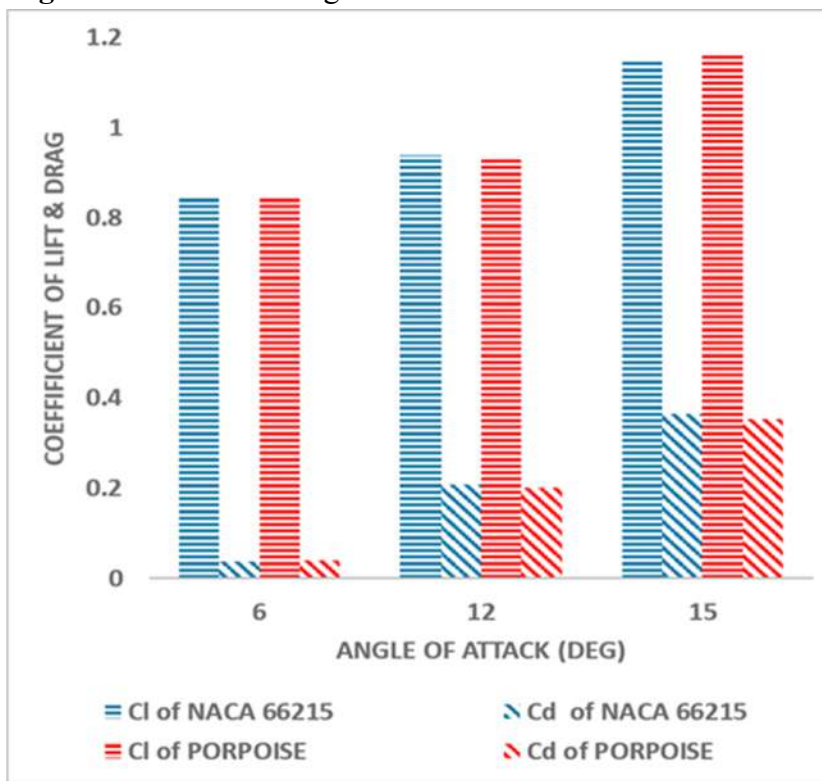


**Figure 4.40** Lift and drag coefficient of airfoils at  $6^\circ, 12^\circ$  &  $15^\circ$  and Re.  $17 \times 10^6$ .

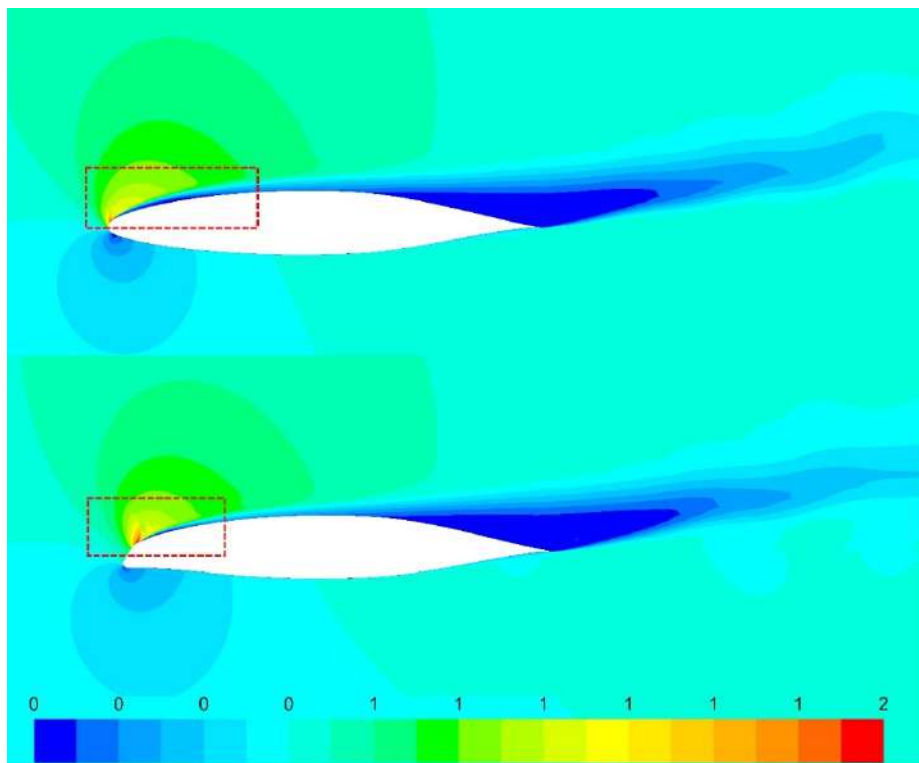
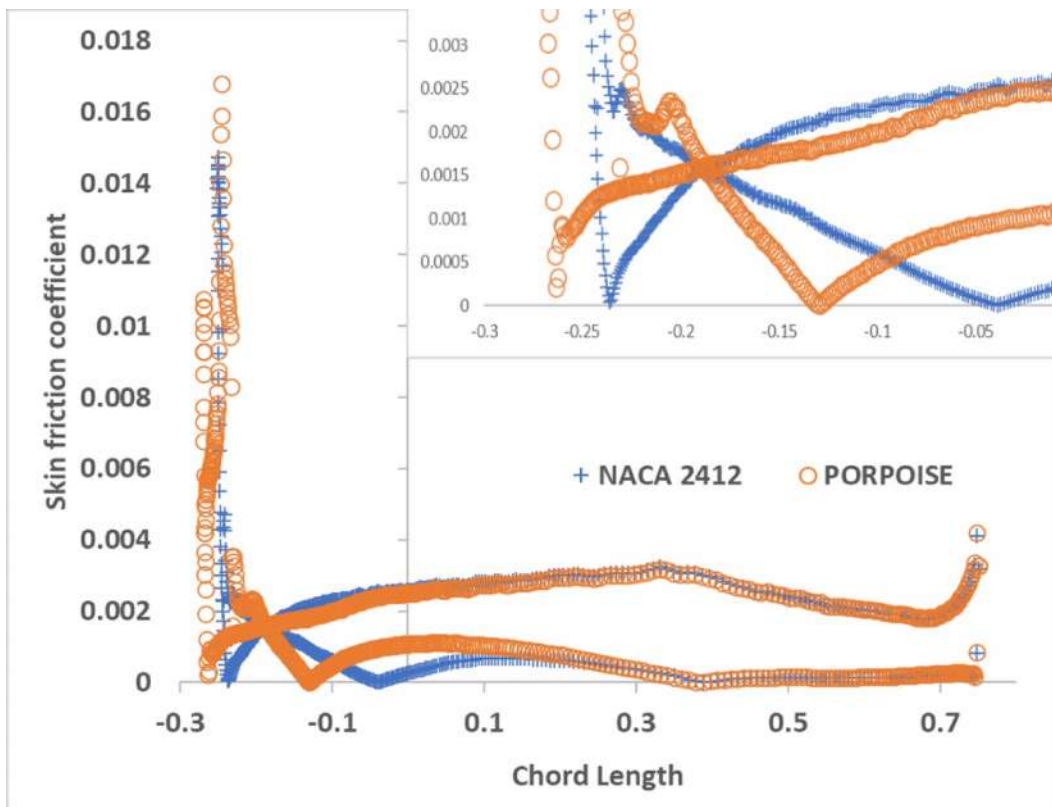


**Figure 4.41** a) Shear stress distribution and b) Velocity contour of airfoils at  $12^\circ$  and  $Re. 12 \times 10^6$ .

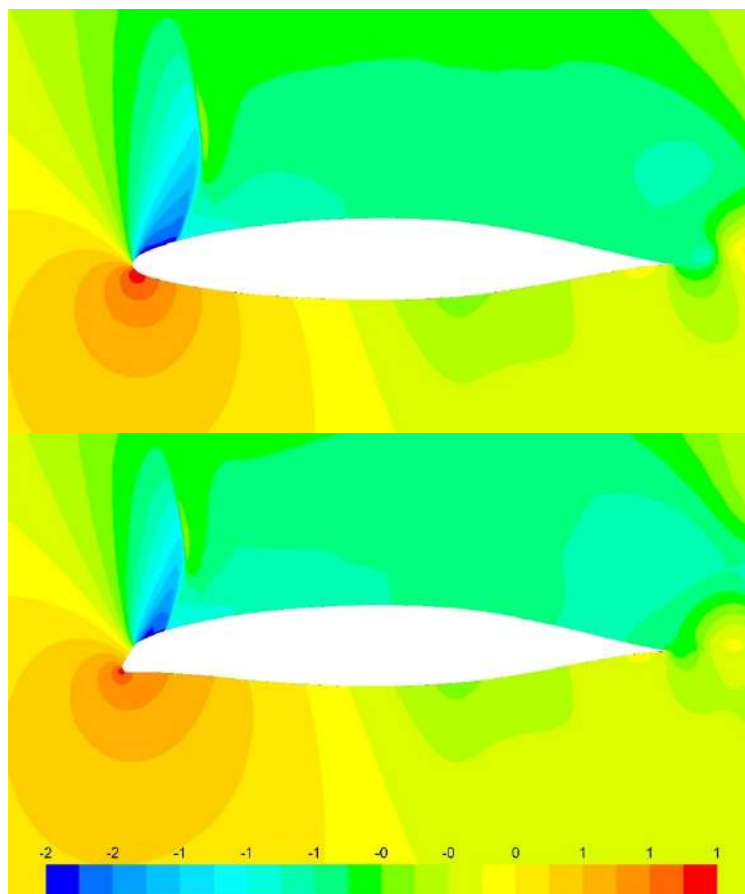
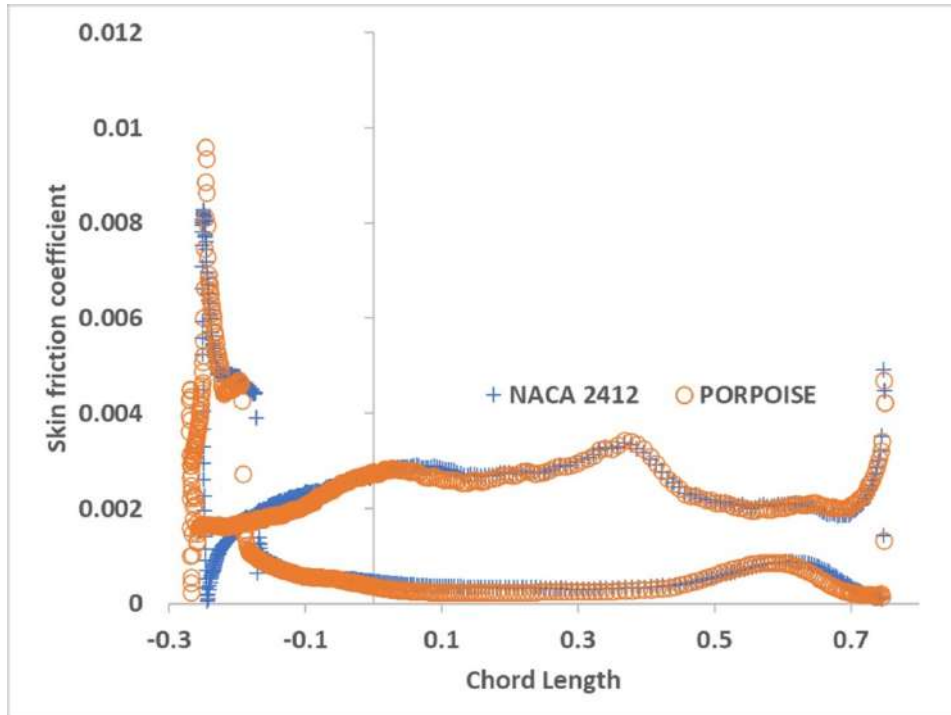


**Figure 4.42** a) Shear stress distribution and b) Velocity contour of airfoils at  $12^\circ$  and  $Re. 17 \times 10^6$ .

Further, the computational analysis of NACA 66215 and porpoise airfoil has been done for higher Reynolds number such as  $12 \times 10^6$  and  $17 \times 10^6$  for few angles of attack ( $6^\circ$ - $18^\circ$ ). These Reynolds number are corresponding to the cruising speed of the aircraft. At cruising phase, as the aircraft flies at high speed, the low angle of attack (Approx. 1-6 deg) is to be maintained to avoid excess drag. To understand the high-speed effect at low and high angles of attack,  $6^\circ$ - $18^\circ$  have been considered for the analysis, the Figure 4.39 shows that, for the angle  $6^\circ$ , lift and drag coefficients are negligible amount of variation in lift and drag. And for  $12^\circ$  it shows the increase in lift and decrease in drag for porpoise nose airfoil. The Figure 4.41 shows the shear stress and velocity distribution of both airfoils at  $12^\circ$ . Both airfoils show the pocket of supersonic flow region near the leading edge, but NACA 66215 shows the larger leading-edge separation bubble than the Porpoise airfoil which is highlighted by the dash lined rectangular box. The smaller leading-edge separation bubble increases the attached flow region on the porpoise airfoil than NACA airfoil. Both the airfoils show the similar flow behaviour near the trailing edge. The smaller separation bubble is clearly visible in the shear stress distribution. For the porpoise airfoil (orange colour line with circular markers), the reattachment point is shifted upstream than the NACA airfoil.

For increase in Reynolds number ( $17 \times 10^6$ ), the Figure 4.40 shows the lift and drag coefficient of both NACA and porpoise airfoils at  $6^\circ$ - $12^\circ$ . At  $6^\circ$  angle of attack, there is a noticeable decrease in lift with increase in drag for porpoise airfoil than NACA airfoil. As the speed increases, the flow acceleration over the porpoise airfoil increases, hence it forms the supersonic region and followed by the shock wave. This affects the flow over the porpoise airfoil and reduce the aerodynamic efficiency at low angle. At  $12^\circ$  angle (Figure 4.42), both airfoils develop the supersonic region and shock wave depending upon their nose shapes. The porpoise airfoil shows the similar flow pattern as NACA airfoil and very little increment in aerodynamic efficiency than NACA 66215. Hence at high subsonic speed, due to the shock wave formation on the airfoil, the porpoise nose has no beneficial effect on flow separation control.

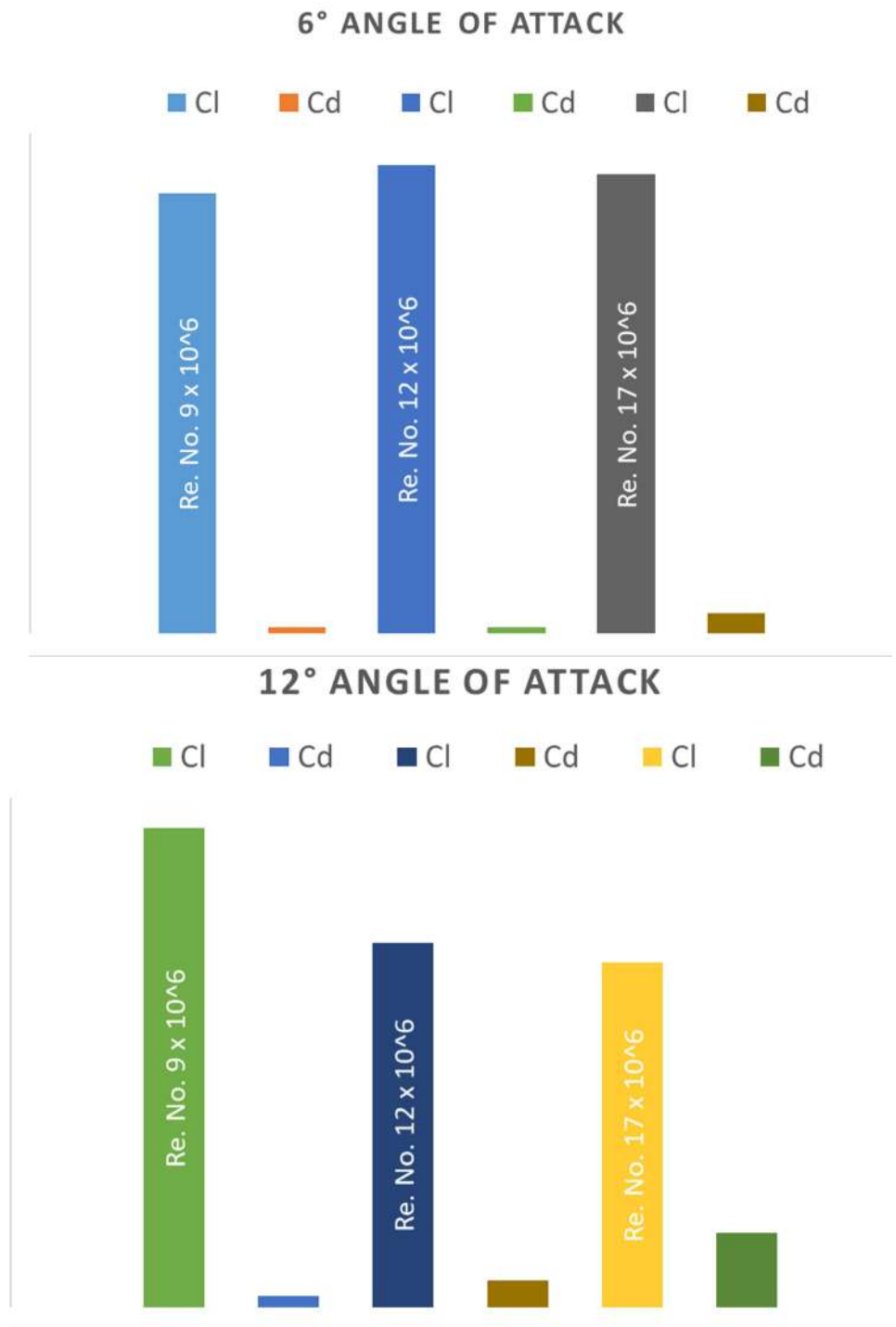


**Figure 4.43**  $C_l$  and  $C_d$  values of porpoise airfoil at a) 6° and b) 12° for different Reynolds number.

From the above analysis on NACA 66215 at different speeds such as Mach number 0.38, 0.5, and 0.7. it was observed that the porpoise nose is effective for Mach number less than 0.7, which is the cruising speed of most of the

medium size commercial aircrafts. Hence it can be effectively used on UAV's, propeller aircrafts, turbo-prop aircrafts and short-range jet transport aircrafts (Figure 4.44). And shows no beneficial effect for  $M=0.7$ , which the cruising speed on most of the larger commercial aircrafts with gas turbine engines. The Figure 4.43 shows the increment in drag for increase in speed for porpoise airfoil, due to the shock wave formation and additional wave drag. For  $M=0.7$ , porpoise nose adversely affects the aerodynamic efficiency of the airfoil. Hence its concluded that, this porpoise design has to be optimised further for high cruising speeds( $M=0.7$ ) or the nose profile has to be employed only during take-off and landing by retracting or morphing techniques. In the future scope, the porpoise nose can be analysed with a propeller slipstream effect, so that it can be effectively used in propeller and turboprop engine aircrafts.

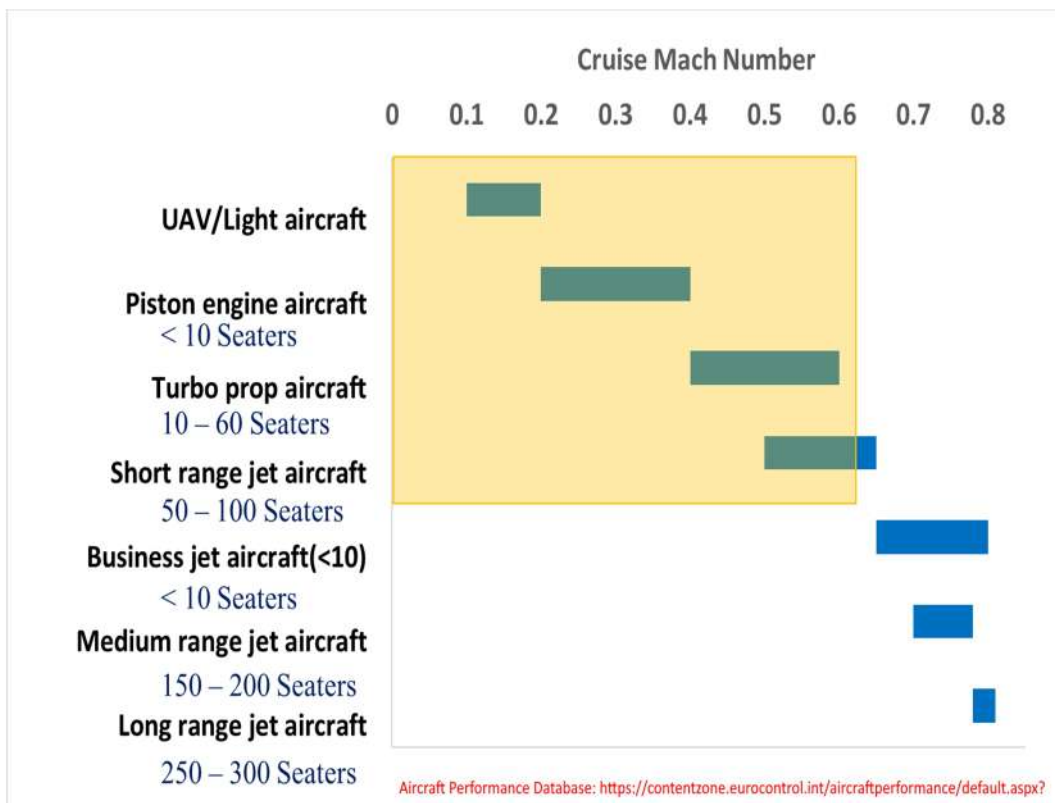


**Figure 4.44** Classification of aircrafts based on cruising Mach number



### 4.3 Optimum Bio-Inspired nose for a finite wing

The three-dimensional analysis has been done using a finite wing with NACA 2412 at angles of  $6^\circ$ ,  $12^\circ$ , &  $18^\circ$  for Re No. of  $3 \times 10^6$  to find the effectiveness of porpoise nose on flow control. Due to the high demanding of computing resources required for the 3D simulation, only few angles of attack were considered. Porpoise nose with full spanwise length was considered for simulation. The comparison of 2D and 3D flow simulation results (Figure 4.45) show the similar type of flow pattern and force behaviour for the porpoise nose design at different angles of attack. At low angles ( $<6^\circ$ ), the porpoise nose shows no or little changes in the aerodynamics efficiency for both 2D airfoil and 3D finite wing. However, due to the tip vortices, lift decreases and drag increases for 3D wing than the 2D airfoil at higher angles ( $>6^\circ$ ). After the stalling angle, the effectiveness of porpoise nose on flow separation control is drastically improved. The enhancement in aerodynamic efficiency reaches the maximum by 66.5% and 42% for 2D airfoil and 3D finite wing at  $18^\circ$  angle of attack respectively (Figure 4.46a). The increased acceleration of flow over the porpoise nose increases the kinetic energy of the flow on upper surface. This makes the flow attached over a larger area on the wing with delayed the flow separation, hence increase the  $C_l/C_d$  than base wing at high angles (Figure 4.46b).

The reduction in spanwise length of porpoise nose will help reducing the weight of overall wing and mounting complexity. Hence different spanwise length porpoise nose wing configurations have been analysed further to find an optimum spanwise length and position of porpoise nose for a finite wing (with NACA 2412) at angles of  $6^\circ$ ,  $12^\circ$ , &  $18^\circ$  and Re No. of  $3 \times 10^6$ . The finite wing with porpoise nose of different spanwise length (such as  $1b$ ,  $0.5b$ , and  $0.25b$ ) and location (such as root, mid portion, and tip of finite wing) were analysed and observed as mentioned below.

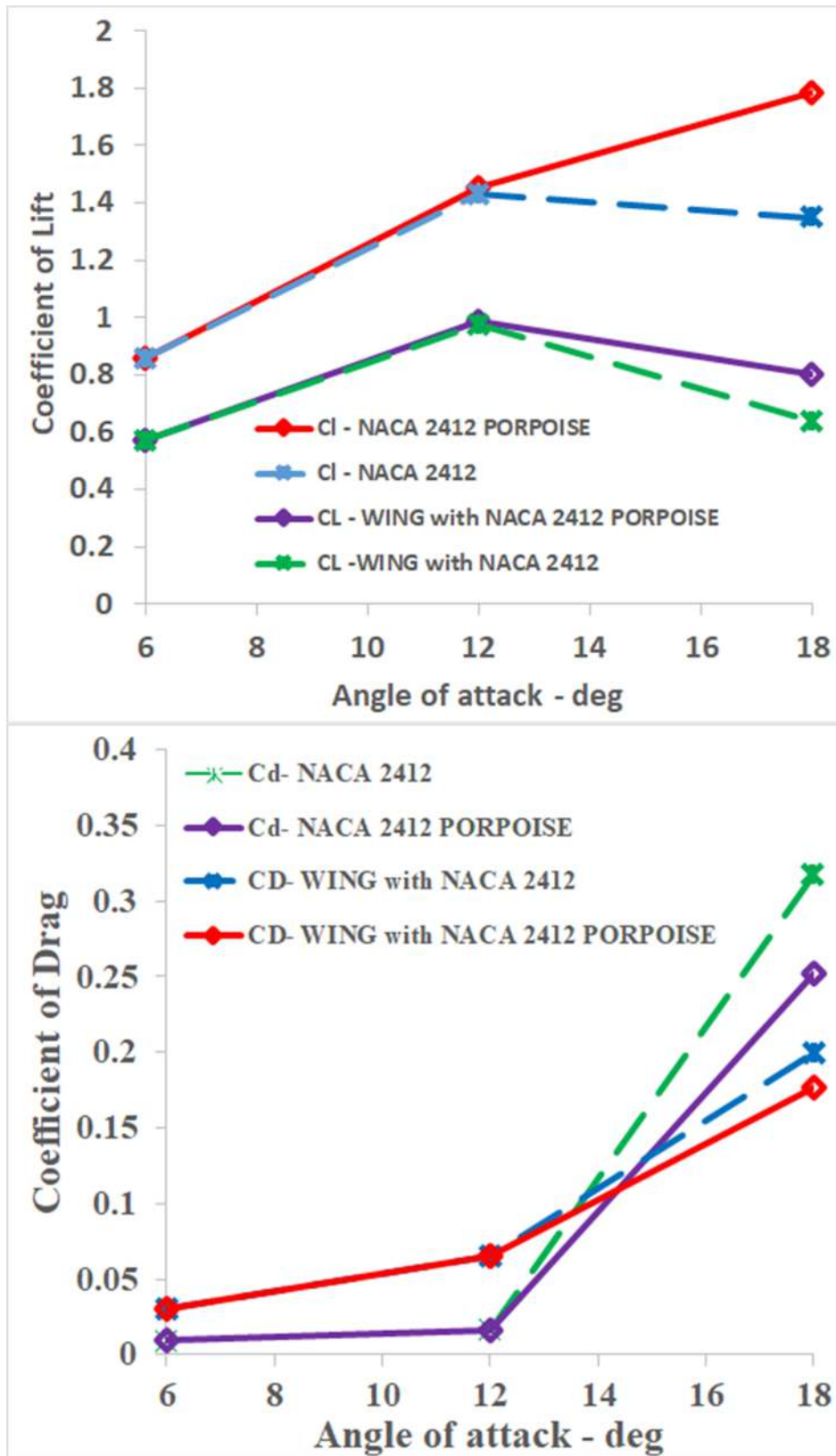
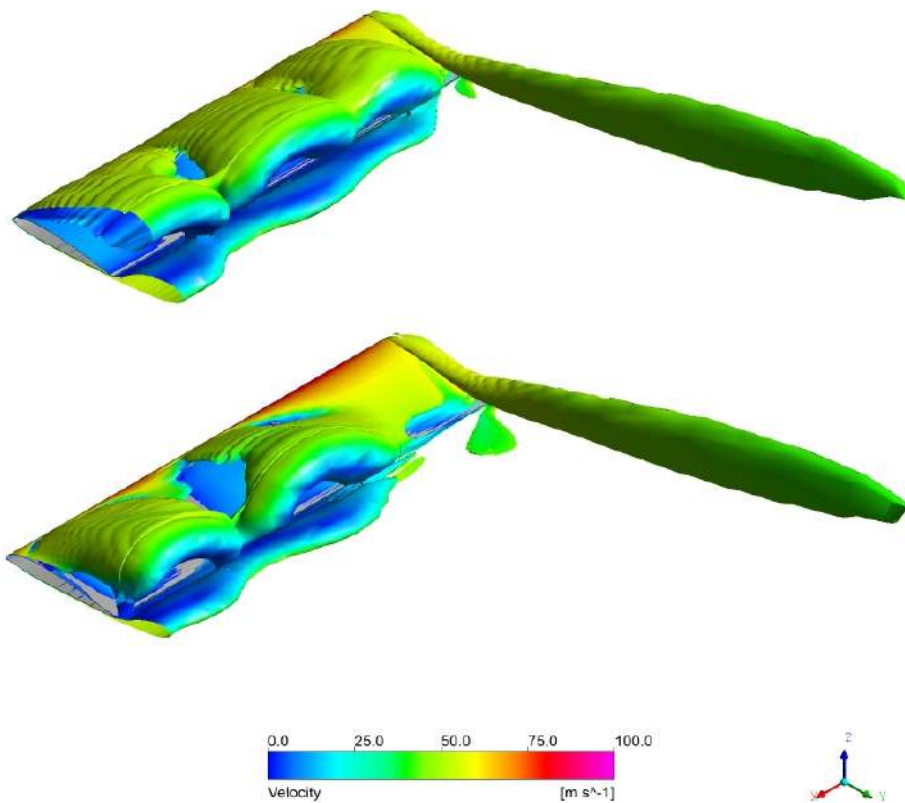
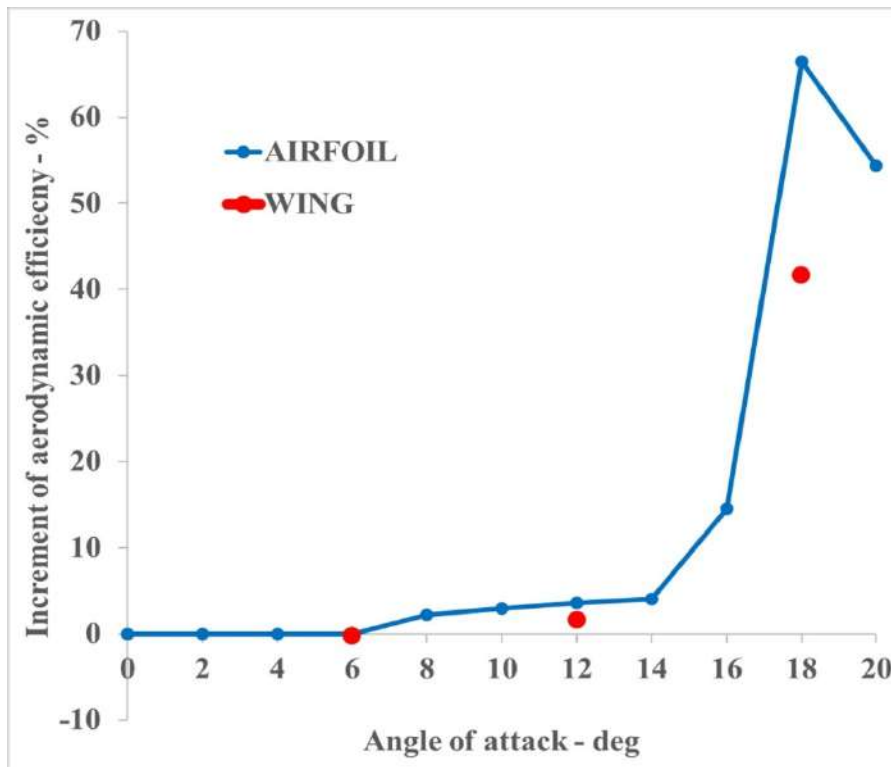
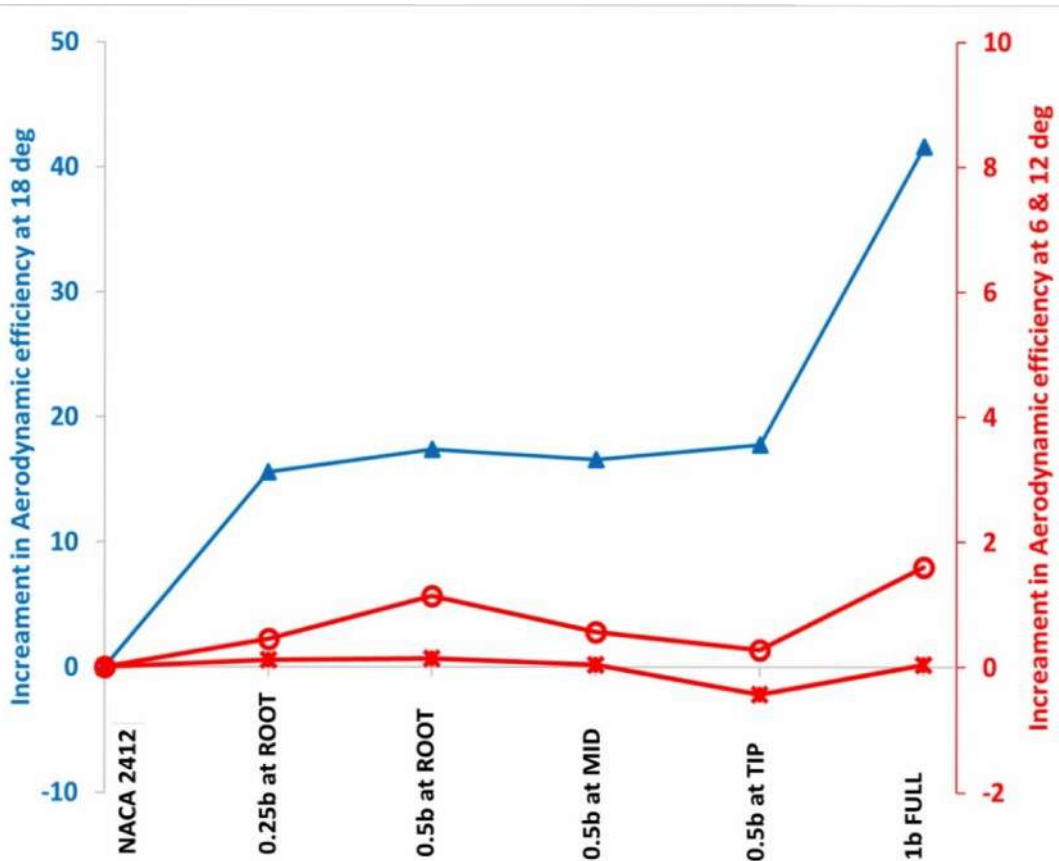


Figure 4.45 Lift and drag coefficient of wings at  $Re. 3 \times 10^6$ .



**Figure 4.46** a) Increment in  $C_l/C_d$  of porpoise nose on airfoil and wing. b) Velocity distribution (Q-Criterion) of NACA & porpoise nose wings at  $18^\circ$ .



**Figure 4.47** Increment in  $C_l/C_d$  for wing with different porpoise nose geometries.

The Figure 4.47 shows that, the porpoise nose covered the entire finite wing leading edge (porpoise nose with 1b spanwise length) gives better enhancement in aerodynamic efficiency at all angles of attack (left extreme points are corresponding to the wing with NACA 2412, and right extreme points are corresponding to the wing with full span(1b) porpoise nose.). Even the porpoise nose with 0.25b spanwise length shows the little improvement in aerodynamic efficiency at low angles, and noticeable increase in aerodynamic efficiency at high angles. Hence, for larger aircrafts, the porpoise nose with full spanwise length can be used. However, for the UAV's and smaller aircraft, the smaller length porpoise nose device is adequate to enhance the aerodynamic performance at all angles. Because the adding full span porpoise nose model will be difficult and it will unnecessarily increase the weight of the overall smaller aircrafts.

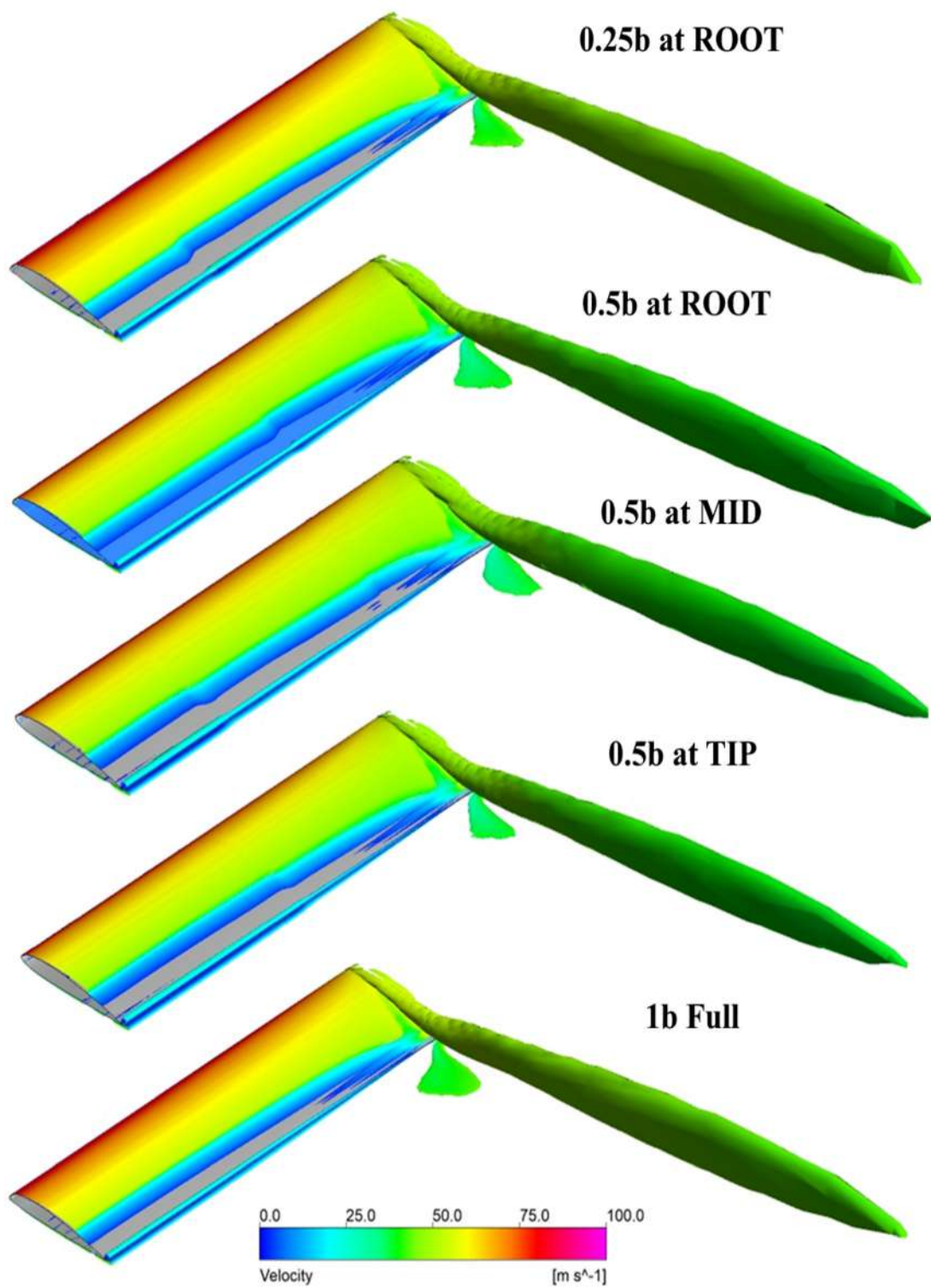


**Figure 4.48** Velocity distribution (Q-Criterion) of Porpoise nose wing with different spanwise length and location at  $12^\circ$ .

As the spanwise length of porpoise nose decreases, its effectiveness on flow separation control is decreases. In addition, it shows porpoise nose is very effective on flow control at high angles particularly after stalling angles (red lines with star markers (6 deg) and circular markers (12 deg) are far below than the blue line with triangular markers (18 deg). After stalling angle, the porpoise nose with 0.25b and 0.5b span at different location shows almost similar improvement on increase in aerodynamic efficiency (the blue line is more or less a straight line). Before stalling angle, as the location of porpoise nose moves from ROOT to TIP, the increment in  $C_l/C_d$  decreases (both red lines deflected downwards towards right).

The Figure 4.48 shows the extended low-pressure attached flow region behind the porpoise nose portion at  $12^\circ$  angle. When the porpoise nose is located near the root section of wing, it shows increased aerodynamic efficiency, because the flow is merely 2D near the root section. Hence, porpoise nose effectively accelerates the flow over the airfoil and delay the separation. When the porpoise nose is located near the wing tip where the flow is 3D in nature with vortex and turbulent flow structures, the porpoise nose is less effective on flow control of whole wing. Because the quality of the flow is higher near the root and it's not affected by the porpoise nose attached at the tip. The wing tip vortices are prominent before stalling angle. When the porpoise nose moves away from the root, it accelerates the flow near wing tip region and increase the pressure difference, hence the formation of strong tip vortices. However, after stalling angle, the flow detached from the upper surface of the airfoil and porpoise nose contribution to tip vortices formation is reduced, hence, the porpoise nose with 0.5b spanwise length located at MID, TIP & ROOT shows almost the similar type of flow behaviour and force enhancement (Figure 4.47).

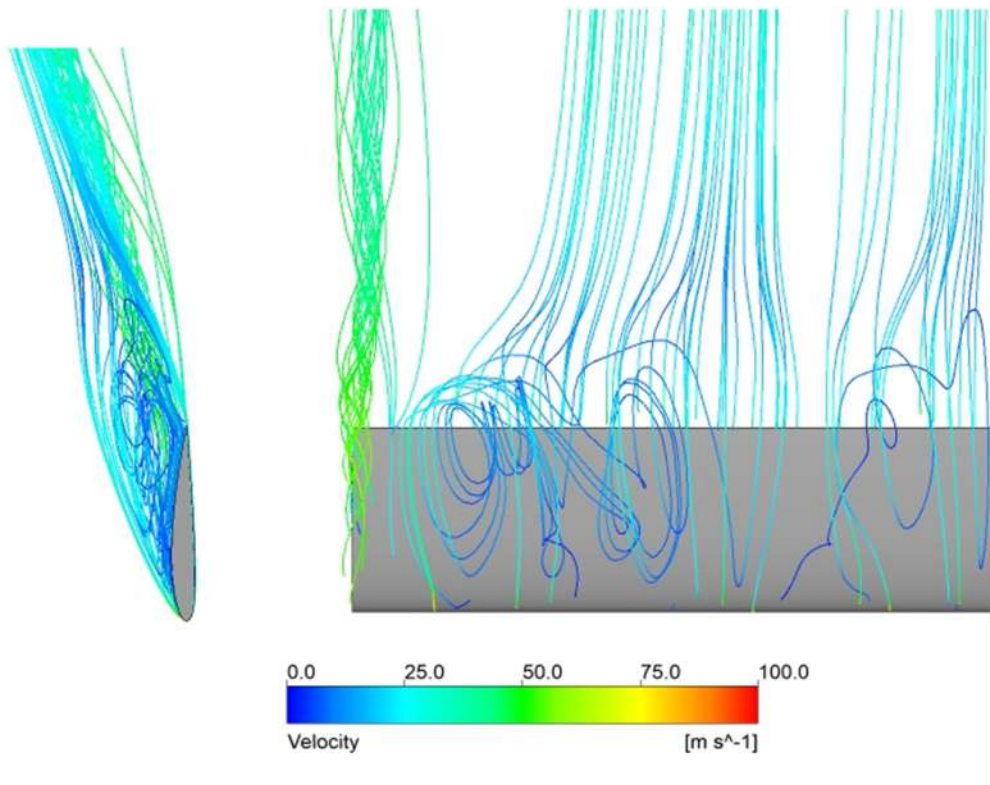


**Figure 4.49a** Streamline pattern of wing with NACA 2412 at  $18^\circ$  angle.

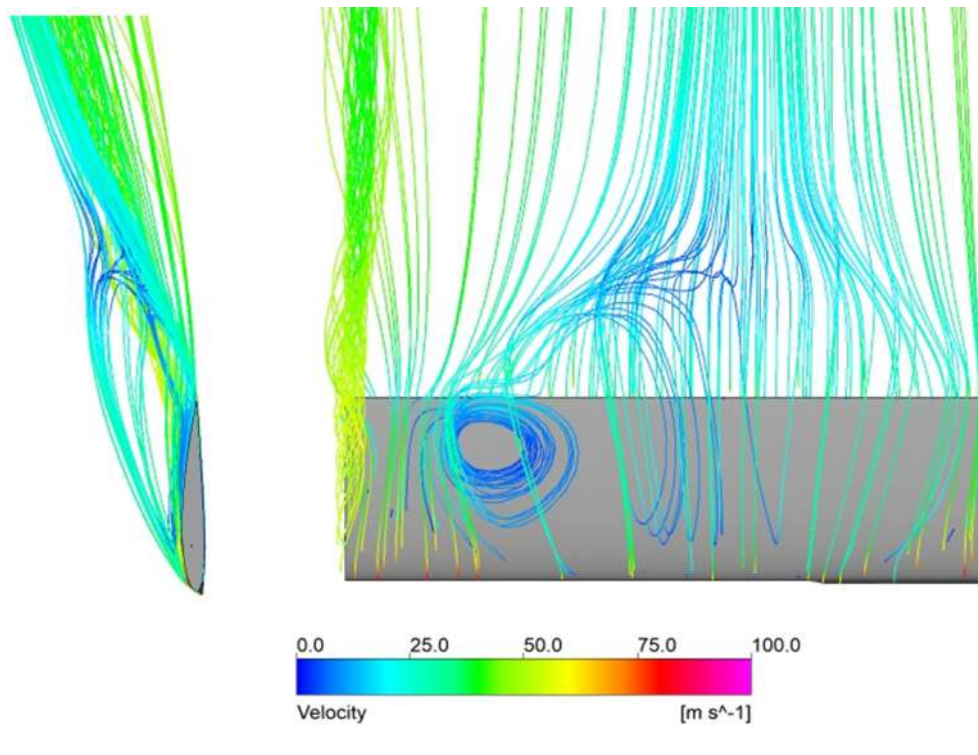


**Figure 4.49b** Streamline pattern of porpoise nose with  $0.25b$  at root ( $18^\circ$  angle).

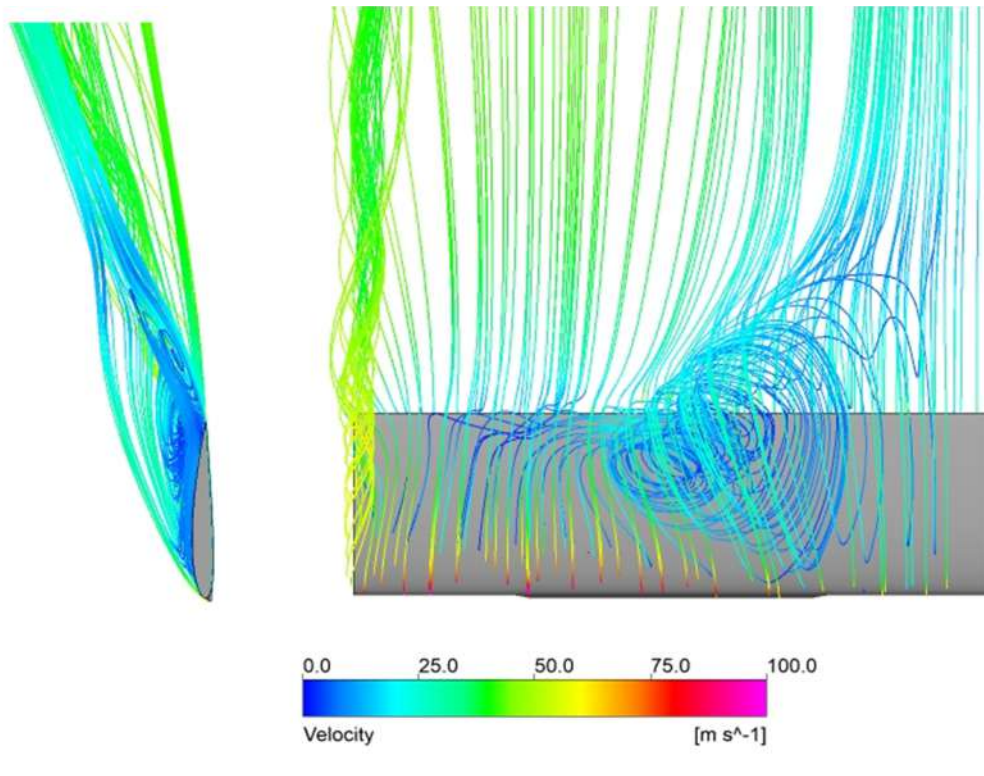


**Figure 4.49c** Streamline pattern of Porpoise nose with 0.5b at mid (18° angle)

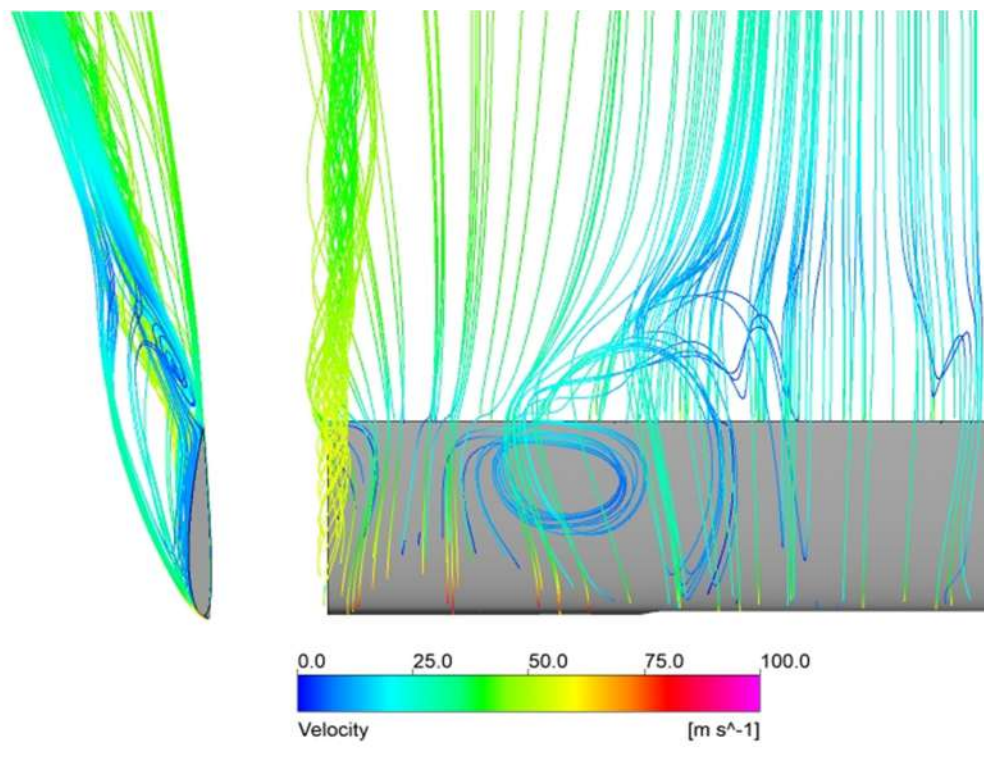


**Figure 4.49d** Streamline pattern of Porpoise nose with 0.5b at tip (18° angle)



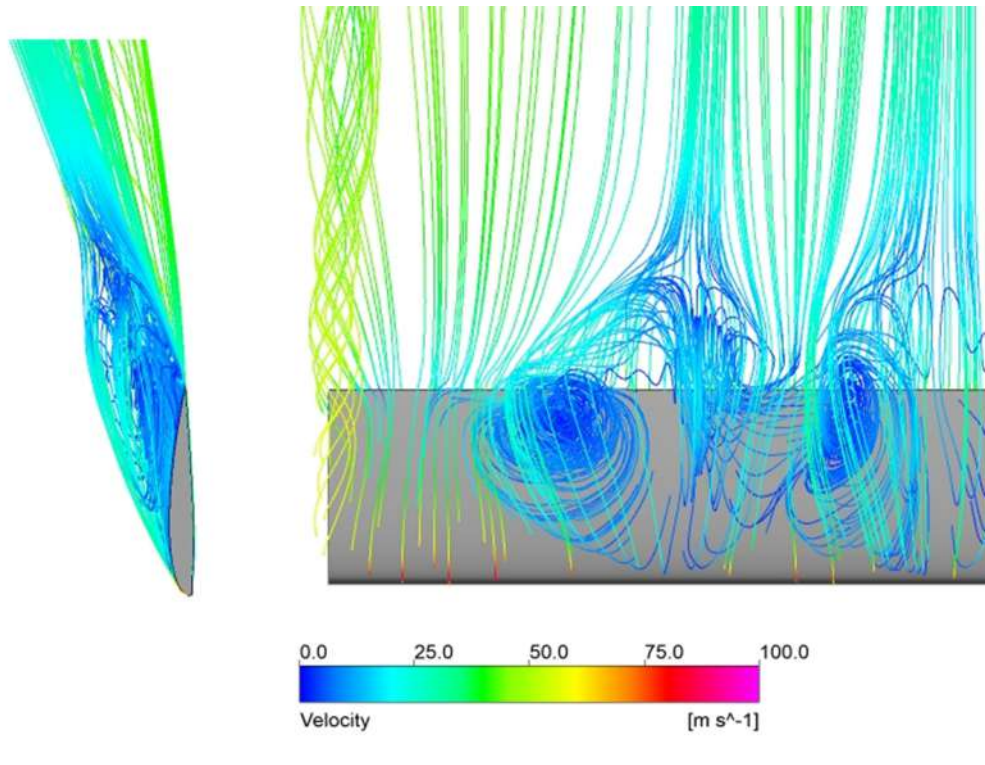


**Figure 4.49e** Streamline pattern of Porpoise nose with span 1b Full at  $18^\circ$  angle. (side view and top view).

The Figure 4.49a – 4.49e show the streamline pattern (velocity distribution) of different configurations of Porpoise nose wing at  $18^\circ$  angle of attack. As the length of porpoise nose decreases, the recirculation region formed on the airfoil also reduces. The porpoise with 1b length shows strong and maximum coverage of recirculation region on the upper surface of airfoil and shows reduction in the strength of wing tip vortices than other configurations (Figure 4.49e show the lesser number of yellow colours streamlines at the tip compared to other nose configurations). Hence shows maximum increment in  $C_l/C_d$ .

Figure 4.50 shows that, for  $12^\circ$  angle, porpoise nose shows accelerated flow on the upper surface (which increases the lift) than base airfoil (more dark blue colour low velocity streamlines) and reduced tip vortices (which decreases the drag).

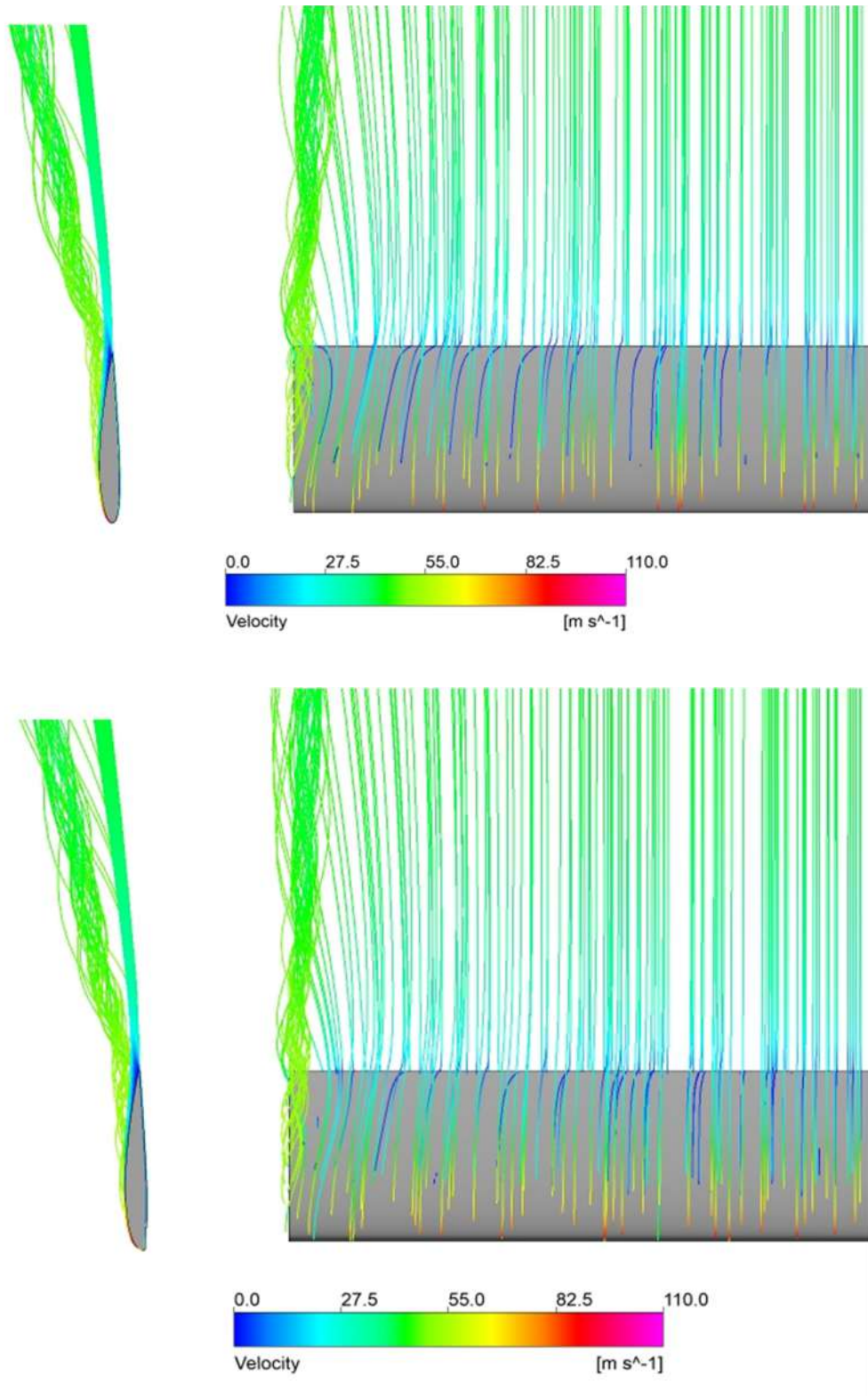


**Figure 4.50** Streamline pattern with velocity distribution of NACA wing and porpoise nose wing with full spanwise length (1b) at 12° angle.

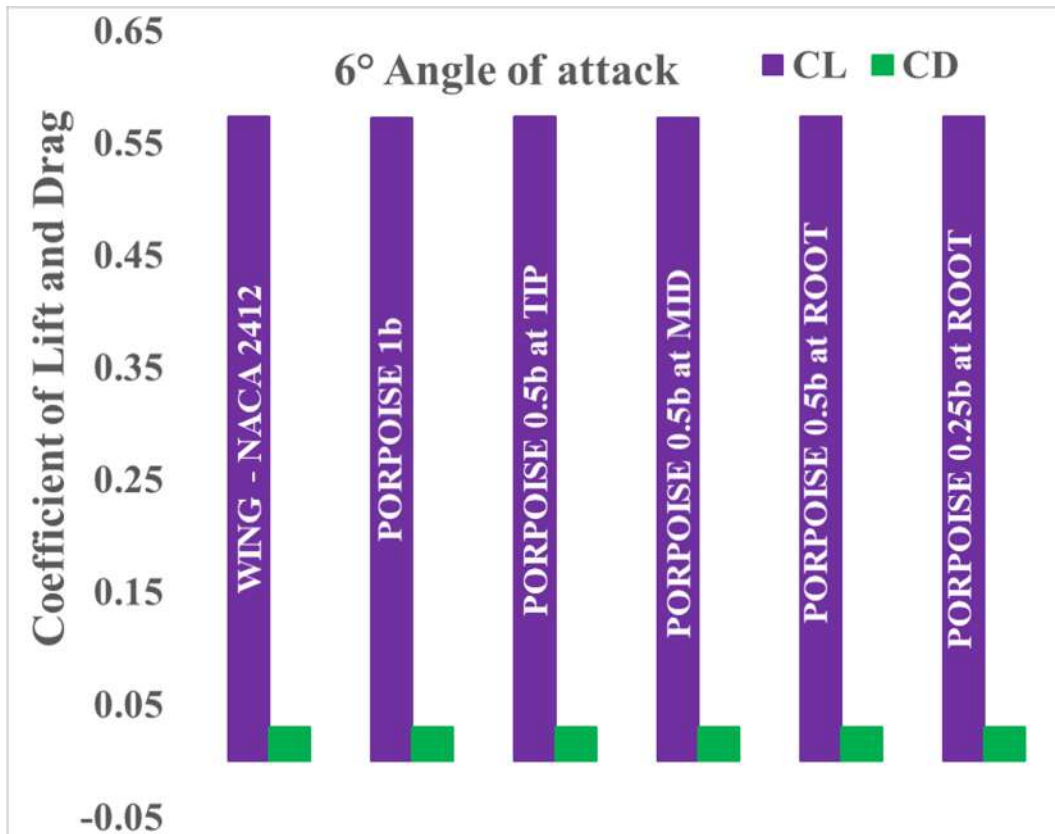


**Figure 4.51** Lift and drag coefficient of Porpoise nose wing with different length and location at 6°.

Figure 4.51 compares the lift (purple colour bars) and drag coefficient (green colour bars) of different porpoise nose wing configurations with NACA 2412 wing at 6°. The Figure 4.52 compares the velocity distribution (Q-Criterion) of different porpoise nose wing configurations with NACA 2412 wing at 6°. It was observed that, for 6° angle of attack, the change in spanwise length and position of porpoise nose does not show much variation in lift coefficient, drag coefficient, and velocity distribution compared to the base wing model. This porpoise airfoil shows a slight increase in flow acceleration on the upper surface but almost similar type of flow behaviour as base model. Force coefficients are same for all configurations.

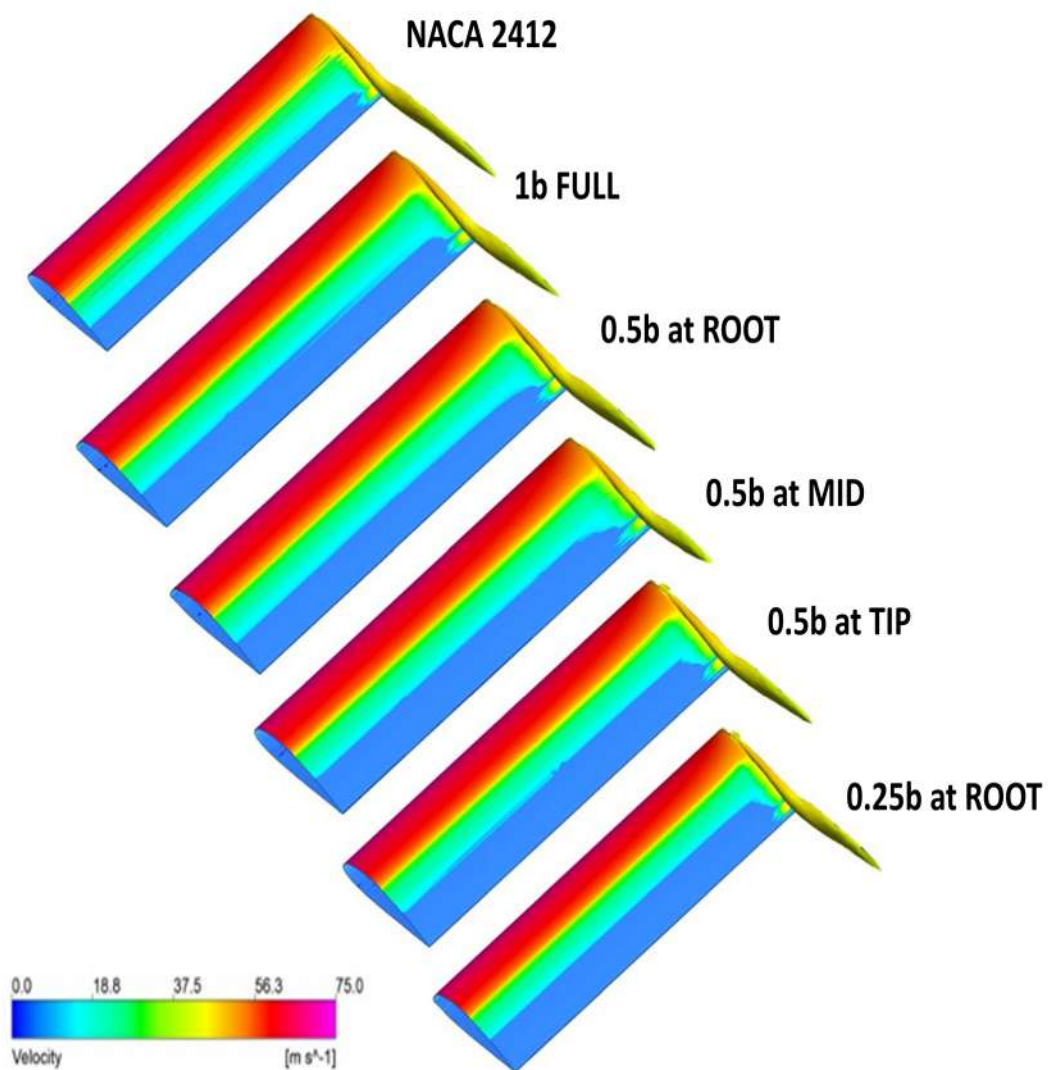


**Figure 4.52** Velocity distribution (Q-Criterion) of Porpoise nose wing with different spanwise length and location at  $6^\circ$ .

From the 3D analysis, it is observed that, the porpoise nose is effective on flow separation control of the finite wing, not only on the 2D airfoil. The porpoise nose shows almost same behaviour as NACA airfoil wing at low angles. It does not affect the aerodynamic performance of the wing adversely. And shows improvement in aerodynamic efficiency at high angles. However, most of the conventional flow separation control methods affect the aerodynamic performance adversely at low angles and effect only at high angle of attack. Hence, in future scope, the porpoise nose can be analysed with different 3D

wing geometries at different speed, and wings with other high lift devices using 3D numerical simulations and experimental analysis. The effect of porpoise nose design on wind turbine and propeller can be analysed using 3D sliding mesh simulations and experiment analysis. The design and mechanism of Universal device (porpoise nose) can be found to fit the porpoise nose device into the existing aircraft wing.

#### **4.4 Comparison of porpoise with conventional flow control devices.**

The effect of Bio-inspired nose (Porpoise nose) on flow separation and increment in the aerodynamic efficiency of the airfoil has been compared with other conventional flow control methods and high lift devices aerodynamic performance. In the flow control methods, the leading-edge modifications such as Wavy LE / sinusoidal LE / LE tubercle, drooped LE, Airfoil with LE Slat, Airfoil with the addition of thickness near the LE, and Airfoil with LE micro cylinder has been considered for comparison. For trailing edge modifications, Airfoil with TE profile modification, Airfoil with slotted flap, and Airfoil with backward step near the TE have been considered for comparison. In addition, airfoil with vortex generator at  $0.2C$  and Airfoil with a slot which connects lower and upper surface has been considered for comparison.

The figure 4.54a and b, show the aerodynamic efficiency of base and Wavy leading edge airfoil (Rocha, (2018)). The wavy LE increase the aerodynamic efficiency only after the stalling angle due to the effective axial vortex generation which increases the Lift and decreases the drag at high angles. The figure 4.55a and b, show the aerodynamic efficiency of base and droop nose and trailing-edges morphing airfoil (Aziz et. al. (2019)). The droop nose affects the lift adversely within the stalling angle and increases the drag, but maintains the attached flow on the airfoil upper surface at high angles hence increases the lift and decreases the drag. It shows the improvement in aerodynamic efficiency only after the stalling angle.

The figure 4.56a and b, show the  $C_l / C_d$  of a base airfoil and airfoil with slat (Tung et. al. (1993)). The slat improves the lift and lowers the drag only after the stall angle by injecting high momentum flow through the slot between slat and airfoil. At low angles, the slot decreases the pressure difference and lift without noticeable changes in the drag. The figure 4.57a and b, show the  $C_l / C_d$  of a base airfoil and airfoil with an increase in thickness near the LE and morphed trailing edge (Allison and Sewall (1995)). It showed a noticeable increase in the lift with a small rise in drag at all angles. It shows a noticeable improvement in aerodynamic efficiency within the working range of angles of attack even though it fails at few angles. But implementing the profile change or morphing in exiting aircraft wing is very complex.

The figure 4.58a and b, show the  $C_l / C_d$  of the base airfoil and airfoil with L.E. Micro Cylinder (Luo et. al. (2017)). The micro cylinder placed in front of the airfoil disturbs the flow over an airfoil, hence lift decreases and drag increases. But after the stall angle, the micro cylinder increases the aerodynamic efficiency as similar to the airfoil with leading edge slat and slot.

The figure 4.59a and b, show the  $C_l / C_d$  of the base airfoil and airfoil with a morphed trailing edge (Allison and Sewall (1995)). It shows the enhancement in the aerodynamic efficiency only at low angles. But at high angles, the drag increases because of the more curved trailing edge. The figure 4.60a and b, show the aerodynamic efficiency of the base airfoil and airfoil with slotted flap (Muraleedharan and Menon (2016)). The slotted flap with positive deflection increases the lift of an airfoil by increasing the camber. But it increases the drag at all angles. The increment in the lift after stall angle is very high compared to the increment in drag. Hence it shows an increase in aerodynamic efficiency after stall.

The figure 4.61a and b, show the aerodynamic efficiency of the base airfoil and airfoil with a backward step at 75% of the chord (Mishriky and Walsh (2016)). The backward step on the suction side of the airfoil produces high pressure stream of disturbed flow, hence decreases the lift and increases the drag. The drop in aerodynamic efficiency increases if the backward facing step location

moved towards the LE of the airfoil. The figure 4.62a and b, show the aerodynamic efficiency of the base airfoil and airfoil with vortex generator at 20% of the chord (Sørensen et. al. (2014)). At low angles of attack, the vortex generator acts as a drag device by creating an unnecessary disturbed flow on the airfoil. But the lift increases at high angles due to the effective axial vortices with low pressure region to suck the detached flow over the airfoil. The figure 4.63a and b, show the aerodynamic efficiency of the base airfoil and airfoil with a slot which connect upper and lower surfaces of the airfoil (Belamadi et. al. (2016)). The slot shows the improvement in aerodynamic efficiency at high angles of attack, due to the additional accelerated flow from the high-pressure region (lower surface) to low pressure region (upper surface) which delays the separation. At low angles, it reduces the pressure difference and attached flow on the upper surface, hence decreases the aerodynamic efficiency.

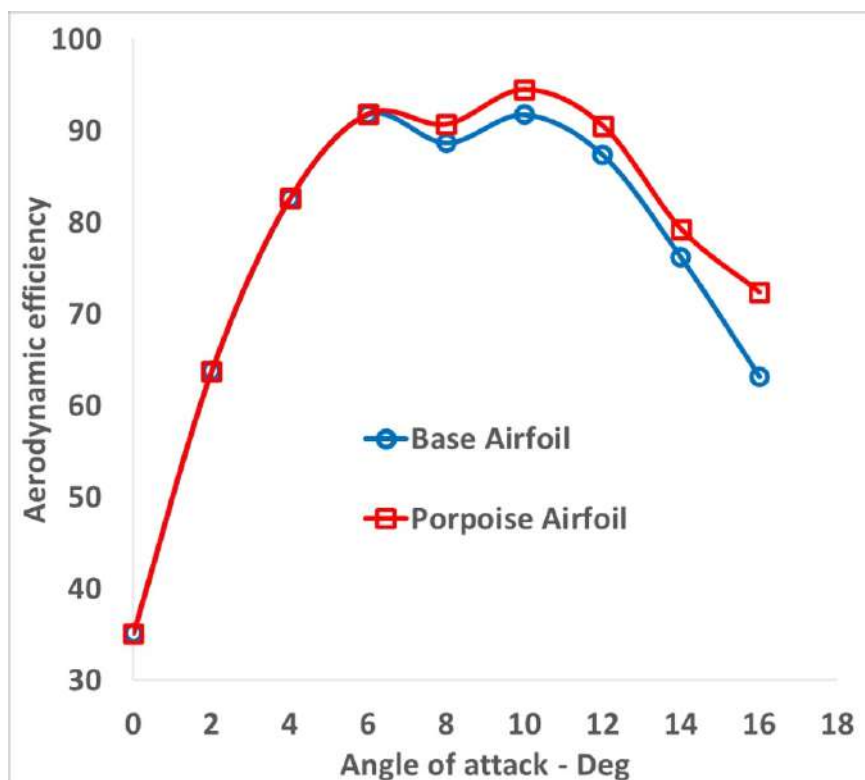


**Figure 4.53** Comparison of aerodynamic efficiency of Base and Porpoise airfoil at  $Re\ 3.1 \times 10^6$ .

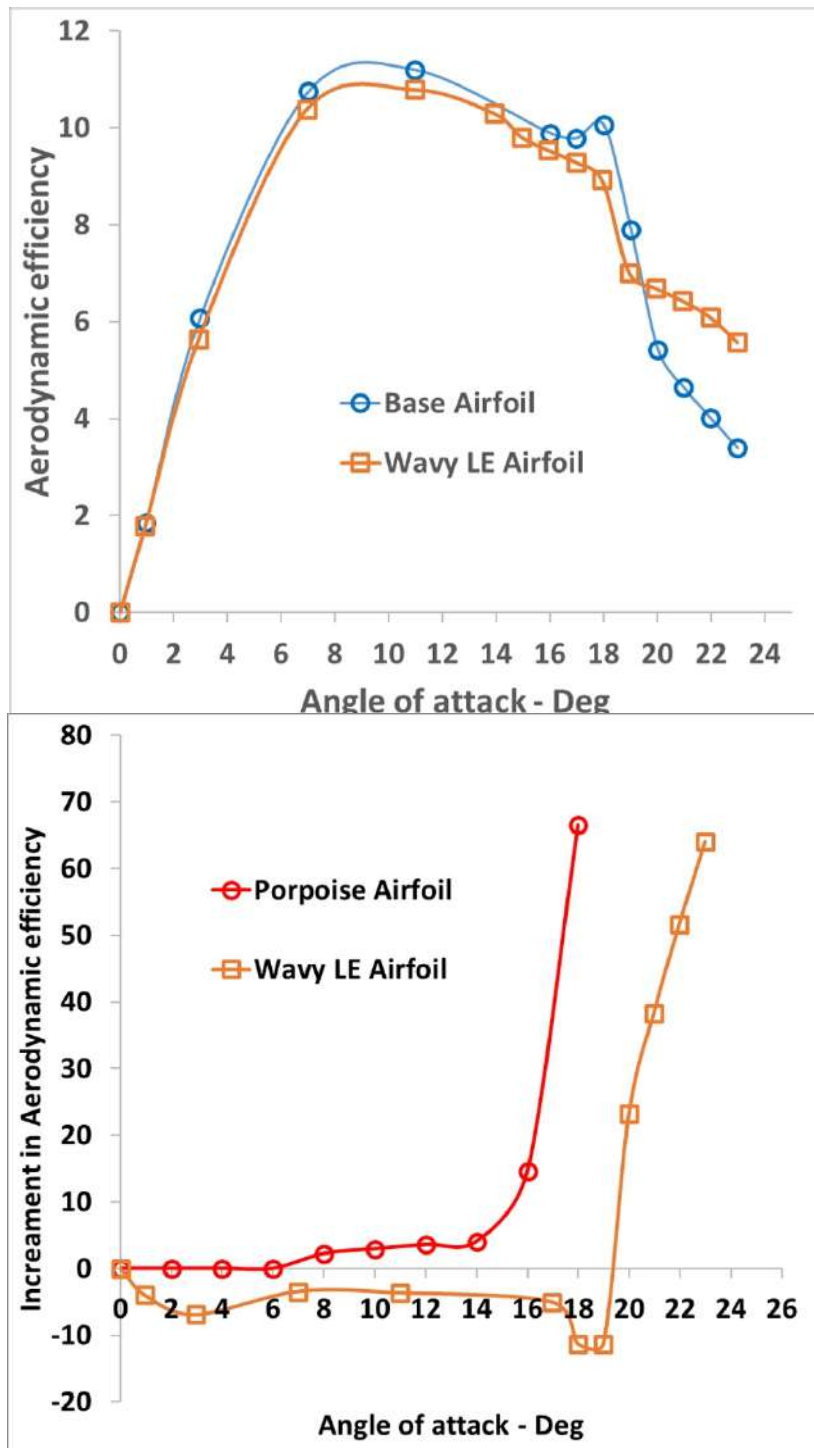


**Figure 4.54** Comparison of (a) aerodynamic efficiency of Base airfoil and Wavy LE airfoil. (b) increment in aerodynamic efficiency of Wavy LE airfoil and Porpoise airfoil



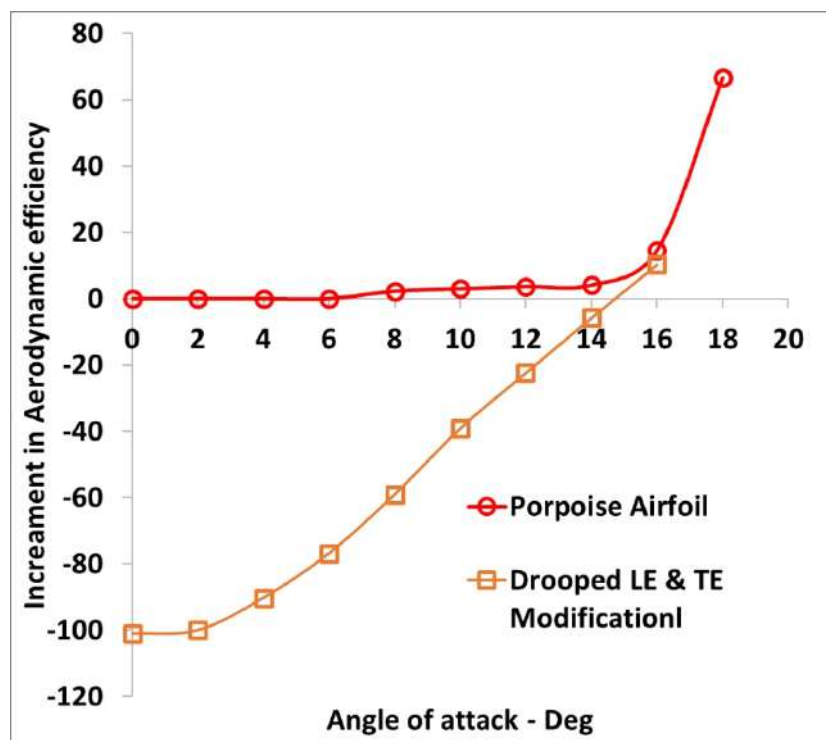
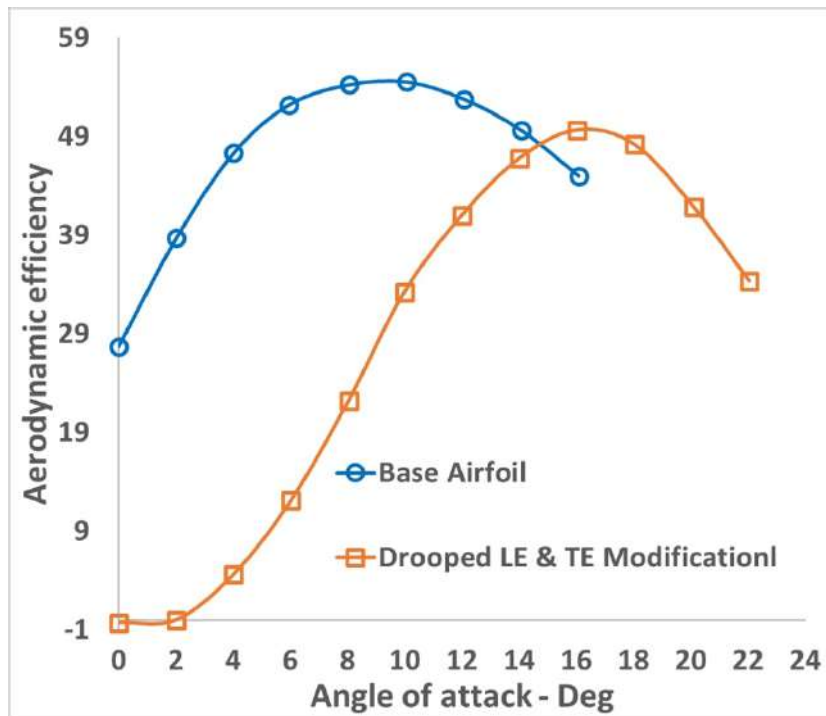


**Figure 4.55** Comparison of (a) aerodynamic efficiency of Base airfoil and Drooped LE and TE modified airfoil. (b) increment in aerodynamic efficiency of Drooped LE and TE modified and Porpoise airfoil

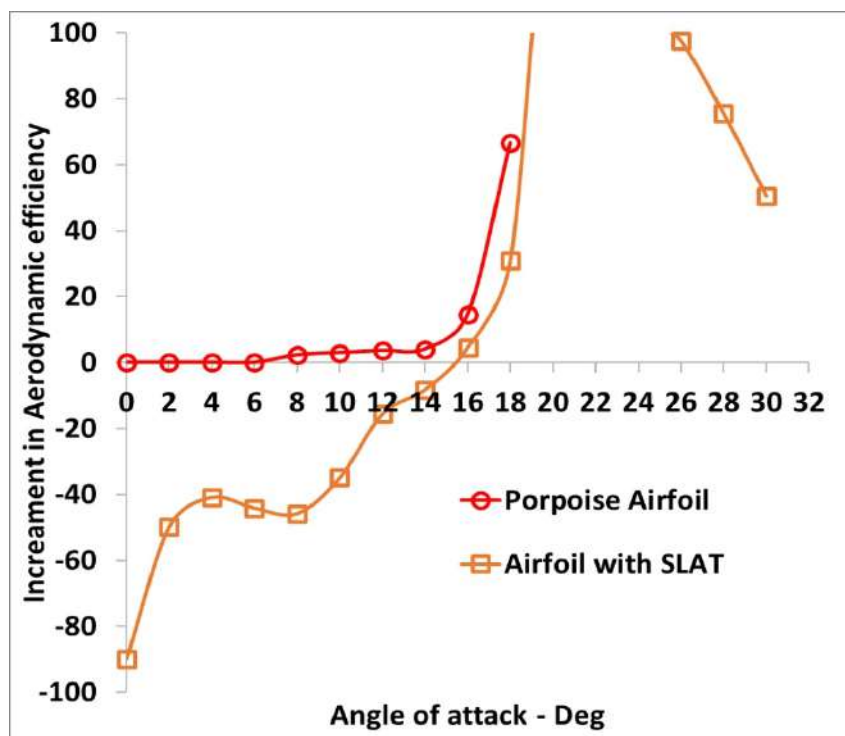
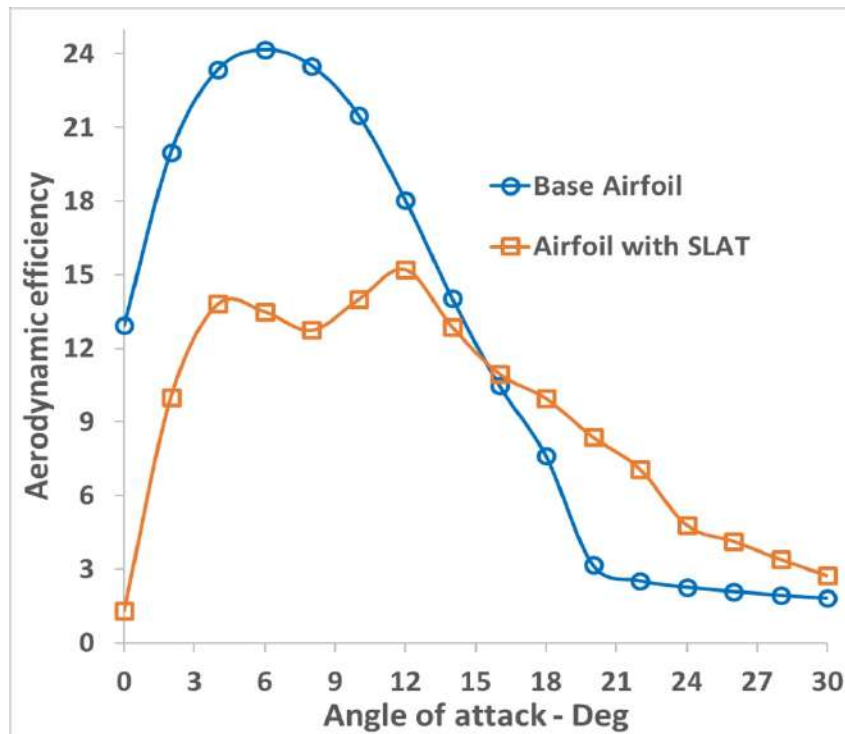


**Figure 4.56** Comparison of (a) aerodynamic efficiency of Base model and airfoil with Slat. (b) increment in aerodynamic efficiency of airfoil with slat and Porpoise airfoil.

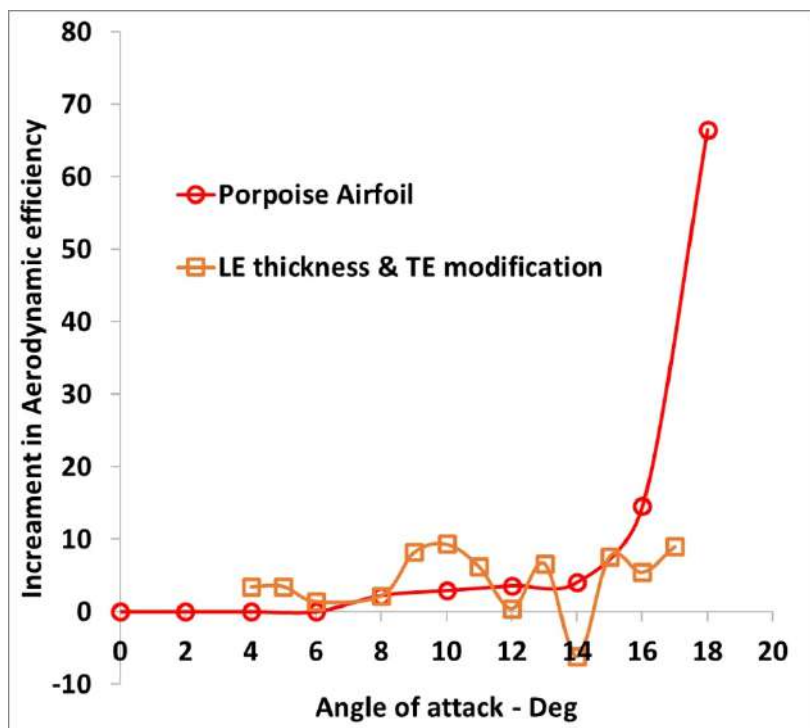
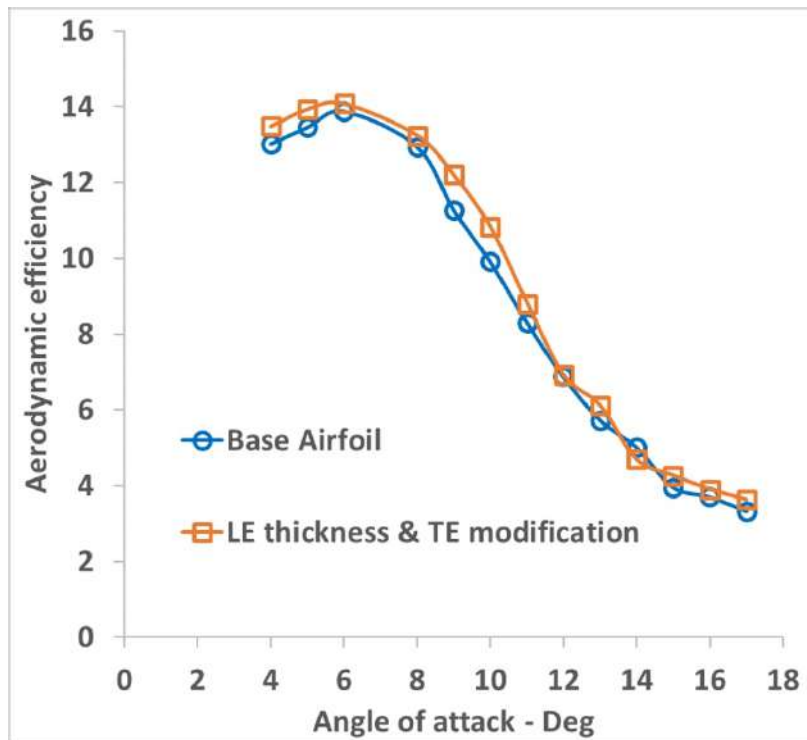


**Figure 4.57** Comparison of (a) aerodynamic efficiency of Base airfoil and LE Thickness and TE modified airfoil. (b) increment in aerodynamic efficiency of LE Thickness and TE modified airfoil and Porpoise airfoil

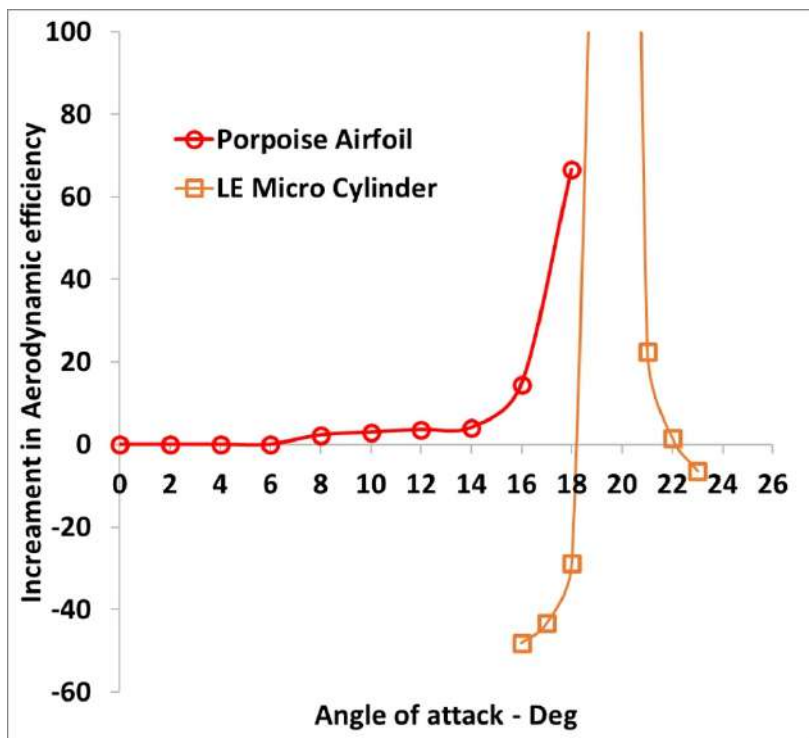
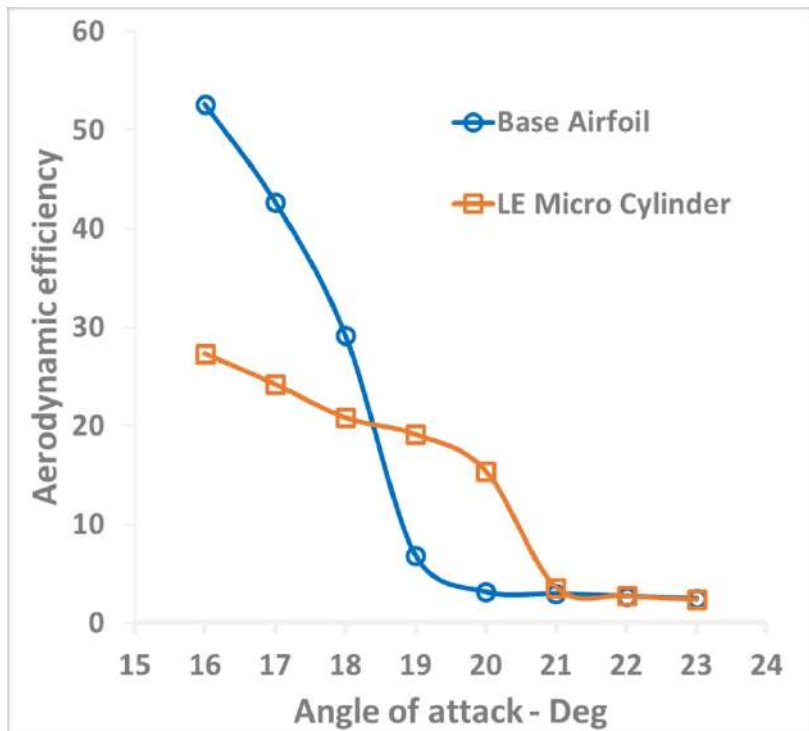


**Figure 4.58** Comparison of (a) aerodynamic efficiency of Base airfoil and airfoil with LE Micro Cylinder. (b) increment in aerodynamic efficiency of airfoil with LE Micro Cylinder and Porpoise airfoil

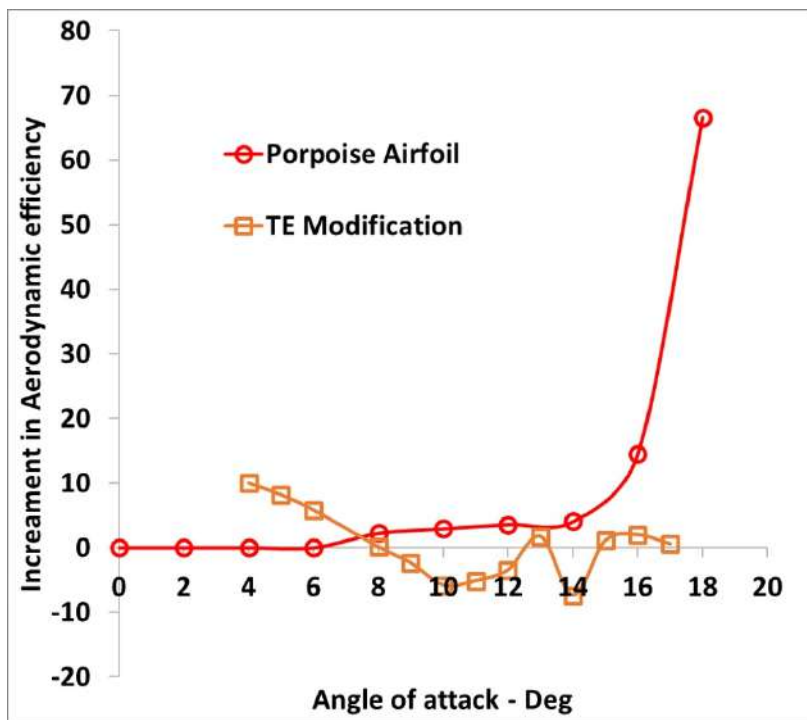
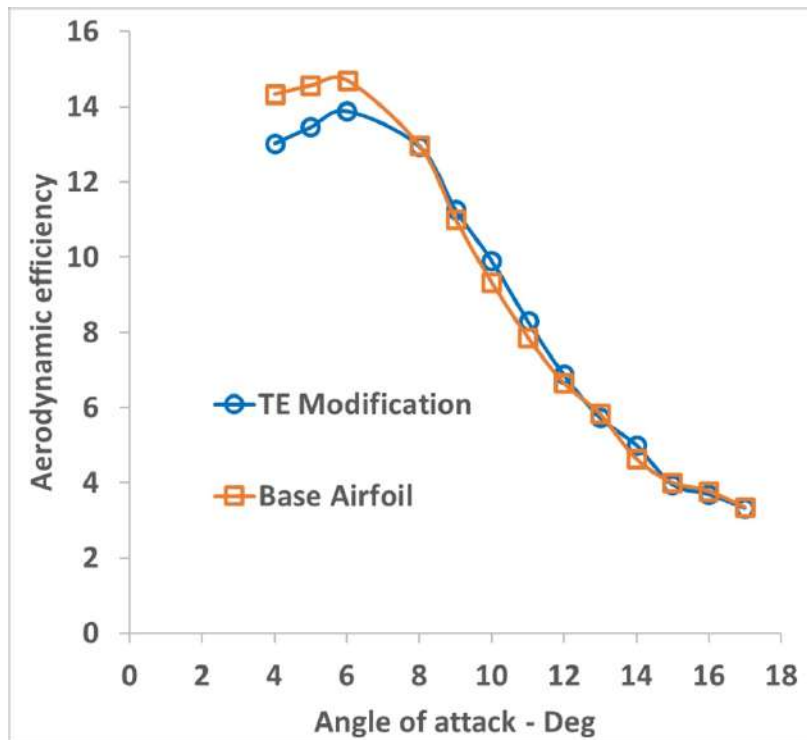


**Figure 4.59** Comparison of (a) aerodynamic efficiency of Base airfoil and airfoil with TE modification. (b) increment in aerodynamic efficiency of airfoil with TE modification and Porpoise airfoil

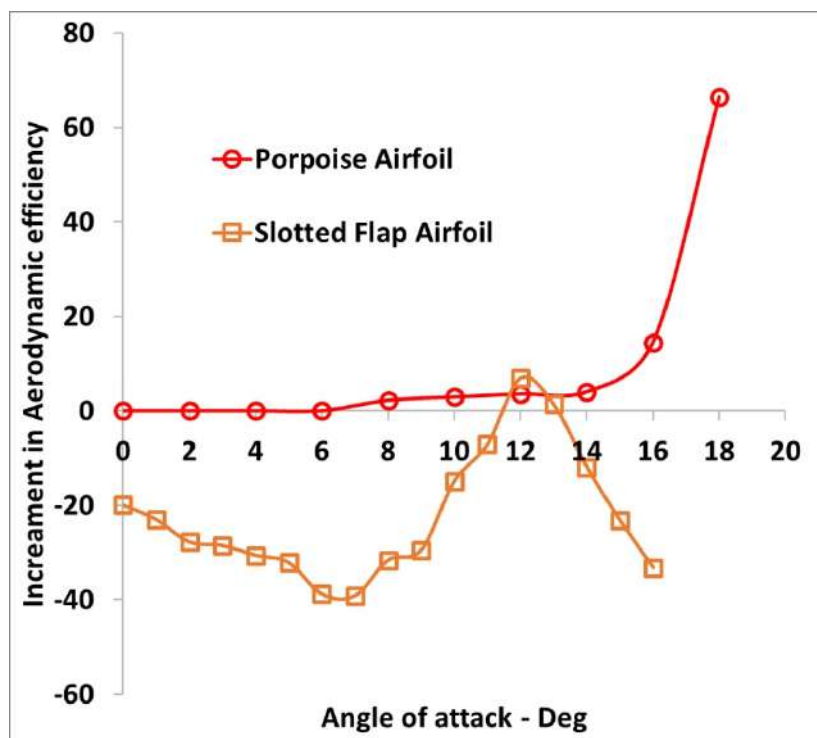
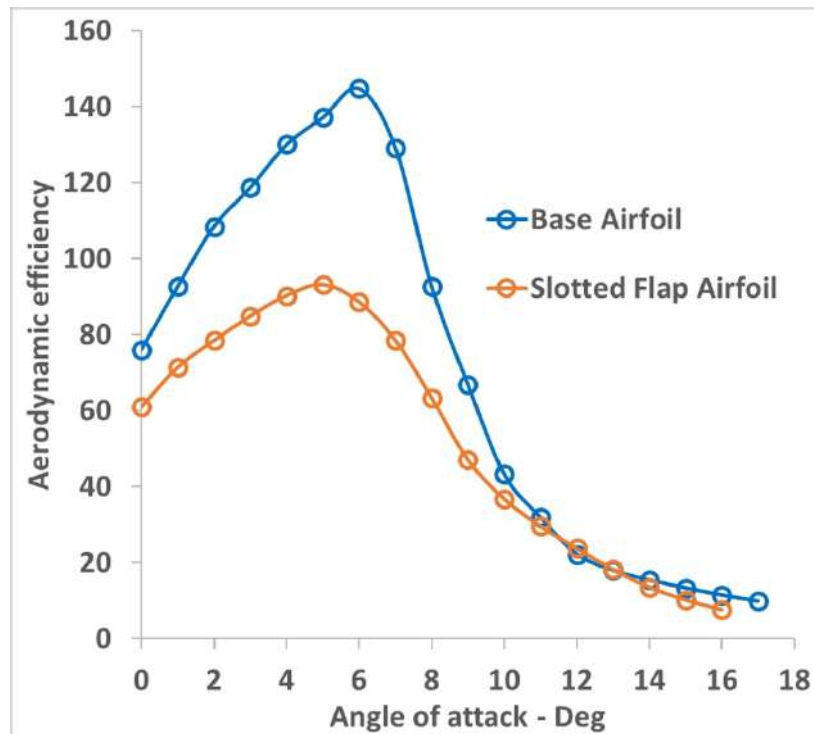


**Figure 4.60** Comparison of (a) aerodynamic efficiency of Base airfoil and Slotted flap airfoil. (b) increment in aerodynamic efficiency of Slotted flap airfoil and Porpoise airfoil

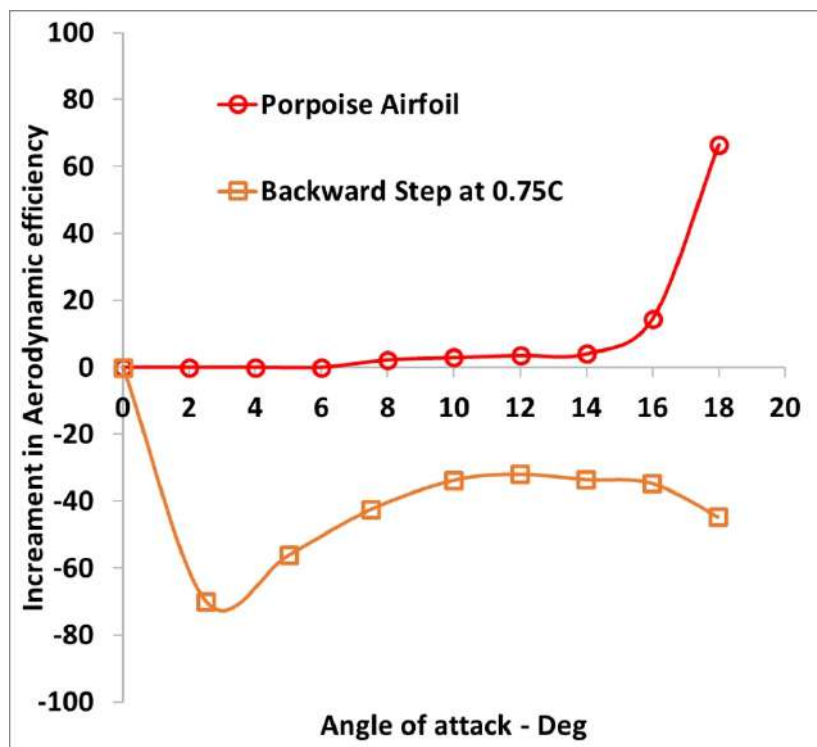
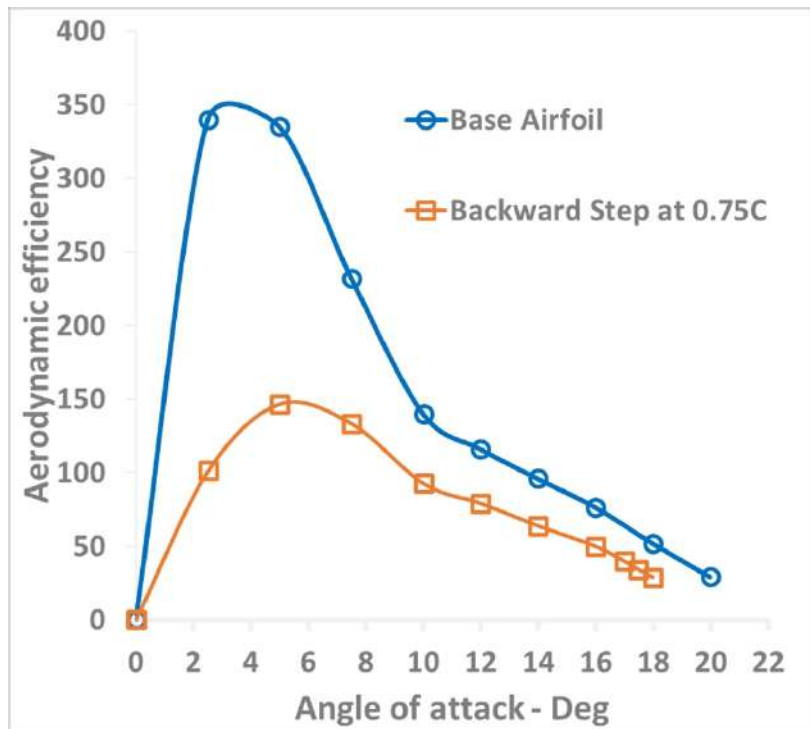


**Figure 4.61** Comparison of (a) aerodynamic efficiency of Base airfoil and airfoil with backward step at 0.75C. (b) increment in aerodynamic efficiency of airfoil with backward step at 0.75C and Porpoise airfoil

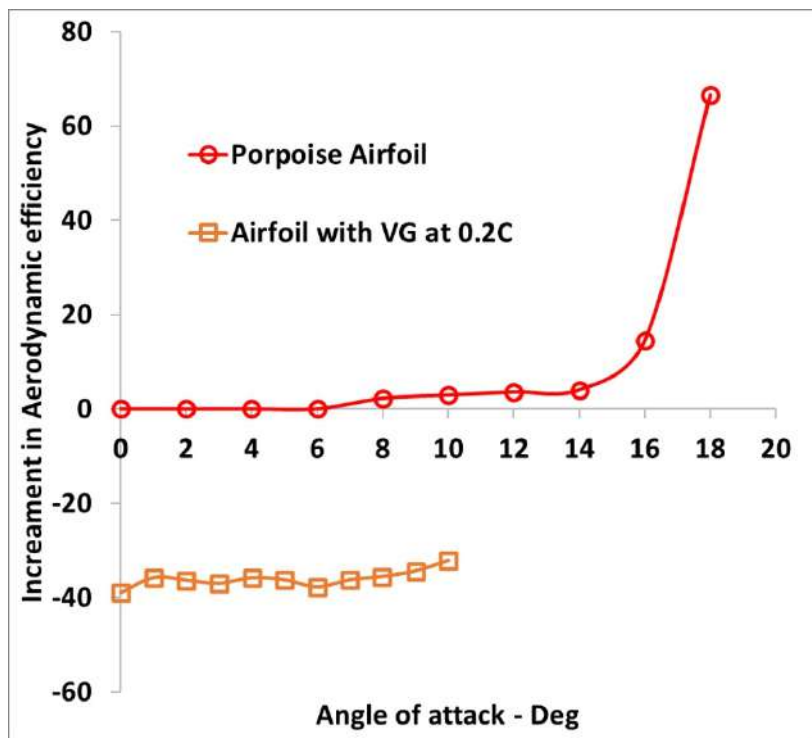
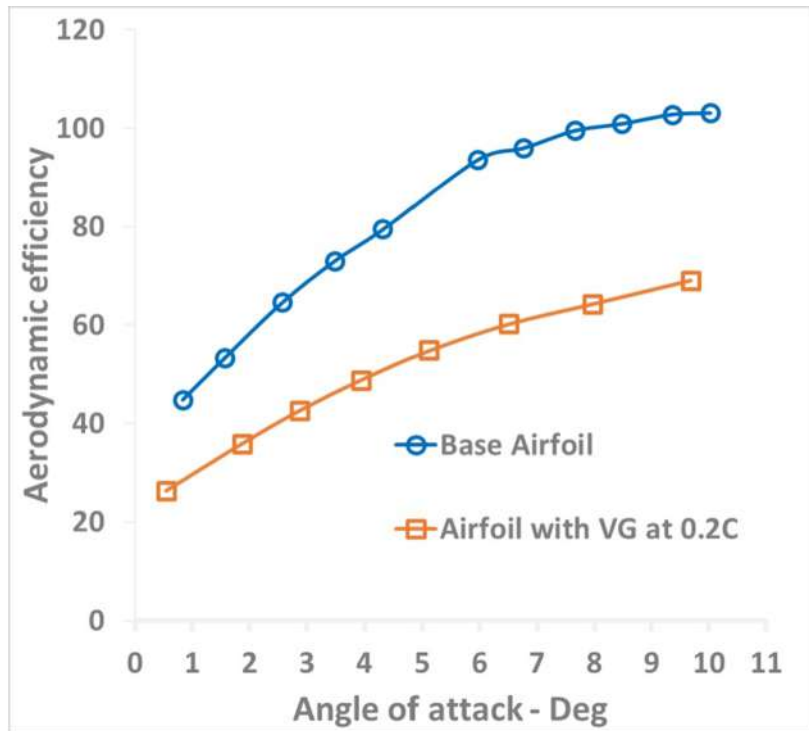


**Figure 4.62** Comparison of (a) aerodynamic efficiency of Base airfoil and airfoil with VG at 0.2C. (b) increment in aerodynamic efficiency of airfoil with VG at 0.2C and Porpoise airfoil



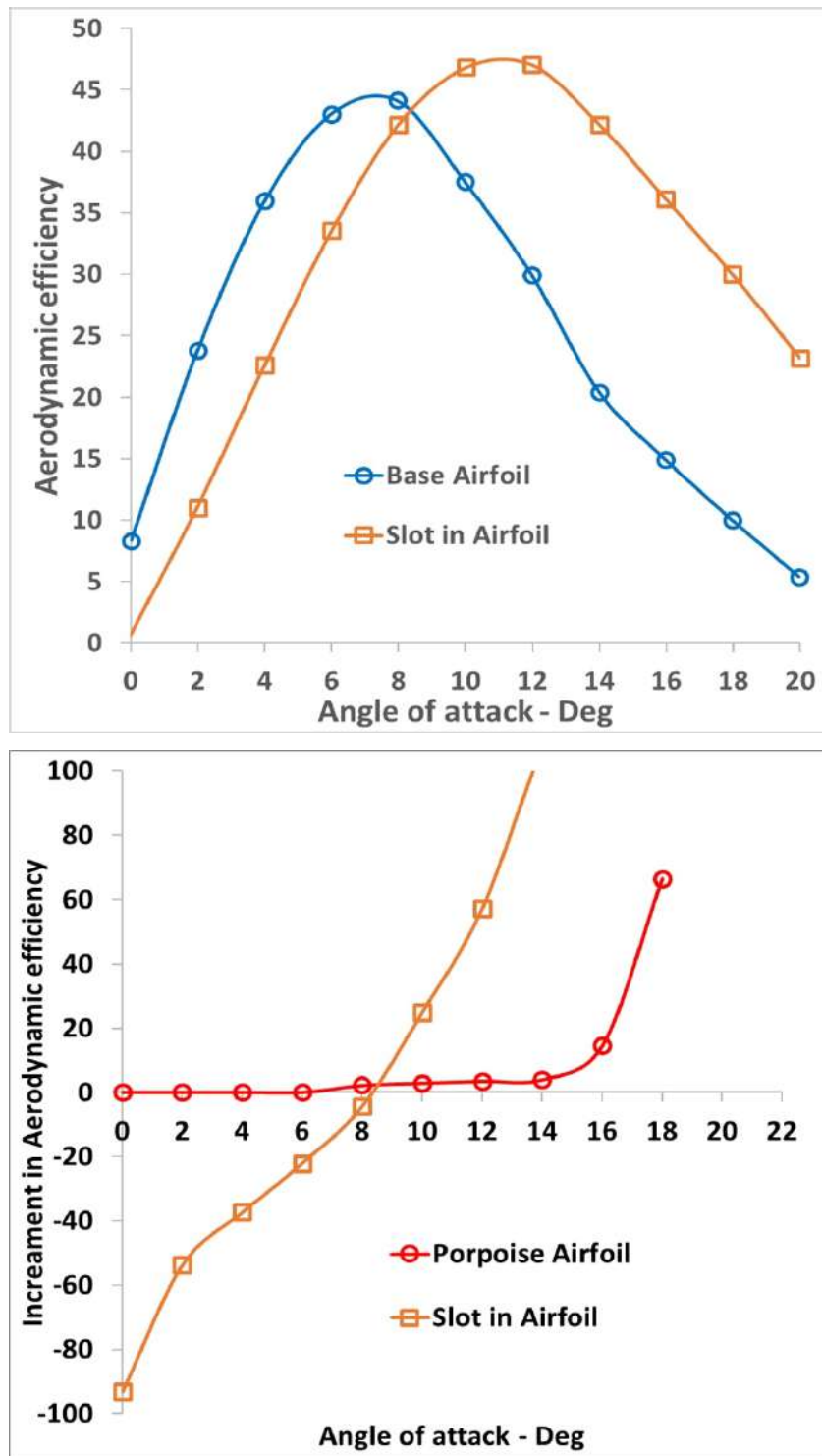


**Figure 4.63** Comparison of (a) aerodynamic efficiency of Base airfoil and airfoil with Slot. (b) increment in aerodynamic efficiency of airfoil with slot and Porpoise airfoil

From the comparison study, it is observed that most of the conventional flow separation control and high lift methods enhance the aerodynamic efficiency

only at high angles and adversely affect the cruise performance. The profile modification or morphing shows the improvement in lift to drag ratio at all angles but incorporating in the existing aircraft wing is very complex. Hence it is observed that the porpoise nose shows the increment in aerodynamic efficiency within the working range of angle of attack (Fig. 4.53). And this fixed leading edge nose design is practically feasible to attach in the existing aircraft wing.

## CHAPTER 5

### CONCLUSION

The bio-inspired nose designs which are inspired by the cetacean family marine mammals have been analysed on flow separation control of NACA series airfoils at subsonic speed. The major geometrical parameters such as nose leading edge radius, nose length, nose (depth) vertical positions are considered for the analysis. The objective of the nose designs is to form the forward-facing step at low angles of attack and cavity at high angles of attack, which enhances the acceleration on the upper surface of airfoil and delays the flow separation.

NACA 2412 airfoil has been modified with 54 different bio-inspired nose designs which are inspired by the cetacean family marine mammals and analysed at low subsonic speed computationally. It is found that, with the decreasing nose length, the aerodynamic efficiency is increasing. The longer nose with shallow cavity airfoil increases the aerodynamic efficiency at low angles of attack. This is due to the multiple acceleration of flow over the forward-facing step. But it decreases the aerodynamic efficiency at high angles of attack due to early flow separation from nose. Therefore, shorter nose (0.75c) gives optimum aerodynamic performance at all angles of attack than the base airfoil.

It is also found that, with increasing cavity's depth aerodynamic efficiency is increasing at high angles of attack by creating the axial vortices and induces multiple acceleration of flow on the upper surface. But it decreases the aerodynamic efficiency at low angles of attack due to the movement of stagnation pressure to the upper surface which reduces the pressure difference over the nose. Therefore, medium depth cavity (2.25c) gives optimum aerodynamic performance at all angles of attack than the base airfoil.

It is observed that airfoil nose having shorter length and medium depth (i.e. depth - 2.25 % of chord, nose length - 0.75 % chord, and nose diameter – 2 % chord) shows noticeable increase in aerodynamic efficiency almost at all angles of attack (operating range). This is achieved by forming the optimum forward-facing step at low angles of attack and optimum cavity/backward facing step at high angles of attack.

This airfoil is further modified as the porpoise airfoil which is inspired by Dall's porpoise (*Phocoenoides dalli*), a fastest cetacean species. The porpoise airfoil increases the lift coefficient and decreases the drag coefficient. The higher acceleration on the upper surface is due to the higher deflection of attached flow on the nose. It increases the aerodynamic efficiency at all angles of attack (operating range) than NACA 2412 airfoil without affecting the pitching moment. The rate of increase of aerodynamic efficiency is proportional to the increasing angle of attack.

The bio-inspired nose designs have been analysed on different NACA 4 and 6 series airfoils at low and high subsonic speeds. Flow behaviour of different nose designs have been analysed and the following flow behaviour is found.

The shorter nose with a medium depth cavity shows optimum enhancement within the operative range of angles of attack for all NACA 4 and 6 series airfoils taken for the analysis. The effectiveness of the length and depth of the bio-inspired nose on aerodynamic performance is higher than the effectiveness of diameter of the nose circle. The bio inspired nose design with the nose circle diameter of 2 % chord shows better aerodynamic performance for all NACA airfoil configurations considered for the research.

The porpoise nose design (shorter length and medium depth i.e. depth - 2.25 % of chord, nose length - 0.75 % chord, and nose diameter – 2 % chord) delays the flow separation and improves the aerodynamic efficiency by increasing the lift and decreasing the parasitic drag for all the NACA 4 & 6 series airfoils irrespective of airfoil geometry, without affecting the pitching moment.

The porpoise nose airfoil shows more or less similar aerodynamic efficiency and flow behaviour as base airfoil at low angles of attack. And its effectiveness

increases with increasing angle of attack by suppressing the flow separation and the wake region behind the airfoil. The maximum improvement in aerodynamic efficiency is achieved after the stall angle. However, before the stall angle, an average improvement in L/D by 5.5% from 6° angle of attack is achieved. The porpoise nose on NACA 2412 airfoil shows maximum increment in aerodynamic efficiency by 66.5% at 18° angle of attack for Re. No. of  $3 \times 10^6$ . The porpoise nose on NACA 66215 shows maximum increment in aerodynamic efficiency by 77.7%, at 12° angle of attack for Re. No. of  $9 \times 10^6$ . As the Reynold number increases, the effectiveness of porpoise on flow separation control also increases upto the critical Mach number. After critical Mach number, the shock wave formation affects the porpoise nose performance and shows similar flow behaviour as base airfoil.

For the conventional NACA airfoils, the maximum lift coefficient is increases for increasing airfoil thickness, and reaches the maximum value when the thickness is 12% to 15% of the chord. Even though the low thickness airfoils are producing low drag at low angles of attack, it is not preferable as it stalls soon. From the analysis, it is found that the effect of bio inspired nose design is maximum for low thickness airfoils. The porpoise design increases the lift and decreases the drag of low thickness airfoil at high angles, hence the stalling angle increases for the low thickness airfoils. Compared to the conventional NACA 0015 airfoil, the NACA 0008 airfoil with porpoise nose design gives the less drag at low angles of attack, and shows more or less the same aerodynamic behaviour as NACA 0015 airfoil at high angles of attack. Similarly, the NACA 0006 shows better aerodynamic performance than NACA 0012, the NACA 2406 shows better aerodynamic performance than NACA 2415, the NACA 2408 shows better aerodynamic performance than NACA 2418, and the NACA 63210 shows better aerodynamic performance than NACA 63221. So, it is inferred from the analysis that, instead of thick airfoils, thin airfoils with porpoise nose design can be used to get maximum aerodynamic efficiency.

It is also found that the addition of porpoise nose with NACA airfoil improves the aerodynamic performance and matched with other NACA airfoils. The NACA 4412 airfoil with porpoise nose shows similar aerodynamic performance

as NACA 6412, the NACA 63415 airfoil with porpoise nose shows similar aerodynamic performance as NACA 63615, and the NACA 67215 airfoil with porpoise nose shows similar aerodynamic performance as NACA 64215. Hence, the addition of porpoise nose can also be used instead of morphing of airfoil or wing to alter the aerodynamic behaviour of airfoil or wing upto certain extend.

This design improves aerodynamic performance and increases the structural strength of the aircraft wing compared to other conventional high lift devices and flow control devices. This universal leading-edge flow control device can be adapted to aircraft wings incorporated with any NACA 4 & 6 series airfoil.

The three-dimensional simulation has been done to find the optimum span wise length and the position of nose on a finite wing. Nose with spanwise length of 100%, 50%, and 25% of a finite wingspan ( $1b$ ,  $0.5b$ , and  $0.25b$ ) and positions such as root, mid portion, and tip of the finite wing were considered for the analysis. The finite wing with porpoise nose of full spanwise length ( $1b$ ) shows the better aerodynamic efficiency than base and other porpoise configurations at all angles of attack. It produces strong recirculation region on the upper surface and reduced wing tip vortices at high angles. The porpoise nose on the finite wing with NACA 2412 shows maximum increment in aerodynamic efficiency by 42% at  $18^\circ$  angle of attack for Re. No. of  $3 \times 10^6$ . The effectiveness of porpoise nose on flow control decreases as the spanwise length of porpoise nose decreases.

For the porpoise nose with 50% of wing span length, the wing root location shows maximum increment in aerodynamic efficiency than other locations on the wing leading edge, because the flow is merely two dimensional near the root section of wing. The effectiveness of porpoise nose ( $0.5b$ ) was decreasing when its location moved from wing root to tip. However, after stalling angle, the porpoise nose with  $0.5b$  span at different location along the wing span shows almost similar improvement on increase in aerodynamic efficiency, as the flow separates form the surface. Even the porpoise nose with 25% of wing span length shows the increment in aerodynamic efficiency by 15% at  $18^\circ$  angle of

attack for Re. No. of  $3 \times 10^6$  without adversely affecting the aerodynamic performance at low angles. The smaller length porpoise nose located at wing root can be effectively used for the flow control of UAV's and smaller aircrafts.

Hence, for larger aircrafts, the porpoise nose with full spanwise length can be used. However, for the UAV's and smaller aircraft, the smaller length porpoise nose device is adequate to enhance the aerodynamic performance at all angles without increasing the weight of the overall smaller aircrafts. This rigid leading-edge design increases the structural strength of the aircraft wing compared to movable conventional leading-edge devices.

From the comparison study, it is found that most of the conventional flow separation control and high lift methods augment the aerodynamic efficiency only the take-off / landing performance and adversely affect the cruise performance of the aircraft. The profile morphing shows the improvement in lift to drag ratio at all angles but incorporating in the existing aircraft wing is very complex. Hence it is observed that the fixed leading edge porpoise nose design shows the increment in aerodynamic efficiency within the working range of angle of attack and it is feasible to mount in the existing aircraft wing without many practical complications.

In the future, this bio inspired nose design (Porpoise nose) analysis can be extended as mentioned below.

The three-dimensional analysis can be done to compare the effectiveness of porpoise nose on flow separation control with other conventional high lift devices (such as flaps, slat, slots etc.).

The three-dimensional analysis can be done to compare the effectiveness of porpoise nose on flow separation control with other conventional flow control devices (such as vortex generators, etc.).

The slot can be introduced between the porpoise nose and the airfoil/wing, and the slot effect can be analysed on the flow separation control.

The same design methodology can be used to analyse the effect of nose designs that are inspired by other marine species such as whales, sharks, etc. on the flow separation control.

The same design methodology can be used to analyse the effect of nose designs that are inspired by the different birds on the flow separation control.

The numerical and experimental analysis to find the effect of porpoise nose design on the aerodynamic performance of wind turbine can be done.

The numerical and experimental analysis to find the effect of porpoise nose design on the aerodynamic performance of propeller blades can be analysed.

As the porpoise nose shows beneficial effect on the medium speed transport aircrafts such as propeller aircrafts, turbo-prop aircrafts, it can be analysed with a propeller slipstream effect, so that it can be effectively used in propeller and turboprop engine aircrafts.

The experimentation on the three-dimensional wing model with porpoise nose can be done with force measurements and flow visualisation for better validation.

The mechanism to mount the porpoise nose design on the aircraft wing as a leading-edge device can be worked out.



## REFERENCES

1. Abbott, I. H. A., & Doenhoff, A. E. (1949). Theory of wing sections: Including a summary of airfoil data. New York: McGraw-Hill.
2. Anderson, J. D. (2005). Fundamentals of Aerodynamics (Fifth Edition ed.). McGraw Hill Inc.
3. Aftab, S.M.A., Ahmad, K.A., “CFD study on NACA 4415 airfoil implementing spherical and sinusoidal tubercle leading edge”, PLOS ONE 12(11), 2017.
4. Agarwal, S., Kumar, P., “Investigation of flow field over NACA 4412 with a vortex generator”, Jr. of adv. research in app. Mech. and computational fluid dynamics, Vol.1, No.3-4, 2014.
5. Akaydin, H. D., Housman, J. A., Kirisy, C. C., Bahr, C. J., and Hutcheson, F. V., “Computational Design of a Krueger Flap Targeting Conventional Slat Aerodynamics,” 22nd AIAA/CEAS Aeroacoustics Conference, 2016, 2016, Pp. 1–12. doi:10.2514/6.2016-2958.
6. Allison, D. O., and Sewall, W. G., “Airfoil Modification Effects on Subsonic and Transonic Pressure Distributions and Performance for the EA-6B Airplane” NASA Technical Paper 3516, May 1995.
7. Anderson, S. B., Faye, A. E., Innis, R. C., “Flight investigation of the low-speed characteristics of a 35deg swept-wing airplane equipped with an area- suction ejector flap and various wing leading- edge devices”, NACA RM A57G10, Sept. 26, 1957
8. Arif, M., Rizwan, U., Vigneshwaran, Abhirami, D., Kumar, A., “Synthetic jet flow control for NACA 2412 aerofoil,” Int. Jr. of Mech. Engg. and Tech., Vol. 8, Pp. 843-850, 2017.
9. Asli, M., Gholamali, B. M., Tousi, A. M., “Numerical analysis of wind turbine airfoil aerodynamic performance with leading edge bump”, Math. Prob. in Engg., Hindawi Pub. Corp., 2015.
10. Ayuso, L., Sant, R., Meseguer, J., “Influence of leading edge imperfections on the aerodynamic characteristics of NACA 632-215 laminar aerofoils at low Reynolds numbers,” Proceedings of the Institution of Mechanical Engineers, Part G: Journal of Aerospace Engineering, Vol 228, Issue 6, 2014, Pp. 859-868. doi:10.1177/0954410013481418

11. Aziz, M.A., Mansour, M., Iskander, D., Hany, A., “Combined droop nose and trailing-edges morphing effects on airfoils aerodynamics.” *SN Appl. Sci.* 1, 1033 (2019). <https://doi.org/10.1007/s42452-019-0796-6>
12. Bahrff, C. J., Hutchesony, F. V., Thomasy, R. H., and Housmanz, J. A., “A Comparison of the Noise Characteristics of a Conventional Slat and Krueger Flap,” 22nd AIAA/CEAS Aeroacoustics Conference, 2016, Pp. 1–19. doi:10.2514/6.2016-2961.
13. Baldacchino, D., Ferreira, C., De Tavernier, D. A. M., Timmer, W. A., & van Bussel, G. J. W., “Experimental parameter study for passive vortex generators on a 30% thick airfoil,” *Wind Energy*, Vol. 21(9), Pp.745-765, 2018.
14. Bamber. M. J., “Wind tunnel tests of several forms of fixed wing slot in combination with a slotted flap on an NACA 23012 airfoil” NACA Tech Note No.702, April 1939.
15. Belamadi, R., Djemili, A., Ilinca, A., Mdouki, R., “Aerodynamic performance analysis of slotted airfoils for application to wind turbine blades,” *Journal of Wind Engineering and Industrial Aerodynamics*, Vol. 151, April 2016, Pp. 79-99. <https://doi.org/10.1016/j.jweia.2016.01.011>
16. Bertagnolio, F., Sørensen, N. N., Johansen, J., Fuglsang, P., “Wind turbine airfoil catalogue,” Denmark. Forskningscenter Risoe. Risoe-R, No. 1280(EN), 2001.
17. Beyhaghi, S., Amano, R. S., “Improvement of Aerodynamic Performance of Cambered Airfoils Using Leading-Edge Slots,” *Jr. of Ene. Resources Tech.*, ASME, Vol. 139, 2017.
18. Bodavula, A., Yadav, R. and Guven, U. (2019), "Numerical investigation of the unsteady aerodynamics of NACA 0012 with suction surface protrusion", *Aircraft Engineering and Aerospace Technology*, Vol. 92 No. 2, pp. 186-200. <https://doi.org/10.1108/AEAT-01-2019-0022>.
19. Bodavula, A., Yadav, R., and Guven, U., "Stall Mitigation and Lift Enhancement of NACA 0012 with Triangle-Shaped Surface Protrusion at a Reynolds Number of 105," *SAE Int. J. Aerosp.* 12(2):133-151, 2019, <https://doi.org/10.4271/01-12-02-0007>.
20. Brandner, P.A., Walker, G.J., “Hydrodynamic Performance of a Vortex Generator,” 14<sup>th</sup> Australasian Fluid Mech. Conf., Adelaide University, 2001.
21. Brendel, M., Mueller, T.J., “Boundary-layer measurements on an airfoil at low Reynolds numbers.” *Journal of Aircraft*, 1988, Vol. 25, No.7, Pp. 612-617
22. Brüderlin, M., Zimmer, M., Hosters, N., and Behr, M., “Numerical Simulation of Vortex Generators on a Winglet Control Surface,” *Aero.*

- Sci. and Tech., Vol. 71, 2017, Pp. 651–660.  
doi:10.1016/j.ast.2017.10.018.
23. Bur, R., Coponet, D., and Carpels, Y., “Separation Control by Vortex Generator Devices in a Transonic Channel Flow,” *Shock Waves*, Vol. 19, No. 6, 2009, Pp. 521–530.
  24. Chaitanya, P., Joseph, P., Narayanan, S., Vanderwel, C., Turner, J., Kim, J., & Ganapathisubramani, B., “Performance and mechanism of sinusoidal leading-edge serrations for the reduction of turbulence–aerofoil interaction noise,” *Journal of Fluid Mechanics*, 818, Pp. 435–464, 2017. doi:10.1017/jfm.2017.141
  25. Chandrasekhara, M. S., Martin, P. B., Tung, C., “Compressible Dynamic Stall Control Using a Variable Droop Leading Edge Airfoil,” *Jr. of Aircraft*, Vol. 41, No. 4, 2004.
  26. Chandrasekhara, M.S., “Optimum gurney flap height determination for “lost-lift” recovery in compressible dynamic stall control”, *Aero. Sci. and Tech.*, Vol. 14, Pp. 551–556, 2010.
  27. Chandrasekhara, M.S., Tung, C., Martin, P.B., “Aerodynamic flow control using a variable droop leading edge airfoil”, *RTO-MP-AVT-111*, 2004.
  28. Chen, H., and Qin, N., “Trailing-edge flow control for wind turbine performance and load control,” *Renew. Energy*, vol. 105, pp. 419–435, 2017.
  29. Chen, K., Liu, Q., Liao, G., Yang, Y., Ren, L., Yang, H., Chen, X., “The sound suppression characteristics of wing feather of owl (bubo bubo),” *J Bionic Eng.*, Vol. 9, Issue 2, 2012, Pp. 192–199.
  30. Chong, T. P., Vathylakis, A., McEwen, A., Kemsley, F., Muhammad, C., Siddiqi, S., “Aeroacoustic and Aerodynamic Performances of an Aerofoil Subjected to Sinusoidal Leading Edges,” *21st AIAA/CEAS Aeroacoustics Conference*, AIAA 2015-2200, 2015. <https://doi.org/10.2514/6.2015-2200>
  31. Choudhry, A., Arjomandi, M., Kelso, R., “A study of long separation bubble on thick airfoils and its consequent effects,” *International Journal of Heat and Fluid Flow*, 52, 84–96, 2015.
  32. Choudhry, A., Arjomandi, M., Kelso, R., “A study of long separation bubble on thick airfoils and its consequent effects,” *Int. Jr. of Heat and Fluid Flow*, Vol. 52, (2015), Pp.84–96.
  33. Ciuryla M., Liu Y., Farnsworth J., Kwan C., Amitay M., “Flight control using synthetic jets on a Cessna 182 model,” *Jr. of Aircraft*, Vol. 44, 2007, Pp.642–653.
  34. Colpitts, R. R., Perez, R. E., Jansen, P. W., “Effect of Leading-Edge Tubercles on Rotor Blades,” *AIAA 2020-2763*, 2020. <https://doi.org/10.2514/6.2020-2763>
  35. De Giorgi, M.G., De Luca, C.G., Ficarella, A., Marra, F., “Comparison between synthetic jets and continuous jets for active flow control

- Application on a NACA 0015 and a compressor stator cascade,” *Aero. Sci. and Tech.*, Vol. 43, 2015, Pp.256–280.
36. De paula, A. A., Meneghini, J. R., “The Airfoil Thickness Effect on Wavy Leading Edge Performance,” 55th AIAA Aerospace Sciences Meeting, AIAA SciTech, AIAA 2016-1306, 2016. DOI: 10.2514/6.2016-1306
  37. De paula, A. A., Meneghini, J. R., Kleine, Vitor. G., Girardi, R. M., “The Wavy Leading Edge Performance for a Very Thick Airfoil,” 55th AIAA Aerospace Sciences Meeting, 2017. DOI: 10.2514/6.2017-0492
  38. Dghim, M., Ferchichi, M., & Fellouah, H., “Mid-wake wing tip vortex dynamics with active flow control”, *Experimental Thermal and Fluid Science*, 98, Pp.38–55, 2018.
  39. Di, G., Wu, Z., Huang, D., “The research on active flow control method with vibration diaphragm on a NACA0012 airfoil at different stalled angles of attack”, *Aero. Sci. and Tech.*, 69, Pp. 76–86, 2017
  40. Donovan, J., Kral, L., Cary, A.,” Active flow control applied to an airfoil,”36th AIAA Aero. Sci. Meeting and Exhibit, 1998.
  41. Ebrahimi, A., and Movahhedi, M. “Wind Turbine Power Improvement Utilizing Passive Flow Control with Microtab.” *Energy*, Vol. 150, 2018, pp. 575–582. doi:10.1016/j.energy.2018.02.144.
  42. Egorov, Y., Menter, F., “Development and Application of SST-SAS Turbulence Model in the DESIDER Project,” *Adv. in Hybrid RANS-LES Modelling*, NNFM 97, Pp. 261–270, 2008.
  43. Fatehi, M., Nili-Ahmadabadi, M., Nematollahi, O., Minaiean, A., and Kim, K.C., “Aerodynamic performance improvement of wind turbine blade by cavity shape optimization,” *Renew. Energy*, vol. 132, pp. 773–785, 2019.
  44. Fernando, A. R., Adson, A. P., Marcos, d. S., André, V. C., Vitor, G. K., “The wavy leading-edge phenomena at high Reynolds number regime,” AIAA 2018-3816, 2018. <https://doi.org/10.2514/6.2018-3816>
  45. Fortin, F., “Shape Optimization of a Stretchable Drooping Leading Edge,”AIAA Scitech Forum, AIAA 2019-2352, 2019. <https://doi.org/10.2514/6.2019-2352>
  46. Fullmer, F.F., “Two -dimensional wind -tunnel investigation of the NACA 641-012 airfoil equipped with two types of leading-edge flap”, NACA TN No 1277, May 1947.
  47. Gámiz, F. U., Zamorano, G., Zulueta, E., “Computational study of the vortex path variation with the VG height,” *Jr. of Physics: Conference Series*, Vol. 524, 2014.
  48. Gao, L., Zhang, H., Liu, Y., Han, S., “Effects of vortex generators on a blunt trailing-edge airfoil for wind turbines,” *Renewable Energy*, Vol. 76, April 2015, Pp. 303-311.

49. Gentry, G.L., Takallu, M.A., Applin, T., “Aerodynamic Characteristics of a Propeller – Powered High-Lift Semi Span Wing,” Tech. Mem. NASA TM-4541, 1994.
50. Geyer, T., Wasala, S., and Sarradj, E., “Experimental Study of Airfoil Leading Edge Combs for Turbulence Interaction Noise Reduction,” *Acoustics*, vol. 2, Apr. 2020, pp. 207–223.
51. Ghaffari, F., Lamar, J. E., “An Attached Flow Design of a Noninterfering Leading Edge Extension to a Thick Delta Wing,” AIAA-85-0350, 1985.
52. Gibertini, G., Boniface, J.C., Zanotti, A., Droandi, G., Auteri, F., Gaveriaux, R., Pape, A.L., “Helicopter drag reduction by vortex generators,” *Aero. Sci. and Tech.*, Vol. 47, Pp. 324–339, 2015.
53. Gim, O. S., Lee, G. W., “Flow characteristics and tip vortex formation around a NACA 0018 foil with an endplate,” *Ocean Engineering*, Vol. 60, (2013), Pp. 28-38.
54. Griffin, D.A., “Investigation of Vortex Generators for Augmentation of Wind Turbine Power Performance,” NREL/SR-440-21399, 1996.
55. Gyatt, G.W., “Development and Testing of Vortex Generators for Small Horizontal Axis Wind Turbines,” NASA CR-179514, 1986.
56. Hahne, D.E., Jordan, F.L., “Full-Scale Semispan Tests of a Business-Jet Wing with a Natural Laminar Flow Airfoil,” NASA Technical Paper-3133, 1991.
57. Haipeng W., Bo Z., Qinggang Q., Xiang X., “Flow control on the NREL S809 wind turbine airfoil using vortex generators” *Energy*, 118, P. 1210 – 1221, 2017.
58. Heyes, A., & Smith, D., “Modification of a wing tip vortex by vortex generators,” *Aero. Sci. and Tech.*, Vol. 9, Pp.469-475, 2005.
59. Hicks, R. M., Mendoza, J.P., Bandettini, A., “Effects of Forward Contour Modification on the Aerodynamic Characteristics of the NACA 641-212 Airfoil Section,” NASA TM X-3293, 1975.
60. Hicks, R. M., Mendoza, J.P., Bandettini, A., “Effects of Forward Contour Modification on the Aerodynamic Characteristics of the NACA 641-212 Airfoil Section,” NASA TM X-3293, 1975.
61. Hopkins, E. J., “Aerodynamic study of a wing-fuselage combination employing a wing swept back  $63^\circ$  - effects of split flaps, elevons, and leading- edge devices at low speed,” NACA Res. Mem., No. A9C21, May 19, 1949.
62. Houghton, E.L., Carpenter, P.W., (2003) “Aerodynamics for Engineering Students”, 5<sup>th</sup> edition, Butterworth-Heinemann.
63. Ismail, M. F., Vijayaraghavan, K., “The effects of aerofoil profile modification on a vertical axis wind turbine performance,” *Energy*, Vol. 80, 2015, Pp. 20 -31.

64. Jacobs, E. N., Ward, K. E., Pinkerton, R. M., “The characteristics of 78 related airfoil sections from tests in the variable-density wind tunnel”, NACA Technical Report – 460, 1933.
65. James, S. E., J., Suryan, A., Sebastian, J. J., Mohan, A., Kim, H. D., “Comparative study of boundary layer control around an ordinary airfoil and a high lift airfoil with secondary blowing” *Computers and Fluids*, Vol. 164, Pp. 50–63, 2018.
66. Jang, C.S., Ross, J.C., Cummings, R.M., “Numerical investigation of an airfoil with a gurney flap”, *Aircraft Design*, Vol.1, Issue 2, Pp.75-88, 1998.
67. Johari, H., Henoch, C., Custodio, D., Levshin, A., “Effects of Leading-Edge Protuberances on Airfoil Performance,” *AIAA Journal*, 45, 2634-2642, 2007. <https://doi.org/10.2514/1.28497>
68. Juknevičius. A., Chong. T. P., “On the leading edge noise and aerodynamics of thin aerofoil subjected to the straight and curved serrations,” *Jr. of Sound and Vib.*, Vol. 425, Pp.324–343. 2018.
69. Justin W. J., Peake, N., “Aeroacoustics of Silent Owl Flight,” *Annual Review of Fluid Mechanics*, 2020, Vol. 52, Pp. 395-420.
70. Kelly, J. A., “Effects of modifications to the leading-edge region on the stalling characteristics of the NACA 631-012 airfoil section”, NACA TN 2228, November 1950.
71. Kelly, J. A., Hayter, N. F., “Lift and Pitching Moment at Low Speeds of The NACA 64<sub>a</sub>010 Airfoil Section Equipped with Various Combinations of a Leading-Edge Slat, Leading-Edge Flap, Split Flap, And Double-Slotted Flap,” NACA TN 3007, 1953.
72. Khor, Y. S., Xiao, Q., “CFD simulations of the effects of fouling and antifouling”, *Ocean Engineering*, Vol. 38, (2011), Pp. 1065–1079.
73. Kim, S.J., Choi, Y.S., Cho, Y., Choi, J.W., Hyun, J.J., Joo, W.G., and Kim, J.H., “Effect of Fins on the Internal Flow Characteristics in the Draft Tube of a Francis Turbine Model,” *Energies*, vol. 13, Jun. 2020, p. 2806.
74. Kobæk C.M., and Hansen M.O., “Numerical study of Wavy Blade Section for Wind Turbines,” *J. Phys.: Conf. Ser.* 753, 022039, 2016. doi:10.1088/1742-6596/753/2/022039
75. Koike, M., Nagayoshi, T., Hamamoto, N., “Research on Aerodynamic Drag Reduction by Vortex Generators”, *Mitsubishi Motors, Tech. Review*, No.16, 2004.
76. Kozlov, A., Chowdhury, H., Mustary, I, Loganathan, B., Alam, F., “Bio-inspired design: aerodynamics of boxfish,” *Procedia Engineering*, Vol. 105, 2015, Pp. 323-328.
77. Kumar, B.S.A., Ramalingaiah, Manjunath, S., Gangannad, R., “Computational investigation of flow separation over NACA23024 airfoil at 6 million free stream Reynolds number using k-epsilon

- turbulence model”, *Materials today: proceedings* Vol. 5, Issue 5, Part 2, Pages 12632–12640, 2018.
78. Kupper, C., Henry, F.S., “Numerical study of air-jet vortex generators in a turbulent boundary layer,” *App. Math. Mod.*, Vol. 27, (2003), Pp. 359–377.
  79. Lange, R.H., May, R.W., “Effect of Leading-Edge High-Lift Devices and Split Flaps on the Maximum-Lift and Lateral Characteristics of a Rectangular Wing of Aspect Ratio 3.4 with Circular-Arc Airfoil Sections at Reynolds Numbers from  $2.9 \times 10^6$  To  $8.4 \times 10^6$ ,” NACA RM No. L8D30, 1948.
  80. Lei, J., Guo, F., Huang, C., “Numerical study of separation on the trailing edge of a symmetrical airfoil at a low Reynolds number,” *Chinese Journal of Aeronautics*, Vol. 26, Issue 4, August 2013, Pp. 918-925.
  81. Leknys, R. R., Arjomandi, M., Kelso, R. M., and Birzer, C. H., “Leading-edge vortex development on a pitching flat plate with multiple leading edge geometries,” *Exp. Therm. Fluid Sci.*, vol. 96, pp. 406–418, 2018.
  82. Leknys, R. R., Arjomandi, M., Kelso, R. M., and Birzer, C. H., “Thin airfoil load control during post-stall and large pitch angles using leading-edge trips,” *J. Wind Eng. Ind. Aerodyn.*, Vol. 179, Pp. 80–91, 2018.
  83. Lengani, D., Simoni, D., Ubaldi, M., Zunino, P., Bertini, F., “Turbulent boundary layer separation control and loss evaluation of low profile vortex generators,” *Exp. Therm. Fluid Sci.*, Vol. 35, Issue 8, 2011, Pp. 1505-1513.
  84. Li, Q., Maeda, T., Kamada, Y., Hiromori, Y., Nakai, A., and Kasuya, T., “Study on Stall Behavior of a Straight-Bladed Vertical Axis Wind Turbine with Numerical and Experimental Investigations,” *Jr. of Wind Engg. and Ind. Aerod.*, Vol. 164, 2017, Pp. 1–12. doi:10.1016/j.jweia.2017.02.005.
  85. Li, Y.C., Wang, J.J., Hua, J., “Experimental investigations on the effects of divergent trailing edge and Gurney flaps on a supercritical airfoil” *Aero. Sci. and Tech.*, Vol. 11, Issues 2–3, 2007, Pp. 91-99.
  86. Lian, Y. and Shyy, W., “Laminar-Turbulent transition of a low Reynolds number rigid or flexible airfoil,” *AIAA Journal*, vol.45, no.7, pp. 1501-1513, 2007.
  87. Lin, J. C., “Review of research on low-profile vortex generators to control boundary-layer separation”, *Progress in aero. Sci.*, 38, vol. 38, Pp.89–420, 2002.
  88. Lin, Y. F., Lam, K., Zou, L., & Liu, Y., “Numerical study of flows past airfoils with wavy surfaces.” *Jr. of Fluids and Structures*, 36, 136–148. 2013. doi:10.1016/j.jfluidstructs.2012.09.008

89. Liu, Y., Guan, X., Xu, C., "An Improved Scale-Adaptive Simulation Model for Massively Separated Flows", *International Journal of Aerospace Engineering*, vol. 2018, Article ID 5231798, 16 pages, 2018. <https://doi.org/10.1155/2018/5231798>
90. Longest, P. W., Vinchurkar, S., "Effects of mesh style and grid convergence on particle deposition in bifurcating airway models with comparisons to experimental data," *Medical Engineering & Physics*, Vol. 29, 2007, Pp. 350–366.
91. Lu, W., Tian, Y., Liu, P., "Aerodynamic optimization and mechanism design of flexible variable camber trailing-edge flap," *Chinese Jr. of Aero.*, Vol. 30, Pp. 988–1003, (2017).
92. Luo, D., Huang, D., Sun, X., "Passive flow control of a stalled airfoil using a micro cylinder" *Jr. of Wind Engg. and Ind. Aerod.*, Vol. 170, Pp. 256–273, 2017.
93. Maki, R. L., and Hunton, L. W., "An Investigation at Subsonic Speeds of Several Modifications to The Leading-Edge Region of The NACA 64a010 Airfoil Section Designed to Increase Maximum Lift" NACA TN 3871, December 1956.
94. Mann, M. J., Huffman, J.K., Fox, C. J., Campbell, R. L., "Experimental Study of Wing Leading-Edge Devices for Improved Maneuver Performance of a Supercritical Maneuvering Fighter Configuration," NASA TP-2125, 1983.
95. Manolesos. M., Spyros G.V., "Experimental investigation of the flow past passive vortex generators on an airfoil experiencing three-dimensional separation," *J. Wind Eng. Ind. Aerodynamics*, 142, Pp.130–148. 2015.
96. McCullough, G. B., Gault, D. E., "An experimental investigation of an NACA 631-012 airfoil section with leading-edge suction slots", NACA technical note 1683, August 1948.
97. Meana-Fernández, A., Fernández Oro, J., Argüelles Díaz, K., and Velarde-Suárez, S., "Turbulence-Model Comparison for Aerodynamic-Performance Prediction of a Typical Vertical-Axis Wind-Turbine Airfoil," *Energies*, vol. 12, Feb. 2019, Pp. 488.
98. Mehraban, A.A, Djavareshkian, M. H., Sayegh, Y., Feshalami, B.F., Azargoon, Y., Zaree, A.H., Hassanalain, M., "Effects of smart flap on aerodynamic performance of sinusoidal leading-edge wings at low Reynolds numbers," *Proceedings of the Institution of Mechanical Engineers, Part G: Journal of Aerospace Engineering*. August 2020. doi:10.1177/0954410020946903
99. Menter, F. R., "Two-equation eddy-viscosity turbulence models for engineering applications," *AIAA Journal*, Vol. 32, No. 8, August 1994, Pp. 1598-1605



100. Merz, A. W., Hague, D. S., “Theoretical effect of modification to the upper surface of two NACA airfoils using smooth polynomial additional thickness distributions which emphasize leading edge profile and which vary quadratically at the trailing edge”, NASA-CR-137703,N75-24676, MARCH 1975.
101. Mishriky, F., Walsh, P., “Effect of the Backward-Facing Step Location on the Aerodynamics of a Morphing Wing,” *Aerospace*, 2016, 3(3), 25; <https://doi.org/10.3390/aerospace3030025>.
102. Moshfeghi, M., Shams, S., Hur, N., “Aerodynamic performance enhancement analysis of horizontal axis wind turbines using a passive flow control method via split blade,” *Jr. Wind Eng. & Ind. Aerod.*, Vol. 167, 2017, Pp. 148–159.
103. Muraleedharan, M., Menon, M., "On the Aerodynamic Properties of Slotted-Flap Flow-Control Devices for Wind Turbine Applications", Open Access Master's Thesis, Michigan Technological University, 2016. <https://doi.org/10.37099/mtu.dc.etdr/134>
104. Mystkowski, A., Jastrzębski, R., “Vibrating a small plate vortex generator to improve control robustness of a micro aerial delta wing vehicle,” *Journal of Vibro engg.*, Vol. 15, Issue 1, 2013.
105. Noonan, K.W., Yeager, W.T., Singleton, J.D., Wilbur, M.L., Mirick, P.H., “Wind Tunnel Evaluation of a Model Helicopter Main-Rotor Blade with Slotted Airfoils at the Tip,” NASA/TP-2001-211260, 2001.
106. Owen, P. R., and Klanfer, L., “On the Laminar Boundary Layer Separation from the Leading edge of a Thin Aerofoil”, C.P. No. 220 A.R.C. Technical Report, 1955.
107. Pastrokakis, V. A., Steijl, R., Barakos, G. N., and Małecki, J., “Computational aeroelastic analysis of a hovering W3 Sokol blade with gurney flap,” *Jr. of Fluids and Structures*, Vol. 53, Pp. 96-111, 2015.
108. Raj Mohamed, M.A., Guven, U. and Yadav, R. (2019), "Flow separation control of NACA-2412 airfoil with bio-inspired nose", *Aircraft Engineering and Aerospace Technology*, Vol. 91, No. 7, Pp. 1058-1066. <https://doi.org/10.1108/AEAT-06-2018-0175>
109. Raj Mohamed, M.A., Yadav, R. and Guven, U., "Flow separation control using a bio-inspired nose for NACA 4 and 6 series airfoils", *Aircraft Engineering and Aerospace Technology*, 2021. <https://doi.org/10.1108/AEAT-08-2019-0170>
110. Ravindran, S. S., “Active control of flow separation over an airfoil”, NASA technical memorandum 209838, December 1999.
111. Reiswich, A., Finster, M., Heinrich, M., and Schwarze, R., “Effect of Flexible Flaps on Lift and Drag of Laminar Profile Flow,” *Energies*, vol. 13, Mar. 2020, p. 1077.

112. Rezaeiha, A., Montazeri, H., Blocken, B., “On the accuracy of turbulence models for CFD simulations of vertical axis wind turbines,” *Energy*, 180, 2019, Pp. 838-857.
113. Roache, P. J., “Perspective: A method for uniform reporting of grid refinement studies,” *Journal of fluid engineering*, Sep. 1994, Vol. 116, Pp. 405-413.
114. Roache, P. J., “Verification of Codes and Calculations,” *AIAA Journal*, Vol. 36, No. 5, May 1998, Pp. 696-701.
115. Rocha, F. A., “The wavy leading-edge phenomena at high Reynolds number regime,” 2018. 107f. Dissertation of Master of Science – Instituto Tecnológico de Aeronáutica, São José dos Campos.
116. Rostamzadeh, N., Kelso, R. M., Dally, B. B., Hansen, K. L., “The effect of undulating leading-edge modifications on NACA 0021 airfoil characteristics,” *Physics of Fluids*, 25, 117101, 2013. <https://doi.org/10.1063/1.4828703>
117. Salmi, R. J., “Effects of leading-edge devices and trailing-edge flaps on longitudinal characteristics of two 47.7° sweptback wings of aspect ratios 5.1 and 6.0 at a Reynolds number of  $6 \times 10^6$ ,” *NACA RML50F20*, 1950.
118. Sankar, L. N., Sahin, M., Gopal, N., “Dynamic stall characteristics of drooped leading edge airfoils”, Graduate research assistants, Georgia institute of technology, Atlanta, July 2000.
119. Saravi, S. S., Cheng, K., Chong, T.P., Vathylakis, A., “Design of Serrate-Semi-Circular Riblets with Application to Skin Friction Reduction on Engineering Surfaces,” *Int. Jr. of Flow Control*, Vol. 6, No. 3, 2014.
120. Seetharam, H. C., Rodgers, E. J., Wentz, W. H. “Experimental studies of flow separation of the NACA 2412 airfoil at low speeds”, *NASA-CR-197497*, P. 69, October 1977.
121. Seifert, A., Shtendel, T., and Dolgopyat, D., “From Lab to Full Scale Active Flow Control Drag Reduction: How to Bridge the Gap?” *Jr. Wind Eng. & Ind. Aerod.*, Vol. 147, 2015, Pp. 262–272.
122. Serson. D., Meneghini. J. R., “Numerical Study of Wings with Wavy Leading and Trailing Edges”, In *Procedia IUTAM*, Vol. 14, Pp. 563–569, 2015.
123. Shaheen, M., and Abdallah, S., “Efficient Clusters and Patterned Farms for Darrieus Wind Turbines,” *Sustainable Energy Tech. and Assessments*, Vol. 19, 2017, Pp. 125–135. [doi:10.1016/j.seta.2017.01.007](https://doi.org/10.1016/j.seta.2017.01.007).
124. Shahmohamadi, H., & Rashidi, M. M., “Experimental investigation and a novel analytical solution of turbulent boundary layer flow over a flat

- plate in a wind tunnel,” *International Journal of Mechanical Sciences*, 133, 121–12, 2017. doi:10.1016/j.ijmecsci.2017.08.043
125. Shan, H., Jiang, L., Liu, C., Love, M., Maines, B., “Numerical study of passive and active flow separation control over a NACA0012 airfoil,” *Computers & Fluids*, Vol. 37, No. 8, Pp. 975–992, 2008.
  126. Shehata, A. S., Xiao, Q., Selim, M. M., Elbatran, A.H., Alexander, D., “Enhancement of performance of wave turbine during stall using passive flow control: First and second law analysis,” *Renewable Energy*, Vol. 113, Pp. 369-392, 2017.
  127. Shi, W., Atlar, M., Norman, R., Aktas, B., Turkmen, S., “Numerical optimization and experimental validation for a tidal turbine blade with leading-edge tubercles”, *Renewable Energy*, 96, Pp. 42–55. 2016
  128. Shi, X., Xu, S., Ding, L., Huang, D., “Passive flow control of a stalled airfoil using an oscillating micro-cylinder”, *Computers and Fluids*, Vol. 178, Pp.152–165, 2019.
  129. Siau, W. L., and Bonnet, J. P., “Transient Phenomena in Separation Control over a NACA 0015 Airfoil,” *Int. Jr. of Heat and Fluid Flow*, Vol. 67, 2017, Pp. 23–29. doi:10.1016/j.ijheatfluidflow.2017.03.008.
  130. Sieradzki, A., “Gurney Flap and T-Strip Influence On Stabilizer Aerodynamic Effectiveness and Hinge Moment Characteristics,” *Transactions of The Institute of Aviation*, No. 4 (245), Pp. 199-208, 2016. Doi: 10.5604/05096669.1226890
  131. Slater, J. W., Dudek, J. C., Tatum, K. E., “The NPARC Alliance Verification and Validation Archive,” *NASA/TM-2000-209946*, ASME 2000-FED-11233, April 2000.
  132. Sobhani, E., Ghaffari, M., and Maghrebi, M. J., “Numerical Investigation of Dimple Effects on Darrieus Vertical Axis Wind Turbine,” *Energy*, Vol. 133, 2017, Pp. 231–241. doi:10.1016/j.energy.2017.05.105.
  133. Soderman, P. T., “Aerodynamic effects of leading edge serrations on a two-dimensional airfoil”, *NASA TM X-2643*, September 1972.
  134. Somers, D. M., “An Exploratory Investigation of a Slotted, Natural-Laminar-Flow Airfoil,” *NASA/CR–2012-217560*, 2012.
  135. Sørensen, N. N., Zahle, F., Bak, C., Vronsky, T., “Prediction of the Effect of Vortex Generators on Airfoil Performance,” *Journal of Physics: Conference Series* 524 (2014) 012019, doi:10.1088/1742-6596/524/1/012019
  136. Sreejith, B.K., Sathyabhama, A., “Numerical study on effect of boundary layer trips on aerodynamic performance of E216 airfoil” *Engg. Sci. and Tech., an Int. Jr.*, Vol. 21, Issue 1, 2018, Pp. 77-88.
  137. Stern, F., Wilson, R. V., Coleman, H. W., Eric G. Paterson “Comprehensive Approach to Verification and Validation of CFD

Simulations—Part 1: Methodology and Procedures,” *Journal of Fluids Engineering*, Vol. 123, DECEMBER 2001, Pp. 793-802

138. Sun, Z. C., Mao, Y.F., Fan, M.H., “Performance optimization and investigation of flow phenomena on tidal turbine blade airfoil considering cavitation and roughness,” *Applied Ocean Research*, Vol. 106, January 2021, 102463.
139. Szelazek, C. A., Hicks, R. M., “Upper-Surface Modifications for C<sub>l</sub>max Improvement of Selected NACA 6-Series Airfoil”, NASA tech. Mem. 78603, August 1979.
140. Tamai, M., Wang, Z., Rajagopalan, G., Hu, H., He, G., “Aerodynamic Performance of a Corrugated Dragonfly Airfoil Compared with Smooth Airfoils at Low Reynolds Numbers,” 45th AIAA Aero. Sci. Meeting and Exhibit, AIAA-2007-0483, 2007.
141. Tang, H., Lei, Y., Li, X., Gao, K., and Li, Y., “Aerodynamic Shape Optimization of a Wavy Airfoil for Ultra-Low Reynolds Number Regime in Gliding Flight,” *Energies*, vol. 13, Jan. 2020, p. 467.
142. Tang, H., Salunkhe, P., Zheng, Y., Du, J., Wu, Y., “On the use of synthetic jet actuator arrays for active flow separation Control,” *Experimental Thermal and Fluid Science*, Vol. 57, 2014, Pp.1–10.
143. Tavella, D., Roberts, L., “A Theory for Lateral Wing-Tip Blowing,” Nasa-Cr-176931, 1983.
144. Tong, F., Qiao, W., Chen, W., Cheng, H., Wei, R., and Wang, X. “Numerical Analysis of Broadband Noise Reduction with Wavy Leading Edge.” *Chinese Journal of Aeronautics*, Vol. 31, No. 7, 2018, pp. 1489–1505. doi:10.1016/j.cja.2018.03.020.
145. Toyoda, K., Kwak, D., Noguchi, M., Rinoie, K., “Aerodynamic Interference Caused by the Inboard Leading-Edge Flap on the Outboard Area of the Cranked Arrow Wing,” *Procedia Engineering*, Vol. 99, Pp. 1642-1646, 2015.
146. Troolin, D.R., Longmire, E.K., Lai, W.T., “Time resolved PIV analysis of flow over a NACA 0015 Airfoil with gurney flap” *Experiments in Fluids*, Vol. 41, 2006.
147. Tung, c., McAlister, K.W., Wang, C. M., “Unsteady aerodynamic behavior of an airfoil with and without a slat,” *Computers & Fluids*, Vol. 22, Issues 4–5, 1993, Pp. 529-547.
148. Turner, T. L., Moore, J.B., Long, D. L., “Computational Modeling of a Mechanized Benchtop Apparatus for Leading-Edge Slat Noise Treatment Device Prototypes,” *American Institute of Aeronautics and Astronautics*, NF1676L-24690, Pp.1874, 2017.
149. Vakilipour, S., Zarafshani, H., Al-Zaili, J., “Numerical study of longitudinal vein effects on the aerodynamic characteristics of a

- corrugated bio-airfoil,” *Computers & Fluids*, Vol. 216, 15 February 2021, 104821.
150. Velte, C.M., Hansen, M.O.L., Jønck, K., “Experimental and numerical investigation of the performance of vortex generators on separation control”, *Journal of physics: conference series*, Vol. 75, 2007.
  151. Viswanath, P. R., "Aircraft viscous drag reduction using riblets," *Progress in Aerospace Sciences*, Vol. 38, Issues 6–7, 2002, Pp. 571-600.
  152. Wagner, H., Weger, M., Klaas, M., & Schröder, W. (2017). Features of owl wings that promote silent flight. *Interface focus*, 7(1), 20160078. <https://doi.org/10.1098/rsfs.2016.0078>.
  153. Wang, J.J., Li, Y.C., Choi, K.S., “Gurney flap-lift enhancement, mechanisms and applications”, *Progress in aerospace sciences*, Vol. 44, Pp. 22–47, 2008.
  154. Wang, Y., Zhao, K., Lu, X.-Y., Song, Y.-B., and Bennett, G. J., “Bio-Inspired Aerodynamic Noise Control: A Bibliographic Review,” *Applied Sciences*, vol. 9, May 2019, Pp. 2224.
  155. Wang, Z., & Zhuang, M., “Leading-edge serrations for performance improvement on a vertical-axis wind turbine at low tip-speed-ratios”, *Applied Energy*, Vol. 208, Pp. 1184–1197, 2017.
  156. Weick, F.E., Wenzinger, C.J., “Effect of Length of Handley Page Tip Slots on the Lateral-Stability Factor, Damping in Roll,” *NACA Technical Note No. 423*, 1932.
  157. Weishuang L., Yun T., Peiqing L., “Aerodynamic optimization and mechanism design of flexible variable camber trailing-edge flap”, *Chinese Journal of Aeronautics*, Pp. 988–1003, (2017).
  158. Xu, F., Gao, Z., Ming, X., Xia, L., Wang, Y., Sun, W., Ma, R., “The optimization for the backward-facing step flow control with synthetic jet based on experiment,” *Experimental Thermal and Fluid Science*, Vol. 64, 2015, Pp.94-107.
  159. Xu, K., Ren, Y., Zha, G., “Numerical Investigation of NASA Hump Using Co-flow Jet for Separation Control,” *AIAA Scitech 2020 Forum*, January 2020. <https://doi.org/10.2514/6.2020-1058>.
  160. Yagiz, B., Kandil, O., Volkan Pehlivanoglu, Y., “Drag minimization using active and passive flow control techniques,” *Aerospace Science and Technology*, Vol. 17, Issue 1, March 2012, Pp. 21-31.
  161. Yoo, N.S., “Aerodynamic Performance Improvement by Divergent Trailing Edge Modification to a Supercritical Airfoil,” *KSME International Journal*, Vol. 15, No. 10, Pp. 1434-1441, 2001.
  162. Zhang, J., Xu, K., Yang, Y., Ren, Y., Patel, P., Zha, G., “Aircraft Control Surfaces Using Co-flow Jet Active Flow Control Airfoil,” *AIAA - Applied Aerodynamics Conference*, AIAA 2018-3067, 2018.

163. Zhang, L., Li, X., Li, S., Bai, J., Xu, J., “Unstable aerodynamic performance of a very thick wind turbine airfoil CAS-W1-450,” *Renewable Energy*, Vol. 132, 2019, Pp. 1112-1120.
164. Zhang, W., Zhang, Z., Chen, Z., Tang, Q., “Main Characteristics of Suction Control of Flow Separation of an Airfoil at Low Reynolds Numbers,” *European Journal of Mechanics, B/Fluids*, Vol. 65, 2017, Pp. 88–97.
165. Zhen, T. K., Zubair, M., Ahmad, K. F., “Experimental and Numerical Investigation of the Effects of Passive Vortex Generators on Aludra UAV Performance,” *Chinese Journal of Aeronautics*, 24, 2011, Pp. 577-583.
166. Zheng, W., Yan, C., Liu, H. et al. Comparative assessment of SAS and DES turbulence modeling for massively separated flows. *Acta Mech. Sin.* 32, 12–21 (2016). <https://doi.org/10.1007/s10409-015-0505-7>.
167. Zhou, Y., Hou, L., and Huang, D., “The Effects of Mach Number on the Flow Separation Control of Airfoil with a Small Plate near the Leading Edge,” *Computers and Fluids*, Vol. 156, 2017, Pp. 274–282. doi:10.1016/j.compfluid.2017.07.014.

## **APPENDIX - A**

### **RESEARCH PUBLICATIONS**

#### **Published:**

1. Raj Mohamed, M.A., Yadav, R. and Guven, U., "Flow separation control using a bio-inspired nose for NACA 4 and 6 series airfoils", Aircraft Engineering and Aerospace Technology, 2021. <https://doi.org/10.1108/AEAT-08-2019-0170>
  
2. Raj Mohamed, M.A., Guven, U. and Yadav, R. (2019), "Flow separation control of NACA-2412 airfoil with bio-inspired nose", Aircraft Engineering and Aerospace Technology, Vol. 91, No. 7, Pp. 1058-1066. <https://doi.org/10.1108/AEAT-06-2018-0175>.













#### **Under review:**

3. Raj Mohamed, M.A., Yadav, R., "Flow separation control using the cetacean species nose design," European Journal of Mechanics / B Fluids, 2021. (EJMFLU\_2020\_495R1)

## Document Information

<b>Analyzed document</b>	INVESTIGATION ON THE FLOW SEPARATION CONTROL OF AIRFOIL WITH BIO-INSPIRED NOSE.pdf (D99432941)
<b>Submitted</b>	3/24/2021 10:44:00 AM
<b>Submitted by</b>	Rajesh
<b>Submitter email</b>	rajeshyadav@ddn.upes.ac.in
<b>Similarity</b>	5%
<b>Analysis address</b>	rajeshyadav.upes@analysis.orkund.com

## Sources included in the report

<b>W</b>	URL: <a href="https://www.x-mol.com/paper/1354174559150858240">https://www.x-mol.com/paper/1354174559150858240</a> Fetched: 3/24/2021 10:54:00 AM	 <b>9</b>
<b>W</b>	URL: <a href="https://www.emerald.com/doi/pdfplus/10.1108/AEAT-06-2018-0175">https://www.emerald.com/doi/pdfplus/10.1108/AEAT-06-2018-0175</a> Fetched: 3/24/2021 10:54:00 AM	 <b>11</b>
<b>W</b>	URL: <a href="https://www.researchgate.net/figure/A-cross-section-of-the-sinusoidal-leading-edge-...">https://www.researchgate.net/figure/A-cross-section-of-the-sinusoidal-leading-edge ...</a> Fetched: 3/24/2021 10:54:00 AM	 <b>8</b>
<b>SA</b>	<b>8531429.pdf</b> Document 8531429.pdf (D37668878)	 <b>1</b>
<b>W</b>	URL: <a href="https://www.researchgate.net/publication/262451001_Effect_of_Leading_Edge_Tubercle_...">https://www.researchgate.net/publication/262451001_Effect_of_Leading_Edge_Tubercle ...</a> Fetched: 3/24/2021 10:54:00 AM	 <b>4</b>
<b>W</b>	URL: <a href="https://www.researchgate.net/figure/Sinusoidal-tubercles-with-different-amplitudes-...">https://www.researchgate.net/figure/Sinusoidal-tubercles-with-different-amplitudes ...</a> Fetched: 3/24/2021 10:54:00 AM	 <b>2</b>
<b>W</b>	URL: <a href="https://worldwidescience.org/topicpages/h/high+lift+airfoils.html">https://worldwidescience.org/topicpages/h/high+lift+airfoils.html</a> Fetched: 10/24/2019 1:11:58 PM	 <b>4</b>
<b>W</b>	URL: <a href="http://etheses.whiterose.ac.uk/12485/1/MPhi_Kanok_Jan2015_Final.pdf">http://etheses.whiterose.ac.uk/12485/1/MPhi_Kanok_Jan2015_Final.pdf</a> Fetched: 11/18/2020 12:45:55 AM	 <b>9</b>
<b>W</b>	URL: <a href="https://www.researchgate.net/publication/343597526_Research_on_aerodynamic_perform-...">https://www.researchgate.net/publication/343597526_Research_on_aerodynamic_perform ...</a> Fetched: 3/24/2021 10:54:00 AM	 <b>3</b>
<b>SA</b>	<b>Gopinath M S thesis.pdf</b> Document Gopinath M S thesis.pdf (D25539501)	 <b>1</b>
<b>W</b>	URL: <a href="http://airfoiltools.com/airfoil/naca4digit">http://airfoiltools.com/airfoil/naca4digit</a> Fetched: 3/24/2021 10:54:00 AM	 <b>1</b>
<b>SA</b>	<b>1014239730-TS(NAVIN KUMAR B).pdf</b> Document 1014239730-TS(NAVIN KUMAR B).pdf (D25468605)	 <b>4</b>